



CONSIDERATION OF WEAR RATES AT HIGH VELOCITY

DISSERTATION

Chad S. Hale, Lieutenant Colonel, USAF

AFIT/DS/ENY/10-08

DEPARTMENT OF THE AIR FORCE
AIR UNIVERSITY

AIR FORCE INSTITUTE OF TECHNOLOGY

Wright-Patterson Air Force Base, Ohio

APPROVED FOR PUBLIC RELEASE; DISTRIBUTION UNLIMITED.

The views expressed in this dissertation are those of the author and do not reflect the official policy or position of the United States Air Force, Department of Defense, or the United States Government. This material is declared a work of the U.S. Government and is not subject to copyright protection in the United States.

AFIT/DS/ENY/10-08

CONSIDERATION OF WEAR RATES AT HIGH VELOCITY

DISSERTATION

Presented to the Faculty
Graduate School of Engineering and Management
Air Force Institute of Technology
Air University
Air Education and Training Command
In Partial Fulfillment of the Requirements for the
Degree of Doctor of Philosophy

Chad S. Hale, B.S.M.E., M.S.A.E.
Lieutenant Colonel, USAF

March 2010

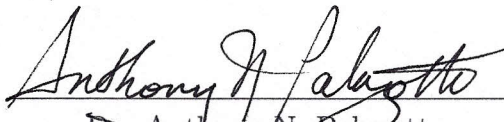
APPROVED FOR PUBLIC RELEASE; DISTRIBUTION UNLIMITED.

CONSIDERATION OF WEAR RATES AT HIGH VELOCITY

Chad S. Hale, B.S.M.E., M.S.A.E.


Lieutenant Colonel, USAF

Approved:



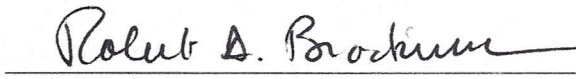
Dr. Anthony N. Palazotto
Committee Chairman

12/21/2009
date




Dr. William P. Baker
Committee Member

12 Dec 09
date



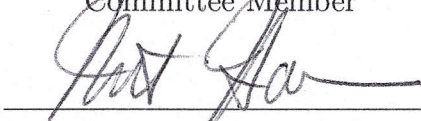
Dr. Robert A. Brockman
Committee Member

12/21/2009
date



Dr. George Z. Voyiadjis
Committee Member

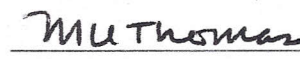
12/21/2009
date



Dr. Michael D. Hooser
Committee Member

21 Dec 09
date

Accepted:



M. U. THOMAS
Dean, Graduate School of Engineering
and Management

22 Jan 2010
date

Abstract

The development of the research presented here is one in which high velocity relative sliding motion between two bodies in contact has been considered. Overall, the wear environment is truly three-dimensional. The attempt to characterize three-dimensional wear was not economically feasible because it must be analyzed at the micro-mechanical level to get results. Thus, an engineering approximation was carried out. This approximation was based on a metallographic study identifying the need to include viscoplasticity constitutive material models, coefficient of friction, relationships between the normal load and velocity, and the need to understand wave propagation.

A sled test run at the Holloman High Speed Test Track (HHSTT) was considered for the determination of high velocity wear rates. In order to adequately characterize high velocity wear, it was necessary to formulate a numerical model that contained all of the physical events present. The experimental results of a VascoMax 300 maraging steel slipper sliding on an AISI 1080 steel rail during a January 2008 sled test mission were analyzed. During this rocket sled test, the slipper traveled 5,816 meters in 8.14 seconds and reached a maximum velocity of 1,530 m/s. This type of environment was never considered previously in terms of wear evaluation. Each of the features of the metallography were obtained through micromechanical experimental techniques. The byproduct of this analysis is that it is now possible to formulate a model that contains viscoplasticity, asperity collisions, temperature and frictional features.

Based on the observations of the metallographic analysis, these necessary features have been included in the numerical model, which makes use of a time-dynamic program which follows the movement of a slipper during its experimental test run. The resulting velocity and pressure functions of time have been implemented in the explicit finite element code, ABAQUS. Two-dimensional, plane strain models were

used to determine the state of stress within the slipper and the pressure distribution along the bottom. Local submodel collisions between the slipper and a 6 μm radius hemispherical asperity were analyzed to determine mechanical and melt wear rates. A simplified damage criterion of maximum Mises stress was used to determine the damaged volume during the slipper and asperity collision. Overall, the model predicts a total wear volume that is approximately 36% of the total wear measured during the metallographic analysis.

Acknowledgements

I could not have accomplished this task without the support and encouragement of my wife, who is my best friend and eternal companion, and our children. During my doctoral studies, especially during the final push to finish this dissertation, my family has all shown great love, encouragement, patience, and support during the long hours, late nights, and weekends at the school. I hope that my pursuit of education will inspire and encourage my family to continue to seek further knowledge.

Additionally, I'd like to thank my research advisor, Dr. Anthony Palazotto, for his excitement, encouragement, and guidance in this research project. He spent much of his personal time researching articles, developing theory, and asking pointed questions to help me gain a better understanding of high velocity wear rates. Dr. Palazotto carefully guided me through the research effort and I value his friendship. His enthusiasm and experience with the high velocity wear phenomenon kept me focused on the final goal. I'd like to thank the other members of my research committee who also provided wonderful technical expertise and support to my various questions: Dr. William Baker, AFIT/ENC; Dr. Robert Brockman, University of Dayton; Dr. George Voyiadjis, Louisiana State University; and Dr. Michael Hooser, 846th Test Squadron, Holloman AFB, NM.

The research project was sponsored and funded by Dr. John Schmisser and Major Michelle Ewy of the Air Force Office of Scientific Research. At the Holloman High Speed Test Track, Mr. George Ayers and Second Lieutenant Julius Puentes provided excellent support with dynamic model data, and slipper/rail specimens. Mr. Larry Perkins, Mr. Adam Long, Mr. Kevin Shiveley and Mr. Robert Lewis of the Air Force Research Laboratory, Materials and Manufacturing Directorate, Wright-Patterson AFB, OH, provided invaluable expertise and support during the metallographic analysis.

Chad S. Hale

Table of Contents

	Page
Abstract	iv
Acknowledgements	vi
List of Figures	xi
List of Tables	xvi
List of Symbols	xvii
List of Abbreviations	xx
I. High Velocity Wear Problem Overview	1
1.1 Objective of the Research	1
1.2 Holloman High Speed Test Track Environment	1
1.3 January 2008 Test Mission	4
1.4 Description of Wear	5
1.5 Mechanisms of Wear	8
1.5.1 Abrasive Wear	9
1.5.2 Adhesive Wear	9
1.5.3 Melt Wear	9
1.5.4 Wear Rate	10
1.6 Wear-Mechanism Maps	11
1.7 Review of Previous Wear Research at Various Velocities	11
1.7.1 Velocity Range: 0 to 10 m/s	11
1.7.2 Velocity Range: 10 to 100 m/s	16
1.7.3 Velocity Range: 100 to 1,000 m/s	22
1.8 Holloman High Speed Test Track (HHSTT) Wear Research	26
1.9 AFIT Initial Wear Research	29
1.10 Key Concepts from the Literature Search	30
II. Metallographic Analysis	32
2.1 Slipper Physical Characterizations	33
2.1.1 Before the Test Mission	33
2.1.2 During the Test Mission	35
2.1.3 After the Test Mission	36
2.2 VascoMax 300 Material Properties	36
2.2.1 Equilibrium and Transformation Phase Diagrams	37

	Page	
2.3	Slipper Surface Characterization	37
2.4	Specimen Preparation	43
2.5	Wear Volume Calculations	46
2.6	Hardness Test Results	51
	2.6.1 Bulk Hardness Tests: Rockwell Hardness	52
	2.6.2 Microindentation Hardness Tests: Knoop Hardness	52
2.7	Optical Micrographs	55
2.8	VascoMax 300 Chemical Composition Analysis	57
2.9	Summary of Metallographic Analysis	59
III.	Numerical Modeling	61
	3.1 Model Components	62
	3.1.1 Dynamic Analysis and Design System (DADS) Model	62
	3.1.2 January 2008 Test Mission Raw DADS Data	64
	3.1.3 DADS Comparison: January 2008 vs. 80X-A1 Test Mission	71
	3.1.4 DADS Statistical Analysis	72
	3.1.5 Frictional Contribution	76
	3.2 Global Finite Element Analysis	79
	3.2.1 Global Model	81
	3.2.2 Model Geometry	83
	3.2.3 Boundary and Initial Conditions	85
	3.2.4 Material Properties	88
	3.2.5 Mesh and Element Definition	90
	3.3 Local Submodel Finite Element Analysis	92
	3.3.1 Model Geometry	93
	3.3.2 Boundary and Initial Conditions	95
	3.3.3 Material Properties	96
	3.3.4 Mesh Convergence Study	99
	3.4 Johnson-Cook Stress Strain Curve for VascoMax 300	108
	3.4.1 Strain Rate Analysis	111
	3.5 Mechanical Wear Rate Calculations	115
	3.5.1 Determining Wear Rate per Unit Width	116
	3.5.2 Wear Rate for Three-Dimensional, Hemispherical 6 μm Asperity	121
	3.6 Preliminary Studies and Results	128
	3.6.1 Global to Local Submodel Stress Mapping	128
	3.6.2 Acceleration, Deceleration and Constant Velocity Comparison	130

	Page	
3.7	Global Model Pressure Distributions	133
3.8	Melt Wear Rate Calculations	134
3.8.1	Frictional Heating and Temperature Profile	137
3.8.2	Flash Temperature Rise	144
3.9	Numerical Modeling Summary	152
IV.	Results and Discussion	155
4.1	Single Asperity Wear Rate Results	155
4.2	Slipper/Asperity Impact Wave Analysis	159
4.2.1	Velocity Case: 20 m/s	163
4.2.2	Velocity Case: 500 m/s	163
4.2.3	Velocity Case: 1,530 m/s	166
4.3	Comparison of Slipper and Model Total Wear Volume	168
4.3.1	Theory of Archard Wear Coefficient	169
4.3.2	Lim and Ashby Wear Coefficient Study	169
4.3.3	Three-Dimensional Proportion Factor, N	172
4.3.4	Total Wear Volume Calculations	173
V.	Conclusions	177
Appendix A.	DADS Statistical Analysis	182
Appendix B.	Wear Rate per Unit Width Results	189
B.1	Wear Rate per Unit Width: 6 μm Asperity	189
B.2	$R = 6 \mu\text{m}, V = 10 \text{ m/s}$	189
B.3	$R = 6 \mu\text{m}, V = 20 \text{ m/s}$	190
B.4	$R = 6 \mu\text{m}, V = 40 \text{ m/s}$	191
B.5	$R = 6 \mu\text{m}, V = 100 \text{ m/s}$	192
B.6	$R = 6 \mu\text{m}, V = 200 \text{ m/s}$	193
B.7	$R = 6 \mu\text{m}, V = 300 \text{ m/s}$	194
B.8	$R = 6 \mu\text{m}, V = 500 \text{ m/s}$	195
B.9	$R = 6 \mu\text{m}, V = 622 \text{ m/s}$	196
B.10	$R = 6 \mu\text{m}, V = 750 \text{ m/s}$	197
B.11	$R = 6 \mu\text{m}, V = 1,000 \text{ m/s}$	198
B.12	$R = 6 \mu\text{m}, V = 1,250 \text{ m/s}$	199
B.13	$R = 6 \mu\text{m}, V = 1,530 \text{ m/s}$	200
B.14	Wear Rate per Unit Width: 4 μm Asperity	201
B.15	$R = 4 \mu\text{m}, V = 10 \text{ m/s}$	201

	Page
B.16 $R = 4 \mu\text{m}$, $V = 100 \text{ m/s}$	202
B.17 $R = 4 \mu\text{m}$, $V = 500 \text{ m/s}$	203
B.18 $R = 4 \mu\text{m}$, $V = 1,000 \text{ m/s}$	204
B.19 $R = 4 \mu\text{m}$, $V = 1,530 \text{ m/s}$	205
B.20 Wear Rate per Unit Width: $2 \mu\text{m}$ Asperity	206
B.21 $R = 2 \mu\text{m}$, $V = 10 \text{ m/s}$	206
B.22 $R = 2 \mu\text{m}$, $V = 100 \text{ m/s}$	207
B.23 $R = 2 \mu\text{m}$, $V = 500 \text{ m/s}$	208
B.24 $R = 2 \mu\text{m}$, $V = 1,000 \text{ m/s}$	209
B.25 $R = 2 \mu\text{m}$, $V = 1,530 \text{ m/s}$	210
Bibliography	211
Vita	219

List of Figures

Figure		Page
1.1	Rocket Sled System at the HHSTT	2
1.2	January 2008 Rocket Test Sled	4
1.3	AISI 4130 Steel Pupfish Pusher Slipper Insert	6
1.4	VascoMax 300 SRR Slipper	6
1.5	Typical Slipper/Rail Configuration	7
1.6	Abrasive and Adhesive Wear [11]	9
1.7	Variation of Coefficient of Friction with Load [34]	14
1.8	Sliding Velocity Effect of Coefficient of Friction [42]	17
1.9	Typical Artillery Projectile [60]	18
1.10	Coefficient of Friction as a Function of Pv [62]	19
1.11	Plate Impact Pressure-Shear Friction Experiment Schematic [65]	20
1.12	Comparison of Simulated and Experimental Results [59]	21
1.13	Schematic of Friction Device [64]	23
1.14	Schematic of High Speed Friction Apparatus [17]	24
1.15	Steel-Steel: Coefficient of Friction [18]	25
1.16	Wear Rate of Projectile Steel as a Function of Pv [61]	26
1.17	HHSTT Coefficient of Friction as a Function of Velocity [45]	28
2.1	VascoMax 300 Test Slipper and New Sample	34
2.2	Slipper Thickness Measurement Locations	34
2.3	Stage 3 and 4 Velocity Profiles, Jan 2008 Test Mission	35
2.4	Iron-Nickel Two-Phase Diagrams [35]	38
2.5	Preparing Slipper for Metallurgical Investigation	39
2.6	Right Half Slipper Surface Locations	39
2.7	Close-Up Views of Test Slipper Surface	41
2.8	Surface Comparisons, SEM, 50x	42

Figure		Page
2.9	Surface Comparisons, SEM, 500x	42
2.10	Surface Comparisons, SEM, 1000x	43
2.11	Metallurgical Analysis Specimen Locations	45
2.12	Metallurgical Analysis Specimen Mounts	45
2.13	Profile of Aft Right Slipper	47
2.14	Slipper Top Thickness Measurements	48
2.15	Slipper Side and Lip Thickness Measurements	49
2.16	Forward Rotation of Test Slipper [2]	51
2.17	Rockwell Hardness of Perpendicular and Parallel Specimens . .	53
2.18	Knoop Hardness of Perpendicular and Parallel Specimens . . .	54
2.19	Optical Micrographs, Perpendicular Specimens, 200x	55
2.20	Optical Micrographs, Perpendicular Specimens, 500x	56
2.21	Energy Dispersive X-ray Spectroscopy, Test Slipper Specimen .	59
3.1	Slipper Impact Marks on White Epoxy Rail	63
3.2	DADS Model for 80X-G1 Forebody Sled	64
3.3	Position of Sled C.G., Jan 2008 Test Mission	65
3.4	Velocity of Sled C.G., Jan 2008 Test Mission	67
3.5	Acceleration of Sled C.G., Jan 2008 Test Mission	67
3.6	Horizontal Position, Velocity, and Acceleration	68
3.7	DADS Contact Locations on Rail Cross Section	68
3.8	Normal Slipper/Rail Contact Forces	69
3.9	Normal Contact Forces, 0-2 seconds	70
3.10	Percentage Distance in Contact	72
3.11	Percentage Time in Contact	73
3.12	DADS Raw and Statistical Contact Force	74
3.13	DADS Statistical Upper Limit Pressure	75
3.14	Montgomery Coefficient of Friction vs. Pressure Velocity	77
3.15	Coefficient of Friction vs. Pressure Velocity	78

Figure		Page
3.16	Global Slipper Bounce Model	83
3.17	Global Model Geometry	85
3.18	Global Model Boundary and Initial Conditions	85
3.19	Global Model Components	87
3.20	ABAQUS Plane Strain Elements	91
3.21	Global and Local Submodel Relationship	92
3.22	Original Slipper Submodel Schematic	94
3.23	Final Slipper Submodel Schematic	94
3.24	Local Submodel Boundary and Initial Conditions	96
3.25	Representative Slipper and Rail Interface Elements	99
3.26	Local Submodel Mesh Size Comparison	100
3.27	Mesh Comparison, SM Mesh 1, 2, and 3, $V = 40$ m/s	101
3.28	Mesh Comparison, SM Mesh 1, 2, and 3, $V = 500$ m/s	102
3.29	SM Mesh Convergence: 45° Path Definition	103
3.30	Mises Stress Along 45° Path, $V = 100$ m/s	103
3.31	Mises Stress Along 45° Path, $V = 1,530$ m/s	104
3.32	Nodal Location Comparison, SM Mesh 2 vs. SM Mesh 4	105
3.33	Mises Stress Comparison at Coincident Nodes, $V = 1,530$ m/s	105
3.34	Mesh Comparison, SM Mesh 2 vs. Mesh 4, $V = 100$ m/s	106
3.35	Mesh Comparison, SM Mesh 2 vs. Mesh 4, $V = 1,000$ m/s	107
3.36	Mesh Comparison, SM Mesh 2 vs. Mesh 4, $V = 1,530$ m/s	107
3.37	VascoMax 300 Temperature Rise Due to Plastic Deformation	110
3.38	VascoMax 300 Stress-Strain Relationships	110
3.39	Single Cube Element Tensile Test	112
3.40	Strain Rate Analysis: Area Ratio, $V = 1,530$ m/s	114
3.41	Strain Rate Analysis, $V = 1,530$ m/s, Undeformed Slipper	115
3.42	Wear Rate per Unit Width, $6 \mu\text{m}$, $V = 10$ m/s	119
3.43	Wear Rate Comparison, SM Mesh 2 vs. Mesh 4, $V = 1,000$ m/s	122

Figure		Page
3.44	Wear Rate Comparison, SM Mesh 2 vs. Mesh 4, $V = 1,530$ m/s	123
3.45	Hemispherical Asperity Model	124
3.46	Single Asperity Wear Rate, $V = 10$ m/s	125
3.47	Single Asperity Wear Rate, $V = 100$ and 500 m/s	126
3.48	Single Asperity Wear Rate, $V = 1,000$ and $1,530$ m/s	127
3.49	Global to Local Submodel Stress Mapping	129
3.50	Accel/Decel Study Results, $V = 1,000$ m/s	132
3.51	Pressure Distribution: Global Total Contact Model	135
3.52	Pressure Distribution: Global Quasi-Steady Model	136
3.53	Pressure Distribution: Global Bounce Model	136
3.54	One-Dimensional Heat Transfer Analysis Schematic	140
3.55	One-Dimensional Heat Transfer Results	143
3.56	Slipper Frictional Heating Temperature Profile, Low Velocities	145
3.57	Slipper Frictional Heating Temperature Profile	145
3.58	Single Contact Area Model [5]	146
3.59	Melt Depth Temperature Profile, Low Velocities	151
3.60	Melt Depth Temperature Profile, High Velocities	152
4.1	Mechanical Wear Rates	157
4.2	Melt Wear Rates	159
4.3	Comparison of Mechanical and Melt Wear Rates	160
4.4	Slipper/Asperity Impact Wave Propagation, $V = 1,530$ m/s . .	161
4.5	Impact Wave Analysis Path and Nodes	162
4.6	Pressure Along Path with Varying Time, $V = 20$ m/s	164
4.7	Pressure at Nodes in Time, $V = 20$ m/s	164
4.8	Pressure Along Path with Varying Time, $V = 500$ m/s	165
4.9	Pressure at Nodes in Time, $V = 500$ m/s	166
4.10	Pressure Along Path with Varying Time, $V = 1,530$ m/s	167
4.11	Pressure at Nodes in Time, $V = 1,530$ m/s	168

Figure		Page
4.12	VascoMax 300 Stress Strain Curve [1; 77]	172
4.13	Total Mechanical Wear Volume	174
4.14	Total Melt Wear Volume	176
A.1	Incremental Approach with Original DADS Data	183
A.2	Sample DADS Statistical Data	185
A.3	DADS Statistical Analysis Force and Pressure	186
A.4	Mean and Upper Limit Pressure Functions	188
B.1	Wear Rate per Unit Width, 6 μm , $V = 10 \text{ m/s}$	189
B.2	Wear Rate per Unit Width, 6 μm , $V = 20 \text{ m/s}$	190
B.3	Wear Rate per Unit Width, 6 μm , $V = 40 \text{ m/s}$	191
B.4	Wear Rate per Unit Width, 6 μm , $V = 100 \text{ m/s}$	192
B.5	Wear Rate per Unit Width, 6 μm , $V = 200 \text{ m/s}$	193
B.6	Wear Rate per Unit Width, 6 μm , $V = 300 \text{ m/s}$	194
B.7	Wear Rate per Unit Width, 6 μm , $V = 500 \text{ m/s}$	195
B.8	Wear Rate per Unit Width, 6 μm , $V = 622 \text{ m/s}$	196
B.9	Wear Rate per Unit Width, 6 μm , $V = 750 \text{ m/s}$	197
B.10	Wear Rate per Unit Width, 6 μm , $V = 1,000 \text{ m/s}$	198
B.11	Wear Rate per Unit Width, 6 μm , $V = 1,250 \text{ m/s}$	199
B.12	Wear Rate per Unit Width, 6 μm , $V = 1,530 \text{ m/s}$	200
B.13	Wear Rate per Unit Width, 4 μm , $V = 10 \text{ m/s}$	201
B.14	Wear Rate per Unit Width, 4 μm , $V = 100 \text{ m/s}$	202
B.15	Wear Rate per Unit Width, 4 μm , $V = 500 \text{ m/s}$	203
B.16	Wear Rate per Unit Width, 4 μm , $V = 1,000 \text{ m/s}$	204
B.17	Wear Rate per Unit Width, 4 μm , $V = 1,530 \text{ m/s}$	205
B.18	Wear Rate per Unit Width, 2 μm , $V = 10 \text{ m/s}$	206
B.19	Wear Rate per Unit Width, 2 μm , $V = 100 \text{ m/s}$	207
B.20	Wear Rate per Unit Width, 2 μm , $V = 500 \text{ m/s}$	208
B.21	Wear Rate per Unit Width, 2 μm , $V = 1,000 \text{ m/s}$	209
B.22	Wear Rate per Unit Width, 2 μm , $V = 1,530 \text{ m/s}$	210

List of Tables

Table		Page
1.1	Summary of January 2008 Mission	7
1.2	Test Track Coefficient of Friction	29
2.1	Summary of VascoMax 300 Slipper Specimens	44
2.2	Chemical Composition of Slipper Specimens by Percent Weight)	58
3.1	Comparison of DADS Contact Percentages	72
3.2	Summary of DADS Statistical Data at Target Velocities	76
3.3	Slipper and Rail Material Properties [29; 30]	90
3.4	Global Model Uniform Mesh Analysis	91
3.5	Local Submodel Step Times in Seconds	95
3.6	Slipper and Rail EOS Material Properties	98
3.7	Local Submodel Mesh Comparison	100
3.8	Maximum Mises Stress Comparison	112
3.9	Strain Rate Analysis Results	115
3.10	Wear Rate per Unit Width, W_{uw} , Various Asperity Radii	121
3.11	Single Asperity Wear Rates	128
3.12	Acceleration/Deceleration Study Conditions	131
3.13	1,000 m/s Acceleration/Deceleration Study Results	132
3.14	Maximum Contact Pressures for Global Models	135
3.15	VascoMax 300 Material Properties	139
3.16	Melt Wear Rate Heat Transfer Analysis Summary	148
4.1	Single Asperity Mechanical and Melt Wear Rates	156
4.2	Wave Propagation Nodes Along Path Length	162
4.3	Sample Variation in Wear Coefficient, k_A [67]	171
A.1	DADS Upper Limit and Mean Pressure Coefficients	187

List of Symbols

Symbol		Page
m	meter	2
s	second	2
N	Newton	2
W	dimensional wear rate	10
V	volume	10
d	sliding distance	10
H	material indentation hardness	10
k_A	Archard wear coefficient	10
ms	microsecond	12
Pv	pressure velocity	18
w_{melt}	melt wear rate	30
w_{k_A}	mechanical wear rate	30
γ	austenite or gamma phase iron	37
α	ferrite or alpha phase iron	37
u_x	horizontal displacement degree of freedom	85
u_y	vertical displacement degree of freedom	85
θ_z	displacement rotation degree of freedom	85
ν	Poisson's ratio	88
T_{melt}	melting temperature	88
ε^p	equivalent plastic strain	89
$\dot{\varepsilon}^{p*}$	dimensionless plastic strain rate	89
$\dot{\varepsilon}_0$	reference strain rate	89
T^*	homologous temperature	89
T_{ref}	reference temperature	89
T_{room}	room temperature	89

Symbol		Page
A	Johnson-Cook coefficient	89
B	Johnson-Cook coefficient	89
C	Johnson-Cook coefficient	89
m	Johnson-Cook coefficient	89
n	Johnson-Cook coefficient	89
β	inelastic heat fraction	89
σ_e	von Mises stress	90
E	specific internal energy	97
ΔT	temperature rise	108
c_p	ratio of specific heats	108
W	wear rate	116
V	volume	116
d	sliding distance	116
L	length dimension	116
W_{uw}	wear rate per unit width	116
A_d	damage area	116
w_{eff}	effective width	116
A_{dtot}	cumulative damage area	117
A_{di}	incremental damage area	117
W_{sa}	single asperity wear rate	125
v_1	initial velocity	130
v_2	final velocity	130
v_{avg}	average velocity	130
a_{avg}	average acceleration	131
q_f	sliding friction rate of work or energy	137
F	normal load	138
α	thermal diffusivity	139
k	thermal conductivity	139

Symbol		Page
Fo	Fourier number	141
T_{frict}	frictional heating surface temperature	144
Pe	Péclet number	146
ΔT_{flash}	flash temperature increase	147
$W_{uw,melt}$	melt wear rate per unit width	148
A_{melt}	melt area	148
$W_{sa,melt}$	single asperity melt wear rate	151
k_A	Archard wear coefficient	169
f_v	volume fraction of inclusions	171
f_A	area fraction of voids	171
γ_0	accumulated plastic shear strain	171
f_A^*	critical area fraction of inclusions	171
F_m	mean force	184
F_{ll}	lower limit force	184
F_{ul}	upper limit force	184
P_{ul}	upper limit pressure	184
P_m	mean pressure	184

List of Abbreviations

Abbreviation		Page
AFB	Air Force Base	1
HHSTT	Holloman High Speed Test Track	1
AISI	American Iron and Steel Institute	2
AFOSR	Air Force Office of Scientific Research	3
MLRS	Multiple Launch Rocket System	4
SRR	Super Roadrunner	5
ASTM	American Society for Testing and Materials	7
NACA	National Advisory Committee for Aeronautics	16
AFRL	Air Force Research Laboratory	32
UTS	ultimate tensile strength	36
IMC	Image Motion Compensation	50
HRC	Rockwell Hardness Test C	52
HK	Knoop Microindentation Hardness Test	52
EDS	Energy Dispersive X-Ray Spectroscopy	57
COTS	Commercial Off the Shelf	63
C.G.	center of gravity	64
EOS	Equation of State	96
PDF	Probability Density Function	183

CONSIDERATION OF WEAR RATES AT HIGH VELOCITY

I. High Velocity Wear Problem Overview

This research is directed towards an understanding of the high speed interaction effects that two sliding bodies have on each other. The experimental high-speed test track at Holloman Air Force Base (AFB) has undergone many design innovations over a span of fifty years. One of the problems that remains in the modern era related to improving the speed characteristics of a rocket test sled is the wear that the interconnecting device, called the slipper, undergoes as it slides down the rail.

1.1 Objective of the Research

The objective of this research is to develop a numerical model for the wear rate between two sliding materials in contact at high velocity. Particular emphasis will be on understanding the necessary features to be considered in the determination of both mechanical and melt wear rates of a VascoMax 300 slipper sliding on a AISI 1080 steel rail at velocities up to 1,530 m/s. High velocity wear rates are evaluated through the metallographic examination of an experimental test slipper, from the January 2008 test mission. A numerical model for determining mechanical and melt wear rates is then developed based on the phenomenological characteristics of the test slipper. A secondary objective of this research is to use the wear rate model to determine the total wear volume and ultimately compare with the experimental results observed in the January 2008 test slipper.

1.2 Holloman High Speed Test Track Environment

The Holloman High Speed Test Track (HHSTT), located at Holloman AFB, NM, is a U.S. Air Force rocket powered sled track facility used for investigating hypersonic environments, aircraft munitions and egress systems, and aerodynamic related effects. This includes testing of a variety of hypervelocity aerospace applications at speeds

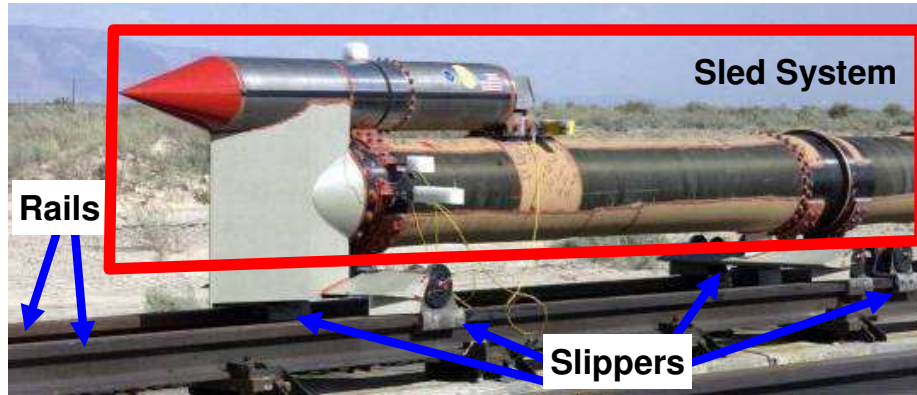


Figure 1.1: Rocket Sled System at the HHSTT

approaching 3,000 m/s. The HHSTT performs this testing using rocket-propelled sleds that travel on steel tracks made from AISI 1080 steel crane rails.

Each rocket sled train usually consists of several pusher stages and one forebody stage. The purpose of each pusher sled is to accelerate the forebody sled to the required test parameter velocity. The test payload is mounted to the forebody rocket sled. Each of the sleds in the train is held on the track by four steel slippers. Figure 1.1 illustrates the rocket sled system and identifies the slippers and rails. The test item for this particular sled, shown with the red nose cone, was the 854 N (192-pound) Missile Defense Agency payload shown mounted above the final, or forebody stage, of the rocket sled train. To date, the fastest sled on record reached a velocity of 2,885 m/s in April 2003 on a newly developed dual rail sled system.

Research at the HHSTT has to consider several features that result from the physics of high velocity. Each rocket sled is designed for the specific test objectives and fabricated at the HHSTT facilities. Track engineers must consider a multitude of factors when designing test sleds and slipper components. After more than fifty years of test track operations and research, several features have been implemented to enable test sleds to reach hypersonic velocities. For most hypersonic testing, a helium environment is used to increase velocity and to reduce aerodynamic drag and aerothermal effects on the sled [3; 57]. A disposable plastic tunnel is inflated with helium and runs for most of the length of the track. As the sled enters the helium

environment, there is a dramatic decrease in the stagnation temperature due to the reduced density and increased specific heat capacity of helium.

Significant research has been conducted in the area of high-energy impact creating gouging at the interface of a slipper/rail boundary brought about by contact of the test sled on the track. These gouges typically are a result of a high pressure core developing at the slipper/rail interface and high viscoplasticity that leads to material mixing. The feature of gouging, associated with high energy impacts characterized by a teardrop shaped shallow depression in both the slipper and rail material, has been studied in recent years by Laird [48; 49; 50], Szmerekovsky [73; 74; 75], and Cinnamon [26; 30; 31] under Air Force Office of Scientific Research (AFOSR) sponsorship. Near the high velocity end of the track, coatings are applied to each rail to help eliminate the slipper/rail gouging phenomenon. The rail is coated first with red oxide coating, and then white epoxy paint. As technology and interest expand, customers have expressed interest in achieving even higher velocities on the order of 3,000 m/s [56; 57].

An even more important phenomenon related to this high velocity impact feature is the amount of wear, which is the removal of material between two interacting surfaces, associated with the slipper/rail interaction. While the gouging event typically occurs at velocities greater than 1,500 m/s, the complex wear event begins as soon as the sled starts to move, and continues for the duration of the test mission. This research is the first AFIT dissertation in a series of studies into high velocity wear as it relates to the Holloman High Speed Test Track. Cameron [23; 24] and Chmiel [25] both studied the HHSTT high velocity wear phenomenon during their AFIT thesis research in 2007 and 2008, respectively.

In addition to the test objective, test environment, and instrumentation, HHSTT track engineers also have many considerations for the slipper design. After all, the slippers are the lone interface between the moving test sled and the stationary rail system. The slipper material must be durable enough to survive the dynamic

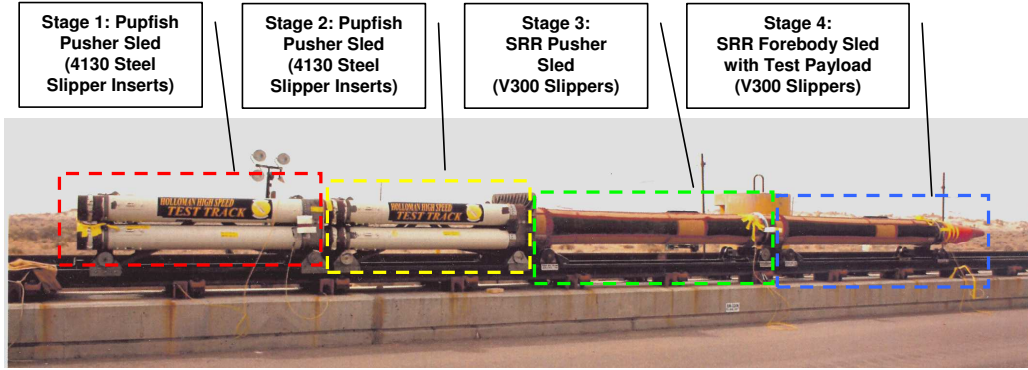


Figure 1.2: January 2008 Rocket Test Sled

loads associated with the high speed test mission. The initial slipper thickness must be sufficiently large so that slipper wear developed during the test run doesn't exceed the initial slipper thickness while maintaining design strength and integrity. As with hypervelocity gouging, excessive wear leads to a weakened structure and ultimately a catastrophic failure where the test sled departs the test track prior to reaching the test target at the required parameters. The HHSTT slipper design must consider the changing dimensions brought about by wear which changes the geometry of the slipper, thus ultimately affecting the slipper/rail interaction.

1.3 January 2008 Test Mission

During a visit to Holloman AFB, NM, in January 2008, a hypervelocity rocket test sled mission was observed. This particular test mission serves as the basis for the overall research investigation. The pre-test modeling prediction and actual test mission data and results are used for verification and comparison with the wear prediction technique. This particular rocket sled train was made up of four stages: three pusher sleds and one forebody test sled. The test payload was mounted to the front of the forebody sled as shown in Figure 1.2. The first two stages, known as Pupfish pusher sleds, used AISI 4130 steel slipper inserts as shown in Figure 1.3 looking towards the front of the pusher sled. The nominally 6.35 mm thick slipper insert was mounted within the slipper housing. Each Pupfish pusher sled was propelled by six U.S. Army M270 Multiple Launch Rocket System (MLRS) rocket motors with a com-

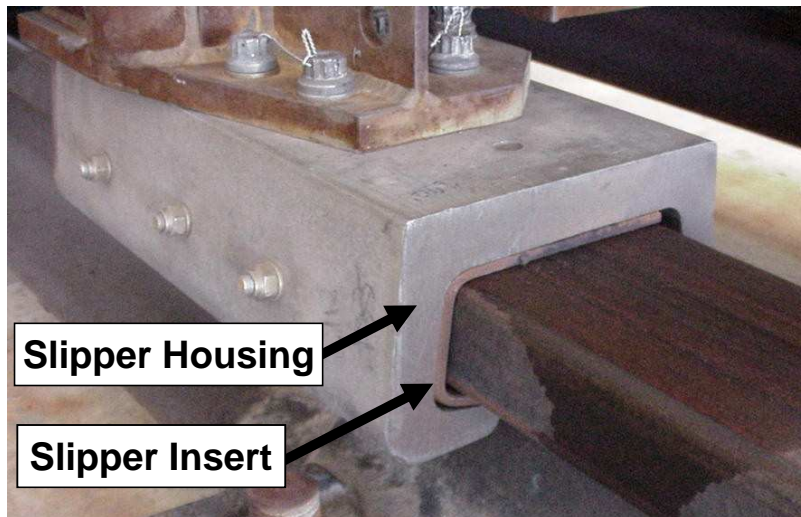
bined thrust of 785 kN (176 kips). After their motors burn out, the Pupfish pusher sleds decelerated and eventually coasted to a stop on the track. Because the entire Pupfish sled is recovered, the worn slipper inserts are removed and replaced with new inserts for subsequent sled tests.

Stages 3 and 4 used a single Super Roadrunner (SRR) rocket motor that provides an average thrust of 667 kN (150 kips) [3]. Figure 1.4 depicts the typical VascoMax 300 (V300) maraging steel slipper again looking towards the front of the sled. The slipper beam is the horizontal structural member that supports the rocket motor, and connects the left and right side slippers. The initial clearance between the rail and slipper, or slipper gap, is nominally 3.175 mm [3]. Because the SRR sleds depart the rail at extremely high velocity, these VascoMax 300 slippers are only used for a single rocket sled test mission. Figure 1.5 shows a schematic of the VascoMax 300 slipper, with dimensions 10.16 cm in width, 20.32 cm in length, and 1.27 cm in thickness, on the rail. This research focuses on the interface between the top of the rail and the bottom of the slipper. In a sense, the slipper is modeled as a box, with the dimensions previously listed, sliding across the top of the rail. Wear is not predicted for the sides and lips of the slipper that wrap around the rail.

The rocket motors for each stage of the test sled are fired sequentially at specific locations along the track. Table 1.1 outlines the distance and maximum velocity information, as calculated by HHSTT after the test mission, for each of the four test sled stages. After the test mission, the slippers and slipper inserts for the first three stages were recovered. No forebody slippers were recoverable due to the extremely violent, high speed impact between the forebody sled and the intended target. Four VascoMax 300 SRR slippers and eight AISI 4130 steel slipper inserts, four from each of the two Pupfish pusher sleds, were delivered to AFIT for physical on-site investigation.

1.4 Description of Wear

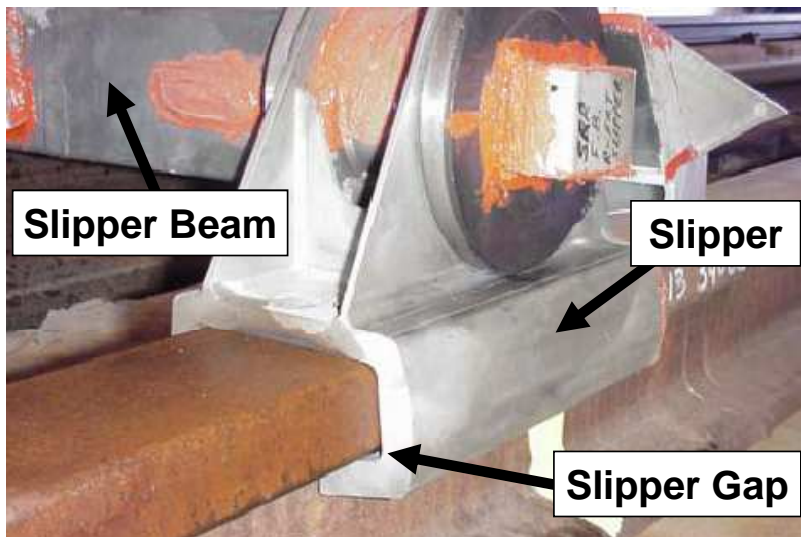
The literature search revealed that there are many different definitions of wear. Hutchings [38] indicates that the widest definition of wear, which has been accepted



Slipper Housing

Slipper Insert

Figure 1.3: AISI 4130 Steel Pupfish Pusher Slipper Insert



Slipper Beam

Slipper

Slipper Gap

Figure 1.4: VascoMax 300 SRR Slipper

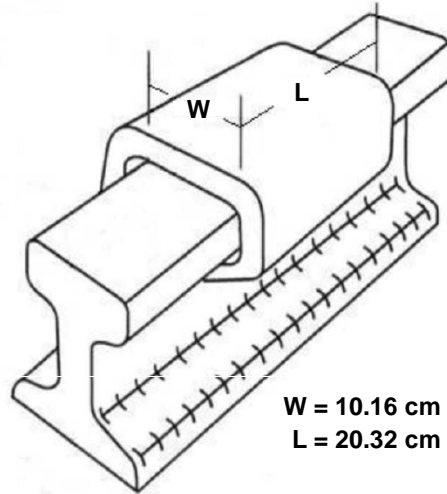


Figure 1.5: Typical Slipper/Rail Configuration

Table 1.1: Summary of January 2008 Mission

Stage #	Sled Type	Slipper Material	Distance (m)	Max Velocity (m/s)
1	Pupfish Pusher	AISI 4130 Steel	2,940	342.0
2	Pupfish Pusher	AISI 4130 Steel	4,761	731.1
3	SRR Pusher	VascoMax 300	5,816	1,530
4	SRR Forebody	VascoMax 300	5,816	2,175

for at least fifty years, “includes the loss of material from a surface, transfer of material from one surface to another or movement of material within a single surface”. From the American Society for Testing and Materials (ASTM) standard terminology, wear is “damage to a solid surface, generally involving progressive loss of material, due to relative motion between that surface and a contacting substance or substances [8]”.

Bayer [11] lists some of the more general aspects of wear behavior. “Wear is a system property, not a material property. Materials can wear by a variety of mechanisms and combinations of mechanisms, depending on the tribosystem in which it is used. Wear behavior is frequently nonlinear. Transitions can occur in wear behavior as a function of a wide variety of parameters.”

1.5 *Mechanisms of Wear*

Just as there are many definitions for wear, there are also many ways to classify wear. Bayer [12] submits that there are three apparent ways to classify wear. In no particular order, the first is in terms of the appearance of the wear scar. For example, terms like scratched, polished, pitted, etc. are often used. Second, in terms of the physical mechanism that causes damage. A few examples of this type of classification are adhesion, abrasion, melt, and oxidative. The third classification is in terms of the situation surrounding the wear condition. Some examples include dry sliding wear, lubricated wear, rolling wear, and metal-to-metal sliding wear. Bhushan states that the wear mechanisms “have only one thing in common: the removal of material from rubbing surfaces [14].” Bayer [10] defines the wear mechanism as

“any mechanism or combination of mechanisms in which change to solid-material components is caused by contact and relative motion between a solid surface and one or more other substances. As a result there is virtually an endless list of wear mechanisms, as attested by the large number of terms used to describe wear behavior and mechanism in different situation.”

Slipper wear at the Holloman High Speed Test Track could be referred to in many ways. The slipper wear can be seen as melt wear because slipper material is removed due to induced temperatures that surpass the material’s melting temperature. It may be considered dry sliding wear because no intentional lubricant or moisture is introduced into the slipper/rail contact area which has a relative sliding velocity. Or, it may be considered compound impact wear as a result of the slipper’s combined effect of both sliding on and impacting the rail during the “bouncing or skipping” motion. Any observed wear can be a mixture of these different wear modes [43].

According to Kato, the mechanisms of wear can be grouped into three types of wear: mechanical, chemical, and thermal [43]. Abrasive, adhesive, flow or fatigue wear are categorized as mechanical wear. Corrosive and oxidative wear are mechanisms of chemical wear. Melt and diffusive wear are categorized as thermal wear. The various mechanisms of wear contribute to the overall coefficient of friction, μ .

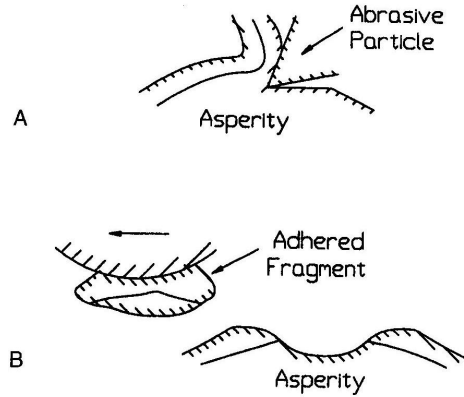


Figure 1.6: Abrasive and Adhesive Wear [11]

In the summary of the literature search, the various researchers use many of these terms to report the findings of their studies. Several of the wear mechanisms are briefly described here.

1.5.1 Abrasive Wear. Abrasive wear occurs when hard particles or asperities are forced against and move along a solid surface [12]. The tangential force is sufficient to plastically deform and eventually remove the asperity. The top schematic, labeled A, in Figure 1.6, depicts an abrasive wear event, where the triangular shaped abrasive particle is cutting into the top of the asperity.

1.5.2 Adhesive Wear. Adhesive wear occurs when the contacting asperities from two different sliding surfaces bond or adhere together. Under continued sliding, the tips of the asperities from the softer material are sheared off and will adhere to the harder material. The sheared tip later breaks free from the other surface forming wear debris. The lower schematic, labeled B, in Figure 1.6, depicts an adhesive wear event, where the fragment has been sheared from the asperity and has adhered to the top surface material.

1.5.3 Melt Wear. Melt wear occurs when the conditions at the interface are sufficient to cause localized melting of the sliding material. Typically, these conditions are high normal load coupled with high sliding velocity. The melting temperature,

T_{melt} , of the material also plays a role. In the case of metals, as the sliding velocity increases, a film of liquid or molten metal forms at the interface which provides “melt lubrication” and a lower coefficient of friction. The molten layer, may be sufficiently thick such that the asperities from opposing surfaces no longer contact each other during sliding action [43].

This study will primarily focus on mechanical wear, caused by the abrasive and adhesive wear events. Also, melt wear will also be considered as another contribution to the total slipper wear.

1.5.4 Wear Rate. Wear rate is defined as the volume of material removed per unit time or per unit sliding distance [14]. As the majority of the literature defines wear rate in terms of sliding distance, the same definition will be used throughout this dissertation unless otherwise noted. Thus, the dimensional wear rate, $W = V/d$ where V is the volume of material removed or damaged, and d is the sliding distance.

Archard’s wear equation, published in 1953 based on his studies of the contact and rubbing of flat surfaces [4], relates the wear rate, normal load, and hardness of the sliding material by

$$W = \frac{k_A F}{H} \tag{1.1}$$

where H is the indentation hardness, and k_A is the proportionality constant or Archard wear coefficient. If the load, wear coefficient and hardness remain constant, then the volume of material lost, V , is directly proportional to the sliding distance, d . If the sliding velocity is also constant, then V is proportional to time. Archard said that k_A corresponds to the probability that an asperity interaction results in the formation of a wear particle. It is also introduced as a means to provide agreement between theory and experiment.

1.6 *Wear-Mechanism Maps*

Lim and Ashby [7; 52; 53] have used wear-maps as a method of presenting the relationships between various wear mechanisms. They surveyed the literature for steel sliding wear data using unlubricated pin-on-disk experiments. Upon grouping the data, they found different dominant regimes of different wear mechanisms. They broadly classified them in four classes: seizure, melt wear, oxidation dominated wear, and plasticity dominated wear. Seizure between two surfaces occurs when, under sufficiently large force or pressure, the real area of contact grows until it is equal to the nominal, or apparent contact area. Melt and oxidation wear were briefly mentioned previously. Plasticity dominated wear is also referred to as adhesive wear.

In order to build their wear maps, Lim and Ashby plotted the surveyed experimental dry sliding pin-on-disk wear data on appropriate axes. Regions of like wear mechanisms are identified. Secondly, they developed model-based wear equations for each of these classes of wear. These wear-mechanism maps will be used subsequently when discussing mild vs. severe wear, and the range of Archard wear coefficients.

1.7 *Review of Previous Wear Research at Various Velocities*

The main focus of this literature review has been studies in archival journal articles related to the study of dry sliding friction and wear of metals. The majority of the published research was based on experiments where the sliding velocity was less than 100 m/s. As this research focuses on the high velocity wear phenomenon, this chapter groups the previously documented and published research into several ranges of velocity: 0–10 m/s, 10–100 m/s, and 100–1000 m/s. These summaries are organized in chronological order and highlight the key concepts presented by the various researchers.

1.7.1 Velocity Range: 0 to 10 m/s. This section discusses previous wear research in the low speed regime. The bulk of the published research falls into this 0 to 10 m/s velocity range. Most researchers consider a sliding velocity of 10 m/s to be

“very high”. By comparison with the sliding velocities achieved during a rocket sled mission, this range is considered to be extremely low speed.

In the 1950s, Bowden and Thomas [20] examined the development of the surface temperature at the contact points between metal and a transparent solid. When one solid slides over another, local points of rubbing contact, or asperities, are raised to a higher temperature, and “hot spots” are observed for a very short time duration.

Their experiments used a loaded cylinder sliding on a rotating glass disk at linear speeds of 100–700 cm/s. The glass surface was chosen so that the infrared radiation could be measured with a photosensitive cell placed under the disk. The load on the 1 mm diameter steel or tungsten cylinder was varied until visible “hot spots” at the sliding interface could be observed. The output of a photosensitive cell was amplified on a cathode-ray oscillograph.

Although the surface temperatures reached very high values for only a short duration of time (1–4 ms), the bulk of the two surfaces “was still quite cold” indicating the existence of localized high temperatures. Bowden and Thomas concluded that at the sliding surface the local temperatures are both high and fluctuating, but that the maximum temperature rise was limited by the melting point of the metal. The concept of flash temperature increase will be used subsequently in the development of the melt wear rate.

In 1956, Archard and Hirst [6] published the results of their study of the wear of metals under unlubricated conditions. They used a pin-and-ring machine where the 2.38 cm diameter ring was mounted on a shaft that rotated at about 180 cm/s. A flat-ended, 0.635 cm diameter pin was pressed under a load (50 g – 10 kg) against the circumference of the ring. Several hundred experiments were performed with different combinations of loads, speeds, and materials.

Archard and Hirst noted that under the test conditions, the metals exhibited two forms of wear: mild and severe. The mild wear, which involves the slow removal of the tips of the higher asperities on a very small length scale, was usually observed

at light loads. The severe wear was observed at heavier loads, where the damage was on a much larger length scale. When the load was increased after a period of mild wear, the severe wear process was initiated “as a patch of heavy damage”.

They observed that as the rubbing begins, changes occur in the condition and structure of the surface layers. In the early stages of rubbing, the wear rate changed with time, but became constant after an initial “running in” period. This constant wear rate tends to begin when the surface layers attain their equilibrium condition. Another observation was that the wear rate became independent of the apparent area of contact.

In 1970, Farrell and Eyre [34] studied the relationship between load and sliding distance in the initiation of mild wear in steels. Mild wear “involves the relatively slow removal of the tops of the highest contacting asperities with little substrate distortion”. They indicated that very little work on the metallurgical aspects of wear behavior of steels had been reported. They tested plain steels of 0.3% carbon (Steel A) and 0.3% carbon/3% chromium (Steel B) makeup using a pin-on-disk wear test machine. The pins were loaded up to 10 kg and the sliding speed was 100 cm/s.

Test results indicated that as the load was reduced, the sliding distance for the onset of mild wear increased for both steels. Figure 1.7 shows the variation of the coefficient of friction with load for the two steels. Using the same transition definitions introduced by Welsh, the coefficient of friction is greater for loads below the T_2 transition loads from severe to mild wear. Also, the coefficient of friction decreases with increasing load. In this investigation, the T_2 transition loads were not dependent on the sliding distance. Finally, using Archard’s technique of calculating flash temperature [5], Farrell and Eyre calculated flash temperatures in the range of 700–1,100°C.

In 1977, Saka et al. [67] studied the unlubricated wear of metals at “high” sliding speeds of 0.5–10 m/s and a normal force of 5 kg. The pin materials, AISI 1020 steel, AISI 304 stainless steel, and 75A titanium, were studied using the pin-on-

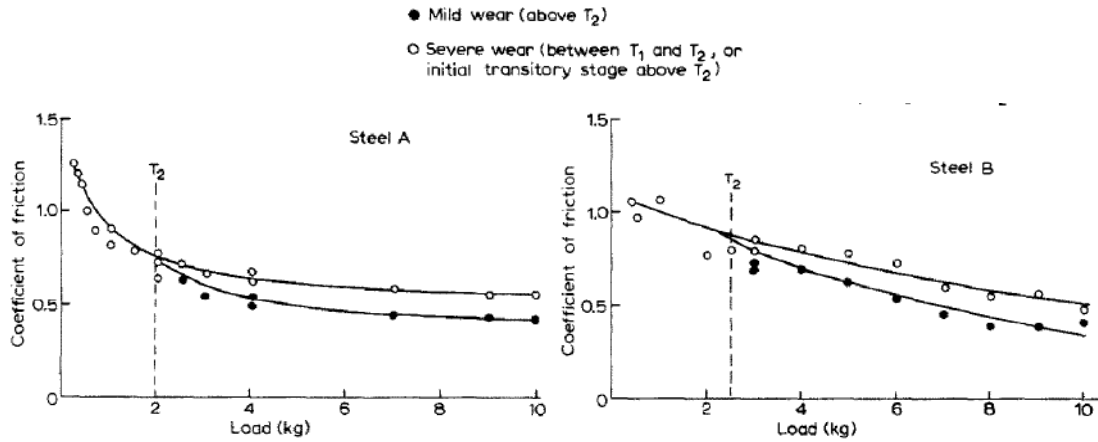


Figure 1.7: Variation of Coefficient of Friction with Load [34]

ring geometry. These test conditions were selected so that the temperature rise was minimal and thermal aspects could be neglected. They noted that the coefficient of friction decreased with increased sliding speed.

In 1989, Lim, Ashby, and Brunton [54] also studied the effects of sliding conditions on the dry friction of metal. Often, the coefficient of friction is treated as a constant. Lim et al. show that in the American Society of Metals and the American Institute of Physics handbooks, $\mu = 0.8$ for dry sliding of mild steels. However, the coefficient of friction in reality depends on the sliding conditions such as force, sliding velocity, surface roughness, etc. In a rather unique test, Lim et al. ran a pin-on-disk experiment inside the vacuum chamber of a scanning electron microscope (SEM) to measure the coefficient of friction and observe the mechanisms of wear. Extremely low sliding velocities ranged from 2×10^{-4} to 4×10^{-4} m/s with nominal contact pressures ranging from 0.01-100 MPa. Copper and iron pins were run on case-hardened steel disks with known surface roughness values.

In 1999, Molinari et al. [58] studied the dependence of the coefficient of friction on sliding conditions in the high velocity range, defined here as $V > 1$ m/s for steels. The coefficient of friction's dependence on sliding velocity, normal pressure, and slider size were investigated. They presented an analytical model that considers failure of the adhesive junctions between sliding surfaces by adiabatic shear banding as the

underlying wear process. The sliding resistance between surfaces was determined by the stress required to shear the adhesive junctions that were formed when contacting asperities on opposing surfaces slide past each other. When considering the failure of asperities, they used the fact that only a fraction of the contacting asperities actually formed adhesive junctions. Molinari et al. developed an explicit equation for the coefficient of friction by considering thermomechanical coupling that was a function of sliding velocity, normal load, normal pressure, and slider size as well as material properties. The equation can also be simplified for very large sliding velocities (above 100 m/s for steels).

In 1999, Põdra and Andersson [63] developed a wear simulation technique using the finite element method. An unlubricated steel pin-on-disk contact was analyzed both experimentally and with the finite element model. Results were compared to Lim and Ashby's wear-mechanism map to identify the wear mechanism. The test and simulation conditions were normal loads of 21 N and 50 N applied to a 5 mm diameter pin with a spherical end. The sliding velocity and distance were 0.025 m/s and 4.5 m, respectively. Results between the simulation and experiment were agreeable.

Põdra and Andersson concluded that the finite element numerical solution accuracy depended on the model discretization. As the mesh was refined, more exact results are obtained, but at the cost of increased computing time. Also, the integration time step was a critical parameter with respect to the reliability of the simulation results. If the time step was too long, erratic results and the possibility of non-convergence was an issue. If the time step was too short, computing time was excessive. An optimized time increment routine was developed that calculated the time increment based on the maximum allowable wear in each increment as specified in the initial input parameters.

In 2006, Benabdallah and Olender [13] used the finite element method to simulate wear in a pin-on-disk configuration. This method was similar to the approach presented by Põdra and Andersson [63]. The pin and disk materials were polyoxymethy-

lene and AISI 304 stainless steel, respectively. The experimental and simulation conditions were 0.1–10 m/s sliding velocity, 1–10 MPa applied pressure, and 20–80 km sliding distance. For each increment, the amount of wear was calculated and removed, the geometry was adjusted so that the pin makes contact with the disk, and the pin geometry was remeshed before proceeding to the next increment. The wear profile eventually reached a steady state condition where any subsequent wear was evenly distributed across the contact surface of the pin. Their numerical results produced good agreement with the experimental results. Friction induced heating was not introduced into the finite element model. Chmiel [25] modeled Benabdallah and Olender’s pin-on-disk model in ABAQUS as part of his AFIT thesis. This model provided greater understanding for development and implementation of the wear prediction model used in this research.

1.7.2 Velocity Range: 10 to 100 m/s. In 1947, Johnson et al. [42] published a National Advisory Committee for Aeronautics (NACA) technical report on their studies of friction at high velocity. Dry and lubricated experiments were conducted using a kinetic-friction apparatus similar to a pin-on-disk machine with the exception that the pin was replaced by a restrained spherical rider (ball). The 6.35 mm diameter balls were made of SAE 1095 steel and the disk was SAE 1020 steel. Sliding velocity and applied load ranged from 0.254–33.5 m/s and 745 MPa–1.76 GPa, respectively. Figure 1.8 shows the effect of sliding velocity on the coefficient of friction for dry and boundary-lubricated steel surfaces. The kinetic coefficient of friction is nearly constant below a sliding velocity of 10.2 m/s (2000 ft/min). As the sliding velocity increases, the coefficient of friction decreases. For the range of applied loads in this experiment, the coefficient of friction was essentially independent of the load.

Johnson et al. presented two possible reasons for the variation in μ with sliding velocity: 1) physical change of surfaces, and 2) chemical change of surfaces. First, heat generated during sliding resulted in higher temperatures and a change of the physical characteristics of the material that affected its resistance to sliding. An

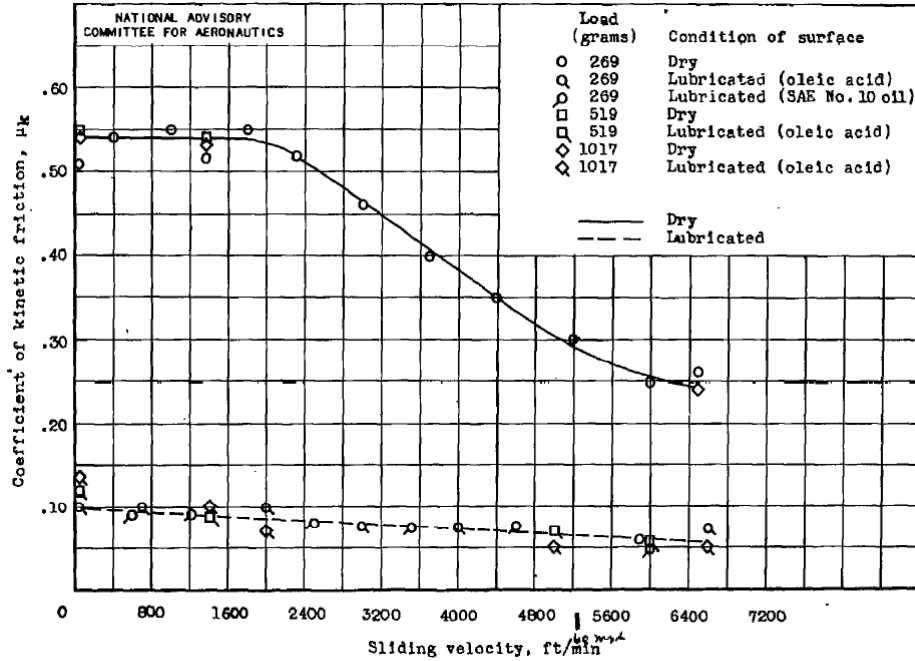


Figure 1.8: Sliding Velocity Effect of Coefficient of Friction [42]

increase in temperature “probably reduces the shear strength of the surface and in consequence decreases friction”. Second, during the experiment, a black powder was visible without magnification. Although the transition mechanism of the surface chemistry was unknown, an X-ray diffraction investigation revealed that this residue was ferrous oxide (FeO). An appreciable reduction in friction was observed when the ferrous oxide became visible on the surface of the ball.

In the 1970s, Montgomery [62] published research on the study of the surface melting of the rotating bands found on an artillery projectile. As the projectile traveled down the barrel of the cannon, the rotating bands slide along the rifling, or grooves in the barrel that impart a spin on the longitudinal axis of the projectile. A molten film of copper alloy forms on the surface of these rotating bands causing a transition from dry to lubricated sliding. Figure 1.9 shows the rotating bands on a typical artillery projectile. As the barrel wears, the useful life of a cannon is limited by unacceptable increases in range and azimuth dispersion of the projectile.

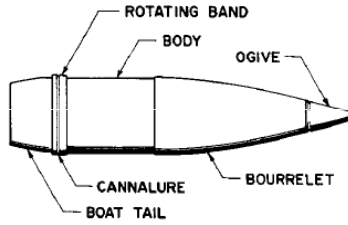


Figure 1.9: Typical Artillery Projectile [60]

A molten surface film was produced during pin-on-disk experiments. Results from the laboratory were compared with actual 155 mm howitzer artillery experiments. The pin material, chosen to represent the rotating band material, varied between annealed iron, copper, and projectile steel. Chemical composition of these materials and results of the pin-on-disk experiments are reported in Reference [61]. Montgomery introduced *pressure velocity*, the product of bearing pressure and sliding velocity, Pv , as a parameter for presenting results. Units for Pv are (Pa)(m/s) or (psi)(ft/s). The pressure velocity for these experiments was 6.3×10^9 (Pa)(m/s). The coefficient of friction as a function of Pv is presented in Figure 1.10. Several key items from this figure should be pointed out. First, there is a large discrepancy between the laboratory experiments and the projectile data. Montgomery indicated that known limitations and assumptions in the laboratory experiments account for the discrepancy. For example, additional heat sources due to the projectile's hot propellant gases and the gun tube's heightened temperature due to previous projectile firings were not replicated in the laboratory experiments. Also, the pin-on-disk measurements were made at constant velocity, as opposed to an increasing velocity, albeit of short duration, in the gun tube. Due to these and other factors, the molten surface film forms more rapidly on the actual projectile rotating bands than predicted by the experiments.

Secondly, Montgomery concluded that the sliding of projectiles down a gun tube “must be considered to be hydrodynamic lubricated sliding with a coefficient of friction determined only by the character of the film and not the properties of the sliding surfaces themselves.” Figure 1.10 shows that the coefficient of friction drops

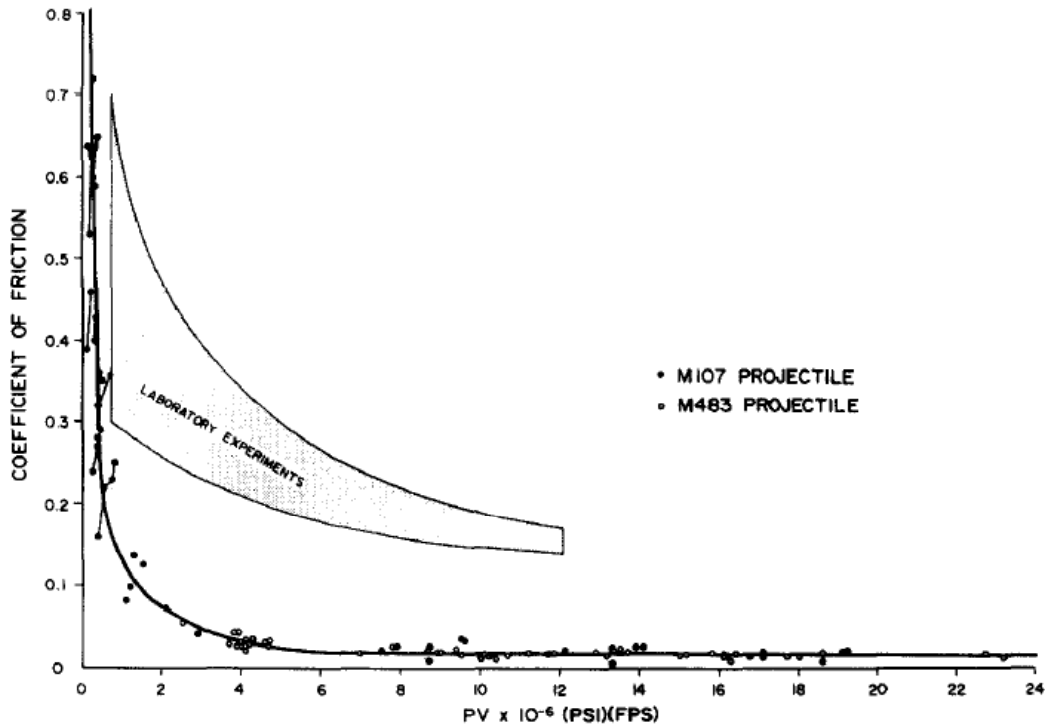


Figure 1.10: Coefficient of Friction as a Function of Pv [62]

rapidly to a value of 0.02 after approximately 13 cm (5 in) of travel down the muzzle. By comparison, μ for the laboratory experiments approached 0.2.

In 1996, Lesquois et al. [51] studied the thermal effects on surface wear for high speed conditions. Their particular application was similar to Montgomery as it also related to the wear and friction of a projectile fired through a gun barrel. Their objective was to correlate the mechanical and thermal behavior for an uncoated steel and a hard chromium-coated steel. This coating was used to protect the gun tube. Experiments were conducted with “tribometer great velocity” experimental device that resembled a pin-on-cylinder wear test device. Thermocouples were installed along the length of the 8 mm by 8 mm square-faced pin made from pure iron, alloy steel, and hard chromium-coated steel. The linear sliding speed range was 14–75 m/s. For this study, a thermal code was developed that could calculate the contact surface temperature and incoming heat flux in the pin based on the thermocouple temperature measurements.

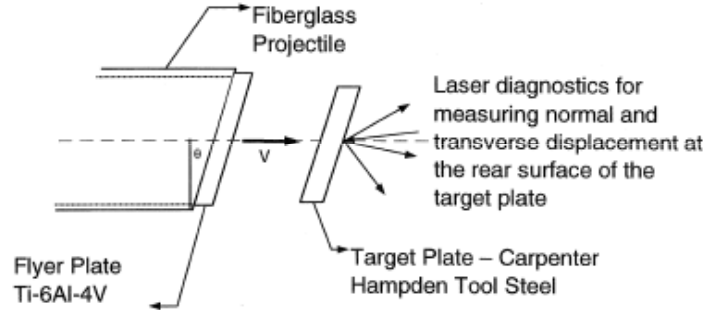


Figure 1.11: Plate Impact Pressure-Shear Friction Experiment Schematic [65]

In 1999, Rajagopalan et al. [65] presented several novel experimental techniques for investigating high speed friction of a dry sliding interface. The two techniques were the plate impact pressure-shear friction experiment, and the torsional Kolsky bar friction experiment. Several tool steels were investigated under high normal pressures (1–2 GPa), high sliding velocities (1–60 m/s), and elevated temperature. Wave propagation, as it applies to these experimental devices, was reviewed in the paper. In the first experiment, a flyer plate was propelled from a gas gun to impact a target plate. While the flyer and target plates are parallel to each other, the impact took place at an angle relative to the direction of approach. A laser interferometer technique was used to measure the normal and transverse particle velocity at the rear of the target plate. Figure 1.11 shows a schematic of this test.

In 2001, Molinari et al. [59] applied the finite element method to model the dry sliding of wear in metals. Their three-dimensional FE model was formulated within a Lagrangian framework capable of accounting for large plastic deformations. Continuous adaptive remeshing, applied in the contact boundary region, was employed to eliminate deformation-induced element distortion.

Another aspect of the model was that Archard’s law was modified so that the hardness of the material was temperature dependent instead of being a constant. This allowed for the model to capture the observed experimental transitions between mild and severe wear. The model was validated by comparing with a brass pin sliding on a rotating metal plate. Test conditions for both the simulation and experiment

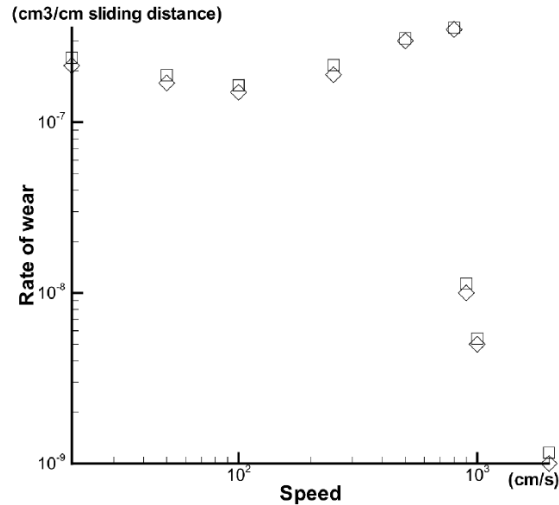


Figure 1.12: Comparison of Simulated and Experimental Results [59]

were sliding velocities in the 0.2–20 m/s range, applied contact pressure of 0.182 MPa, contact area of 1.6 mm², and coefficient of friction, $\mu = 0.3$. Numerical wear rates, shown as the squares, are compared with the experimental rates, shown by the diamonds, in Figure 1.12.

The authors noted that the simulated results were systematically 10% higher than the experimental results because three-dimensional effects not accounted for in calibration of the FE model. Leading edge effects, where the pressure was higher than the average contact pressure, were also captured by this model. The higher pressure results in higher wear rates and mass loss at the leading edge. Benabdallah and Olender’s model also captured this feature.

In 2004, Phillipon et al. [64] performed an experimental study of friction at high velocities. They first summarized the experimental techniques to study dry sliding wear at high velocities. Several of these techniques, namely pin-on-disk, friction cutting, modified torsional Kolsky bar, and pressure-shear plate impact, have been summarized. Other techniques for evaluating friction and wear at velocities greater than 100 m/s were also presented. Phillipon et al. also summarized the influence of increased velocity on the coefficient of friction.

Their experimental device was designed to study friction in the sliding velocity range of 0.01–60 m/s, normal pressures up to 230 MPa, and sliding distances of up to 30 mm. For low velocities, a hydraulic machine was used. For velocities greater than 10 m/s, a gas gun was used. In both cases, the same friction device, shown in Figure 1.13, was used. Two material specimens, labeled Specimen M_A and Specimen M_B , were initially placed in contact. The fired projectile forced Specimen M_B to slide between two samples of Specimen M_A . Coefficients of friction measured by this experimental device were in agreement with those published in the literature for dry sliding of steel on steel.

Specimens of the VascoMax 300 and AISI 1080 steel rail were provided by HHSTT to Voyiadjis for analysis in Phillipon’s experimental device. The rail pieces were mounted as Specimens M_A and the slipper pieces were used for Specimens M_B . Coefficient of friction results between these HHSTT materials at velocities up to 3 m/s have been determined at this time [76], and have been correlated with the coefficient of friction function that was used to determine mechanical wear rates. Results of this experiment will increase our understanding of the frictional relationship between the slipper and rail materials at higher velocities.

1.7.3 Velocity Range: 100 to 1,000 m/s. In 1958, Bowden and Freitag [17] studied the friction of solids at very high speeds. Their research focused on metal sliding on both metal and diamond. In some of their previous experiments [19; 20], they focused on friction at low or moderate speeds. Bowden and Freitag described a method of experiment where they were able to study the friction of rubbing solids at speeds of up to 800 m/s. In vacuum conditions, a 1.27 cm diameter steel ball was suspended in the magnetic field of a solenoid. A photo-electric feedback system was used to maintain vertical stability. As the magnetic field rotated, the ball began to spin about its vertical axis until reaching the desired velocity. When the current was removed, the ball was trapped between three vertically arranged flat plates, two of which were fixed. The third was attached to a leaf spring so that the normal load

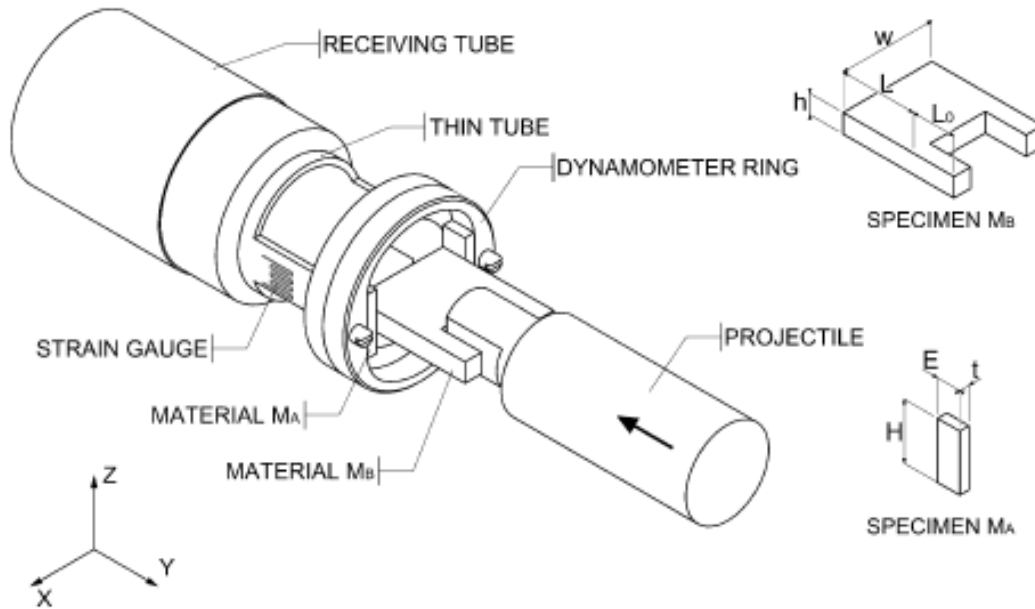


Figure 1.13: Schematic of Friction Device [64]

could be varied. The deceleration of the spinning ball due to friction was measured electronically. Figure 1.14 shows a schematic of this experimental device.

The steel ball was evaluated against copper, aluminum, duralumin, bismuth, antimony, molybdenum, and tungsten flat plates. Surface temperatures were also measured by mounting the ends of two very small thermocouple wires, separated by 0.3 mm, to the surface of one of the flat plates. At high speeds, friction caused the flow to melt, thus completing the thermo-electric circuit.

The results indicated that sliding resistance, related to the coefficient of friction, decreased as the spinning, or sliding speed increased. In the regions of contact, high speed sliding produced high temperatures and caused the surface to soften and melt in the contact area. A final conclusion was that “friction and wear at very high speeds are determined mainly by the relative physical properties of the sliding materials at elevated temperatures.”

In 1961, Bowden and Persson [18] published additional research on deformation, heating, and melting of high speed solids based on a new method for calculating friction of low melting materials under high load. The previous spinning ball experiment

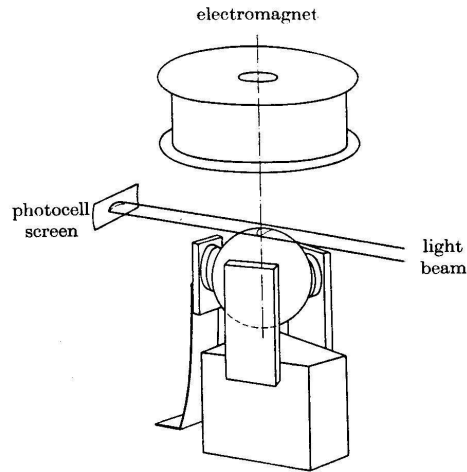


Figure 1.14: Schematic of High Speed Friction Apparatus [17]

was modified by removing the flat plates and allowing the spinning ball to drop approximately 5 cm. The dropped ball impacted an inclined specimen plate set at 30° with respect to the vertical. A vertical brass cylinder, concentric with the vertical axis of the ball, surrounded the spinning ball and inclined specimen plate. A non-spinning ball would bounce off of the inclined plate normal to the original direction. On the other hand, a spinning ball would deviate to one side due to friction. By measuring the angle of deviation, α , the friction was calculated. Piezo-electric measurements of the load and friction force were also recorded. Other materials, in addition to those previously tested, were also evaluated. Figure 1.15 shows the coefficient of friction for steel on steel sliding. On the vertical axis, the coefficient of friction was calculated as $\bar{\mu} = \cos \beta \tan \alpha$, where β was the angle of inclination of the specimen plate.

Two of Bowden and Persson’s key conclusions are included here:

- “At loads sufficiently large to cause plastic deformation over the apparent contact area in a stationary contact, the initial deformation in high-speed sliding is mainly plastic, even at extremely high rates of shear (on the order of 5×10^8 /s)”
- “Within a very short time (approx. $10 \mu\text{s}$) after being brought into contact with a fast moving surface, solids with a sufficiently low melting point melt on a large scale so that a continuous film of liquid separates the two solids. The

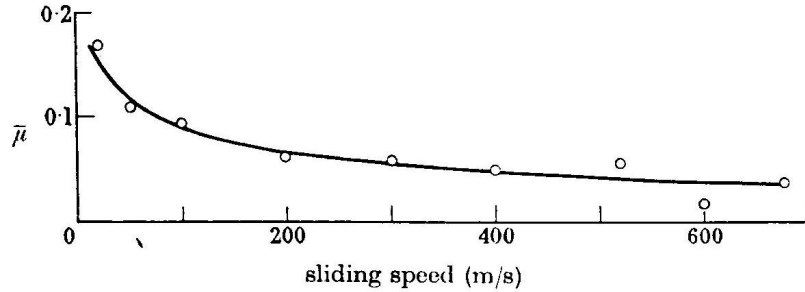


Figure 1.15: Steel-Steel: Coefficient of Friction [18]

resistance to motion is due primarily to this liquid film so that it may increase as the speed increases. Under these conditions, the wear rate, governed by the rate of melting, is in general found to be very great”.

As previously observed, the coefficient of friction decreased with increasing sliding speed for a given normal load.

In 1975, Montgomery [61] published a study based on classified Army research from the 1940s and 1950s. As with his previous work [60; 62], this study focused on friction and wear at high sliding speeds with particular emphasis on artillery projectile and muzzle wear. High speed pin-on-disk experiments were conducted at sliding speeds up to 548 m/s. Normal and frictional forces were measured with strain gauges mounted on the 2.032 mm diameter pins. The pin material included gilding metal, annealed iron, copper, projectile steel, constantan, zinc, aluminum and nickel. The disk, made of gun steel, was 60.96 cm in diameter. Wear was determined by measuring the weight loss of the pin. Length loss was measured for each test. However, the soft copper pins had a tendency to “mushroom” during sliding under the applied load. This “mushrooming” led to artificially low wear rates for copper because the bearing area was much greater than that of a 2.032 mm diameter pin.

The wear rates for steel, shown in Figure 1.16, are plotted as a function of Pv . Below Pv values of 3×10^6 (psi)(ft/s), the wear rate was very high and inconsistent. Above this Pv value, there was a smooth increase in the wear rates. For both the copper and steel experiments, wear rate was a function of the rate of heat generation.

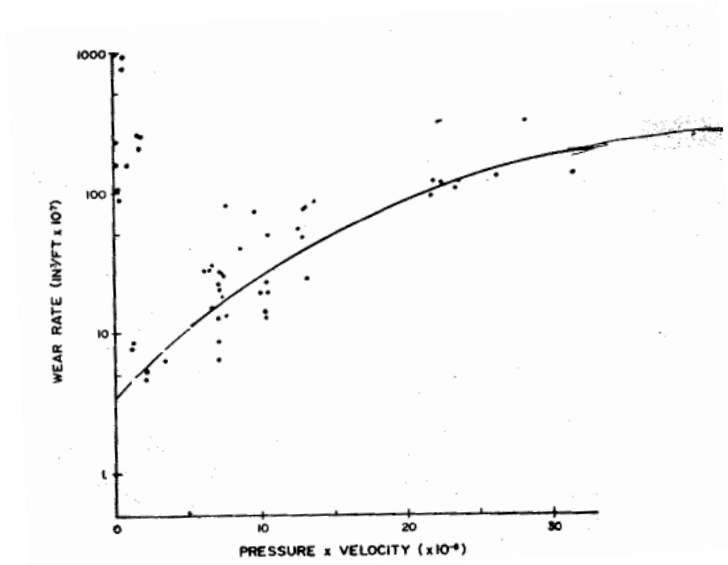


Figure 1.16: Wear Rate of Projectile Steel as a Function of Pv [61]

Montgomery concluded that the mechanism of wear at these high speeds was surface melting followed by the removal of some of the molten metal layer. The wear rate, W , was almost entirely a function of the melting temperature. Lim and Ashby included Montgomery's large amount of data to help verify their melt equation [53].

1.8 Holloman High Speed Test Track (HHSTT) Wear Research

Although not published in archival journals and readily available to the research community, several key technical reports, based on research from the HHSTT, provide direct insight into the test track's research and studies in minimizing slipper wear. These reports document the planning, execution, and results of many years of HHSTT research.

Since the beginning of test track operations, track engineers have been concerned with slipper wear. Many different studies have been performed at the track to improve this issue. A variety of slipper configurations, materials, and track lubricants, both solid and liquid, have been investigated. Several technical reports of these studies, available in the HHSTT Technical Library, are summarized in this section and provide key insights from the test track engineer's perspective.

In 1960, Wolfson [78] studied slipper wear and the influence of solid lubrication and bearing materials on high speed track applications. High-speed wear and lubrication were investigated during 60 track tests with various combinations of velocity, bearing material, nominal bearing pressure, and track condition. The slipper specimen materials, Type 304 stainless steel, molybdenum, vanadium, SAE 4140 steel, and tantalum, were evaluated at 835, 1200, and 2500 ft/s. Track conditions included the default bare rail and aluminum, antimonial lead, tin base babbitt, molybdenum disulfide, and slaked lime coatings.

When the test slipper reached a specific velocity, a material specimen was pneumatically forced into contact with the rail. After a specified distance of travel, the test specimen retracted back into the test slipper. The amount of wear was analyzed by comparing the pretest and posttest specimen thicknesses and weights. Wear rates were determined by dividing the volume of wear by the known sliding distance.

Wolfson concluded that slipper wear may be reduced by selecting slider (i.e. slipper) material with a high melting point, and by choosing slipper geometry in order to optimize “melt lubrication”. Also, wear may be reduced by coating the track with a low melting alloy in order to absorb heat before it can cause the slipper to melt.

In 1982, Krupovage and Rassmussen’s technical report [47] described the Holoman High Speed Test Track’s technical developments of a Mach 5 monorail rocket sled. Two different slipper wear mechanisms were noted during the test runs. In runs up to Mach 4, the slipper’s bearing surface was characterized by

“a longitudinal streak pattern along the sliding surfaces, indicating removal of slipper materials by sliding or grinding action. Motion pictures show the “slipper fire”, i.e. the wear products leaving the aft end of the slipper gap, to be an essentially homogenous stream of luminous material resembling the spark pattern of a grinding stone. The light emission is white to yellow. In many cases the stream of wear products is discontinuous, indicating a “jumping” motion of the sled within the slipper clearance. These observations indicate slipper wear produced by sliding friction.”

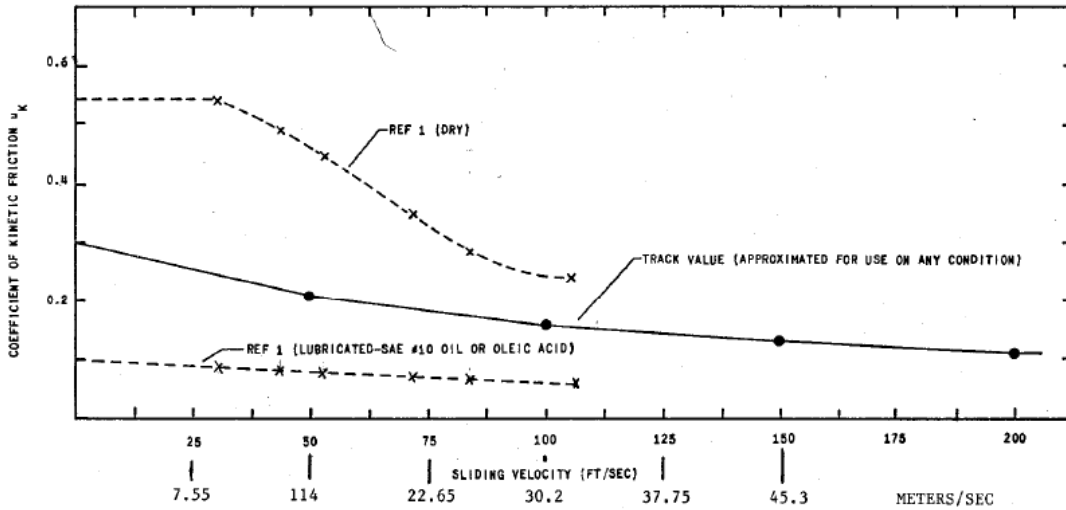


Figure 1.17: HHSTT Coefficient of Friction as a Function of Velocity [45]

“The wear pattern observed in the 5,000–7,000 feet per second (1,525–2,135 m/s) range shows additional features. The “grinding” action on the sliding surface is also present, however, strong erosion occurs at spots subject to direct air impact. The affected surfaces show intense melting, and droplets of molten metal can be observed. The “slipper fire” indicates extremely intense light emission from the affected parts of the sled and also from the surrounding air. Spots of very intense light density are observed in the air surrounding the sleds, suggesting droplets of molten metal being released into the air. These effects are attributed to aerodynamic heating and to erosive oxidation of sled and slipper material.”

In 1987, Krupovage [45] published a paper that was presented at the 38th Meeting of the Aeroballistic Range Association at the Tokyo Institute of Technology, Japan. This paper summarized test track operations and slipper wear reduction studies. Krupovage summarized the NACA Technical Note No. 1442 by Johnson et al. [42] and Wolfson’s 1960 report. The coefficient of friction used at the track for calculating vehicle performance, presented in Figure 1.17, appears to be the average of Johnson’s dry and lubricated coefficient of friction results. Table 1.2, from the 1991 HHSTT Design Manual [46], lists these values in tabular format. This coefficient of friction as a function of velocity is currently used by HHSTT test engineers to predict frictional forces and distances that test sleds will travel during a test mission.

Table 1.2: Test Track Coefficient of Friction

Velocity (ft/sec)	Velocity (m/s)	Coefficient of Friction, μ
0	0	0.30
50	15.2	0.21
100	30.5	0.16
150	45.7	0.13
200	61.0	0.11
10,000	3,048	0.11

Krupovage concluded by indicating the slipper bearing pressure, the normal force divided by the slipper contact area, could be used to predict slipper wear with “an acceptable accuracy”. Bearing pressures below 2.07 MPa did not produce serious slipper wear. Bearing pressures above 4.14 MPa produced large wear rates, and could only be tolerated for an interval much less than one second.

1.9 AFIT Initial Wear Research

Cameron [23; 24] performed the initial AFIT wear research and approached high velocity wear using two separate techniques. The first technique relied on the research of Lim and Ashby’s [53] pin-on-disk survey and the equations that were developed to model different modes of wear at low velocities. This technique included the use of Archard’s wear equation [4] and Montgomery’s friction and wear data at higher sliding velocities [61]. The first objective was to relate low velocity wear experiments to higher velocity applications by using parameters such as pressure and velocity. The second technique used CTH to model the macro level wear created by the slipper sliding into an asperity on the rail. The second objective was to evaluate high velocity wear using CTH considering the effects of temperature, rail geometry, velocity, and coatings.

Following Lim and Ashby’s analysis, mechanical and melt wear were calculated using the DADS test data for the specific test mission. It is important to point out that the equations found in Lim and Ashby were developed from pin-on-disk experimental data accumulated from close to one hundred references in which velocity of sliding

was a great deal smaller than the velocities to be considered in the eventual sled studies. The data would automatically include irregularities present in the event. These irregularities are referred to as asperities. This last idea is important to keep in mind for the method that will eventually be presented.

Slipper wear was determined analytically from the DADS data using the Lim and Ashby equations for melt wear rate, w_{melt} , and mechanical wear rate, w_{k_A} , respectively. The total melt and mechanical wear depths for the entire run were calculated to be 0.08 cm and 0.27 cm, respectively. The amount of wear, as determined by the analytical models, produced realistic results. The calculated total wear of 0.35 cm in thickness was acceptable. Recovered VascoMax 300 slippers from the HHSTT do not typically wear completely through the initial thickness.

Chmiel [25] continued this wear research by looking at the feasibility of using finite element analysis to predict the wear of the slipper during a simulated test run down the track. Two methods were investigated, one was a macro-scale, incremental method utilizing traditional wear equations from Archard, and the other was a micro-scale, material property method that used a failure criterion to determine the amount of wear. Chmiel modeled the VascoMax 300 slipper's interaction with a sinusoidal asperity with an amplitude of 40 μm at a velocity of 1 m/s and normal pressure of 15 MPa. These methods were implemented at low velocities to allow for comparison to results from the literature.

1.10 Key Concepts from the Literature Search

Several key concepts from previous wear research have helped to formulate the current research direction. Bowden, Thomas, and Archard each observed flash temperature increases that occurred when under sufficient loading condition [4; 20]. Archard developed flash temperature increase models for elastic and plastic deformation at high and low sliding speeds. These models, presented in Chapter III, will be used to determine the contribution that flash temperature has on melt wear rates.

Johnson et al. study of dry and lubricated steel-on-steel sliding provided insight into the nature of the coefficient of friction with increased sliding velocity [42]. Specifically, their results showed that the frictional coefficient decreased with increased sliding velocity for both the dry and lubricated test conditions. The HHSTT Design Manual has a function for the coefficient of friction that is based on test track experimental results and closely followed the results of this NACA research. As with Johnson's observations of decreasing coefficient of friction as a function of velocity, Montgomery's data as a function of pressure-velocity [61] also showed a decrease in the coefficient of friction with increasing pressure-velocity. Montgomery's data is used in the present research as the frictional relationship between the slipper and rail.

These concepts and experimental observations will be used to accomplish the objective of developing a numerical model for wear rates between two sliding materials in contact at high velocity. Emphasis will be placed on determining the wear rates for the VascoMax 300 slipper sliding on AISI 1080 steel rail, which are in use at the HHSTT. A metallographic examination of a test slipper from the January 2008 test mission will provide insight into the major considerations necessary for a numerical wear rate model. Although this research is focused mainly on high velocity wear at the Holloman High Speed Test Track, the developed wear rate model can be used to determine the mechanical and melt wear rates between any two sliding materials in contact at high velocity. Results of this wear rate model will be used to determine the total wear volume for comparison with the total wear volume of the January 2008 test mission slipper.

II. Metallographic Analysis

A VascoMax 300 test slipper, recovered from the January 2008 test mission, was used for a metallurgical investigation. The ultimate goal was to characterize certain features of high velocity wear which can be used subsequently for the model development of a general wear rate model. By observing the microstructure and wear surface of the slipper with both optical and scanning electron microscopy, several important findings, not visible to the naked eye, were observed. Determining the total volume of worn material helped to bound our investigation and study of high velocity wear rates.

The aft right slipper from the Stage 3 SRR pusher sled was used in this metallurgical analysis. The Stage 3 time, distance, velocity, and acceleration profiles were also provided by HHSTT test engineers. It should be noted that this test slipper represents the end state of the slipper following the entire test run. For obvious reasons, the metallurgical analysis could not be accomplished during the test event, and had to be accomplished with a post-test slipper.

This analysis determined the volume of worn material and how thermal effects had changed the microstructure of the slipper material. Empirical bulk hardness and microindentation hardness testing were also accomplished on both new and used VascoMax 300 slipper specimens. Optical microscopy revealed regions of wear surface damage. The comparisons allow for the development and further modification of a wear rate model and a better understanding of the high velocity wear phenomenon.

Standard metallographic techniques including sectioning, mounting, polishing, and chemical etching were accomplished at the Air Force Research Laboratory (AFRL), Materials and Manufacturing Directorate (AFRL/RX) to analyze the slipper microstructure and wear volume. Similar work was performed in this facility by Cinnamon during his investigation of the gouged AISI 1080 steel rail material [26; 28; 29].

2.1 *Slipper Physical Characterizations*

This section describes the VascoMax 300 SRR slipper and outlines the historical timeline that each slipper undergoes before, during and after the sled test mission.

2.1.1 Before the Test Mission. The slippers must first be manufactured and then mounted to the sled on the test track. During the manufacturing process, the welded VascoMax 300 slipper components were solution annealed at 815°C (1500°F) for one hour and aged at 480°C (900°F) for 6 hours. After heat treatment, the blocks were machined with an electrical discharge machining (EDM) hot wire to remove the core from the slipper housing. Removal of this core piece enabled the slipper to fit onto the rail. Figure 2.1 shows the aft right test slipper with the removed core material, referred to as the “new sample”. This is the same type of slipper that is annotated in Figure 1.1. Prior to running down the sled track, no additional surface preparation or machining was performed. Thus, the slipper and core piece are assumed to have the same material properties and surface conditions. Both pieces have experienced the same annealing and ageing processes. The new slipper material provided a baseline for comparison with the used, worn test slipper.

An end view of the slipper with the top, side, and lip locations identified, is shown in Figure 2.2. The slipper top slides along the top of the rail and this interface is the primary sliding wear interface of interest throughout this research. By design, the slipper lip contacts the bottom of the rail’s flange during sled movement away from the rail and keeps the sled system from departing the rail.

Once all of the slippers have been fabricated, the sleds are mounted to the rails. Following the mounting process, the individual sleds are towed by a truck driving at low speed to the start, or launch location. For the January 2008 test mission, each of the four sleds in the sled train was towed approximately 400 meters from the mounting point to the launch location. Some of the slipper material, most likely the EDM recast layer, will wear during this low speed sliding event. The exact volume of

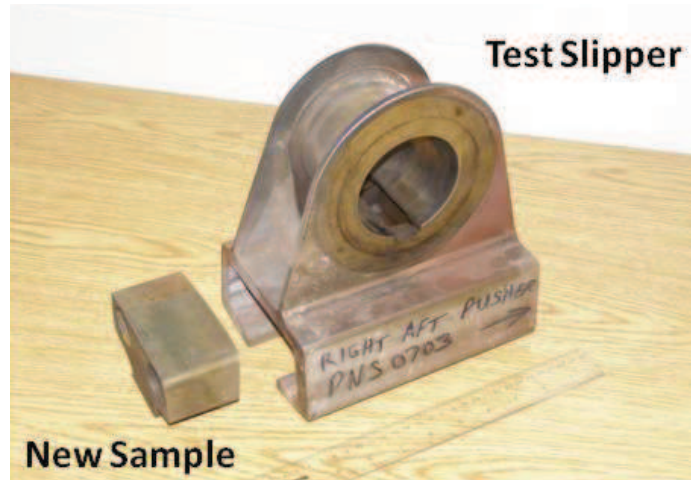


Figure 2.1: VascoMax 300 Test Slipper and New Sample

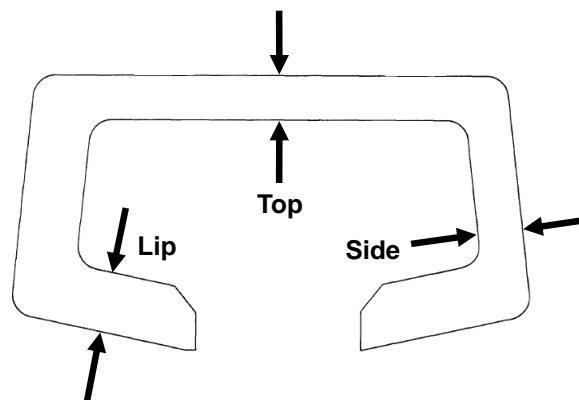


Figure 2.2: Slipper Thickness Measurement Locations

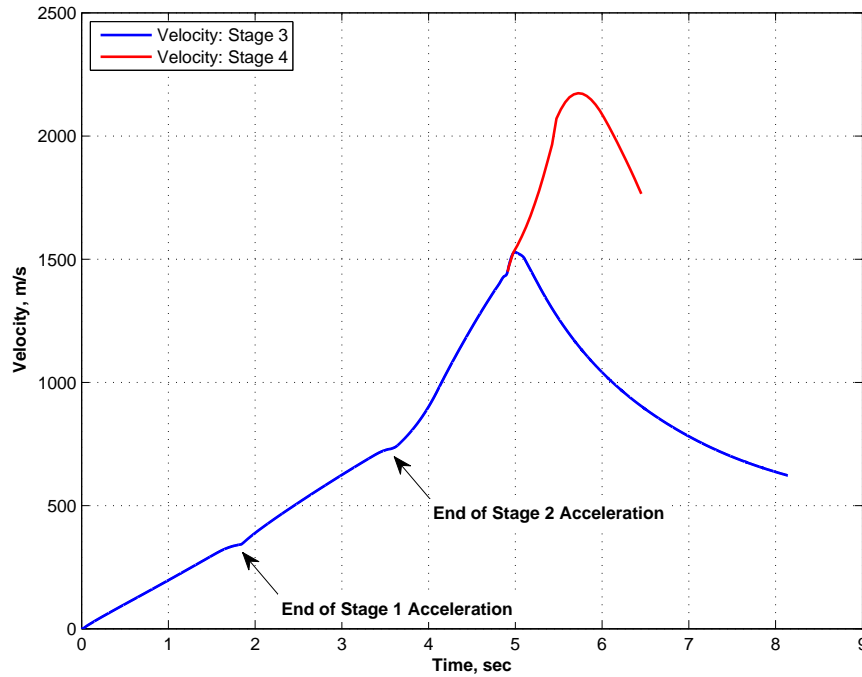


Figure 2.3: Stage 3 and 4 Velocity Profiles, Jan 2008 Test Mission

worn material attributed to sliding the sleds into launch position was not known, but assumed to be negligible.

2.1.2 During the Test Mission. Upon ignition of the Stage 1 rocket motors, the Stage 1 pusher sled accelerated the Stage 2, 3, and 4 sleds until the six MLRS rocket motors burned out. While Stage 1 began to decelerate, the Stage 2 pusher sled accelerated the Stage 3 and 4 sleds. After the rocket motors on the Stage 1 and 2 pusher sleds burned out, these sleds both coasted to a stop on the test track.

The first two Pupfish pusher sled stages accelerated the Stage 3 pusher and Stage 4 forebody sled to velocities of 340 m/s and 730 m/s, respectively. The Stage 3 SRR rocket ignited at approximately 3.8 seconds into the sled test run. The Stage 3 and 4 velocity profiles for the January 2008 test mission are shown in Figure 2.3. The change in slope of the velocity profile is evidence of the increased thrust imparted by the SRR rocket motor. The Stage 3 maximum velocity, 1,530 m/s, was achieved

approximately 5.0 seconds into the sled test run. After traveling 5,816 meters in 8.14 seconds, this Stage 3 sled departed the end of the test track with a velocity of 622 m/s. Following the test mission, the Stage 3 slippers were recovered and delivered to AFIT for physical investigation.

The Stage 4 forebody sled's rocket motor ignited at approximately 4.8 seconds, and reached a maximum velocity of 2,175 m/s at 5.72 seconds. This sled also traveled 5,816 meters and departed the end of the test track at a velocity of 1,765 m/s. Because Stage 4 was traveling faster than the Stage 3 sled, it reached the end of the track at 6.45 seconds. Due to the high velocity impact with the intended target, Stage 4 slipper specimens were not recoverable.

2.1.3 After the Test Mission. When the Stage 3 sled departed the rail, it came to rest in the desert of the sled track target area. Due to safety planning requirements and the fact that this was a nighttime test mission, the sled components were not recovered until the following day. Thus, the slipper was able to reach ambient air temperature before it was recovered and delivered to AFIT.

2.2 VascoMax 300 Material Properties

Maraging steels, developed in the early 1960's, are highly alloyed low-carbon, iron-nickel martensites. VascoMax 300 is the commercial designation by ATI Allvac, Inc., for their 18% nickel maraging steel. VascoMax 200, 250 and 350 grades are also available. The numerical designation for each grade are generally representative of their ultimate tensile strength, UTS, expressed in units of ksi. For example, VascoMax 300 has a UTS of approximately 300 ksi [9]. This material is also known by the non-commercial designation as the ultra-high strength steel Fe-18Ni-9Co-5Mo-Ti-Al, which reflects the chemical composition, by percent weight, of nickel, cobalt, molybdenum, titanium, and aluminum, respectively.

The strength of hardened carbon steels is achieved from transformation-hardening mechanism and the precipitation of carbides during tempering. Conventional quench

and tempered steels are hardened by a metallurgical reaction that does not involve martensitic strengthening. By contrast, maraging steels

“derive their strength from the formation of a very low-carbon, tough, and ductile iron-nickel martensite, which can be further strengthened by subsequent precipitation of intermetallic compounds during age hardening” [68].

The term “maraging” is derived from the age hardening of the martensitic structure [66]. The matrix will transform to martensite on cooling to room temperature directly after solution annealing.

2.2.1 Equilibrium and Transformation Phase Diagrams. The equilibrium phase diagram for this iron-nickel binary system is shown in Figure 2.4(a). The vertically dashed line indicates the 18% nickel content similar to VascoMax 300. In this figure, γ represents austenite, or gamma phase iron, and α represents ferrite, or alpha phase iron. When held at equilibrium at temperatures of 590°C (1100°F) and above under equilibrium conditions, the structure will consist entirely of austenite (γ). Below this temperature at 18% nickel, the equilibrium structure is a mixture of austenite and ferrite ($\alpha + \gamma$). When not in equilibrium, during actual heating and cooling of the material, the transformation reactions occur at different temperatures. Figure 2.4(b) shows the transformation phase diagram for the material based on the percentage of nickel content. At 18% nickel, the transformation from γ to α occurs between approximately 200–315°C (400–600°F), which is a much lower temperature range than that shown in the equilibrium phase diagram. If the nickel content is high enough, then the product of austenite transformation upon cooling from the γ field will be martensite and no other iron phases will be present [35].

2.3 Slipper Surface Characterization

In order to access the wear surface of the slipper, the aft right slipper had to be cut down to size. Using the EDM machine, several horizontal cuts, represented by the dashed lines in Figure 2.5(a), were made across the width and length of the

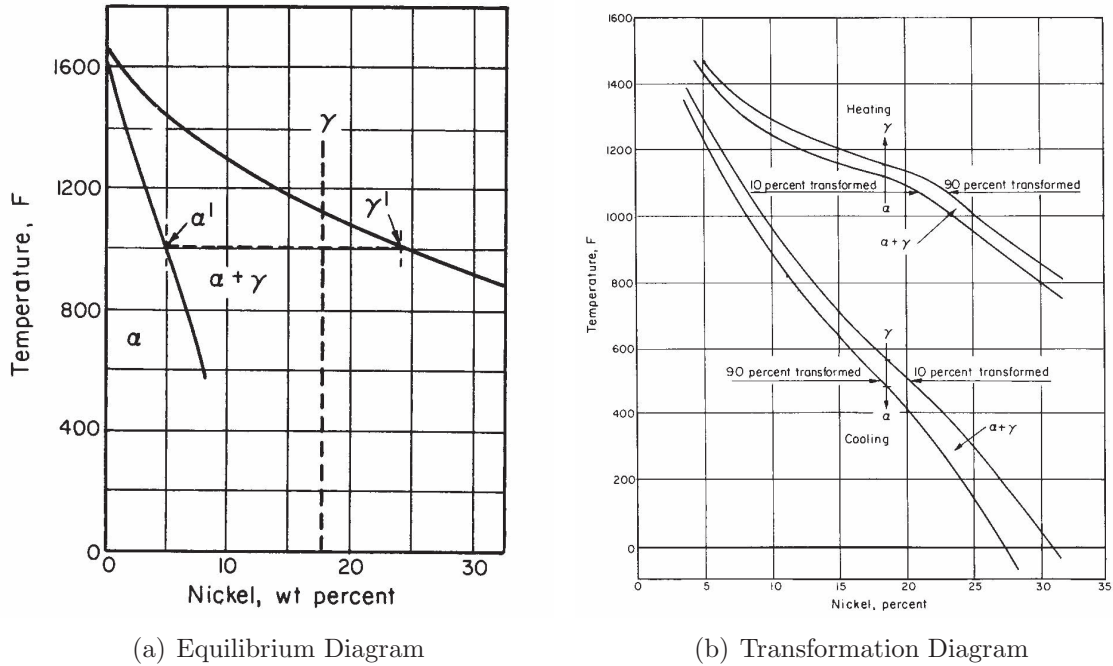
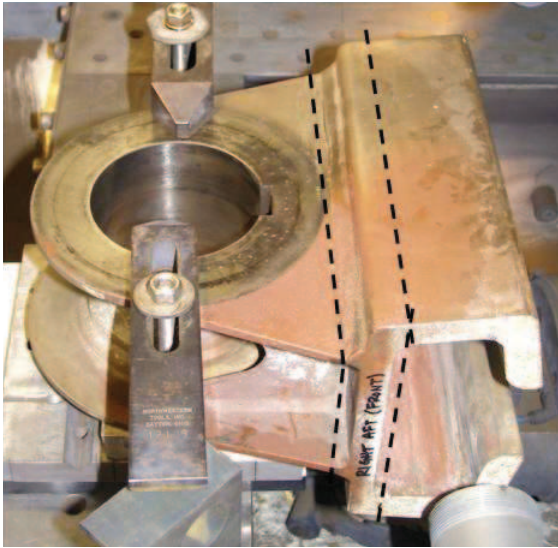


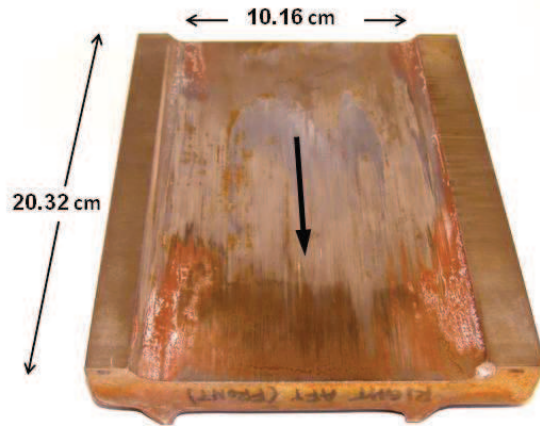
Figure 2.4: Iron-Nickel Two-Phase Diagrams [35]

slipper. By removing the circular housing from the top and the slipper sides and lips, that wrap around the rail, the remaining slipper section resembled a flat plate. Figure 2.5(b) shows the dimensions of the slipper which measured 10.16 cm in width, 20.32 cm in length, and 1.47 cm in thickness. This view shows the region of interest for this investigation, namely the bottom of the slipper sliding surface that interfaces with the top of the rail. The arrow represents the slipper's direction of travel.

One of the first tasks in the metallurgical analysis was to characterize, in general, the wear surface of the slipper. Figure 2.6 depicts the right half of the Stage 3 aft right test slipper. The left half of the slipper had been sectioned further to prepare and mount various specimens for optical and SEM investigation. The slipper surface was characterized by a highly polished surface with parallel wear tracks that were parallel to the direction of travel. Both red oxide and white epoxy coatings have adhered to the slipper and are visible to the naked eye. Several of these features, outlined in the four locations, labeled A–D, are highlighted in this figure. Each location shows a different feature of mechanical wear that was previously discussed in Chapter I.



(a) Cutting Slipper in EDM Machine



(b) Test Slipper Dimensions and Sliding Surface

Figure 2.5: Preparing Slipper for Metallurgical Investigation

Close-up views of these four locations are depicted in Figures 2.7(a)–2.7(d) where a one millimeter scale reference is shown at the bottom of each figure.

Locations A and B, near the front of the slipper, show regions of dry sliding wear with parallel wear tracks. The parallel wear tracks are consistent with unidirectional sliding. Locations C and D are of particular interest because they show evidence of the adhesive wear discussed previously in Section 1.5.

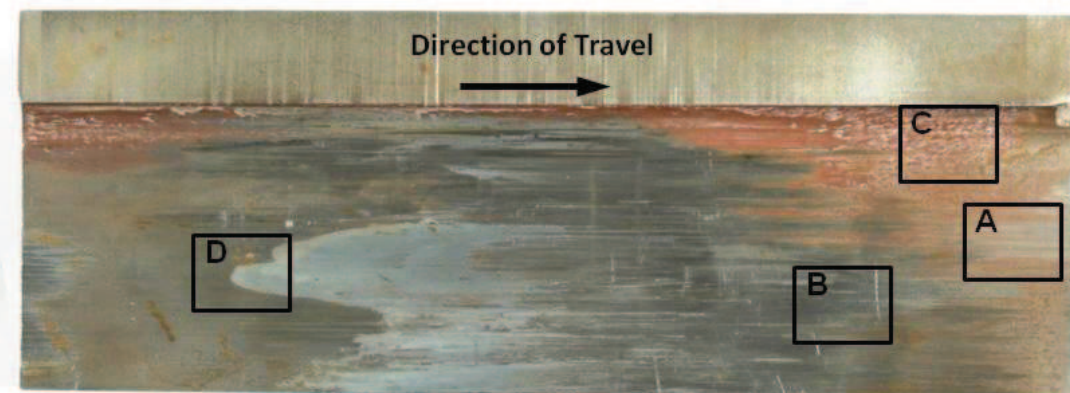


Figure 2.6: Right Half Slipper Surface Locations

A close-up view of the red oxide coating is shown in Figure 2.7(c). Recall that adhesive wear during sliding occurs when softer material is transferred to the surface of the harder material. While the exact hardness values of the red oxide and white epoxy coatings are not known, one can surmise that the coatings are definitely softer than the steel slipper material. Examination of the half slipper show that the majority of red oxide that has adhered to the slipper was found in the rounded, interior corner formed by the slipper top and side.

Near the center of the slipper, the white epoxy coating appears as a gray deposit on the slipper surface, as shown in Figure 2.7(d). During the January 2008 test mission, the red oxide and white epoxy coatings were applied to the rail surface at depths between 0.15–0.22 mm. While traveling down the track, the slipper slid on bare AISI 1080 steel rail for the first 4,000 meters from the launch point. The red oxide coating was applied to the next section of the rails for a length of 760 meters. After the bare rail and red oxide coatings, the slipper next encountered the white epoxy coating which was applied for the remaining 1,060 meters of the track. Based on the order of exposure to the coatings, it makes sense to see white epoxy coating on the bulk of the slipper surface.

Both the test slipper surface and the surface of the new VascoMax 300 sample were examined in the SEM. Micrographs of both surfaces, taken at magnifications of 50x, 500x, and 1,000x, are presented in Figures 2.8–2.10. The surface of the new sample, removed from the bulk of the VascoMax 300 slipper by the EDM process, is shown on the left hand side of these figures. The test slipper surface is shown on the right hand side for comparison.

During the EDM process, an electric current is passed through a wire creating sufficient energy to locally melt through the metal. A layer of resolidified molten metal, known as the recast layer, forms on the surface. With increasing magnification, it becomes evident that the surface was very rough. However, Figure 2.10(a) shows voids in the recast layer indicating that this may be a brittle layer. Once the sled was

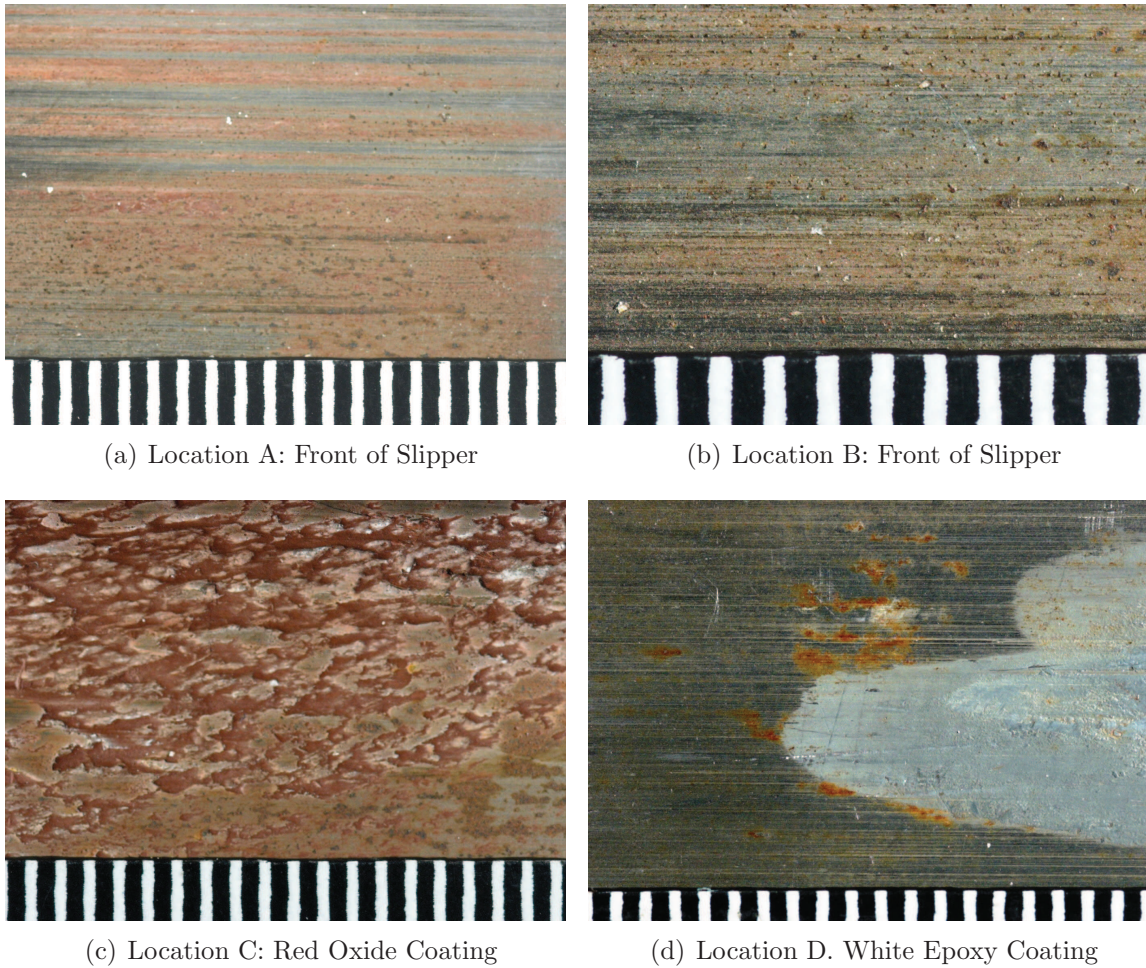


Figure 2.7: Close-Up Views of Test Slipper Surface

mounted to the rails and towed to the launch point, this recast layer was most likely worn away during the low speed towing event.

By comparison, the test slipper surfaces no longer show the original recast layer. In Figure 2.8(b), parallel wear tracks, indicative of the unidirectional sliding, show that the direction of travel is up or down with reference to the top of the figure. As the magnification is increased to 500x and 1,000x, these parallel wear tracks are no longer evident. However, evidence of large plastic deformations become more visible at the higher magnifications as shown in Figure 2.9(b) and 2.10(b). These deformations are the result of collisions with asperities and wear debris on the rail surface. Because the plastic deformations have coalesced towards the bottom of each individual wear

track, it is concluded that the relative direction of motion of the slipper in the SEM micrograph was bottom to top with reference to a stationary rail surface.

The SEM micrographs of the test slipper surface also revealed many different slipper/rail asperity impacts and various sized plastic deformations. The asperities become an important feature of a wear rate model. The overall characteristics of the wear event is three-dimensional. The total wear phenomenon is so complicated that in order to relate to the actual wear, one needs to construct a model that is truly three-dimensional.

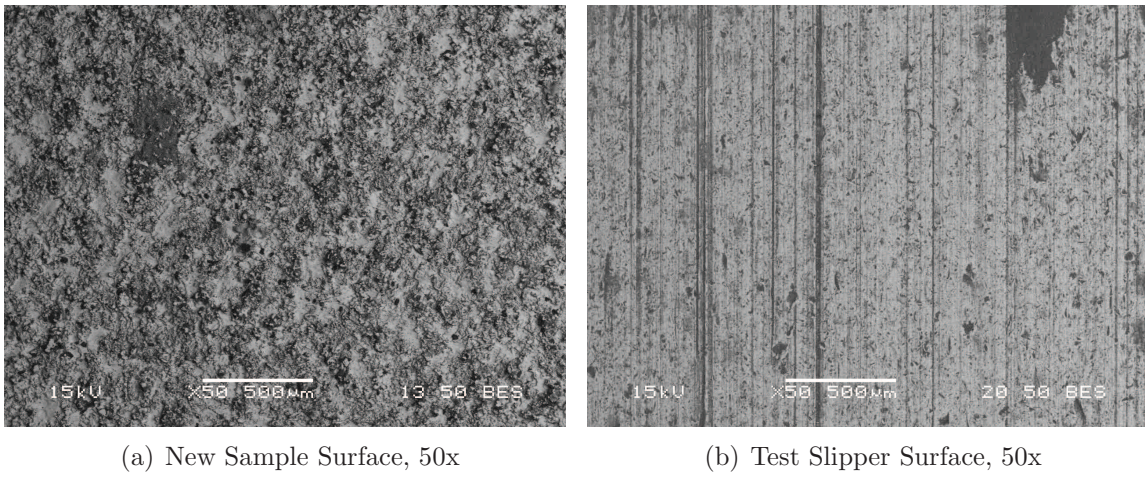


Figure 2.8: Surface Comparisons, SEM, 50x

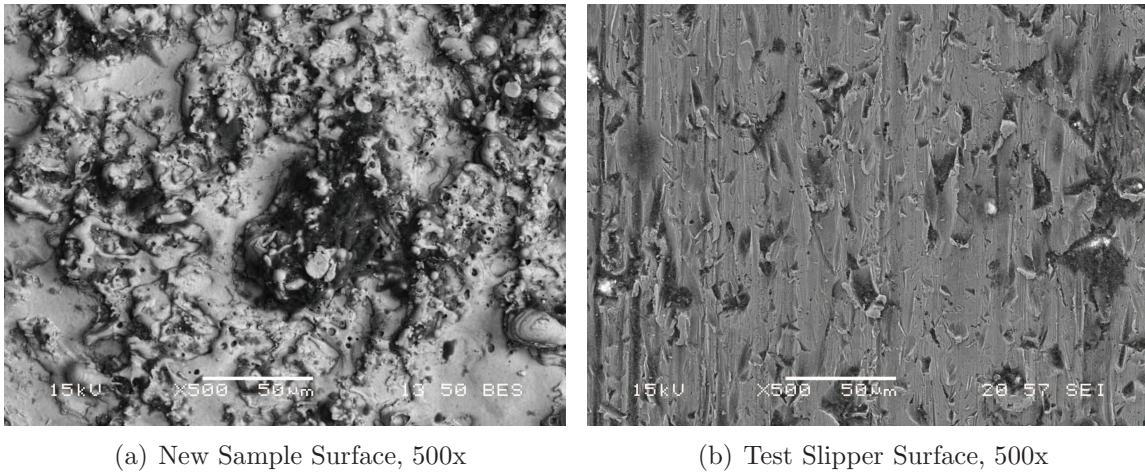


Figure 2.9: Surface Comparisons, SEM, 500x

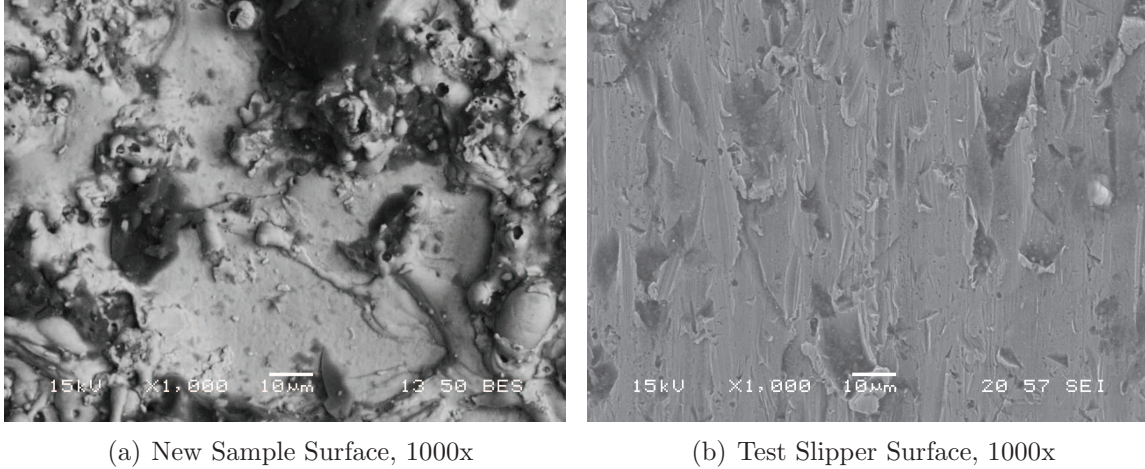


Figure 2.10: Surface Comparisons, SEM, 1000x

From the high magnification SEM images, it is readily apparent that plastic deformation of the slipper material occurs at the micron level. This observation provides further insight into the requirements for a numerical model. Namely, the model must include plasticity to account for the plastic deformation. Also, the deformation occurred on a micrometer length scale so any model developed must also take this scale into account.

Additionally, because friction plays such an important role in the sliding event, a numerical model must include these effects. Fortunately, the nature of the unlubricated sliding event was known, namely a single, unidirectional sliding event where the slipper didn't slide over the same section of rail. Because of the wide range of velocities, from 0 to 1,530 m/s, and the wide range of normal contact forces, the coefficient of friction must take into account varying velocity and pressure effects.

2.4 Specimen Preparation

Additional EDM hot wire cuts were made along the centerline of the Stage 3 aft right slipper. An additional parallel cut, offset by 2.54 cm, was also made so that six specimens could be cut from the centerline of the test slipper. Parallel and perpendicular samples, with respect to the direction of travel down the rail, were prepared at the front, middle and aft slipper locations. Evaluating the material properties in these

Table 2.1: Summary of VascoMax 300 Slipper Specimens

Source	Location	Orientation	Distance (cm)	Name	Thickness (mm)
Test Slipper	Front	Perpendicular	0.75	1xfu	13.24
Test Slipper	Middle	Perpendicular	10.0	2xmu	14.66
Test Slipper	Aft	Perpendicular	19.25	3xau	14.49
Test Slipper	Front	Parallel	0.75	4pfu	12.93
Test Slipper	Middle	Parallel	10.0	5pmu	14.39
Test Slipper	Aft	Parallel	19.25	6pau	14.48
New Sample	-	Perpendicular	-	7xn	20.95
New Sample	-	Parallel	-	8pn	20.31

orthogonal directions was accomplished to determine if the VascoMax 300 material was isotropic or not. In Figure 2.11, the three perpendicular locations are labeled as 1, 2, and 3. The three parallel locations are labeled as 4, 5, and 6. The front, middle, and aft locations were 0.75, 10.0, and 19.25 cm from the leading edge of the slipper, respectively. The arrow indicates the slipper’s direction of travel from right to left. Thus, the front of the slipper is on the left hand side of the figure. Additionally, two new VascoMax 300 samples, taken from the new sample shown in Figure 2.1, were prepared in the same parallel and perpendicular orientations for direct comparison with the test slipper specimens.

The specimen source, location, orientation, distance from the leading edge, name, and thickness for the eight VascoMax 300 specimens is summarized in Table 2.1. In the specimen naming convention, ‘x’ refers to a cross-section, or perpendicular orientation and ‘p’ refers to the parallel orientation. The specimen location is denoted by ‘f’, ‘m’, and ‘a’ for the front, middle, and aft locations in the slipper, respectively. Finally, ‘n’ refers to the new VascoMax 300 sample and ‘u’ refers to the test slipper specimens. Thus, *5pmu* is the name of the specimen from the *middle* of the *used* test slipper that was *parallel* to the direction of travel. All eight specimens were mounted in conducting material and polished to a 0.05 μm finish using standard techniques.



Figure 2.11: Metallurgical Analysis Specimen Locations

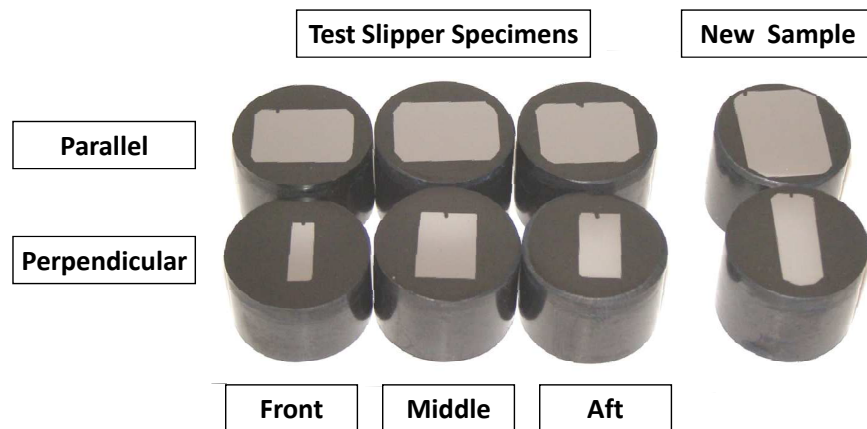


Figure 2.12: Metallurgical Analysis Specimen Mounts

2.5 *Wear Volume Calculations*

In order to determine the total wear volume, the thickness of the slipper top along the centerline, as shown in Figure 2.13, was measured with digital calipers. The accuracy of measurement was ± 0.0254 mm. In this figure, the slipper is oriented upside down and the rail would be located at the top of the figure near the wear surface as shown. The front, middle, and aft thicknesses were 12.9, 14.4, and 14.5 mm, respectively. Most of the wear occurred at the front of the slipper as indicated by the smaller thickness. The top subplot in Figure 2.14, shows the actual thickness measurements along the centerline. The most significant change in slipper top thickness occurred in the front 12 cm along the slipper length. Between 13 and 20 cm along the slipper length, the thickness remained fairly constant at 0.1 mm.

Unfortunately, the actual pre-test slipper top thickness was unknown and unavailable. However, based on technical drawings and slipper top measurements of a new slipper manufactured by HHSTT for this research, the nominal slipper top thickness was determined to be 14.7 mm. The lower subplot shows the difference between the nominal 14.7 mm and the measured thicknesses. By integrating the worn centerline thickness along the length of the slipper, the wear area for the centerline cross-section was 103.5 mm^2 . By assuming this wear profile was uniform across the width of the slipper, the total wear volume was 10.52 cm^3 .

With initial length, width, and height dimensions of 202.3 mm, 101.2 mm, and 14.7 mm, respectively, the initial volume of the slipper top was 300.9 cm^3 . The ratio of total wear volume to the initial slipper volume was 3.49% which indicated a mild wear scenario when one considers that the slipper has traveled a distance of 5,816 m. In their calibration of plasticity-dominated wear model, Lim and Ashby summarized the wear rates for fourteen different dry sliding, steel-on-steel studies in a wear-mechanism map [53]. Where available from the wear test data published in these studies, the percent volume of material worn during these particular wear tests was calculated. The largest percent of volume of material worn was approximately 3.1% in the study

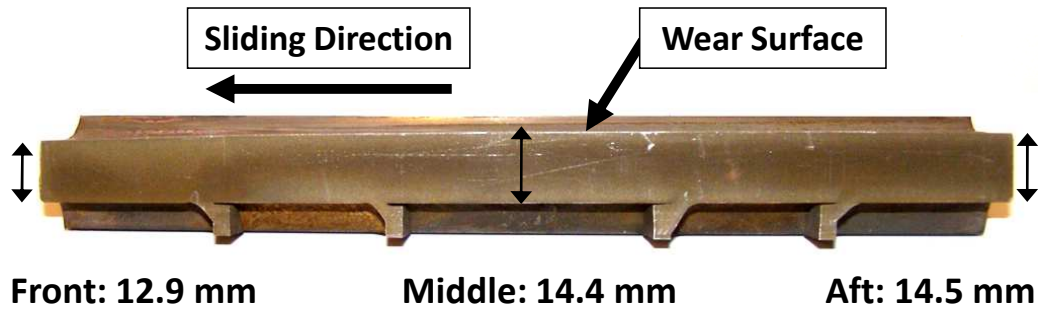


Figure 2.13: Profile of Aft Right Slipper

by Saka et al. [67]. This percentage is associated with mild wear. By comparing the percentage of wear volume between the test slipper and Saka's results, we also assume that mild wear has occurred.

When normalized by the full length of the slipper, the average slipper wear depth was 0.52 mm. In other words, assuming uniform wear over the entire area of the slipper, the slipper thickness would be evenly worn by 0.52 mm during this particular rocket sled test.

Slipper side and lip thickness measurements, for both the inboard and outboard sides of the slipper, are presented in Figure 2.15. Side and lip measurements were made at distances of 2.5 and 2.0 mm, respectively, from the corner made by the slipper side and lip. Inboard and outboard refer to the sides of the aft right slipper that are closest to and furthest from the sled train centerline, respectively. In the top subplot, both left and right side thicknesses were almost constant from the front to aft edges of the slipper, which indicated that wear at this interface between the sides of the rail and slipper was negligible. Thus, rolling of the slipper did not appear to occur.

In the bottom subplot, a reduction in slipper lip thickness was observed when moving from the front to aft edge along the length of the slipper. For the first 6 cm, as measured from the front edge of the slipper, the slipper lip thickness was fairly constant at 16.25 or 16.5 mm. Between 6–20 cm from the leading edge, the thickness of both right and left side slipper lips decreased gradually. Both the left and right slipper lips were approximately 2.5 mm thinner at the aft edge than at the front edge.

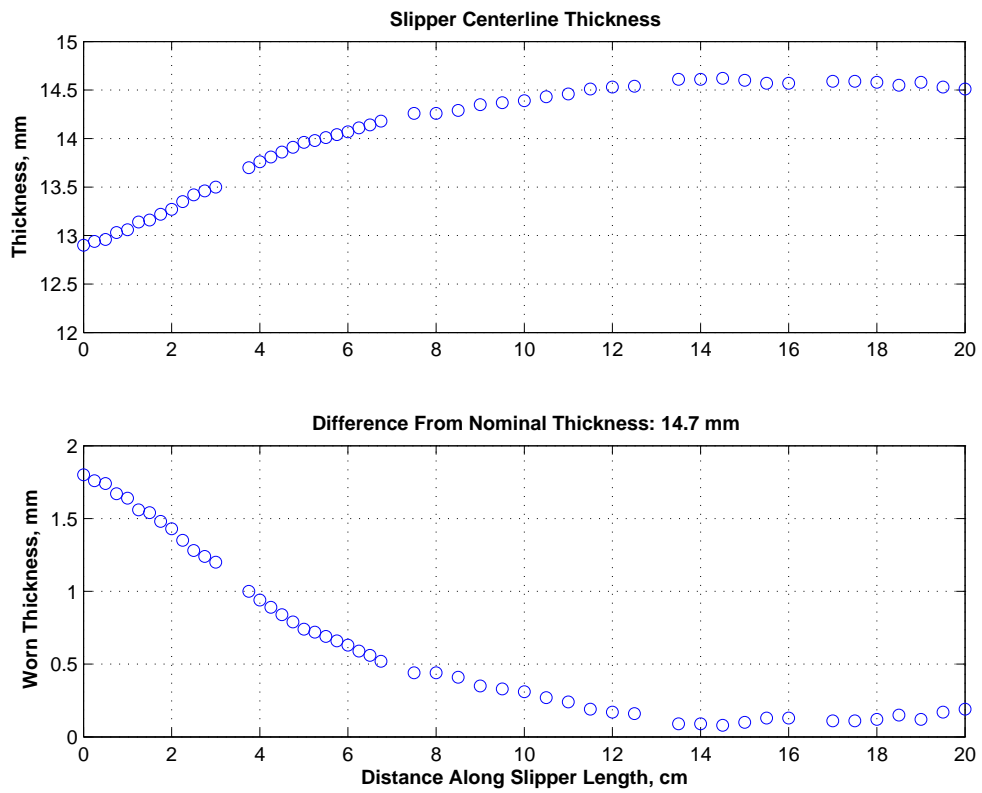


Figure 2.14: Slipper Top Thickness Measurements

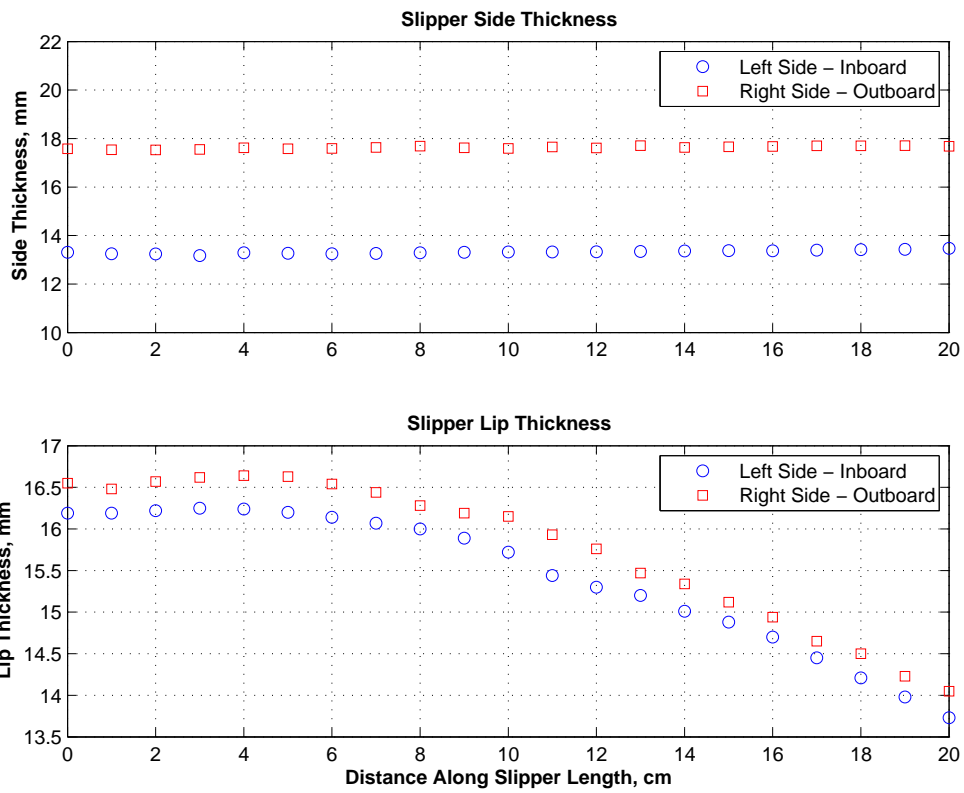


Figure 2.15: Slipper Side and Lip Thickness Measurements

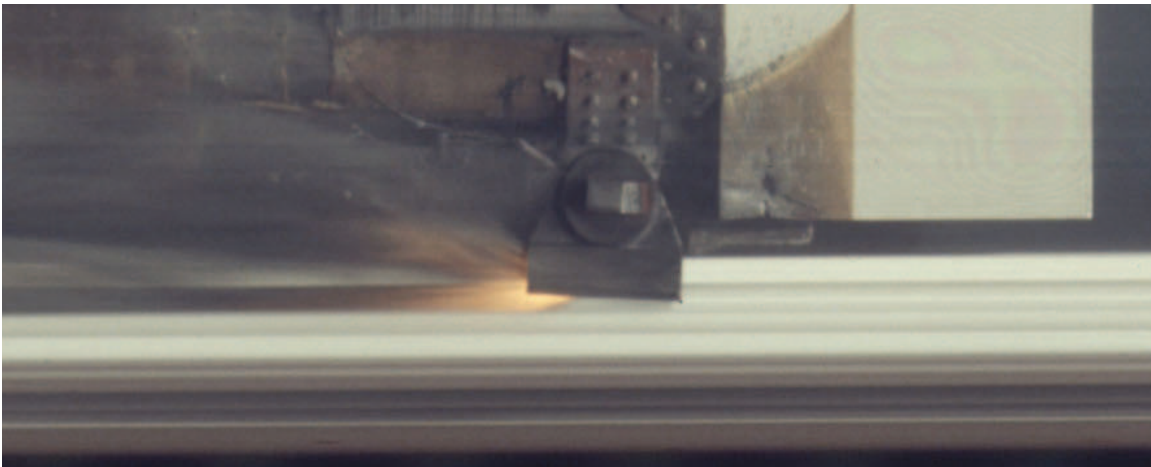
The reduction in slipper top and lip thickness was due to the uneven wear that occurred during the sled run. The slipper rotated about the axis of the slipper beam, which is the horizontal cross member that supports the rocket motor and also connects the slippers on the left and right side of the sled. From the frame of reference of the slipper beam axis (round part of top of slipper), the slipper pitched forward in a front edge down configuration. On the top surface, more wear occurred at the front of the slipper, as this surface impacted the top of the rail. Conversely, on the lip surfaces, more wear occurred at the aft end of the slipper as these surfaces contacted the bottom of the rail flange.

During the April 2003 test, designated by HHSTT as the 80X-G1 test mission, forward rotation of a slipper was captured in several high speed image motion compensation (IMC) photographs [2]. The forebody test sled, from Figure 1.1, was captured while sliding at velocities of 2,853 m/s and 2,861 m/s, respectively, in Figure 2.16. In both images, the forebody sled was traveling from left to right. The rail, with white epoxy coating, can clearly be seen in both figures. The white square on the right side of each image is the aerodynamic wedge that can be seen below the test payload in Figure 1.1. The slipper beam axis is located at the center of the round housing located above the slipper.

The “slipper fire”, or wear products departing the aft end of the slipper, that was referred to by Krupovage and Rasmussen [47] was clearly visible in Figure 2.16(b). At this instant, the slipper lips are contacting the lower part of the rail flange. Corresponding IMC images from the January 2008 test mission were not available for verification. However, both four stage sled trains were similar in design and desired maximum velocity. The photographic evidence from the April 2003 test mission imply that the same slipper rotation occurred in the January 2008 test mission. Slipper top and lip thickness measurements also confirm the slipper rotation as well.



(a) 80X-G1 Test Mission, April 2003, $V = 2,853$ m/s



(b) 80X-G1 Test Mission, April 2003, $V = 2,861$ m/s

Figure 2.16: Forward Rotation of Test Slipper [2]

2.6 *Hardness Test Results*

The hardness, a measure of the resistance of the material to plastic deformation, is measured by forcing an indenter into the surface [70]. One method of characterizing the heat-affected zone is by evaluating the microstructure hardness when traversing from the surface into the depth of the material.

Rockwell hardness and Knoop microindentation hardness tests were performed across the thickness of each slipper specimen. Loads of 1471 N (150 kgf) and 0.98 N

(100 gf) were used for the Rockwell hardness “C” (HRC) and Knoop (HK) microindentation hardness tests, respectively.

2.6.1 Bulk Hardness Tests: Rockwell Hardness. Because the shortest distance from the wear edge to the first indentation was 2.2 mm, material hardness between the wear edge and the first indentation was not measured. The test slipper material had a higher Rockwell hardness number in both the parallel and perpendicular directions than the new VascoMax 300 sample. In Figure 2.17, the top and bottom subplots show the HRC values for the perpendicular and parallel specimens, respectively. The abscissa represents the depth into the surface, while the ordinate represents the Rockwell hardness number. For the new samples, the parallel and perpendicular specimens both had a fairly constant hardness of 54 HRC. With the exception of the front perpendicular specimen (1xfu), the bulk hardness for all other test slipper specimens was 56 HRC. The front perpendicular specimen’s bulk hardness was approximately 55 HRC across the specimen.

The higher Rockwell hardness numbers for the test slipper specimens can be attributed to the work hardening that occurred as the slipper slid down the track. Due to the highly dynamic nature of the test event as depicted in the DADS data, the slipper intermittently impacts the rail. The normal contact pressure continued to increase until the Stage 3 sled began to decelerate. This increased pressure, along with an increased temperature due to frictional heating effects, caused the test slipper material to have a higher hardness than that of the new VascoMax 300 sample.

2.6.2 Microindentation Hardness Tests: Knoop Hardness. The Knoop microindentation hardness tests were also performed on each of the eight VascoMax 300 specimens. For each specimen, the first indentation was located 25 μm from the wear surface. Thus, the Knoop tests gave a better indication of the material hardness near the wear surface than the Rockwell hardness tests. Results of the Knoop microindentation hardness tests are shown in Figure 2.18, where the perpendicular and parallel specimens are presented in the upper and lower subplots, respectively. The abscissa

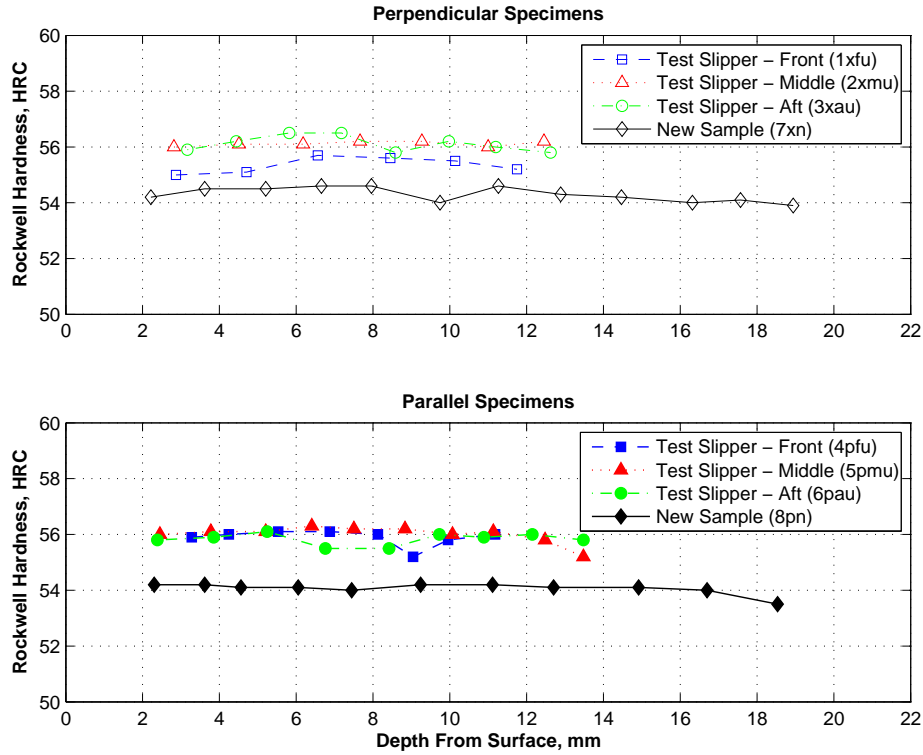


Figure 2.17: Rockwell Hardness of Perpendicular and Parallel Specimens

represents the depth into the surface, while the ordinate represents the Knoop hardness number. The Knoop hardness number for the new sample material was fairly constant through the thickness at approximately 700 HK.

For each of the test slipper specimens, the Knoop hardness number of the first indentation were between 450–550 HK as shown in Figure 2.18, which depicts HK values from the wear surface to a depth of 400 μm . The front, middle, and aft specimens showed similar HK values in both the perpendicular and parallel orientations. Each of the test slipper specimens approached the new sample microhardness of 700 HK at a depth of approximately 400 μm . Overall, there was a consistent softening in the front, middle, and aft test slipper specimens indicating the softening in the heat-affected zone brought about by the frictional heating as the slipper slid down the test track.

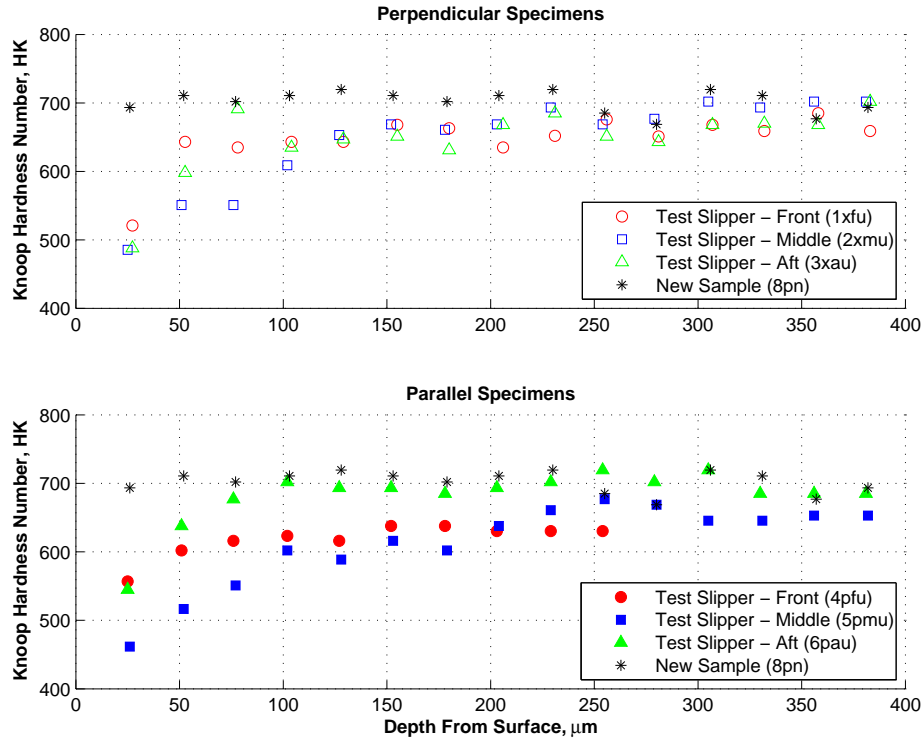


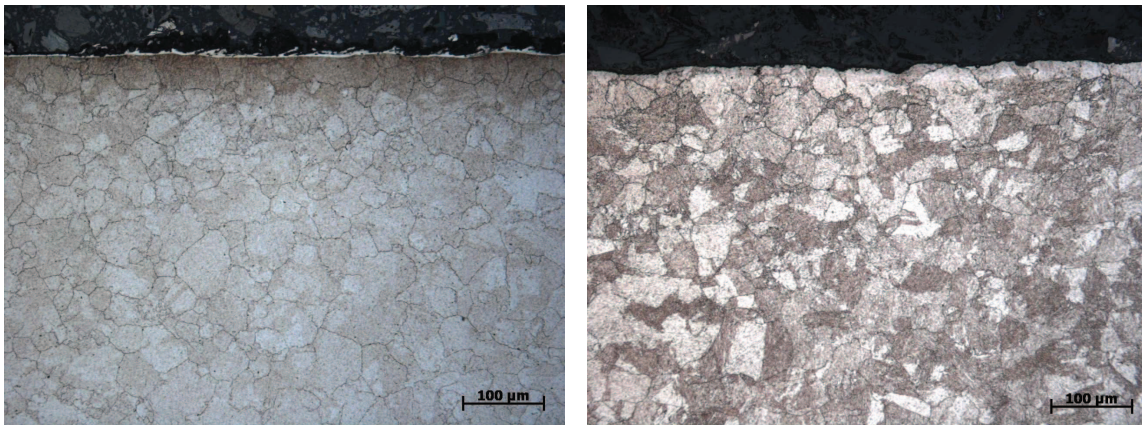
Figure 2.18: Knoop Hardness of Perpendicular and Parallel Specimens

The Knoop microindentation hardness testing indicated a uniform temperature effect/heat-affected zone across the entire length of the slipper. Melt wear occurs when material is removed due to induced temperatures that surpass the material's melting temperature. Because of the uniform material softening along the slipper length, we assume that uniform melt wear has also occurred at the slipper/rail interface. From the slipper centerline thickness measurements, Figure 2.14, this uniform thickness of worn slipper material was 0.1 mm. By multiplying this 0.1 mm thickness by the overall slipper length and width, the volume was 2.06 cm³. This uniform wear volume is therefore a combination of the mechanical wear and melt wear. It is possible to obtain a range of percentages to compare mechanical and melt wear contributions. If this 2.06 cm³ is attributed entirely to melt wear, then 19.6% of the worn material was caused by melt wear, and the remaining 80.4% was caused by mechanical wear. On the other hand, if only half of the 0.1 mm were attributed to melt wear, the ratio of

melt and mechanical wear then become 9.8% and 90.2%, respectively. Information of this kind is invaluable for the formulation of a numerical wear model.

2.7 Optical Micrographs

Upon completion of the hardness testing, each specimen was repolished, etched with oxalic acid (50% oxalic acid, 50% water), and viewed under bright field light with an optical microscope at 200x and 500x magnification. For the sake of brevity, the microstructure of only a few of the specimens are shown in the following figures. Comparisons between the new sample and test slipper wear edges and microstructure at 200x magnification are shown in Figure 2.19 for the perpendicular orientation. Figure 2.20 shows a similar comparison for perpendicular orientation specimens at 500x. In each of these figures, the new sample is on the left and the test slipper is on the right. The black material at the top of each figure is the carbon material for holding each specimen in the mount. The direction of travel for each test slipper specimen was right to left in each figure.

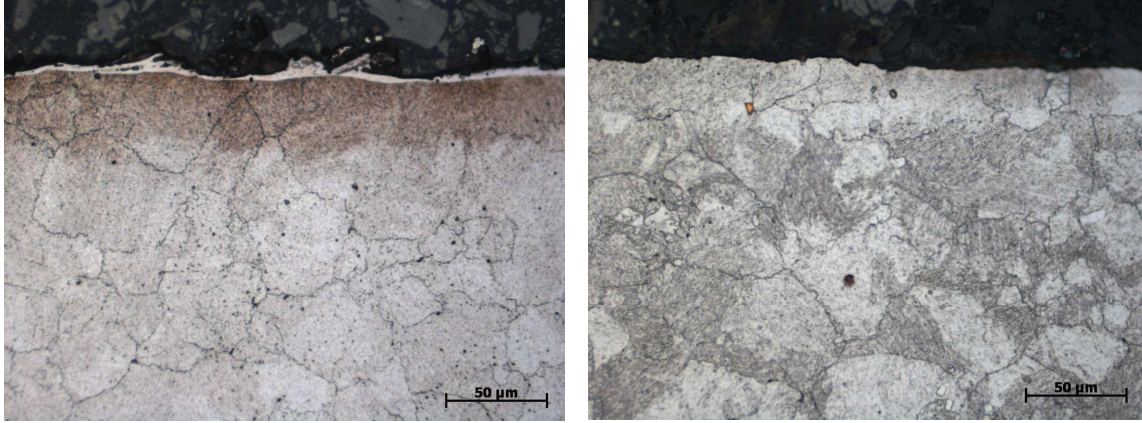


(a) New Sample, Perpendicular, 200x

(b) Test Slipper - 1xfu, Front, 200x

Figure 2.19: Optical Micrographs, Perpendicular Specimens, 200x

At both 200x and 500x magnifications, with the exception of etch response, there is little visual distinction between the new sample and test slipper microstructure. The microstructure for both specimens is characterized by lath martensite as expected for a maraging steel. Because of the slow transformation kinetic of maraging steels and



(a) New Sample, Perpendicular, 500x

(b) Test Slipper - 1xfu, Front, 500x

Figure 2.20: Optical Micrographs, Perpendicular Specimens, 500x

the rapid heating during the 8.14 second duration of the January 2008 sliding event, little microstructural changes are optically evident. There is a very thin layer right at the surface of the eroded or melted region in contact with the rail that appears to have been heated and worked sufficiently to recrystallize during cooling to form slightly finer lath martensite. The Knoop hardness traverses indicate there has been some overaging of the precipitates and tempering of the lath martensite. However, these effects would not be evident via optical microscopy.

Coarsening of the precipitates would require diffusion. The diffusion of elements in metallic materials is time and temperature dependent. Because the time that the slipper is in contact with the rail is so short, there is inadequate time for gross coarsening of the precipitates to occur. Recall that during the manufacturing process, the slipper was age hardened for 6 hours at 480°C, which was the necessary time and temperature for diffusion to occur. Finally, the material at the surface was melting due to frictional heating at the slipper/rail interface and being removed faster than the material properties of the remaining slipper could be changed. Thus, much of the metallurgically altered material would already have been eroded away.

As previously mentioned, the sliding event was characterized as mild wear because approximately 3.5% of the initial volume was worn away. Archard and Hirst

indicate that for mild wear “there is little indication of subsurface damage” [6]. The microstructure of the new sample and test slipper specimens was nearly identical. However, the Knoop microindentation hardness testing showed that there were differences in material hardness near the surface of the test slipper specimens.

It was assumed that microstructure changes would be readily apparent based on the optical microscopy and microindentation hardness testing. A similar metallurgical investigation of the AISI 1080 rail material revealed distinct features of the rail microstructure [27]. While both the wear and gouging events under study both occurred on the test track, the slipper and rail materials are different. In the gouged rail, a clear dark band revealed where the overtempered region was located [26; 29]. The AISI 1080 steel is a quench and tempered steel that exhibited different response to the thermal environment and the gouging event.

2.8 VascoMax 300 Chemical Composition Analysis

A chemical compositions analysis was performed on both the test and new sample slipper material specimens. Atomic absorption spectrometry and inductively coupled plasma atomic emission spectroscopy techniques were used to determine the elemental composition of these specimens. The weight percent for the constituent elements in both samples is shown in Table 2.2. With the exception of carbon and sulfur, both specimens had nearly identical chemical composition, which confirmed that both of the slipper specimens were from similar VascoMax 300 material. It is not known if the new sample material was removed from the aft right slipper used in this research. Slight differences in the chemical composition indicated that the core new sample specimen may have been cut from one of the other three Stage 3 or 4 slippers.

In order to determine material composition near the wear surface, Energy Dispersive X-ray Spectroscopy (EDS) was also performed at the wear sliding surface and substrate of the front, parallel test slipper specimen (4pfu). The substrate of the material was sampled approximately 90 μm below the wear surface. The results of

Table 2.2: Chemical Composition of Slipper Specimens by Percent Weight)

Element	Test Slipper	New Sample
Nickel (Ni)	18.19	18.12
Cobalt (Co)	8.74	8.84
Molybdenum (Mo)	4.85	4.87
Titanium (Ti)	0.73	0.73
Aluminum (Al)	0.11	0.10
Manganese (Mn)	0.034	0.034
Silicon (Si)	<0.079	<0.081
Carbon (C)	0.0087	0.0076
Sulfur (S)	0.0036	0.0030
Chromium (Cr)	0.12	0.12
Copper (Cu)	0.060	0.058
Iron (Fe)	Balance	Balance

the EDS of the VascoMax 300 slipper material are shown in Figure 2.21 where the solid red color indicates the sliding surface sampling, and the black line indicates the substrate material sampling. The sampling locations of the surface and substrate are depicted in the SEM micrograph insets.

The surface of the slipper closely matched the composition of the substrate with the exception of several constituents. Iron, nickel, and molybdenum at the surface were slightly higher than the substrate composition. Several peaks corresponding to other constituents that did not show up in the substrate sampling, namely carbon, titanium, oxygen, aluminum and silicon can be seen in the wear surface spectroscopy. This suggests that transfer of some of the AISI 1080 steel rail or rail coating material occurred during the wear event. From the Material Safety Data Sheet for the white epoxy coating [69], one of the components of the paint was TiO_2 , which was used to achieve the white pigment. The titanium and oxygen peaks that occur at the surface are most likely due to the white epoxy coating that has adhered to the sliding surface of the slipper as shown in Figure 2.7(d).

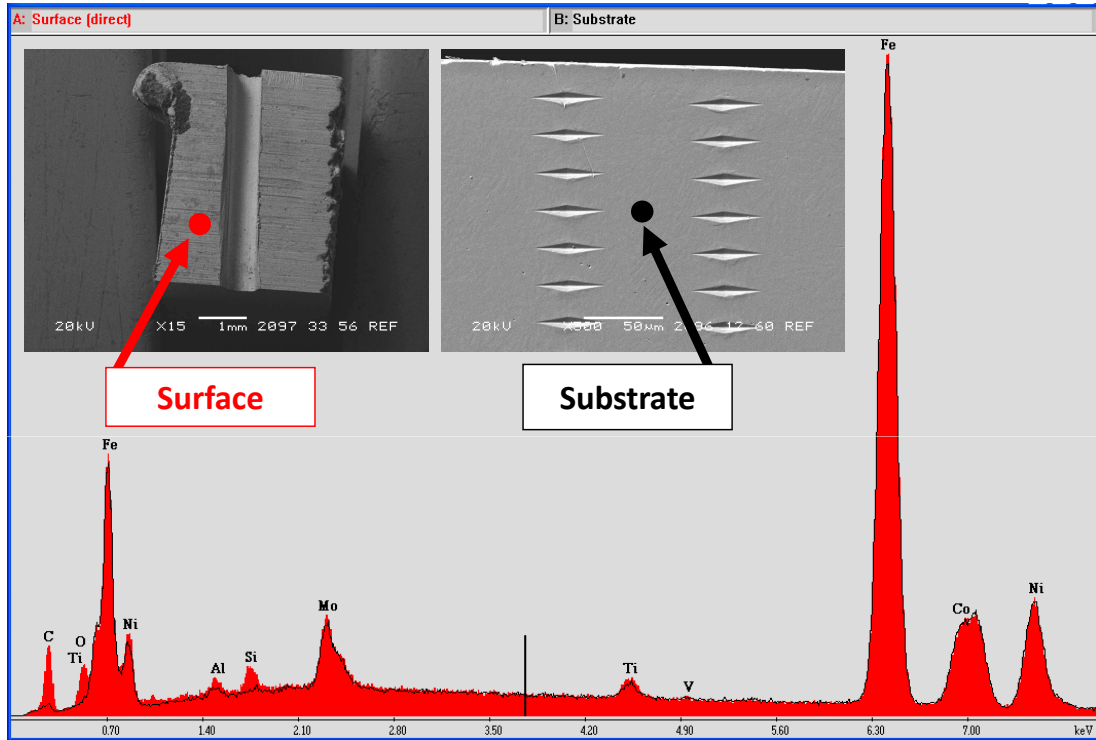


Figure 2.21: Energy Dispersive X-ray Spectroscopy, Test Slipper Specimen

2.9 Summary of Metallographic Analysis

The metallographic analysis of the aft right test slipper from the January 2008 test mission provided a greater knowledge of the dry sliding event. This slipper traveled a distance of 5,816 meters in 8.14 seconds and reached a maximum velocity of 1,530 m/s. The wear event was characterized as unlubricated, unidirectional steel-on-steel sliding. The total volume of worn slipper material was 10.52 cm³, which was 3.49% of the initial slipper top volume of 300.9 cm³. This was a mild wear event because of the low percentage of worn material.

Several characteristics from the metallographic investigation can be used in developing a numerical model of the wear event. Scanning electron microscopy inspection of the slipper sliding surfaces revealed plastic deformation which occurred as a result of many impacts and collisions between the slipper and rail asperities of varying size. Several factors must also be included in any numerical model. First, the model must account for this plastic deformation by including a viscoplasticity consti-

tutive model for VascoMax 300 slipper and AISI 1080 steel rail. Secondly, the plastic deformations were on the order of $10\ \mu\text{m}$. Thus, the model must account for slipper and micron-sized asperity collisions, and a method of incorporating the coefficient of friction into the slipper/rail interaction. The sliding event between this slipper and the entire 5,816 m rail is impractical to model in three dimensions. The model must be simplified.

Finally, the microindentation hardness testing revealed softening of the VascoMax 300 to a depth of $400\ \mu\text{m}$ below the surface. When compared to the overall initial 14.7 mm thickness of the slipper, we note that the effects of the frictional sliding event were very localized and this heat-affected zone occurred near the slipper/rail interface. Thermal energy generated during frictional heating doesn't have time to diffuse through the bulk of the slipper during the 8.14 second sliding event. The melt wear model should also be on the micro scale and reflect this short diffusion distance into the slipper.

III. Numerical Modeling

Before we begin presenting the features of wear rate analysis, it is important to indicate the procedure followed to arrive at a firmer understanding behind the physics related to high velocity wear. The objective of this chapter is to detail the methodology that was used to determine the mechanical and melt wear rates for the January 2008 test mission.

As outlined in Chapter I, most of the wear research to date has been at low velocity using pin-on-disk or similar experimentation. While helpful in developing the basis for high velocity research, previous research has limited application to the work being investigated. One aspect of the low velocity wear research is experimentation.

Much of the wear environment is three-dimensional and the wear occurs at the micron level. From the SEM micrographs in Section 2.3, there is evidence of this three-dimensional wear as well.

The observations during the metallographic analysis outlined in Chapter II give us an insight into the necessary features for the numerical wear rate model. The model has been oriented to a two-dimensional, plane strain analysis, where the three-dimensional physical features are depicted by the collision between the slipper and a single, hemispherical asperity centered at the surface of the rail. This is similar to a global discontinuity or “bump in the road”.

From the metallographic analysis, observations as related to the wear environment can be represented by material properties that include viscoplasticity, the need for consideration of high speed dynamics, a function to represent frictional interaction, and observations of mild wear of the test slipper.

Since the major characteristics of the high velocity wear environment relate to friction associated with a time dynamic event, a functional relationship was needed to yield this information. The results from Design Analysis of Dynamic Systems (DADS), time dynamic data provided by HHSTT was incorporated. DADS data yielded the force versus time function for each slipper, the horizontal velocity versus

time function of the test slippers, and the vertical velocity of the sled as a function of time. Since friction is a major player related to wear, it was necessary to establish a friction function related to the slipper dynamics.

Each topic area in Chapter II is used in generating the component parts of the numeric model's development.

3.1 Model Components

Since the major characteristics of a wear environment relate to friction associated with a time dynamic event, a functional relationship was needed to yield this information. The results from the use of time dynamic software was incorporated. This software goes by the name of DADS (Design Analysis of Dynamic Systems). The program yielded the force versus time function for each slipper, the horizontal velocity versus time function of the test slippers, and the vertical velocity of the sled as a function of time.

The highly dynamic movement is effected by the geometry of the sled and the surrounding aerodynamics. When aerodynamic forces exceed the dead sled weight, the slipper lips will impact the bottom of the rail flange. The vertical distance that the slipper can travel is limited by the slipper gap. As the slipper moves vertically through the slipper gap, there may be times when neither the slipper top or lip is in contact with the rail. This intermittent contact between the slipper and the rail occurs for the duration of the test run above a certain velocity threshold. Following the January 2008 test mission, HHSTT engineers captured several slipper impact marks, on the rail in the vicinity of the white epoxy coating, as shown in Figure 3.1. It is not known if these marks were made by the same slipper, or if they were made by two different VascoMax 300 slippers passing over this section of the track.

3.1.1 Dynamic Analysis and Design System (DADS) Model. In order to trace this intermittent contact, the HHSTT engineers use Dynamic Analysis and Design Systems (DADS) software which predicts the dynamic loads experienced by

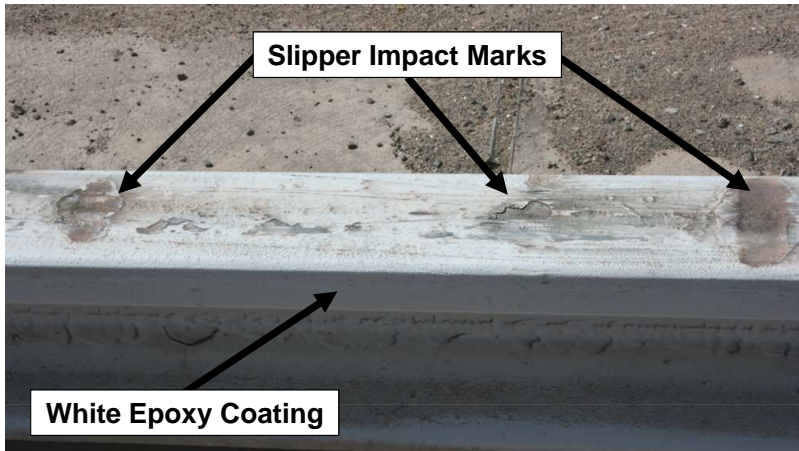


Figure 3.1: Slipper Impact Marks on White Epoxy Rail

the sled [36; 37]. Dynamic Analysis and Design System, developed by Computer Aided Design Software, Inc., is a commercial-off-the-shelf (COTS) software package used by the HHSTT engineers to predict the dynamic loads experienced by the sled traveling down the track [36; 37].

The sled components and their interactions are modeled with appropriate values of mass, inertia, and stiffness. Figure 3.2 depicts the slippers, slipper beam, aerodynamic wedge, rocket motor, and test payload for the rocket sled shown in Figure 1.1. A mathematical model of the test track rails, based on actual laser rail survey and alignment data, is input into the DADS model to represent the sled’s trajectory along the rail. The DADS model data include simulation time, normal vertical slipper contact forces on the rail, and slipper displacement and velocities in the vertical, lateral, and horizontal directions. As this DADS model is extremely complex, these data are accepted as “truth” data with no subsequent modification.

To validate the predicted dynamic loads, HHSTT test engineers instrumented a test sled with on-board accelerometers and the output was recorded during several validation test missions. The predicted measurements were then compared to the recorded measurements. The DADS model was then adjusted to more accurately follow the actual test data. Hooser [36] described how the DADS technique was effective in accurately duplicating the sled-borne measured accelerations from a sled

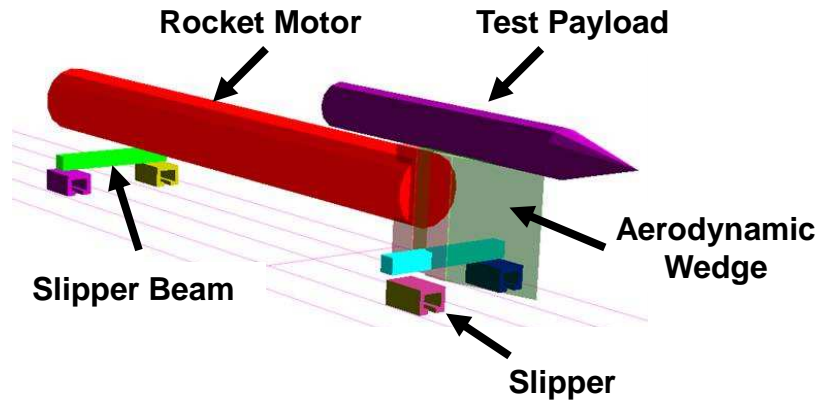


Figure 3.2: DADS Model for 80X-G1 Forebody Sled

test. Also, Hooser and Schwing [37] describe the DADS model validation process in more detail.

Early in the DADS model development, the track was modeled as a perfectly flat rail with no imperfections or welding inconsistencies. This limitation resulted in sleds that would slide along the rail without the “bouncing” effect described previously. The mathematical model of the rail, based on actual laser rail survey and alignment data, is input into the DADS model to represent the sled’s trajectory along the rail. The sled now responds to the rail variations, due to manufacturing and rail alignment tolerances, resulting in a more realistic response [37].

3.1.2 January 2008 Test Mission Raw DADS Data. The HHSTT provided the DADS data for the January 2008 Stage 3 pusher sled. Typically, the HHSTT only performs a detailed DADS data analysis of the forebody, as this sled is where the test payload is mounted. However, in support of this research, Mr. George Ayers modified the DADS model to provide the Stage 3 pusher sled raw DADS data. Raw data refers to the fact that this data was supplied by HHSTT and has yet to undergo the DADS statistical analysis described later in this chapter.

The DADS file provided the following data at 0.0002 second increments during the 8.14 second test mission run: simulation time, Sled center of gravity (C.G.) Position, Velocity, Acceleration, and normal vertical slipper contact forces on the rail.

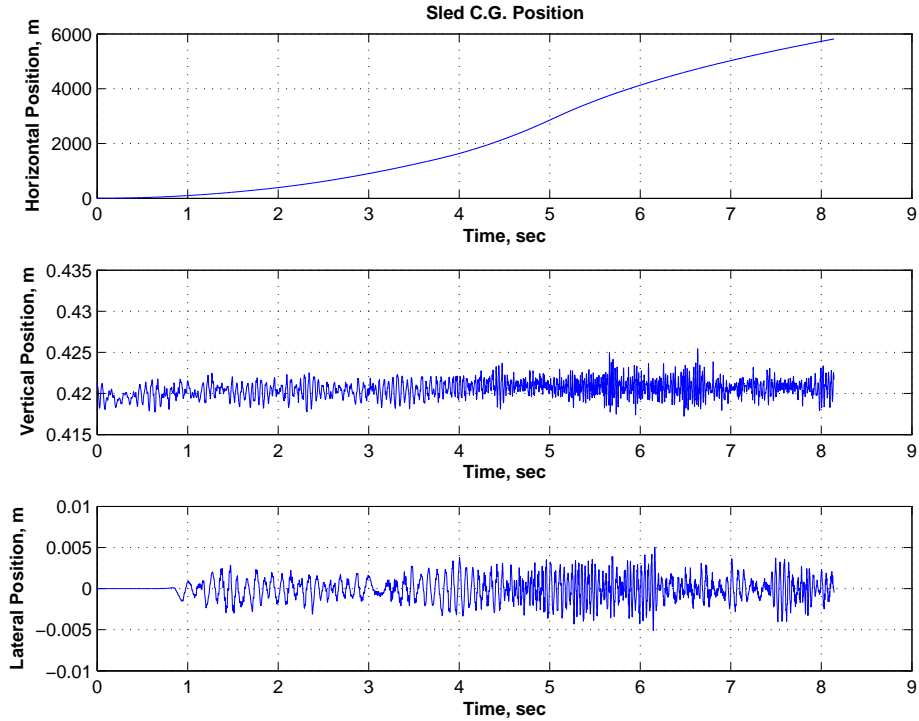


Figure 3.3: Position of Sled C.G., Jan 2008 Test Mission

Upon receipt of the DADS data, all English units were converted to equivalent SI units.

The position, velocity, and acceleration data as a function of time were given for the lateral, vertical and horizontal directions. The lateral direction corresponds to the crosstrack direction across the width of the rail. The horizontal direction corresponds to the downtrack direction. Slipper C.G. velocities and contact forces were provided for each of the four VascoMax 300 slippers. The position, velocity, and acceleration of the center of gravity of the Stage 3 sled are presented in Figures 3.3–3.5, respectively. Moving from top to bottom, each subplot in these figure shows the horizontal, vertical and lateral values, respectively, as a function of time.

Figure 3.3 shows the position of the sled C.G. During the test run, the sled travels horizontally a distance of 5,816 meters. The change in the slope of the horizontal position at about 3.5 seconds corresponds with the higher velocity due to the Stage 3 rocket motor. The vertical position of the sled C.G. was 0.42 meters above the DADS

horizontal datum plane. During the test run, this vertical position remains within ± 0.5 cm of the datum plane. The lateral position for the duration of the test run was within ± 5 mm of the track centerline. Figure 3.4 shows the velocity of the sled C.G. The horizontal velocity, shown in the top subplot, is the same velocity profile that was presented in Figure 2.3. Both the vertical and lateral velocities were within ± 1.5 m/s.

In Figure 3.5, the accelerations have been converted from m/s^2 to the acceleration due to gravity, or “G’s”, by dividing each acceleration by 9.81 m/s^2 . The horizontal acceleration in the top subplot shows the change in acceleration during the Stage 2 and Stage 3 rocket ignitions at approximately 1.8 and 3.5 seconds during the test run. The peak horizontal acceleration is approximately 155 G’s. The change from positive to negative G’s at approximately 5.0 seconds corresponds to the time when the maximum velocity is reached, and the sled begins to decelerate. In Figure 3.6, the horizontal position, velocity, and acceleration are presented as a means of showing the relationships between each parameter. No vertical or lateral values are presented in this figure.

The DADS data provides normal contact forces at six locations around the rail as depicted in Figure 3.7. Positions 3 and 4 give the location of the normal contact forces between the top of the rail and the bottom of the slipper. The sum of the Position 3 and 4 contact forces give the actual normal contact force at this rail/slipper interface. Positions 1 and 6 give the location of the normal contact force between the bottom of the rail flange and the slipper lips. Positions 2 and 5 correspond to side-to-side contact between the rail and the side of the slipper. As this research focuses on the top of the rail/bottom of the slipper contact interface, wear at Positions 1, 2, 5 and 6 are not evaluated in this research. When the slipper is in contact with the rail, the normal contact force values are positive. When the slipper is not in contact with the rail, the magnitude of the force is zero.

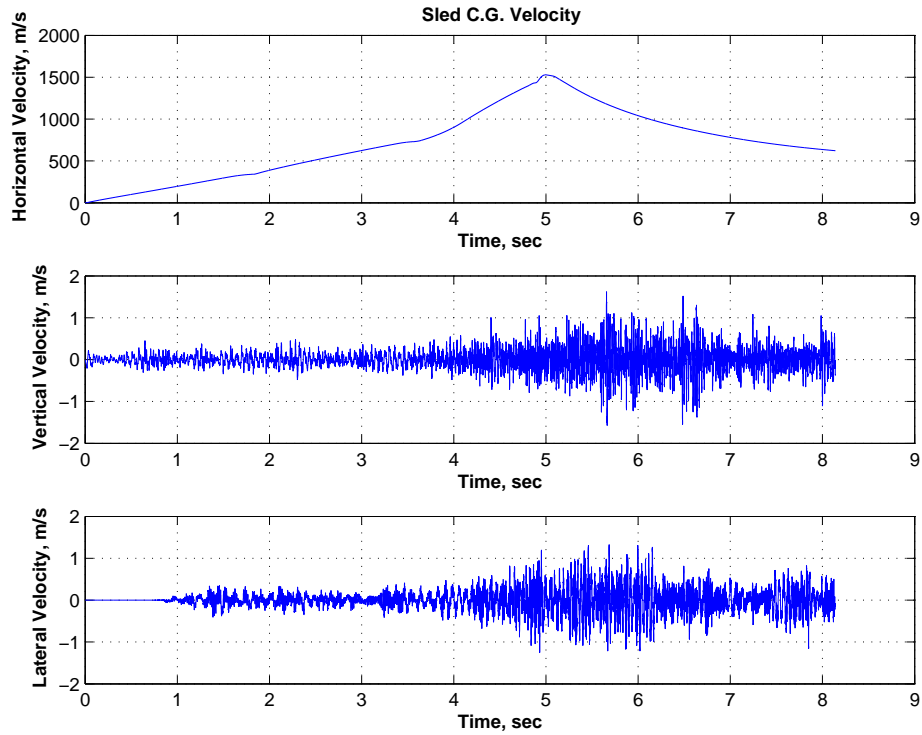


Figure 3.4: Velocity of Sled C.G., Jan 2008 Test Mission

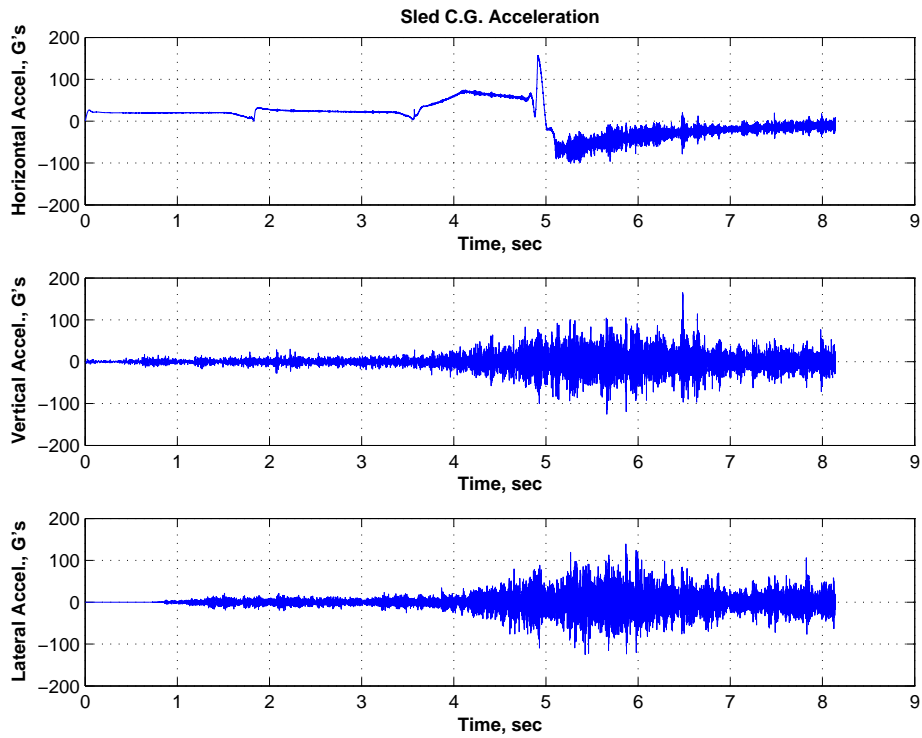


Figure 3.5: Acceleration of Sled C.G., Jan 2008 Test Mission

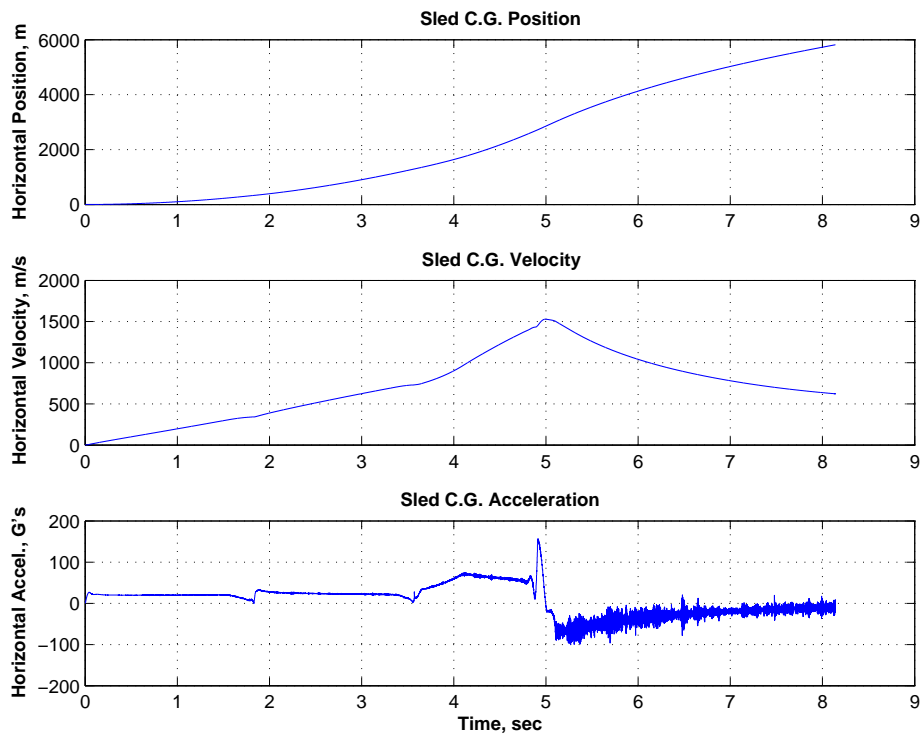


Figure 3.6: Horizontal Position, Velocity, and Acceleration

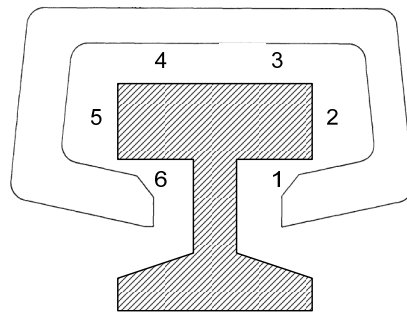


Figure 3.7: DADS Contact Locations on Rail Cross Section

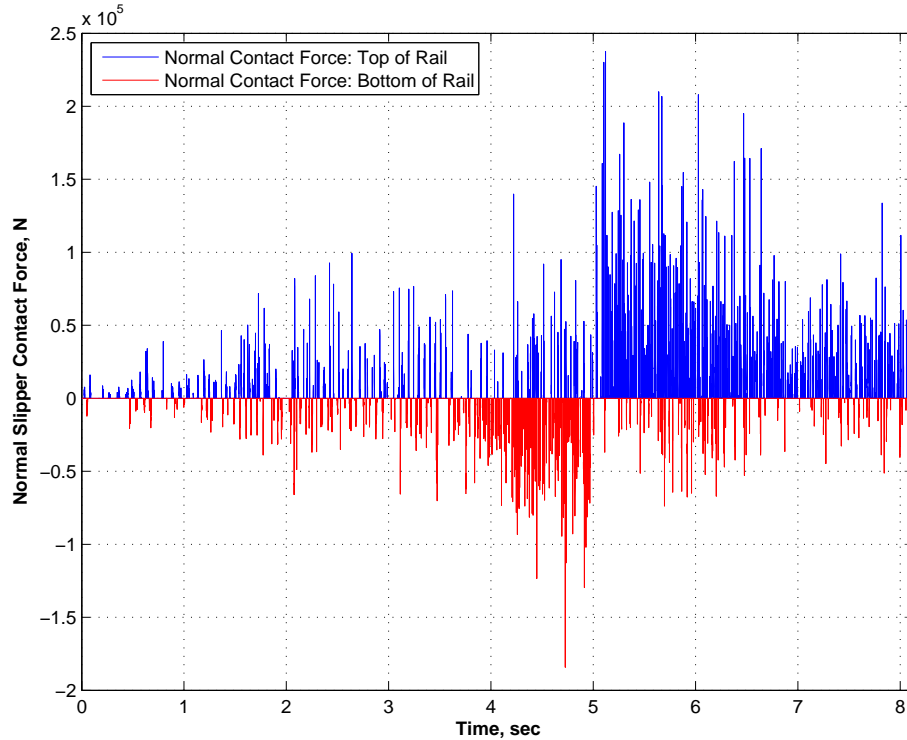


Figure 3.8: Normal Slipper/Rail Contact Forces

Although there are six slipper locations for the DADS contact forces, these forces are all reported for only one location along the length of the slipper at the slipper C.G. Thus, we are unable to use the DADS forces to predict the nose-down pitch, or slipper rotation, as was depicted in Section 2.5.

Two sets of raw DADS normal slipper contact force data for the aft right test slipper are depicted in Figure 3.8. The sum of the contact forces at Positions 3 and 4 are designated as the “top of the rail” contacts. Conversely, the sum of the contact forces at Positions 1 and 6 are designated as “bottom of the rail” which represent the contact between the bottom of the rail and the slipper lips. In order to depict both top and bottom contact forces with the rail on the same figure, the “bottom of the rail” contact forces have been given a negative magnitude, so that they appear below the abscissa.

The relationship between the top and bottom contact forces can clearly be seen in this figure. For the first 3.5 seconds of the test run, the DADS data shows that the

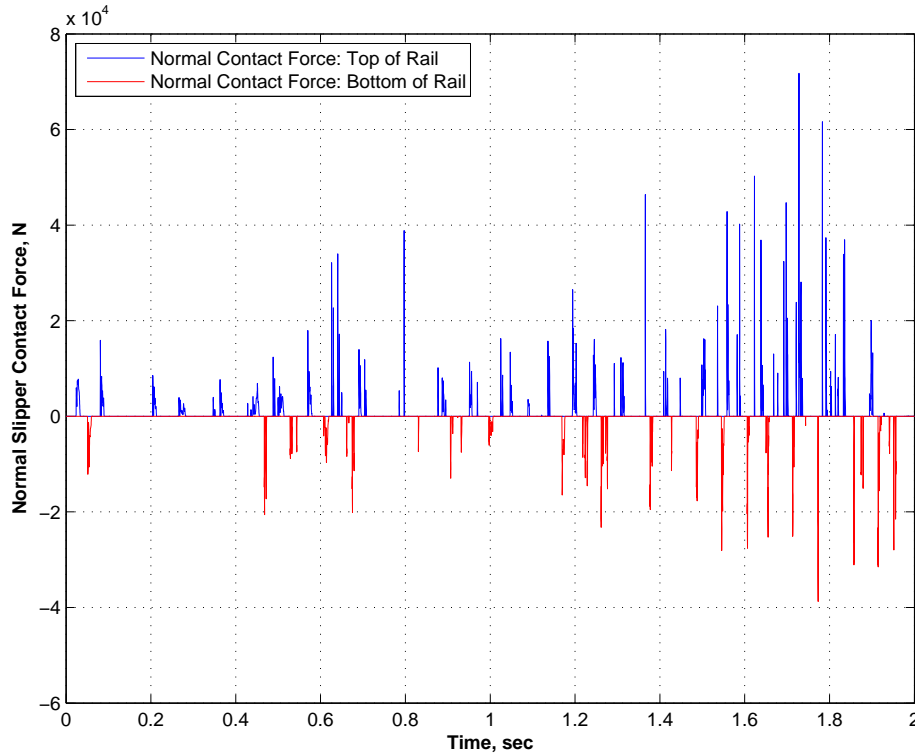


Figure 3.9: Normal Contact Forces, 0-2 seconds

contact forces for the top and bottom of the slipper have a similar density, or number of impacts or contact events per unit time. When the Stage 3 rocket motor fires at approximately 3.5 seconds, the number of impacts along the bottom of the slipper increases until 5.0 seconds, which corresponds to the beginning of the deceleration phase. At this time, the density of contact forces at the top of the rail increases as an indication that the slipper is decelerating.

The intermittent nature of the slipper contacts can be seen by looking at the first two seconds of the test run as shown in Figure 3.9. At any given point in time, there are three possible contact conditions: only top of rail contact, only bottom of rail contact, or no slipper/rail contact. The first two conditions occur when the slipper has reached the end of the slipper gap distance and either the slipper top or lip contacts the rail. Periods of no slipper/rail contact indicate that the slipper is moving vertically through the slipper gap.

3.1.3 DADS Comparison: January 2008 vs. 80X-A1 Test Mission. The HHSTT engineers have provided DADS data for two separate test missions. The DADS data for the January 2008 test mission have been discussed in detail earlier in this section. An additional set of DADS data, for a mission designated by the HHSTT as 80X-A1, was provided to Cameron for his thesis research in January 2007 [23; 24]. This data set was for a single SRR forebody sled, and didn't include data from the first three pusher sleds. The velocity profile was a nearly constant acceleration from 0 to 3,000 m/s in 2.5 seconds. Data were provided at 0.0001 second intervals.

Both sets of DADS data were analyzed to determine the incremental sliding distance during each contact event, characterized by non-zero contact forces in the DADS data. At any given time in the analysis, the cumulative percentage of contact distance was calculated by dividing the sum of these sliding distance increments by the total distance traveled up to the given time in the analysis. Using similar methodology, the percent time in contact was also calculated for each DADS data set. If the velocity were held constant, then both time and distance in contact percentages would be the same. The cumulative percent of contact distance for both DADS data sets are presented in Figure 3.10. Similarly, the cumulative percent of contact time for both DADS data sets are presented in Figure 3.11. Table 3.1 summarizes these contact percentages based on time and distance for both DADS data sets. From both the figures and the table, it is apparent that the 80X-A1 has higher contact percentages for both the time and distance parameters.

Several differences between the DADS data sets lead to the differences in the contact percentages. In the 80X-A1 data set, DADS data was provided at 0.0001 sec intervals. To reduce the file size, DADS data for the January 2008 test mission were provided at 0.0002 sec intervals, or twice that of the 80X-A1 data set. Perhaps by having a longer time interval, the January 2008 data set is aliasing some of the actual contact forces that may have been reported at the 0.0001 sec interval. A reduction in the number of actual contact forces would lead to a lower total sliding distance, and consequently a lower overall percent in contact for both the time and distance

Table 3.1: Comparison of DADS Contact Percentages

DADS Data	Parameter	Sliding Total	Overall Total	Percent
January 2008 80X-A1	Distance	614.8 m	5,816 m	10.57 %
	Distance	1,186.7 m	3,874 m	30.63 %
January 2008 80X-A1	Time	0.90 sec	8.14 sec	11.04 %
	Time	0.87 sec	2.50 sec	34.84 %

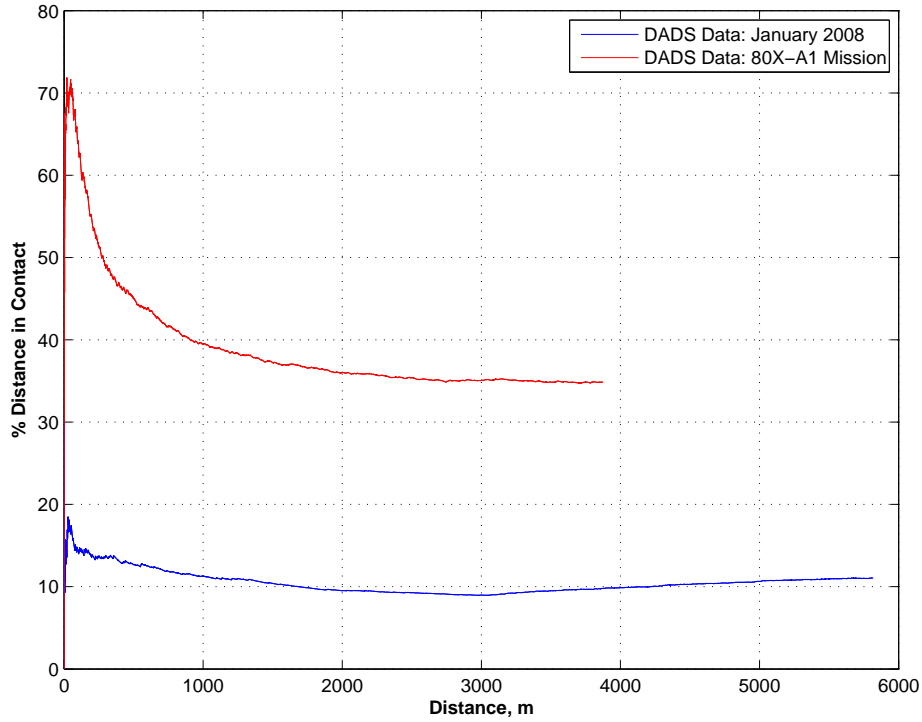


Figure 3.10: Percentage Distance in Contact

parameters. Also, the 80X-A1 data is for a Stage 4 forebody sled only, and doesn't include dynamic force data associated with the Stage 1, 2, and 3 pusher sleds. The 2.5 second run time only accounts for the single forebody sled trajectory, and doesn't include the time and distance associated with three pusher sleds. To increase the accuracy, we will incorporate the distance contact percentages associated with the more refined DADS data set.

3.1.4 DADS Statistical Analysis. Rather than use the intermittent raw DADS contact force data in the FE model, the following DADS statistical analysis

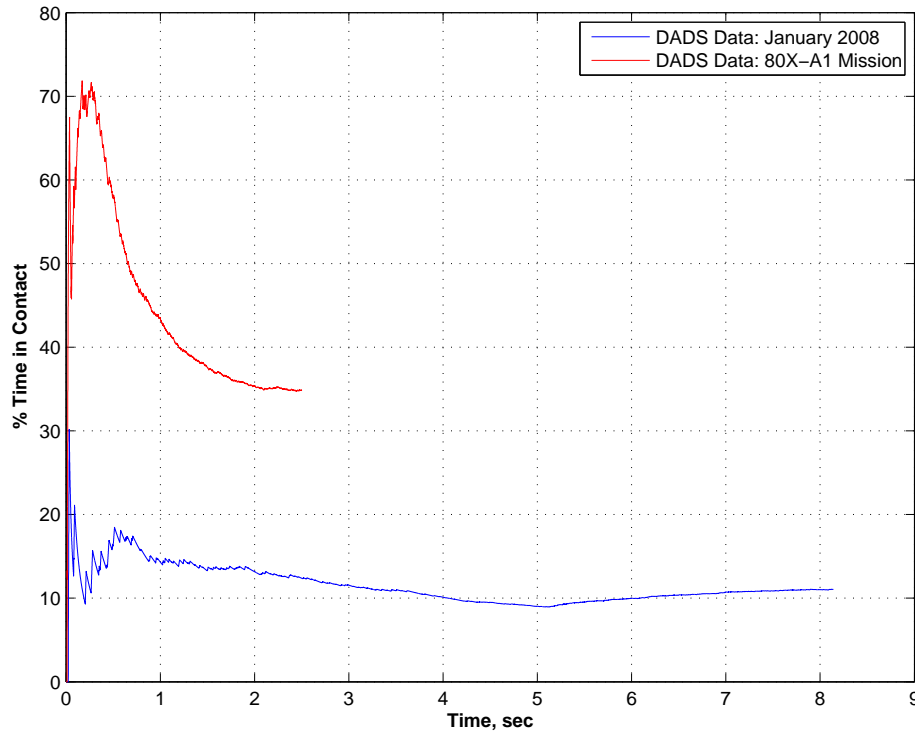


Figure 3.11: Percentage Time in Contact

technique was developed to create a smooth force or pressure function as a function of time. It would be impractical to incorporate the exact contact force profile into the FE model. A moving window averaging approach is used during the statistical analysis of the DADS contact force data. For this analysis, a 0.4 second time window and a 0.2 second time shift were used. The time increment window is shifted by half the initial time window increment to overlap some of the data. As the slipper/rail interface at Locations 3 and 4 is of primary interest in this research, this statistical analysis was only accomplished on these contact forces.

For a given time interval window, a statistical analysis of the raw DADS data is performed to determine a distribution for the slipper normal contact force and velocity to be applied during the finite element model analysis. A gamma distribution is fit to the non-zero contact forces. From this distribution, a mean force and an upper limit force (95% bound on all contact forces), as well as the mean velocity during the time increment are determined. Statistical upper limit normal contact forces from

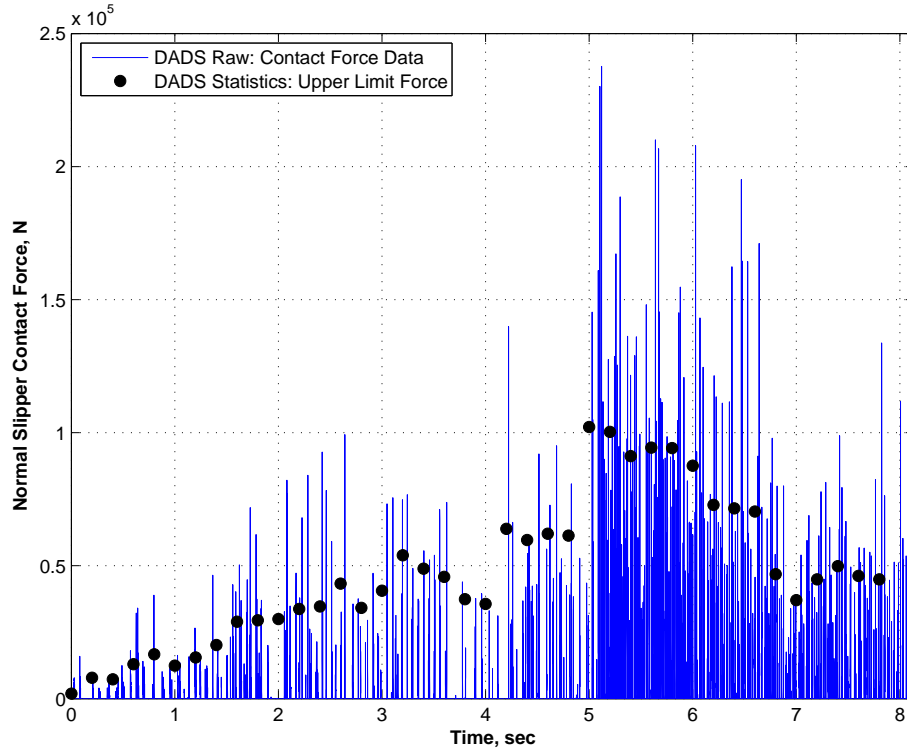


Figure 3.12: DADS Raw and Statistical Contact Force

the moving window analysis are also included in Figure 3.12. Corresponding normal pressure is derived by assuming that this normal contact force is fully distributed over the slipper contact area of 206.4 cm^2 . Smooth curve fits to the discrete pressure data points are generated to provide continuous functions. This upper limit pressure, shown in Figure 3.13, was used as an input along with the horizontal sled velocity to the appropriate boundary conditions of the finite element model. Details of the DADS statistical analysis are found in Appendix A.

Rather than determine wear rates for every instant of time during the sled run, twelve velocities along the horizontal velocity profile were selected. These “targeted velocities” correspond to key velocities in the Stage 3 velocity profile. Several low velocities at 10, 20, 40, and 100 m/s were selected so that results of the wear rate model could be compared with low velocity data from published literature. The 1,530 m/s corresponds to the maximum velocity of the Stage 3 sled, while 622 m/s corresponds to the final sled velocity as it departed the test track. The pressure at

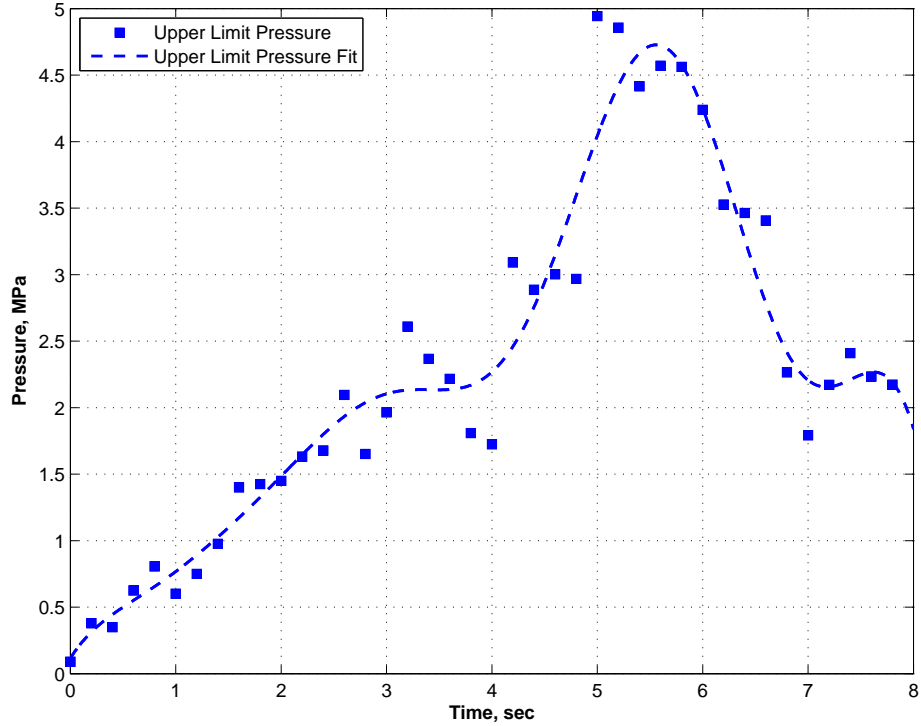


Figure 3.13: DADS Statistical Upper Limit Pressure

each of these targeted velocities was computed by evaluating Equation A.3 with the curve fit coefficients for the upper limit pressure as shown in Table A.1 in Appendix A.

A summary of the DADS statistical data for the given target sled velocities is given in Table 3.2. The target time and distance correspond to the elapsed time and distance traveled from the starting location, respectively, before reaching the target velocity. The upper limit pressures are also listed for each target velocity. Thus, for $V = 300$ m/s, the sled has traveled 230.08 meters in 1.521 seconds, and the corresponding upper limit pressure is 1.113 MPa.

By analyzing the January 2008 DADS data, we now have applied pressure and forces as a function of time. The DADS statistical analysis has converted the intermittent contact forces into a smooth function where we can approximate the pressure on the slipper at any given point in time during the test run. The raw DADS data provided the horizontal velocity profile for the Stage 3 slipper. We are now able to

Table 3.2: Summary of DADS Statistical Data at Target Velocities

Target Velocity (m/s)	Target Time (sec)	Target Distance (m)	Upper Limit Pressure, P_{ul} (MPa)
10	0.055	1.94	0.180
20	0.100	2.63	0.226
40	0.195	5.49	0.309
100	0.501	26.98	0.500
200	1.017	104.30	0.778
300	1.521	230.08	1.113
500	2.451	593.38	1.836
622	8.140	5,815.50	1.373
750	3.661	1,359.34	2.141
1,000	4.150	1,779.43	2.403
1,250	5.515	3,575.81	4.727
1,530	4.998	2,850.29	4.037

develop the functional relationships for friction, by making use of these established pressure, force, and velocity functions.

3.1.5 Frictional Contribution. The finite element model for predicting wear rates at high velocity is based on the dynamic events that occur as the slipper interacts with the rail. For the present study, we are not interested in a three-dimensional or tribological analysis that takes into account the micromechanical regime of the slipper and rail interaction. The slipper and rail interaction is modeled by a collision between the slipper and a single asperity, or “bump in the road”. In reality, there are many asperities of different shapes and sizes distributed on the surface of the rail. The single asperity, which represents the many multiple asperities, is not a real individual asperity on the rail surface. This is our way of accumulating all of the asperity impacts that occur in the numerous wear events during the course of the sled run.

Since friction is a major factor related to wear, it was necessary to establish a frictional function related to the slipper dynamics. This is one of the key findings from the metallographic analysis in Chapter II. During the test run, the slipper velocity range is 0–1,530 m/s and the pressure range is 0–4.7 MPa. The DADS data

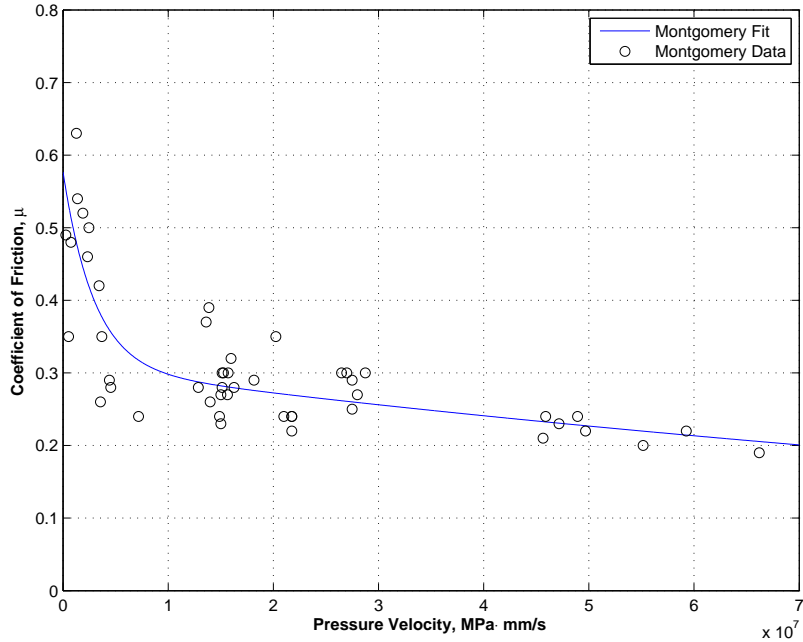


Figure 3.14: Montgomery Coefficient of Friction vs. Pressure Velocity

shows that there are numerous contact events with the rail. Therefore, to establish the frictional function, we make use of Montgomery’s study that focused on friction and wear at high sliding speeds with particular emphasis on artillery projectile and cannon muzzle wear [61].

Data points for Montgomery’s pin-on-disk studies of projectile steel on gun steel were used to create the coefficient of friction, μ , between the slipper and rail as a function of pressure velocity, Pv . Pressure velocity is the product of applied pressure, P , and velocity, v . Montgomery’s data points were plotted and fit with an exponential curve fit as depicted in Figure 3.14. Equation 3.1 gives the coefficient of friction as a function of pressure velocity, Pv . When the pressure velocity product exceeds 4.45×10^8 MPa mm/s, the coefficient of friction is held constant at 0.02, which corresponds to that noted by Montgomery at very high pressure velocity [61]. In the ABAQUS finite element model, the base length unit is in millimeters and the base pressure unit is MPa. Thus, the equation and figure depict pressure velocity with

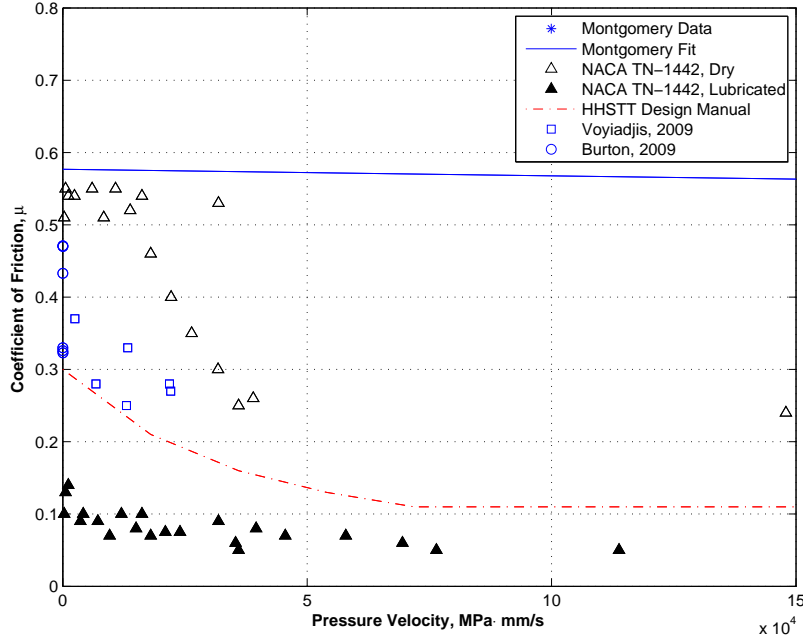


Figure 3.15: Coefficient of Friction vs. Pressure Velocity

units of $\text{MPa} \cdot \text{mm/s}$.

$$\mu(Pv) = \begin{cases} 0.2696e^{-3.409 \times 10^{-7} \cdot Pv} + 0.3074e^{-6.08 \times 10^{-9} \cdot Pv} & : 0 < Pv < 4.45 \times 10^8 \\ 0.02 & : Pv \geq 4.45 \times 10^8 \end{cases} \quad (3.1)$$

This coefficient of friction as a function of pressure velocity is now compared with several other studies. As was shown in Figure 1.17, the HHSTT coefficient of friction function appears as the average of the dry and lubricated test results. As published in NACA TN-1442 by Johnson et al. [42], the coefficient of friction is presented only as a function of velocity. The NACA TN-1442 $\mu(Pv)$ for both the dry and lubricated conditions was computed by multiplying each data point by the corresponding applied pressure. The pressure for the majority of the dry and lubricated data points was 1.18 MPa. The HHSTT $\mu(Pv)$ function was also determined by multiplying the HHSTT coefficient of friction by 1.18 MPa.

In a 2009 technical report to AFIT, Voyiadjis et al. detailed the use of VascoMax 300 slipper and AISI 1080 steel rail specimens in Phillipon's friction device to evaluate

the coefficient of friction [76]. The maximum sliding velocity was 3 m/s and the applied pressure was 8 MPa. The Voyiadjis $\mu(Pv)$ is also plotted in Figure 3.15.

During his master's thesis in 2009, Burton conducted a study to determine a frictional coefficient for the slipper and rail sliding event at the HHSTT. Detailed profiles of the VascoMax 300 slipper and AISI 1080 steel rail were incorporated into a two-dimensional plane strain finite element model to simulate the sliding interaction. The maximum velocity in Burton's study was 4.6 mm/s and the pressure was 8.76 MPa [21; 22]. The Burton $\mu(Pv)$ values are also included in Figure 3.15.

When compared to the Montgomery data, the range of Pv values for the NACA TN-1442, HHSTT, Voyiadjis et al, and Burton are all very low. In Figure 3.15, the range of the abscissa has been changed to $0-15 \times 10^4$ MPa \cdot mm/s for easier comparison of these additional data sets. No raw Montgomery data points show up in the figure because the lowest raw Montgomery data point occurs at 2.7×10^5 MPa \cdot mm/s. However, the Montgomery curve fit still applies. As expected, the HHSTT Design Manual frictional function appears as the average of the NACA TN-1442 dry and lubricated values. The frictional function from Voyiadjis et al. follow the slope of the HHSTT data but are higher by about 0.1. While at extremely low Pv values, Burton and Brockman's coefficient of friction values are similar to those of Voyiadjis et al.

The Montgomery frictional function is conservative at low pressure velocity. However, this coefficient of friction as a function of Pv is necessary during the local submodel slipper and asperity collisions in the finite element analysis. It accounts for the combined effect of the slipper velocity and the contact pressure to determine the frictional coefficient.

3.2 Global Finite Element Analysis

Results of the DADS statistical analysis are incorporated into a the wear rate model. Analytically, the high velocity wear phenomenon has been approached by first developing this wear model for low velocities. This wear prediction model, made of a

global analysis incorporated into a local submodel with an asperity collision, has been carried out in ABAQUS and has been extended to account for the higher velocities represented at the HHSTT. The wear rate, defined as the volume of worn material per unit sliding distance, is calculated at specific target velocities. The numerical integration over time and velocity with these incremental wear rates produces the total wear for the test slipper during the sled test run. Preliminary results show that the predicted total wear is less than the initial thickness of the slipper [23].

ABAQUS employs two methods for solving time-dependent linear and non-linear dynamic equations that govern the response of the dynamic system [33]. The first method is the “standard” implicit solver and will be referred to as ABAQUS/Standard. ABAQUS/Standard is a general-purpose analysis solver that can solve a wide range of linear and nonlinear problems involving static, dynamic, thermal, and electrical response of the model components. It solves a system of equations implicitly at each solution increment. In the current time increment, the solver must iterate to determine unknown values from current information. The ABAQUS/Standard solver is better suited for dynamic analysis problems with slowly varying applied loads.

The second method is an explicit dynamic integration solver and will be referred to as ABAQUS/Explicit. Small time increments are used to march a solution forward through time without solving a coupled system of equilibrium equations at each increment. Thus, the unknown values are obtained from information that is already known. ABAQUS/Explicit was designed to efficiently solve highly discontinuous, high-speed dynamic problems such as impact problems that include wave propagation. The ABAQUS/Explicit solver will primarily be used during the finite element analysis in this research. It should also be noted that no coupled displacement/thermodynamics analysis was used in the finite element model. We assume that the material properties are not a function of temperature and therefore remain constant for the short duration of the local submodel slipper and asperity collision analysis.

3.2.1 Global Model. The two-dimensional plane strain global model was created to represent the interaction between the slipper and rail. The intent of the global model was twofold. First, the goal was to determine the state of stress within the slipper at any time during the sled run. Once the state of stress was determined, it would then be applied to a local submodel at one of the target velocities to further evaluate the asperity collision. Wear rates were determined exclusively by using the submodel slipper/asperity collision. Second, the goal was to see if the dynamics of the global slipper could successfully be modeled in the finite element analysis. The pressure function and horizontal velocity from the DAD analysis, along with the frictional function from Montgomery, were applied to the slipper, which was modeled as a rectangular box sliding on top of a flat rail.

Three different global analysis cases were modeled in ABAQUS to determine the state of stress within the slipper. Material properties and boundary conditions for each model will be detailed following this introduction to the three cases, which are designated as:

1. Global Total Contact Model,
2. Global Quasi-steady Model, and
3. Global Bouncing Model.

For the first case, the global VascoMax 300 slipper sliding down the AISI 1080 steel rail for the entire 8.14 second test run was modeled. The pressure and velocity functions of time were applied to the slipper model. Thus, at any given instance in time, the horizontal velocity and applied pressure were known from the DADS data analysis. From the contact pressure and velocity, ABAQUS employs a look up table to determine the corresponding coefficient of friction. Data from the Montgomery coefficient of friction were input over the range of velocities and pressures experienced during the January 2008 test mission. The entire test run was broken up into different steps, or analysis increments, within ABAQUS. By specifying the step time, or analysis time, for each step, the slipper reached the target velocity at the end of each

analysis step. The state of stress could then be extracted from the global model and applied to the local submodel.

DADS data from the 80X-A1 test mission was incorporated into the initial global model development while waiting for HHSTT to deliver the January 2008 test mission DADS data. Using the initial pressure and velocity functions, it was determined that the slipper remained in contact with the rail at all times during the analysis. At this point in time, the global model had been fully developed to the extent that only the velocity and pressure profiles from the new DADS data needed to be substituted for the old DADS data profiles. With the January 2008 pressure and velocity profiles included, the global slipper analysis showed a change in dynamics such that the slipper unintentionally bounced away from the rail during the analysis. A comparison of the two DADS data sets showed that the 80X-A1 contact forces were larger in magnitude than those in the January 2008 test mission. This corresponded to higher pressure applied to the top of the slipper in the finite element model. In the new DADS data, the normal pressure was not sufficiently large to keep the slipper in contact with the rail.

As our focus was to determine wear rates at specific target velocities, it became apparent that at some target velocities the entire slipper was “airborne” and not in contact with the rail. The bouncing effect was important, as it modeled what actually occurs during a sled test run, but it was difficult to use to determine wear rates at the targeted velocity. To overcome this unintended consequence, the bottom of the slipper was constrained such that it could not translate in the vertical direction. Thus, in global total contact model analysis, the slipper remained in contact with the analytically rigid rail for the duration of the test mission.

In the global quasi-steady model, the analysis was limited to the study of slipper dynamics at a given targeted velocity. Instead of developing the stress history by starting the slipper from rest as in the previous case, the slipper was modeled as if it were initially at the target velocity, but with no initial state of stress. The quasi-

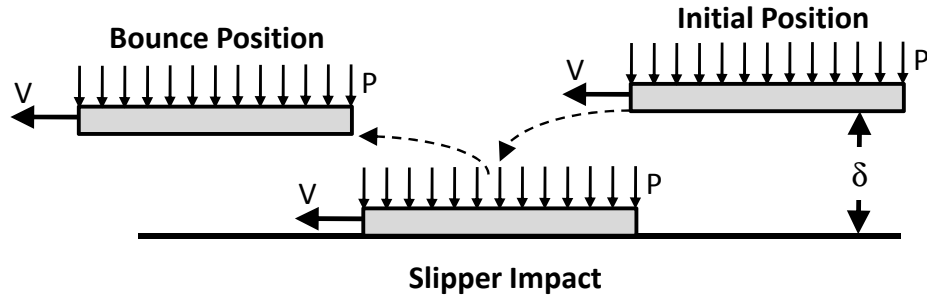


Figure 3.16: Global Slipper Bounce Model

steady model was analyzed for 0.001 seconds to determine the state of stress in the slipper and the corresponding contact pressure at the slipper/rail interface along the entire length of the global slipper.

In the global bouncing model, the slipper was initially displaced vertically above the rail by 3.175 mm, which corresponds to the nominal slipper gap as outlined in the HHSTT Design Manual [3]. As with the quasi-steady model, the slipper was initially at the target velocity but had no initial state of stress. With the applied pressure and velocity, the model was evaluated during a single bounce event to determine the state of stress within the slipper and contact pressure along the length of the slipper at the interface of the slipper/rail impact. The analysis step time during each test was 0.001–0.004 seconds and depended on the initial horizontal velocity. Figure 3.16 depicts the slipper moving from right to left down the track during this single bounce event. While not drawn to scale, δ is the nominal slipper gap distance of 3.175 mm. When in the initial position at this maximum vertical displacement, the slipper lips would be in contact with the bottom of the rail flange. The slipper stress and contact pressure along the bottom of the slipper are evaluated at slipper impact when $\delta = 0$ and contact has been established between the slipper and rail.

3.2.2 Model Geometry. From the beginning, the HHSTT test event would be modeled with a deformable slipper. On the other hand, two modeling options were possible for the rail, either deformable or rigid.

One of the first global finite element modeling studies incorporated both a deformable slipper and rail for the first few moments of a sled run. At the time, only the 80X-A1 DADS data was available. Based on the 80X-A1 horizontal velocity profile, the slipper velocity reached 75 m/s in 0.06 seconds after traveling 2.9 m. The deformable rail was 3.0 m in length and 50 mm in height. This analysis showed that it was possible to use a deformable rail with the slipper. With the intent of modeling the slipper during the entire 8.14 sec test run, it was quickly realized that using a deformable rail would be too computationally intensive in terms of computer solution time and data storage capacity.

During their study of the frictional interactions that occur during the HHSTT sliding event, Burton and Brockman [21; 22] also incorporated a deformable rail in their finite element model. Surface profile measurements, taken from VascoMax 300 slipper and AISI 1080 steel rail specimens, were used to generate deformable slipper and rail parts. Using the deformable rail at low velocity required a great deal of computational time and it was felt that more emphasis on the total run, at higher velocities and longer sliding distances, was more beneficial.

Given the computationally intensive nature, and difficulty of modeling the entire test sled run with a deformable rail, the decision was made to eliminate the deformable rail, and to use an analytically rigid rail instead. The global slipper model consists of a two-dimensional, plane strain, deformable slipper sliding horizontally on an analytically rigid rail. As depicted in Figure 3.17, the slipper length and thickness are 20.32 cm and 1.27 cm, respectively. In the global total contact model, the rail length is 6,000 m, slightly longer than the distance traveled by the Stage 3 slipper during the January 2008 test mission. In the global quasi-steady and bounce models, the rail length is only 1,000 mm. In all three global model cases, the rail and bottom of the slipper are modeled as perfectly flat surfaces. With the exception of the global bounce model, the slipper and rail are in contact at the beginning of each analysis.

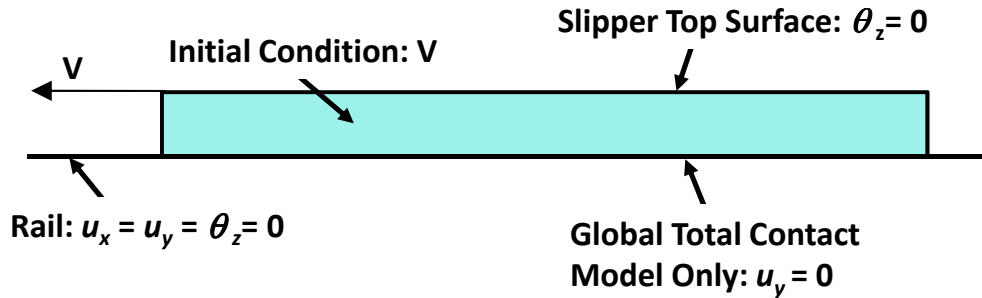


Figure 3.18: Global Model Boundary and Initial Conditions

3.2.3 Boundary and Initial Conditions. This subsection outlines the boundary and initial conditions that were implemented in each of the global model cases. Because the global total contact model runs through a longer time period, it will be addressed separately from the global quasi-steady and bounce models. In the two-dimensional plane strain model, each node has three degrees of freedom: two translation in the horizontal, u_x , and vertical, u_y , directions, respectively, and one rotation, θ_z , about the z-axis. In all three global model cases, all three degrees of freedom were constrained to zero so that the rigid rail could not translate or rotate. Thus, the slipper moved relative to a stationary rail. The initial and boundary conditions for the global models are shown in Figure 3.18.

The January 2008 Stage 3 velocity profile is applied as a horizontal velocity boundary condition to all nodes along the top surface of the slipper. ABAQUS makes use of an amplitude function, or lookup table as a function of time. When this velocity amplitude is used, the nodes at the top of the slipper follow exactly the DADS velocity profile. For example, at any given time in the global analysis, the top of the slipper surface's horizontal velocity will match the horizontal Stage 3 velocity profile shown in Figure 2.3. Because no vertical velocity is applied to the model, the velocity boundary condition is only in the horizontal direction.

For each node along the top surface of the slipper, $\theta_z = 0$ so that the upper surface of the slipper remains horizontal and parallel to the rail. Along the bottom of the slipper surface, each node is constrained so that the vertical displacement is zero by setting $u_y = 0$. This boundary condition, which keeps the slipper in contact with the rail, was only applied during the global total contact model analysis.

During the global total contact model analysis, the DADS pressure is applied to the entire length of the top of the slipper surface as a uniform pressure load. The pressure function is also implemented by way of the ABAQUS amplitude function so that the pressure at this surface is consistent with the DADS pressure depicted in Figure 3.13 for any given time in the analysis. Because no horizontal pressure load is applied to the slipper, the pressure load is only in the vertical direction.

At the slipper and rail interface, the coefficient of friction is determined by the contact pressure and the horizontal velocity. In ABAQUS, this interaction is also given by a lookup table that is based on contact pressures ranging from 0–100 GPa, and velocities ranging from 0–3,000 m/s, the maximum velocity for the 80X-A1 test mission. The maximum contact pressure of 100 GPa corresponded to contact pressures observed during subsequent slipper and asperity submodel collisions at 1,530 m/s. ABAQUS refers to this interaction as a pressure and slip rate dependent analysis. The slip rate, or horizontal displacement rate, is actually the slipper velocity. By determining the contact pressure and velocity at each node along the surface, the coefficient of friction can then be determined.

The horizontal velocity and pressure functions, as derived from the DADS statistical analysis, along with the Montgomery coefficient of friction make up the components of the global total contact model. The schematic in Figure 3.19 shows how each component contributes to the global model. The DADS velocity, which is highlighted in red, is applied as a horizontal velocity boundary condition to the top surface of the slipper. The DADS upper limit pressure, applied as a pressure load to the top surface of the slipper, is highlighted in black. The coefficient of friction, highlighted

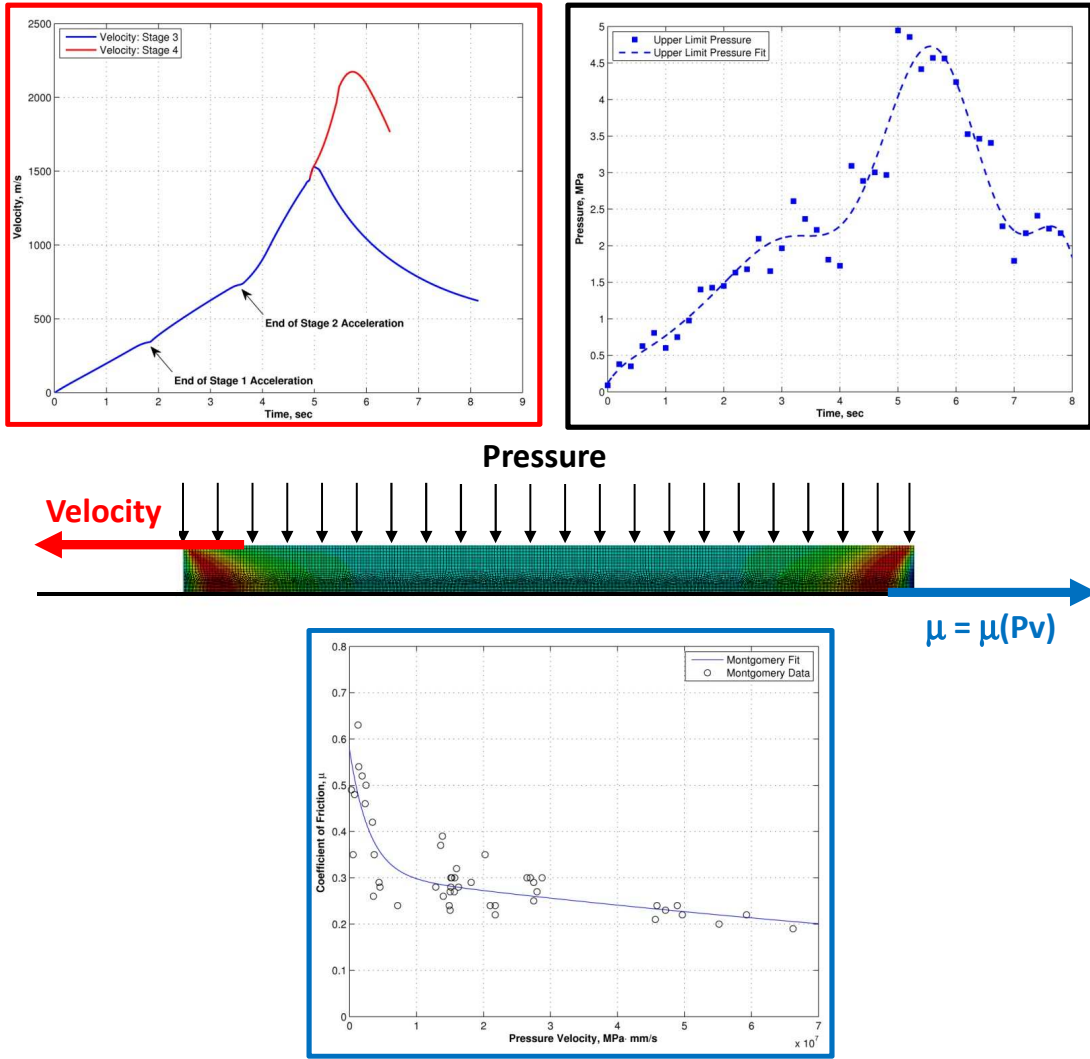


Figure 3.19: Global Model Components

in blue and determined from the pressure velocity of the Montgomery data, is applied at the slipper/rail interface. The three plots in Figure 3.19 serve as a reminder of the source of the specific boundary condition data.

The boundary and initial conditions for the global quasi-steady and bounce models differ slightly from those of the global total contact model. Instead of running the model for the full 8.14 second test run duration, and over the full range of velocities, the second and third global model cases focus on the slipper/rail interaction at one of the target velocities for a very short period of time. The horizontal velocity

was specified to be constant during the analysis and was applied horizontally to the same top of the slipper surface as was previously specified in the global total contact model.

During the analysis at each target velocity, all nodes in the slipper were set equal to each target velocity as the initial velocity condition. While developing his proof of concept wear model, Chmiel noted that without initial velocity conditions, particularly at high velocity, severe deformation of the slipper mesh would occur [25]. Without specifying this initial velocity, the default velocity is zero. At 500 m/s, for example, the slipper would initially have zero velocity, and then during the first time increment of the analysis the velocity would instantly jump to the constant 500 m/s target velocity causing severe distortion. At target velocities less than 100 m/s, this severe deformation would not occur because the slipper acceleration from zero to the low target velocity was relatively low. Nevertheless, for consistency, velocity initial conditions were applied in the global quasi-steady and bounce models for all twelve of the target velocities.

As with the constant horizontal velocity, a constant pressure was applied to the top of the slipper surface in both of the global quasi-steady and bounce models. The applied pressure is the pressure listed in Table 3.2 for the given target velocity.

3.2.4 Material Properties. In the global models, the slipper was modeled as an elastic material with the Johnson-Cook plasticity constitutive model. This was necessary because of the viscoplastic deformations observed on the surface of the slipper in Section 2.3. In the global models, no material properties were required to define the rail properties because the rail was modeled as an analytically rigid part. However, in the local submodel analysis, a deformable rail was used and AISI 1080 steel material properties were used. The material properties of density, ρ , modulus of elasticity, E , Poisson ratio, ν , melting temperature, T_{melt} , and elastic wave speed, c_0 , for the VascoMax 300 slipper and AISI 1080 rail are listed in Table 3.3.

The Johnson-Cook constitutive model [41] includes strain hardening, strain rate, and temperature dependencies that relate the dynamic yield stress, σ , as:

$$\sigma(\varepsilon^p, \dot{\varepsilon}^p, T) = [A + B(\varepsilon^p)^n] [1 + C \ln(\dot{\varepsilon}^{p*})] [1 - (T^*)^m] \quad (3.2)$$

where ε^p is the equivalent plastic strain, $\dot{\varepsilon}^{p*} = \dot{\varepsilon}^p / \dot{\varepsilon}_0$ is the dimensionless plastic strain rate for the reference strain rate, $\dot{\varepsilon}_0 = 1.0 \text{ s}^{-1}$, and T^* is the homologous temperature defined as:

$$T^* = \frac{T_{ref} - T_{room}}{T_{melt} - T_{room}} \quad (3.3)$$

where T_{ref} is the reference temperature, T_{room} is the room temperature, and T_{melt} is the melting temperature. The first term in Equation 3.2 is the static yield strength and a modification for strain. The second term introduces strain rate dependency and the final term includes temperature effects. The Johnson-Cook coefficients A , B , C , m and n in Equation (3.2) are determined from experimental testing. Table 3.3 lists the Johnson-Cook constitutive model coefficients from Cinnamon's Flyer Plate experiments that are detailed in References [29; 30]. These Johnson-Cook coefficients are used in the finite element analysis.

At low strain rates, heat generated by plastic deformation has time to dissipate. The plastic deformation can often be treated as isothermal. Conversely, during high strain rate deformation, heat generated does not have time to diffuse. The plastic deformation during these conditions is adiabatic, and the work during deformation is transformed into heat with temperature rise in the specimen [55]. The fraction of the plastic deformation that is converted into heat, β , is called the inelastic heat fraction. The rise in temperature due to plastic deformation work is accounted for in the temperature dependency term of the Johnson-Cook constitutive model. In the global total contact model, and subsequently in the local submodels, we use an inelastic heat fraction of 0.9.

Table 3.3: Slipper and Rail Material Properties [29; 30]

Property	VascoMax 300	AISI 1080 Steel
ρ (kg/m ³)	8,000	7,800
E (GPa)	180.7	202.8
ν	0.283	0.27
T_{melt} (K)	1,685	1,670
c_0 (km/s)	4.87	5.11
JC: A (GPa)	2.1	0.7
JC: B (GPa)	0.124	3.6
JC: C	0.03	0.17
JC: m	0.8	0.25
JC: n	0.3737	0.6

The global quasi-steady model was evaluated using ABAQUS/Standard. The Johnson-Cook plasticity model is not available in ABAQUS/Standard. Upon closer analysis of the global total contact model, it was determined that the maximum von Mises stress within the slipper remained below the yield stress indicating that a plasticity model was not required. By definition, the von Mises stress σ_e is given by the following

$$\sigma_e = \frac{1}{\sqrt{2}} [(\sigma_{xx} - \sigma_{yy})^2 + (\sigma_{yy} - \sigma_{zz})^2 + (\sigma_{zz} - \sigma_{xx})^2] \quad (3.4)$$

$$+ 6(\sigma_{xy}^2 + \sigma_{yz}^2 + \sigma_{xz}^2)]^{1/2} \quad (3.5)$$

This stress is known as an equivalent stress because it generates a scalar stress representation of the normal and shear components of the stress tensor. The von Mises stress is non-negative due to the squared terms in Equation 3.5. For the global quasi-steady model, only the VascoMax 300 density, modulus of elasticity, and Poisson's ratio as defined in Table 3.3 were used to define the material properties of the slipper.

3.2.5 Mesh and Element Definition. Plane strain elements were used in each of the three global analysis models. The quadrilateral elements, designated as CPE4R in ABAQUS, and shown in Figure 3.20(a), were 4-node bilinear plane strain reduced integration elements. The triangular elements, designated in ABAQUS as

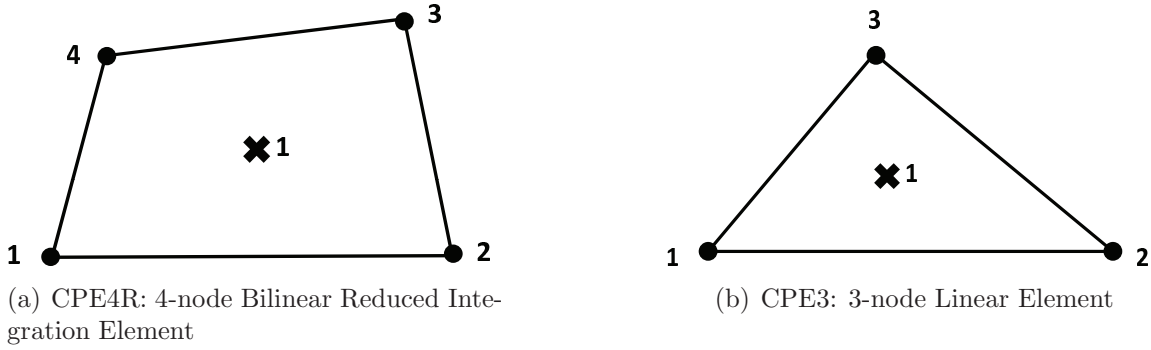


Figure 3.20: ABAQUS Plane Strain Elements

Table 3.4: Global Model Uniform Mesh Analysis

Mesh Name	Edge Length (mm)	# of CPE4R Elements	# of Nodes
1x16 Mesh	12.700	16	34
2x32 Mesh	6.350	64	99
4x64 Mesh	3.175	256	325
8x128 Mesh	1.5875	1,024	1,161
16x256 Mesh	0.79375	4,096	4,369

CPE3 elements and shown in Figure 3.20(b), were 3-node linear plane strain triangle elements.

The global quasi-steady and bounce models both incorporated a uniformly spaced mesh with a 1:16 ratio that corresponded to the slipper height to length ratio. Several uniformly spaced meshes, outlined in Table 3.4, of uniformly spaced CPE4R elements were used during the analysis of these global models. By carefully selecting the seed mesh size, or average element length, each element was essentially a square in the uniformly spaced 1:16 mesh. Ultimately, the 16x256 mesh was used during the global quasi-steady and bounce model analyses.

The mesh for the global total contact model was not uniform. In the vicinity of the slipper/rail interaction, each CPE4R element had sides of length 0.1985 mm, which is 25% of the size of the 16x256 mesh elements. The top half of the slipper used the same uniform 16x256 mesh as the global quasi-steady and bounce models. The final mesh for this global slipper analysis was made up of 8,026 CPE4R and 85 CPE3 elements comprising 8,477 nodes.

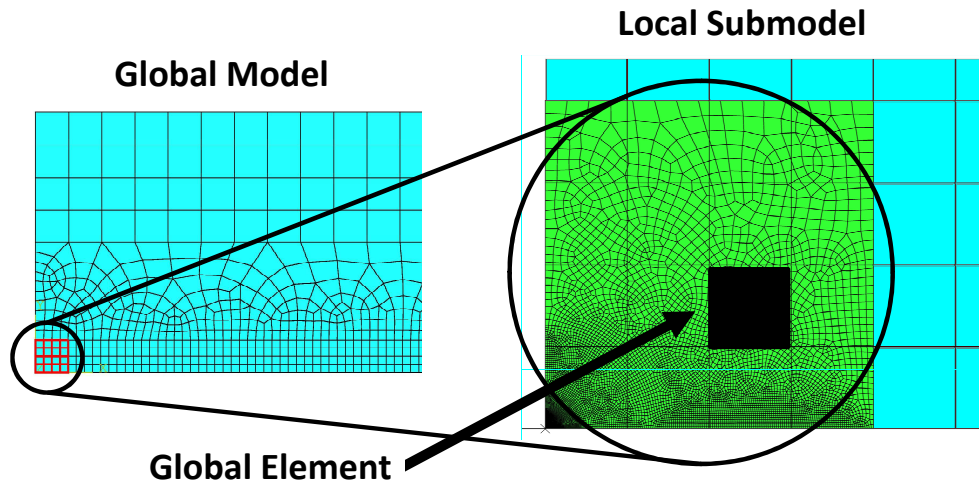


Figure 3.21: Global and Local Submodel Relationship

The fine mesh at the bottom of this model was selected so that a 4x4 element subset, consisting of 25 global nodes, from the global model would have the same dimension as the local submodel. During the subsequent submodel analysis, the submodel region would have an even finer mesh. The front portion of the global model is depicted on the left side of Figure 3.21. On the right side, the local submodel is shown overlapping the global mesh. The single highlighted global element indicates the relative size of the global and local submodel elements. The local submodel will be discussed in more detail in the next section.

3.3 Local Submodel Finite Element Analysis

Based on the metallurgical analysis in Chapter II, there is evidence of plastic deformation of the slipper surface on the micron scale. In order to determine the wear rates and ultimately the total wear during the January 2008 test mission, the finite element model needed to focus on the micron-scale collision between a finite dimension slipper and a rail asperity. The local slipper submodel, which also makes use of a two-dimensional plane strain analysis, is generated from the global model and features the micro level of contact at the interface between the slipper and the rail.

3.3.1 Model Geometry. As the focus of determining wear rate has now changed from the global to this smaller scale in the local submodel, the test track must now be modeled as a deformable rail. The plastic deformation and interaction between the rail and slipper can only be evaluated when both parts are deformable. The rigid rail from the global models is replaced by a deformable rail that includes a single hemispherical asperity with radii of 6, 4, and 2 μm centered at the surface of the rail. The 6 μm asperity is used during the analysis for all twelve target velocities. Surface profilometry measurements of the AISI 1080 steel rail indicate that the average surface height was approximately 6 μm [22; 76]. The 4 and 2 μm asperity models are only used for the analysis of five target velocities to determine the wear rate in terms of damage volume. Use of the smaller asperity radii will be discussed subsequently.

Two different slipper submodel configurations were evaluated during the course of the finite element analysis. The first local submodel was based on the size of the global elements in the global total contact model as was discussed previously. A schematic of the original slipper submodel is shown in Figure 3.22. The slipper submodel is a square with 0.79375 mm sides, and the rail section measured 1.65 mm in length and 0.4 mm in height. The subdivisions in the slipper region represent the 16 elements from the global total contact model. The slipper submodel slides from right to left in this model schematic.

After modeling the collision between the original slipper submodel and the 6 μm asperity at all target velocities, it was determined that the results of the asperity collision were more localized in the vicinity of the collision. Due to the short duration of the analysis, the majority of the original slipper submodel did not feel the effects of the asperity collision. Far away from the asperity, in the upper right corner of the slipper submodel shown in the schematic, the state of stress remained unchanged. The decision to forgo the stress mapping from the global to local submodel had already been made when these analyses were accomplished.

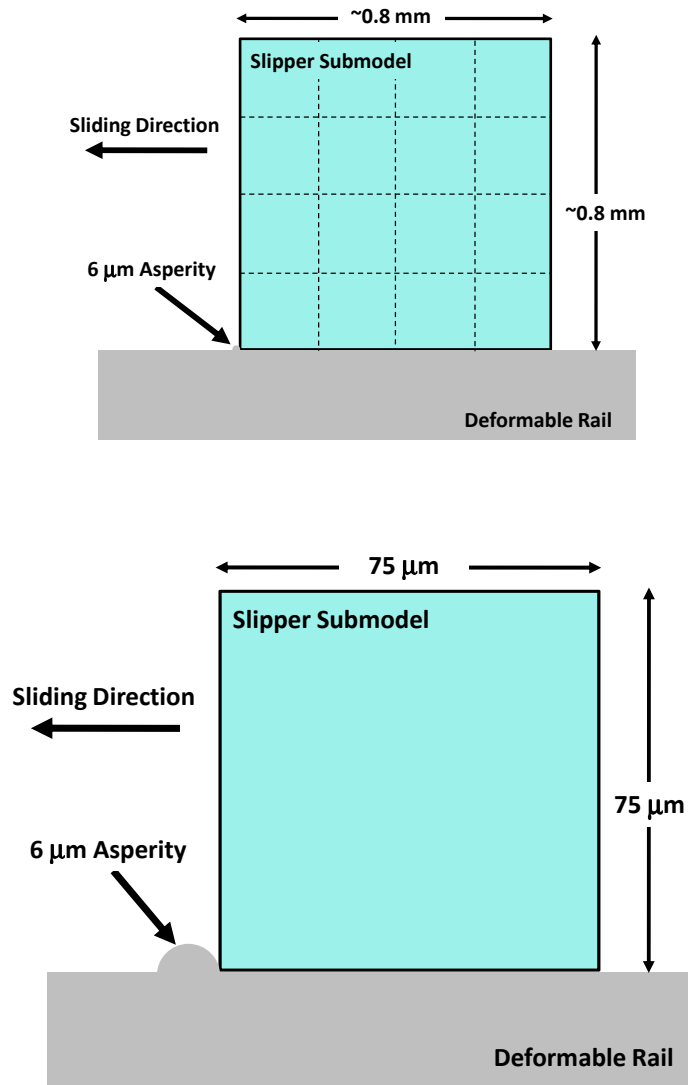


Figure 3.23: Final Slipper Submodel Schematic

The size of the slipper submodel was made smaller in an effort to more closely analyze the results of the slipper/asperity collision. This revised local submodel analysis is referred to as the final submodel. Each side of the square submodel was reduced to a length of $75\ \mu\text{m}$ as shown in Figure 3.23. The location and size of the asperity, as well as the sliding direction, remained the same in this final local submodel configuration. A $2\ \mu\text{m}$ radius fillet was placed at the leading edge of the slipper near the rail contact edge. While not drawn to scale in the final slipper submodel schematic, the rail was modeled as a rectangle with $150\ \mu\text{m}$ length and $75\ \mu\text{m}$ height.

Table 3.5: Local Submodel Step Times in Seconds

V (m/s)	R = 6 μm	R = 4 μm	R = 2 μm
10	6.6×10^{-7}	4.4×10^{-7}	2.2×10^{-7}
20	3.3×10^{-7}	2.2×10^{-7}	1.1×10^{-7}
40	1.7×10^{-7}	1.1×10^{-7}	5.5×10^{-8}
100	6.8×10^{-8}	4.4×10^{-8}	2.2×10^{-8}
200	3.3×10^{-8}	2.2×10^{-8}	1.1×10^{-8}
300	2.2×10^{-8}	1.5×10^{-8}	7.3×10^{-9}
500	1.3×10^{-8}	8.8×10^{-9}	4.4×10^{-9}
622	1.1×10^{-8}	7.1×10^{-9}	3.5×10^{-9}
750	8.8×10^{-9}	5.9×10^{-9}	2.9×10^{-9}
1,000	6.6×10^{-9}	4.4×10^{-9}	2.2×10^{-9}
1,250	5.3×10^{-9}	3.5×10^{-9}	1.8×10^{-9}
1,530	4.3×10^{-9}	2.9×10^{-9}	1.4×10^{-9}

The slipper and asperity collision in the local submodel was evaluated over a very short time interval. This analysis time, or step time in ABAQUS terminology, corresponded to the time required for the slipper to travel 110% of the asperity radius length at constant target velocity. Table 3.5 lists the total step times, in seconds, for each target velocity and the asperity radii, R , evaluated in the present study.

3.3.2 Boundary and Initial Conditions. Several of the global model boundary and initial conditions were also used in the local submodel analysis. Figure depicts the local submodel boundary and initial conditions.

First, the bottom surface of the deformable rail was constrained in the same manner as the global rigid rail to prevent translation and rotation during the analysis. As with the global models, the slipper moved relative to the stationary rail. Secondly, the target velocity was applied to each node in the slipper submodel as an initial velocity condition to prevent excessive mesh distortion at high velocities. As with the global models, this initial velocity condition was used for all of the target velocity analyses.

The top surface of the slipper submodel was constrained in the vertical translation and rotational degrees of freedom by setting $u_y = 0$ and $\theta_z = 0$, respectively, to

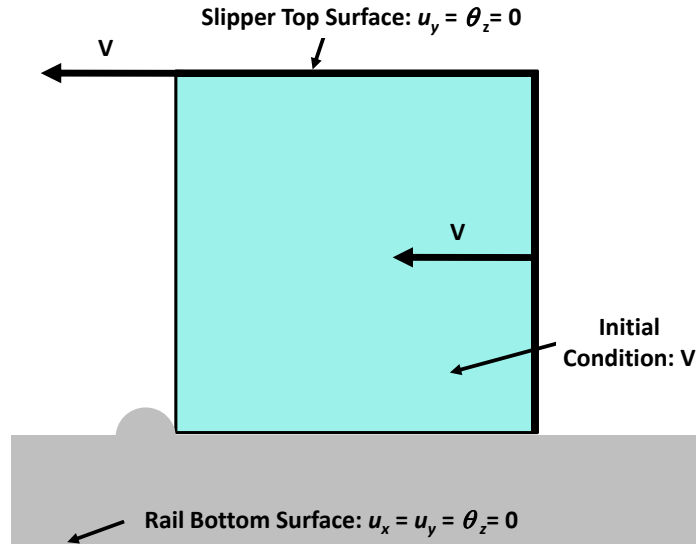


Figure 3.24: Local Submodel Boundary and Initial Conditions

prevent the slipper from riding up over the asperity during the collision event. Also, the top surface of the slipper remained parallel to the rail by preventing rotation.

Initially, the velocity boundary condition, that would drive the slipper during the course of the asperity collision, was applied to the entire slipper domain. Thus, the velocity for every node was specified by this constant target velocity. Applying this constant “bulk velocity” to each node limits the change in displacement between all nodes. The location of application of the velocity boundary condition was changed from all nodes in the slipper to only the nodes along the top and aft surfaces of the slipper submodel. Thus, the nodes within the slipper domain were able to respond appropriately to the applied boundary conditions.

3.3.3 Material Properties. For the local submodels, an equation of state (EOS) was used to model the hydrodynamic or spherical response of the slipper/asperity collision. The deviatoric response was modeled by the Johnson-Cook constitutive model that was incorporated into the global models.

The equation of state relates the thermodynamic properties (pressure and internal energy) of a material to its density and temperature. Also, the equation of state gives all of the possible equilibrium conditions for a given material [79]. In con-

tinuum mechanics, the three conservation laws for mass, momentum, and energy are expressed in terms of the continuous field variables: density, ρ , pressure, P , velocity, u , and energy, E , where each field variable is a function of time and space. Because the three conservation equations have more unknown variables than equations to solve, they are considered incomplete.

The EOS is required to complete the set. Either the pressure and temperature are given as functions of density and internal energy, $P = P(\rho, E)$ and $T = T(\rho, E)$, or the pressure and internal energy are given as functions of density and temperature, $P = P(\rho, T)$ and $E = E(\rho, T)$ [55].

Much of the following discussion is taken from the ABAQUS Analysis User's Manual [33]. The Mie-Grüneisen form of the equation of state is linear in energy. A common form is given by

$$p - p_H = \Gamma \rho (E_m - E_H) \quad (3.6)$$

where p_H is the Hugoniot pressure and E_H is the Hugoniot specific energy per unit mass. Both are functions of density only. The Grüneisen ratio, Γ , is defined as

$$\Gamma = \Gamma_0 \frac{\rho_0}{\rho} \quad (3.7)$$

where Γ_0 is a material property and ρ_0 is a reference density. The Hugoniot specific energy, E_H , is related to the Hugoniot pressure by

$$E_H = \frac{p_H \eta}{2\rho_0} \quad (3.8)$$

and the nominal compressive strain, η , is defined as $\eta = 1 - \rho_0/\rho$. Substitution of the Grüneisen ratio from Equation 3.7, and E_H from Equation 3.8 into Equation 3.6, gives the following simplified relationship for the pressure, p ,

$$p = p_H \left(1 - \frac{\Gamma_0 \eta}{2} \right) + \Gamma_0 \rho_0 E_m \quad (3.9)$$

Table 3.6: Slipper and Rail EOS Material Properties

Track Material	CTH Material	c_0 (km/s)	s	Γ_0
AISI 1080 Steel Rail	Iron-Alpha	4.605	1.456	1.65
VascoMax 300 Slipper	VascoMax 250	3.980	1.580	1.60

The equation of state and the energy equation are coupled equations for pressure, p , and internal energy, E_m . A common fit to the Hugoniot data is given by

$$p_H = \frac{\rho_0 c_0^2 \eta}{(1 - s\eta)^2} \quad (3.10)$$

where c_0 is the reference speed of sound, and s is the linear slope parameter than describe the relationship between the linear shock velocity, U_s , and the particle velocity, U_p by the following

$$U_s = c_0 + sU_p \quad (3.11)$$

With this relationship, the linear Hugoniot form of Equation 3.9 is given by

$$p = \frac{\rho_0 c_0^2 \eta}{(1 - s\eta)^2} \left(1 - \frac{\Gamma_0 \eta}{2} \right) + \Gamma_0 \rho_0 E_m \quad (3.12)$$

To implement this linear $U_s - U_p$ model in ABAQUS, the reference Grüneisen ratio, Γ_0 , reference speed of sound, c_0 , and the linear slope parameter, s , must be known. One of the research tools available at AFIT is a hydrocode, developed by Sandia National Laboratory, known as CTH. Laird, Szmerekovsky, Cinnamon, and Cameron all used CTH for their HHSTT hypervelocity gouging and wear research at AFIT [24; 26; 48; 73]. The CTH database provides these necessary material properties for the slipper and rail materials as shown in Table 3.6. CTH values for iron-alpha phase were used for the AISI 1080 steel rail, and VascoMax 250 values were used for the slipper material.

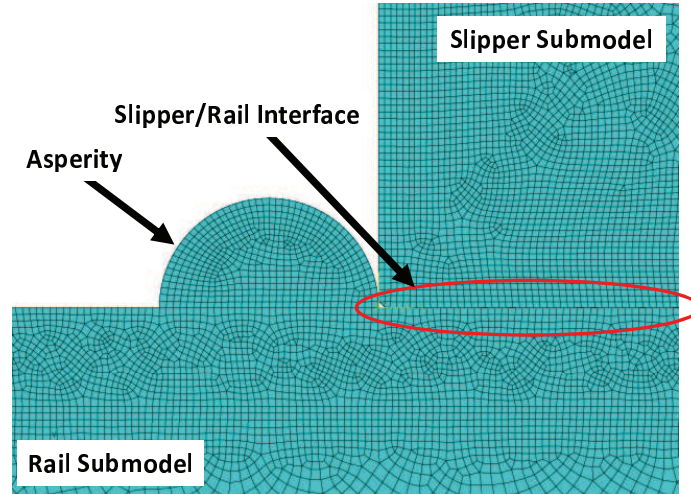


Figure 3.25: Representative Slipper and Rail Interface Elements

3.3.4 Mesh Convergence Study. Several different mesh configurations were evaluated for the local submodel slipper and rail asperity collision. In all of the meshes, elements on either side of the slipper/rail interface were of similar size as shown in Figure 3.25. The size of the elements increased when moving further away vertically from this interface.

The original mesh, designated *SM Mesh 1* or submodel mesh #1, had an average element length of $1.25 \mu\text{m}$. The average element length in the second mesh was $0.625 \mu\text{m}$. Typically, during a mesh convergence study, the mesh size is reduced with each successive mesh to be evaluated. In this evaluation, the evaluated mesh names are out of order relative to size and the average element length for the next mesh, *SM Mesh 3*, was double that of *SM Mesh 1*. Finally, the average element length in the fourth mesh, *SM Mesh 4*, was $0.3125 \mu\text{m}$. The size comparison between square elements in these four submodel meshes is depicted in Figure 3.26. Assuming square elements are used, four *SM Mesh 1* elements, 16 *SM Mesh 2* elements, and 64 *SM Mesh 4* elements would equal the area of 1 *SM Mesh 3* element. The final mesh configuration used in the submodel analysis, depicted as the shaded mesh in this figure, was *SM Mesh 2*.

As with the global slipper models, only CPE4R and CPE3 elements were evaluated in each of these submodel meshes. In fact, the majority of the elements in both

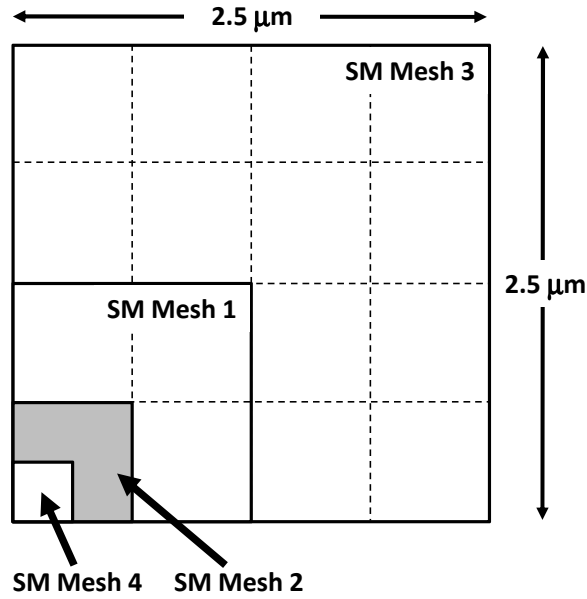


Figure 3.26: Local Submodel Mesh Size Comparison

Table 3.7: Local Submodel Mesh Comparison

Mesh Name	Length (μm)	Slipper Submodel			Rail Submodel		
		# CPE4R	# CPE3	# Nodes	# CPE4R	# CPE3	# Nodes
SM Mesh 1	1.25	4,217	101	4,390	7,248	1	7,432
SM Mesh 2	0.625	16,850	433	17,310	28,981	1	29,348
SM Mesh 3	2.50	1,068	18	1,139	1,811	3	1,905
SM Mesh 4	0.3125	42,924	1,182	43,860	83,674	1,250	84,952

the slipper and rail were quadrilateral CPE4R elements. Table 3.7 shows a comparison of the average element length, number of elements, and number of nodes for the slipper and rail submodels for each of the four meshes evaluated. Obviously, as the mesh size is decreased, the number of elements increases to mesh the same region.

The four submodel meshes were evaluated during $6 \mu\text{m}$ asperity collisions at different velocities. Several techniques were used to determine local submodel mesh convergence. For a given velocity, each mesh needed to be compared at the same moment in time. First, the Mises stress was compared by viewing the slipper/asperity collision results side-by-side. In ABAQUS, the field output variable, Mises stress in this case, can be plotted on either the deformed or undeformed part geometry. As

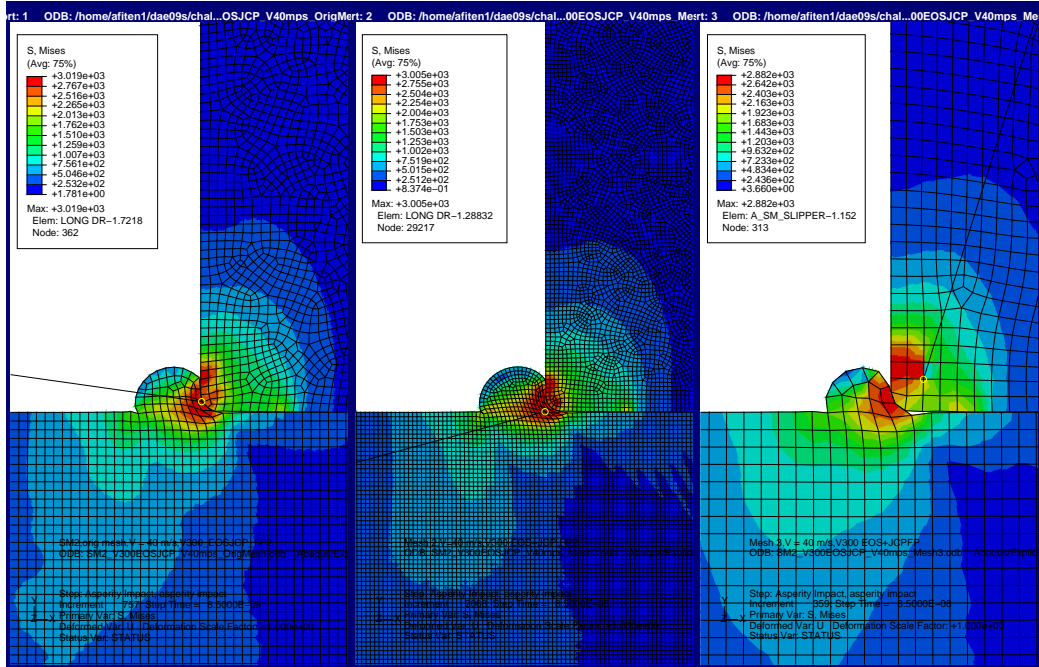


Figure 3.27: Mesh Comparison, SM Mesh 1, 2, and 3, $V = 40$ m/s

an example, the Mises stress for *SM Mesh 1, 2, and 3*, from left to right, at 40 m/s is shown in Figure 3.27. In this figure, both the slipper and rail are shown in their deformed geometry configuration. The stress contours and differences in mesh size can easily be compared in the side-by-side comparisons. In Figure 3.27, the maximum Mises stress in *SM Mesh 1* and *2* are 3,019 MPa and 3,005 MPa, respectively.

The Mises stress for the same three meshes at 500 m/s, now on the undeformed geometry, is shown in Figure 3.28. Again, the rail has been removed from this analysis to allow direct comparison with the slipper region only. Maximum Mises stress in each mesh is, from left to right, 2,899, 3,007, and 3,079 MPa, respectively, and occur nearly at the same location. The stress contours are also very similar for *SM Mesh 1 and 2*.

In the second mesh convergence technique, a 45° path, or line segment, with respect to the horizon was created in the ABAQUS post-processing data analysis. The Mises stress along this path was compared for several different meshes. In Figure 3.29, this path is shown as the red line. In order to compare the stress in only the slipper, the rail part was removed. The Mises stress along this path for *SM Mesh 1*,

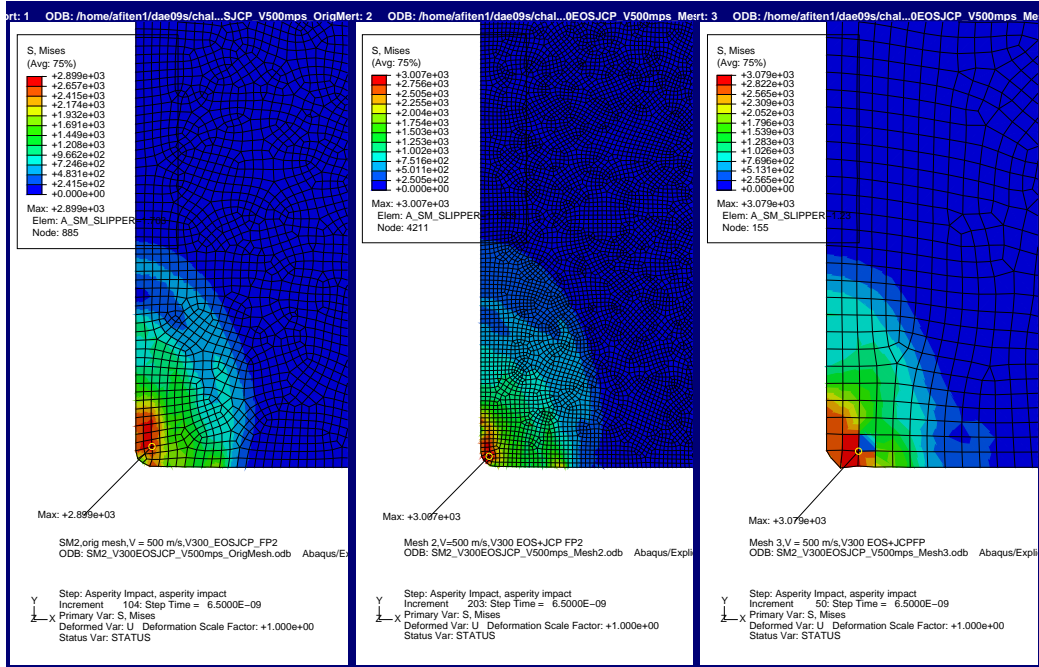


Figure 3.28: Mesh Comparison, SM Mesh 1, 2, and 3, $V = 500$ m/s

2, and 4 at 100 m/s is shown in Figure 3.30. The abscissa is the normalized distance along this 45° path. SM Mesh 2 and 4 both reach a maximum Mises stress near 2,500 MPa, and the curves follow the same trend. Due to the coarseness of the *SM Mesh 3*, it is not depicted in this figure.

Another comparison between the Mises stress along the 45° path for *SM Mesh 2* and *SM Mesh 4* at 1,530 m/s is depicted in Figure 3.31. The maximum Mises stress is approximately 3,230 MPa for both submodel mesh configurations, and the curves follow the same trend.

Finally, the last technique was to identify several nodes in each submodel mesh that were located in close proximity to the asperity collision. Coincident nodes were selected from both *SM Mesh 2* and *SM Mesh 4* geometries as shown on the left and right sides, respectively, in Figure 3.32. For example, the node labeled “1” on the left corresponds to the same location as the node labeled “5” on the right. These nodes are in very close proximity, but may not be at the exact same coordinate locations. Also, this node numbering scheme doesn’t reflect the actual node numbers assigned during

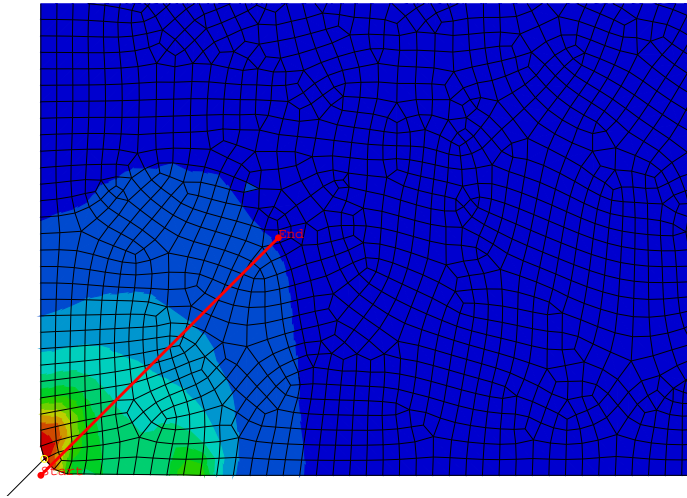


Figure 3.29: SM Mesh Convergence: 45° Path Definition

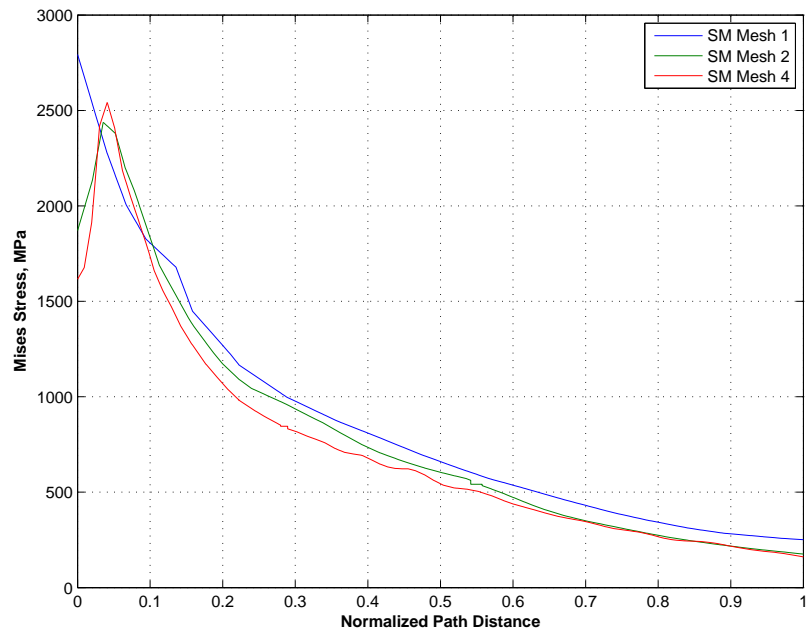


Figure 3.30: Mises Stress Along 45° Path, $V = 100$ m/s

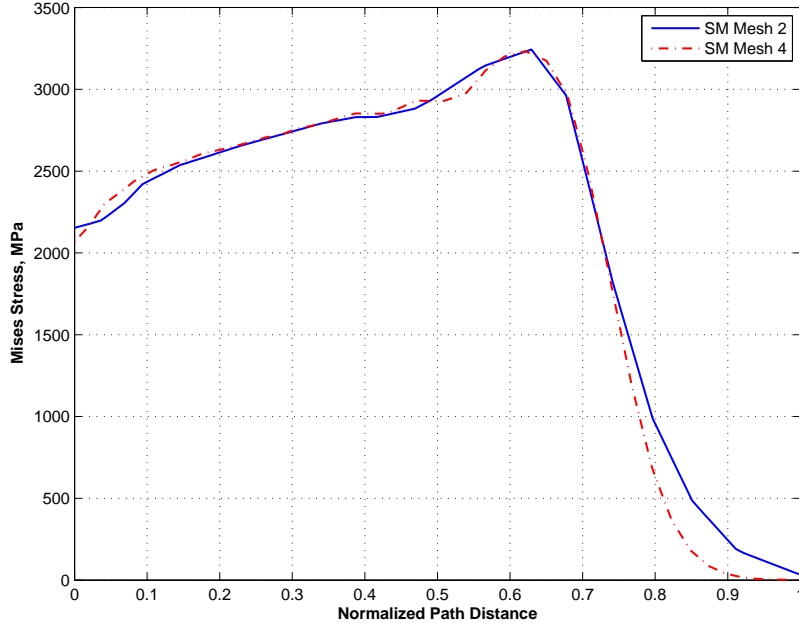


Figure 3.31: Mises Stress Along 45° Path, $V = 1,530$ m/s

the ABAQUS analysis. They have been renumbered to enable a simple comparison between the two local submodel meshes.

The Mises stress at each node was recorded as a function of time during the slipper/asperity collision event. For the 8 nodes depicted in Figure 3.32, the comparison between the Mises stress during the slipper/asperity collision at 1,530 m/s is depicted in Figure 3.33. The four subplots correspond to the four pairs of coincident nodes (i.e. Node 1 and Node 5, Node 2 and Node 6, etc.).

For the most part, the *SM Mesh 2* and *SM Mesh 4* Mises stresses match each other in maximum magnitude and trend. Variations in the Mises stress occurred because the nodes are not exactly in the same place on the slipper. The Node 4 and Node 8 comparison shows that the time to reach the maximum Mises stress is longer than that of the other nodal comparisons which indicates that these nodes are further away from the point of initial slipper/asperity impact. The time to reach the maximum stress values for Nodes 1/5, Nodes 2/6, Nodes 3/7, and Nodes 4/8, is 8.60×10^{-10} , 8.60×10^{-10} , 6.45×10^{-10} , and 1.38×10^{-9} sec, respectively.

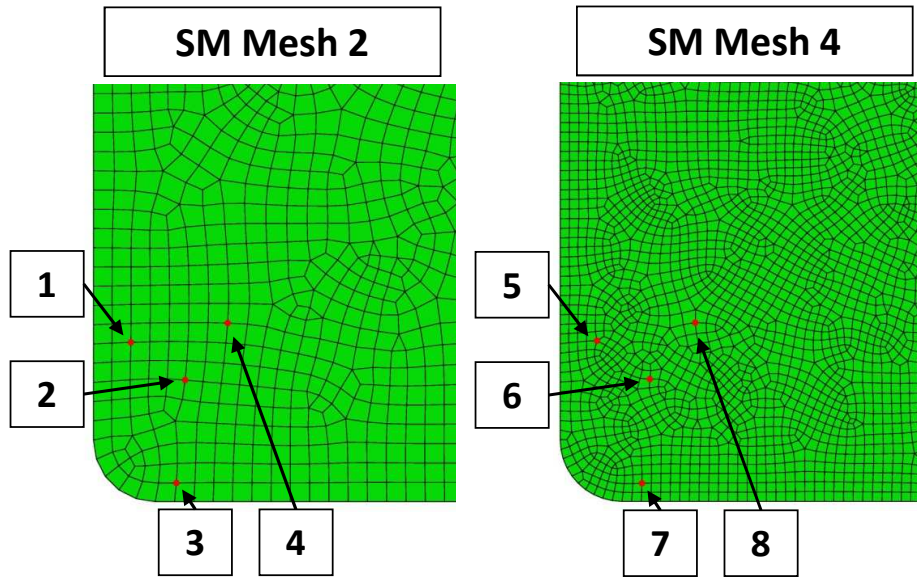


Figure 3.32: Nodal Location Comparison, SM Mesh 2 vs. SM Mesh 4

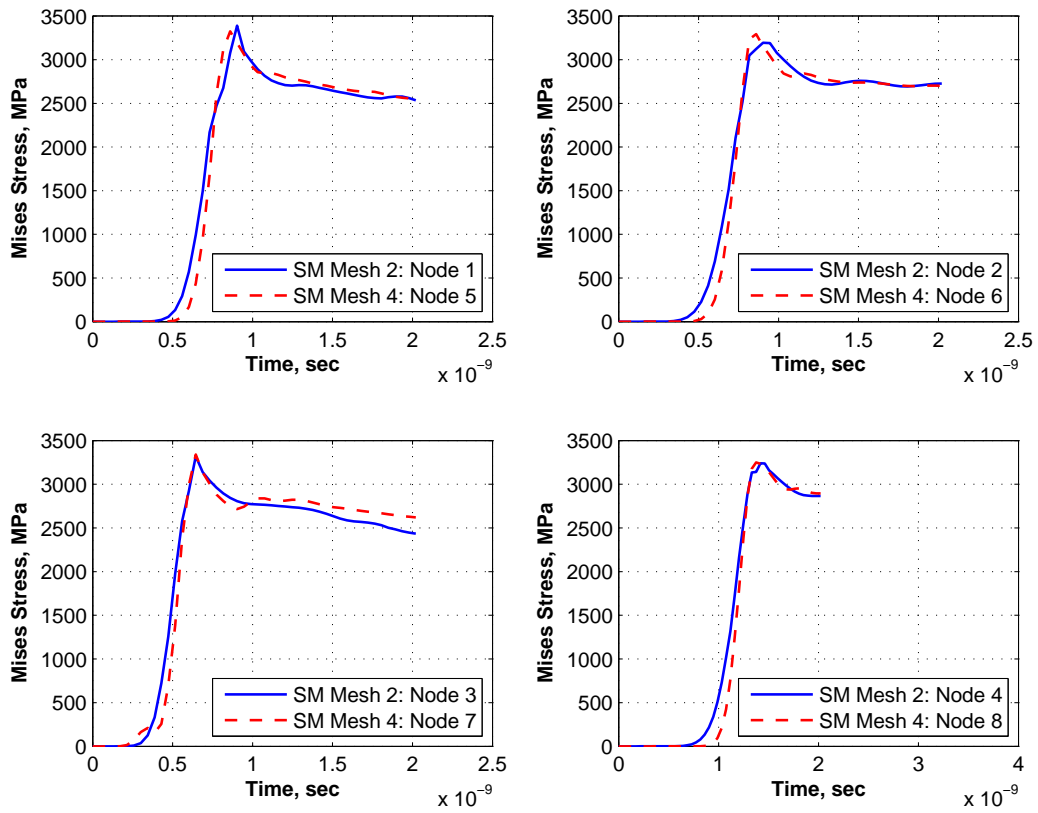


Figure 3.33: Mises Stress Comparison at Coincident Nodes, $V = 1,530$ m/s

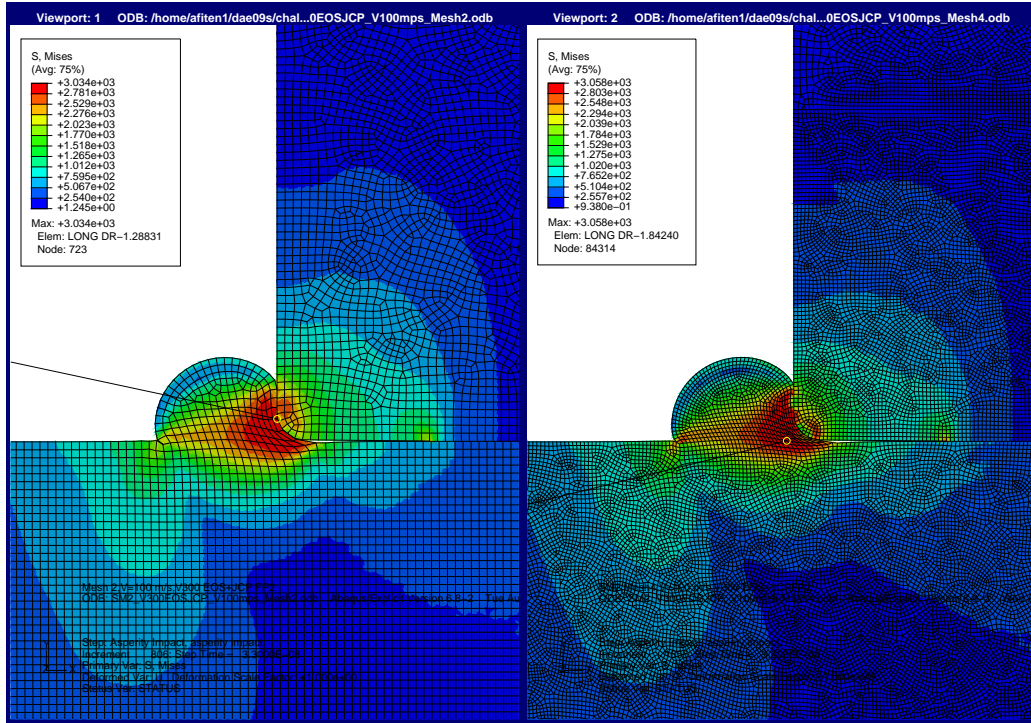


Figure 3.34: Mesh Comparison, SM Mesh 2 vs. Mesh 4, $V = 100$ m/s

After ruling out the *SM Mesh 1 and 3* meshes, the mesh convergence study was narrowed down to *SM Mesh 2 and 4*. An analysis of the *SM Mesh 2 and 4* results indicated that *SM Mesh 2* gave very similar results as *SM Mesh 4*. For example, the Mises stress in both the slipper and rail at 100 m/s is depicted in Figure 3.34. In this figure, *SM Mesh 2* and *SM Mesh 4* are shown on the left side and right side, respectively. The maximum Mises stress was 3,034 MPa and 3,058 MPa, respectively. This is a difference of less than 1%. Stress contours are nearly identical in both the slipper and rail. Similarly, Figure 3.35 depicts the Mises stress for both the slipper and rail at 1,000 m/s in the deformed geometry. Figure 3.36 shows the Mises stress for only the slipper at 1,530 m/s for both meshes.

A wear rate function is evaluated in a subsequent section and it also showed that *SM Mesh 2* is an optimum mesh arrangement compared to *SM Mesh 4*. Thus, *SM Mesh 2* was selected as the final mesh for the local submodel analysis and was used for the remainder of this dissertation research.

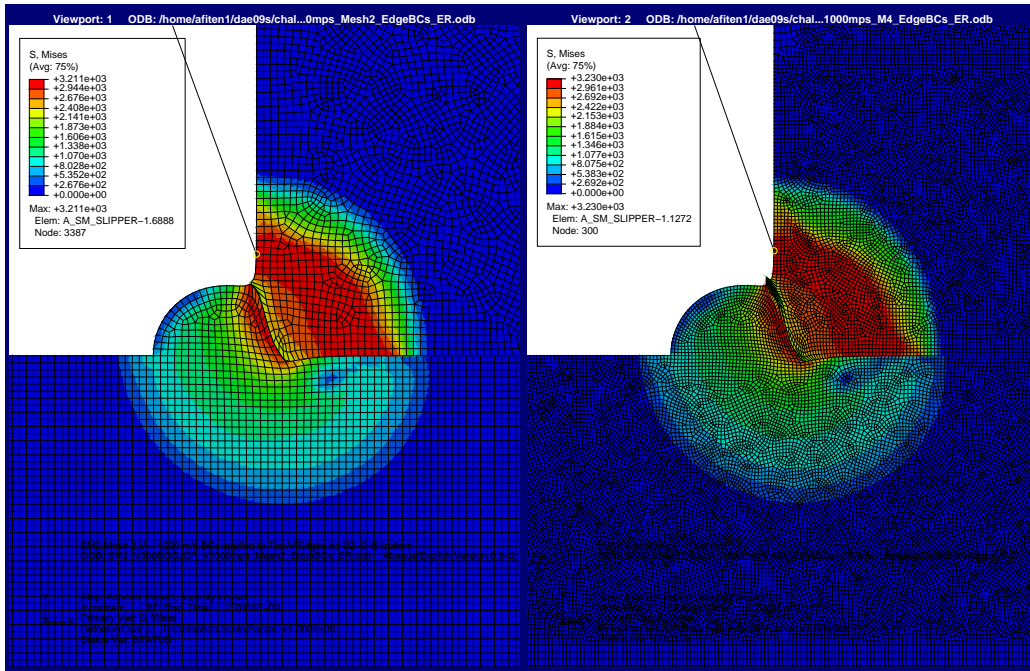


Figure 3.35: Mesh Comparison, SM Mesh 2 vs. Mesh 4, $V = 1,000$ m/s

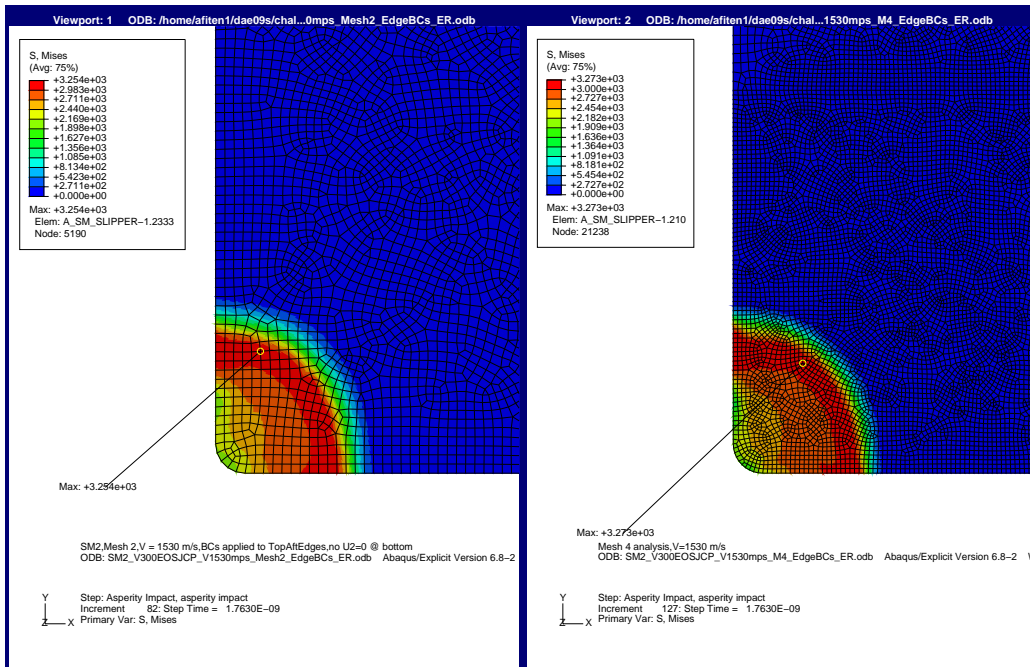


Figure 3.36: Mesh Comparison, SM Mesh 2 vs. Mesh 4, $V = 1,530$ m/s

3.4 Johnson-Cook Stress Strain Curve for VascoMax 300

Wear rate is defined as the volume of worn material per unit distance slid during the sliding wear event. In order to determine the volume of damage, a damage criterion must first be established for the finite element analysis. The maximum Mises stress criteria will be used for this analysis.

Two different techniques were used to determine the maximum Mises stress of VascoMax 300 for a given strain rate. Once the maximum Mises stress was identified, it was used in the wear rate analysis to determine the damage area.

The first method was to calculate the Mises flow stress, using the Johnson-Cook coefficients, for a set of given strain rates, over a range of equivalent plastic strain values.

The temperature rise, ΔT , which softens the material during plastic deformation is related to the stress, σ , and plastic strain, ε^p , by

$$\Delta T = \frac{\beta}{\rho c_p} \int_0^{\varepsilon_f^p} \sigma \, d\varepsilon \quad (3.13)$$

where β is the inelastic heat fraction, ρ is the material density, c_p is the ratio of specific heats, and ε_f^p is the final plastic strain.

By substituting the Johnson-Cook constitutive model, Equation 3.2, into Equation 3.13 for stress, σ , and assuming the strain rate, $\dot{\varepsilon}$, is constant yields

$$\int_{T_0^*}^{T_f^*} \frac{dT^*}{1 - T^{*m}} = \frac{\beta(1 + C \ln(\dot{\varepsilon}^{p*}))}{\rho c_p (T_{melt} - T_{ref})} \int_0^{\varepsilon_f^p} (A + B(\varepsilon^p)^n) \, d\varepsilon^p \quad (3.14)$$

where T_0^* and T_f^* are the initial and final homologous temperatures, respectively. The integral on the left hand side needs to be evaluated numerically if $m \neq 1$. By assuming that $m \cong 1$, Meyer's [55] provides a simplified solution for the homologous temperature, T^* , as

$$T^* = 1 - \exp \left[- \frac{\beta(1 + C \ln(\dot{\varepsilon}^{p*}))}{\rho c_p (T_{melt} - T_{ref})} \left(A \varepsilon^p + \frac{B(\varepsilon^p)^{n+1}}{n+1} \right) \right] \quad (3.15)$$

which is now in terms of the material properties, plastic strain and strain rate. Although $m = 0.8$ for VascoMax 300, Meyer's simplification is used to solve for the Mises stress. The flow stress in the Johnson-Cook equation can now be solved for by substituting Equation 3.15 into Equation 3.2.

The stress-strain curves for VascoMax 300 were determined at several different strain rates by using the flyer plate Johnson-Cook coefficients and assuming that $\beta = 0.9$. The temperature rise, ΔT , from the reference temperature of $T_{ref} = 298$ K, due to plastic deformation at a particular strain rate is given by

$$\Delta T = T - T_{ref} = T^* (T_{melt} - T_{ref}) \quad (3.16)$$

The temperature rise associated with the plastic deformation at each strain rate is shown in Figure 3.37. For a given equivalent plastic strain, higher strain rates yield larger rises in temperature. For example, at $\varepsilon^p = 1.0$, the temperature rise for $\dot{\varepsilon}^p = 100$ /s, is 290 K. At the same equivalent plastic strain, the temperature rise for $\dot{\varepsilon}^p = 1 \times 10^9$ /s is 395 K. The stress-strain curves for these strain rates based on Meyer's simplification are depicted in Figure 3.38. The decrease in flow stress is due to the material softening brought about by plastic deformation temperature rise.

The maximum Mises stress for each strain rate is given in Table 3.8. Slight differences between the Meyer's and ABAQUS technique may be attributed to the $m \cong 1$ assumption. However, both techniques yield similar maximum Mises stress values at higher strain rates. It will be shown later how the higher strain rates, that are observed during the slipper/rail asperity collision, are used to determine damage area and eventually the wear rate. The maximum Mises stress values from the ABAQUS single cube element analysis are used later in the strain rate analysis, and also when determining the wear rate that occurred during each slipper/asperity collision.

The second technique for determining the maximum Mises stress was to perform a tensile analysis in ABAQUS. Originally, an axisymmetric tensile necking specimen

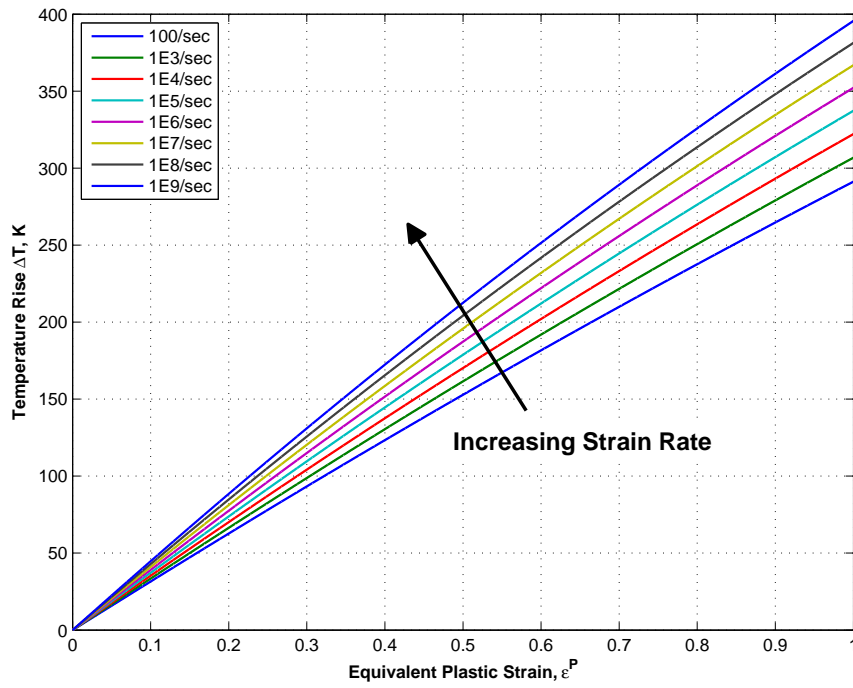


Figure 3.37: VascoMax 300 Temperature Rise Due to Plastic Deformation

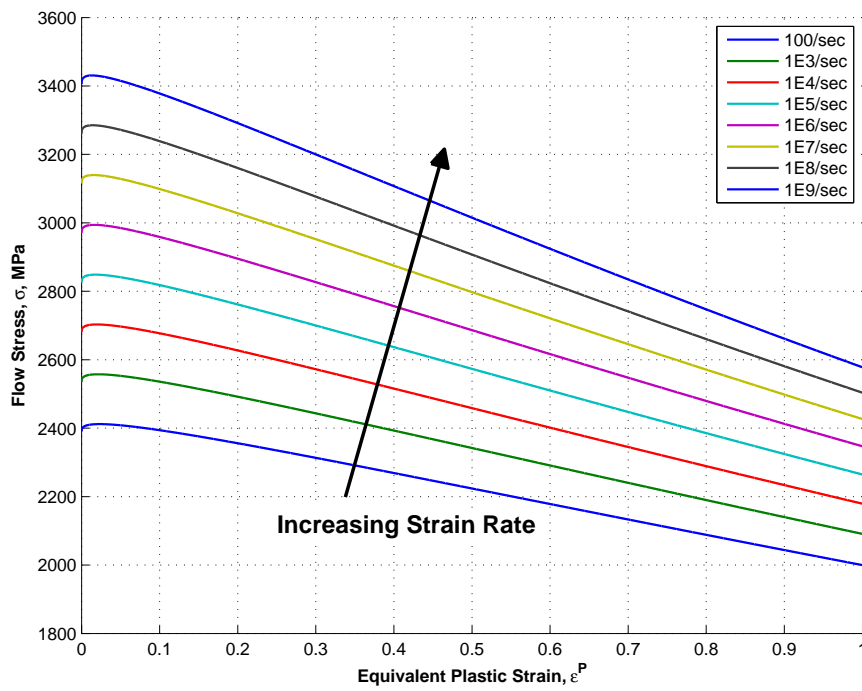


Figure 3.38: VascoMax 300 Stress-Strain Relationships

was modeled with the strain rate applied to the end of the specimen. In order to induce necking in the central part of the bar, a geometric imperfection of 1% radius reduction was introduced. There were problems with model convergence at strain rates greater than 1×10^5 /sec. For this reason, the axisymmetric tensile necking specimen was replaced with a single cube element.

A single, 8-node linear brick element with reduced integration (C3D8R) was used to determine the stress strain curve relationships for VascoMax 300. Adiabatic heating effects were included by setting $\beta = 0.9$ in this analysis as well. Thus, 90% of the energy due to plastic deformation was converted to a temperature rise which further softened the material.

Initially, the element is a cube with 1 mm length on each side and one corner situated at the origin as depicted in Figure 3.39. For boundary conditions, nodes on the *yz-plane* face at $x = 0$ were constrained by $u_x = 0$, and nodes on the *xz-plane* at $y = 0$ were constrained to $u_y = 0$. Similarly, the nodes on the *xy-plane* at $z = 1$ mm were also constrained to $u_z = 0$. A velocity boundary condition that corresponded to the strain rate was prescribed at the top surface, or *xz-plane* at $y = 1$ mm and depicted in yellow in the figure, in the y-direction. The equivalent plastic strain and Mises stress at the single integration point were extracted during post-processing to create the corresponding stress-strain curve. The maximum Mises stress for the given target strain rate is also listed in Table 3.8.

3.4.1 Strain Rate Analysis. High strain rates are observed during the local submodel slipper/asperity collision. The resulting strain rates, for slipper and 6 μm asperity collisions at each of the twelve target velocities, were analyzed to determine the contribution to the max stress observed within the slipper. The outcome of the strain rate analysis was to methodically select a max Mises stress for the damaged elements threshold that was based on the strain rates observed during each slipper and 6 μm rail asperity collision.

Table 3.8: Maximum Mises Stress Comparison

Strain Rate (sec^{-1})	Meyer's $m \cong 1$ (MPa)	ABAQUS Analysis (MPa)
100	2,411.9	2,140.7
1×10^3	2,557.5	2,572.5
1×10^4	2,703.1	2,720.0
1×10^5	2,848.6	2,876.0
1×10^6	2,994.2	2,998.6
1×10^7	3,139.7	3,130.0
1×10^8	3,285.2	3,278.0
1×10^9	3,430.7	3,424.5

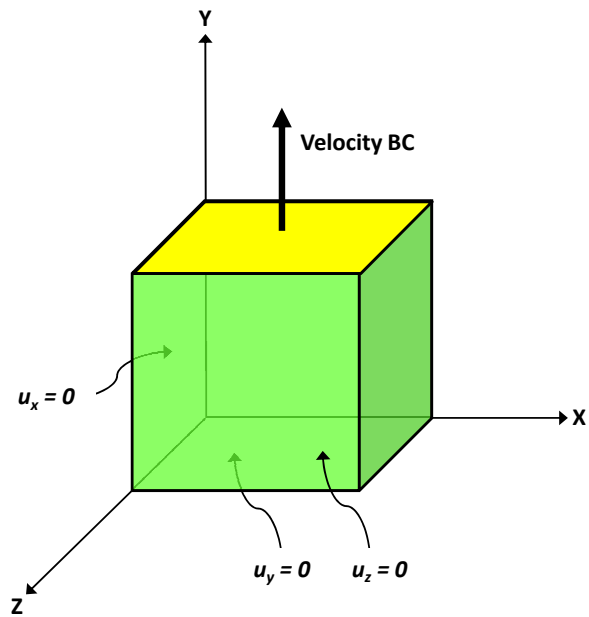


Figure 3.39: Single Cube Element Tensile Test

The step time for the local submodel slipper/rail collision analysis was initially set for the times as listed in Table 3.5. For the local submodel analysis at a particular target velocity, the analysis was divided into 100 equally spaced time increments, or frames. The original intent was to observe the slipper's response during the entire 100 frames. However, in some cases, elements in the asperity experience excessive distortion such that the analysis terminated prematurely. If the full analysis time had been reached, then the slipper would have slid a distance of 110% of the asperity radius, or $6.6 \mu\text{m}$ for this particular case. Although the full step time could not be reached in all velocity and asperity size combinations, each of the analyses did run successfully for at least 50 frames, corresponding to half the originally intended sliding distance. Thus, in order to standardize across all velocity and asperity radius combinations, wear rate and strain rate analysis calculations are for the first 50 frames which correspond to a slipper sliding distance of 55% of the asperity radius, or $3.3 \mu\text{m}$ for the $6 \mu\text{m}$ asperity.

The following process was used to determine the maximum Mises stress threshold for each target velocity at $6 \mu\text{m}$. The first step in the process was to run the local submodel slipper and asperity collision for each of the target velocities. At the 50th frame, maximum principal strain rate, $\dot{\epsilon}$ results were plotted on the undeformed slipper geometry. The ABAQUS "quilt contour plot", which assigns a single value to each element, was used to view this strain rate on an element-by-element basis. The scale for the lines of contour were grouped as follows: 0–100/sec, 100– 1×10^3 /sec, 1×10^3 – 1×10^4 /sec, 1×10^4 – 1×10^5 /sec, etc. Figure 3.41 shows the undeformed slipper at 1,530 m/s with the contour groups as listed previously. The asperity has been removed from the left hand side of the slipper, but the high strain rates indicate the location of the asperity.

The area of each contour group was determined. In the figure, the majority of the slipper area had a maximum principal strain rate between 0 and 100/sec. The interest was in determining the contribution of each of the higher strain rate ranges, so this lower strain rate range contribution was not used in the subsequent calculations.

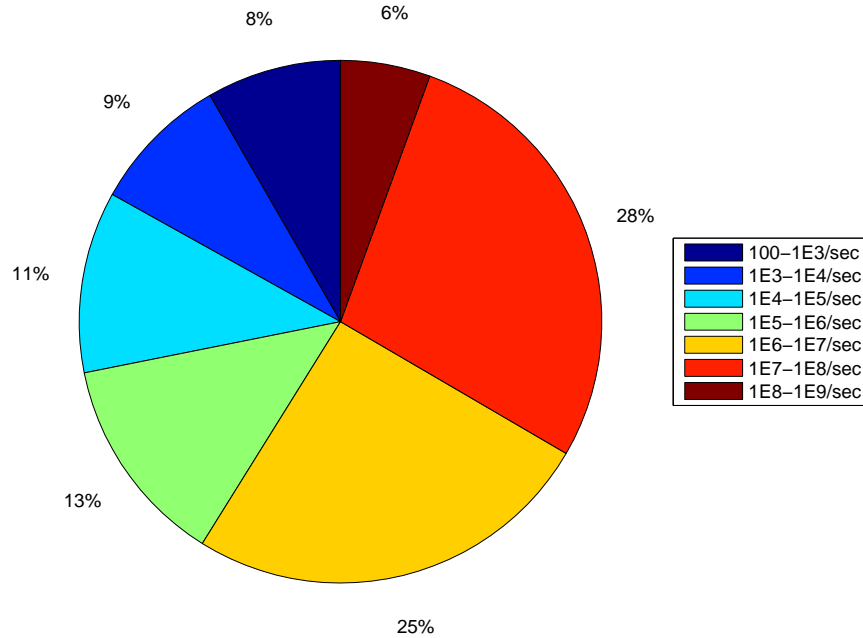


Figure 3.40: Strain Rate Analysis: Area Ratio, $V = 1,530$ m/s

The total area of all elements with maximum principal strain rate greater than 100/sec was determined. Next, the ratios of the area of each strain rate range to the total area was also calculated and plotted in a pie chart format as shown in Figure 3.40. Note that no 0-100/sec strain rate data contributes to the area in this chart.

The dominant strain rate at a given target velocity was computed by summing up weighted values of the average strain rate in each group. For example, the average strain rate in the $1 \times 10^5 - 1 \times 10^6$ /sec range is 5.5×10^5 . In the 1,530 m/s example, the dominant strain rate was computed by summing $0.06 (5.5 \times 10^8) + 0.28 (5.5 \times 10^7) + 0.25 (5.5 \times 10^6) + 0.13 (5.5 \times 10^5)$ etc to reach a final weighted strain rate of 1.38×10^7 /sec. Because this value was at the lower end of the $1 \times 10^7 - 1 \times 10^8$ /sec range, the dominant strain rate for 1,530 m/s was chosen as 1×10^7 /sec. Using Table 3.8, the threshold Mises stress for damaged elements at 1,530 m/s was determined to be 3,130 MPa.

This process was repeated for the other target velocities. It was determined that three different maximum Mises stresses would be used over a range of velocities

Table 3.9: Strain Rate Analysis Results

Velocity Range (m/s)	Dominant Strain Rate (sec ⁻¹)	Maximum Mises Stress (MPa)
10–200	1×10^5	2,900
300–622	1×10^6	3,000
750–1,530	1×10^7	3,130

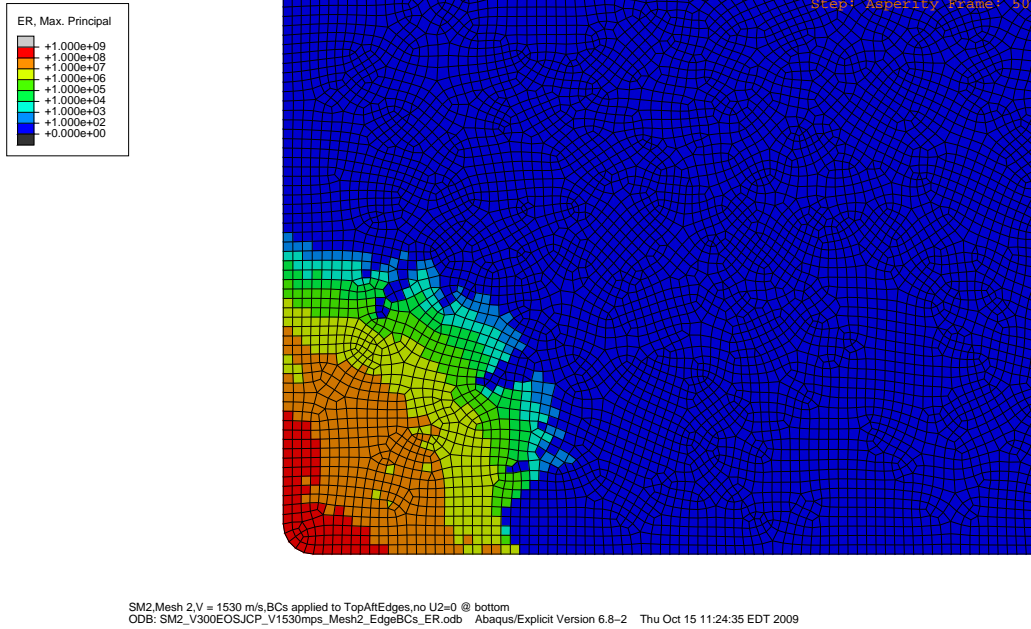


Figure 3.41: Strain Rate Analysis, $V = 1,530$ m/s, Undeformed Slipper

as shown in Table 3.9. The outcome of the strain rate analysis was to methodically select a max Mises stress for the damaged elements threshold that was based on the strain rates observed during each slipper and $6 \mu\text{m}$ rail asperity collision.

3.5 Mechanical Wear Rate Calculations

This section discusses how the mechanical wear rate was calculated from the plane strain analysis of the local submodel slipper and $6 \mu\text{m}$ asperity collision. The single asperity wear rate is also defined and determined by analyzing slipper and smaller radii asperity collisions. Wear rate is the most important function determined in this research. The method developed could be used to evaluate any combination of materials in the wear environment.

Recall that the wear rate is defined as the volume of material removed per unit sliding distance [14]. Because the definition refers to volume of removed or damaged material, one assumes that a three-dimensional analysis is being considered. Numerically, the dimensional wear rate, W , is the volume of material removed, V , divided by the sliding distance, d , as

$$W = \frac{V}{d} = \frac{A_d w_{eff}}{vt} \quad (3.17)$$

The units of the dimensional wear rate are L^3/L or L^2 , where L is the unit of dimensional length. In this ABAQUS analysis, the base unit of length was the millimeter. Although mm^2 is the mathematical simplification of mm^3/mm , the wear rate will be reported as mm^3/mm to indicate a volume per unit length. The sliding distance, d , is the product of velocity, v and time, t . In the ABAQUS analysis, the submodel slipper velocity was held constant at the velocity for the step time duration of each submodel analysis. The wear rate per unit width, W_{uw} , is determined by dividing Equation 3.17 by the effective width, w_{eff} , to yield

$$W_{uw} = \frac{W}{w_{eff}} = \frac{A_d}{vt} \quad (3.18)$$

The volume in Equation 3.17 is the product of the damage area, A_d , and an effective width, w_{eff} . By evaluating slipper collisions with asperities of 4 and 2 μm radii at several velocities, the effective width was determined to extend the two-dimensional plane strain analysis into a three-dimensional effect.

3.5.1 Determining Wear Rate per Unit Width. The following process was used to determine the wear rate per unit width for a given target velocity and asperity size pair. First, the local submodel analysis, using *SM Mesh 2* for both the slipper and rail/asperity regions, was performed in ABAQUS for each of the twelve target velocities (see Table 3.5 for the step time based on velocity and asperity radius). These step times were divided into 100 evenly spaced time increments, or frames as defined

by ABAQUS. At each velocity, the intent was to determine the wear rate at the same sliding distance equal to 110% of the asperity radius. This slipper sliding distance would be reached if all 100 time increments or frames were used in the analysis. Due to some numerical convergence issues, every analysis at the target velocity did not complete for the entire step time. However, in each case, the solution ran for 50 frames, or half of the original step time, which corresponded to a total sliding distance of 55% of the asperity radius.

Next, for each target velocity, the maximum Mises stress criterion, as listed in Table 3.8, was used to determine the damage area, A_d . The interest was on determining wear rate in the VascoMax 300 slipper and not in the rail. During post-processing, the deformable rail/asperity part was removed. A Python script macro was created that displayed only slipper submodel elements that exceeded the damage criterion, in this analysis the maximum Mises stress. The slipper submodel element was considered damaged if the integration point within the submodel element exceeded this Mises stress threshold.

The element volume, which is actually the element area in the two-dimensional analysis, was extracted while stepping incrementally through each of the 50 analysis frames. By removing the rail/asperity part, only the area of slipper elements that exceeded the maximum Mises stress was recorded. Each analysis frame corresponded to an instance in time during the slipper and asperity collision. The damage area, A_d , now available as a function of analysis time, was saved and imported into a Matlab script for further post-processing and plotting of results.

Within the Matlab script for determining wear rate, the damage area as a function of time was evaluated. The cumulative damage area, $A_{d_{tot}}$, is the sum of the incremental damage area, A_{d_i} , given by

$$A_{d_{tot}} = \sum_{i=1}^n A_{d_i} \quad (3.19)$$

where $n = 50$ corresponds to the maximum number of increments used in the evaluation. Any instance in time, t_i , corresponds to a given sliding distance, d_i . At the k^{th} time increment, and consequently at the corresponding sliding distance, a cumulative average wear rate, W_k , is determined by dividing the cumulative damage area by the sliding distance given by

$$W_k = \frac{\sum_{i=1}^k A_{d_k}}{d_k} \quad (3.20)$$

The overall average wear rate was determined by dividing the sum total of damage area by the total sliding distance during the asperity collision. When plotted as a function of time, the cumulative average wear rate at the final time of analysis approaches the overall average wear rate.

An example wear rate calculation for a $6 \mu\text{m}$ asperity at 10 m/s is shown in Figure 3.42. For this velocity, the time increment per frame, Δt , was 6.6×10^{-9} sec and the Mises threshold for damaged elements was $2,900 \text{ MPa}$. The top subplot in the figure depicts the wear rate per unit width as a function of time. The bottom subplot shows the cumulative area of damaged elements also as a function of time.

The incremental wear rate, is determined by dividing the area of damaged elements (from the lower subplot) by the distance slid from the start of the analysis to the given time increment. For example, to calculate the incremental wear rate at the 10th increment, the elapsed time is $10 \times \Delta t$ which is 6.6×10^{-8} seconds. At a constant velocity of 10 m/s , during this 6.6×10^{-8} seconds, the sliding distance is $(10 \times \Delta t) \times 10 \text{ m/s}$ which is $6.6 \times 10^{-4} \text{ mm}$. From the lower subplot, the damage area at 6.6×10^{-8} seconds, indicated by the circular data point, is $1.739 \times 10^{-6} \text{ mm}^2$. Thus, in the top subplot, the incremental wear rate at the 10th increment or 6.6×10^{-8} sec, also highlighted as the circular data point, is $1.739 \times 10^{-6} \text{ mm}^2 \div 6.6 \times 10^{-4} \text{ mm}$ which is $2.635 \times 10^{-3} \text{ mm}^2/\text{mm}$.

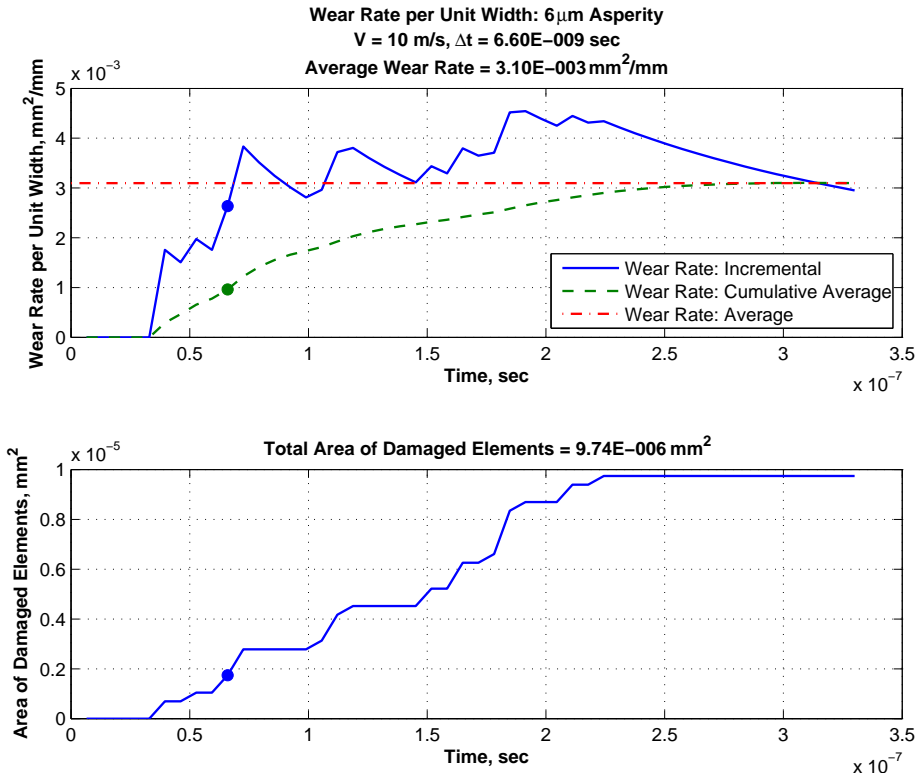


Figure 3.42: Wear Rate per Unit Width, $6 \mu\text{m}$, $V = 10 \text{ m/s}$

The cumulative average wear rate at the 10th increment is computed by summing up the incremental wear rates for the first 10 increments and dividing by the number of increments. The sum of the first 10 incremental wear rates is $9.63 \times 10^{-3} \text{ mm}^2/\text{mm}$. Thus, the cumulative wear rate at the 10th increment is $9.63 \times 10^{-3} \text{ mm}^2/\text{mm} \div 10$ which is $9.63 \times 10^{-4} \text{ mm}^2/\text{mm}$ as depicted by the green data point on the cumulative average wear rate line.

The average wear rate is determined by dividing the final area of damaged elements by the total sliding distance during the analysis. Thus, the cumulative average wear rate will equal the average wear rate at the end of the analysis time.

Of particular note is a unique relationship between the incremental wear rate and the area of damaged elements. In the lower subplot, there are increments of time where the area of damaged elements remains constant, indicating that no additional elements have met the damage criteria. Over this same time interval of interest, the

incremental wear rate continues to decline in magnitude. This occurs because the damage area remained constant, yet the sliding distance continues to increase. This relationship is easy to observe in the lower subplot on the interval from 2.2×10^{-7} to 3.3×10^{-7} seconds where the area of damaged elements is constant at 9.738×10^{-6} mm². Over this same time interval, the incremental wear rate decreases from 4.34×10^{-3} to 2.95×10^{-3} mm²/mm due to the increasing sliding distance.

It should also be noted that for the first 5 increments, in this 10 m/s example, from 0 to 3.3×10^{-8} sec, the area of damaged elements is zero. This means that up until this point in the analysis, no elements have had a Mises stress greater than 2,900 MPa. Consequently, because the area of damaged elements is zero, the incremental and cumulative average wear rates during this initial time interval are also zero. When the area of damaged elements begins to increase, the incremental and cumulative average wear rates also begin to increase.

At each of the 12 target velocities, the average wear rate per unit width for the collision between a local submodel slipper and a 6 μ m asperity was calculated. The wear rate per unit width for each of the 12 target velocities is shown in Table 3.10. The wear rate per unit width calculations for all twelve target velocities and the 6 μ m case are presented in Appendix B.

Previously, in the local submodel mesh convergence discussion in Section 3.3.4, it was stated that wear rates for *SM Mesh 2* and *SM Mesh 4* would be compared. Now that the wear rate per unit width has been defined, the results of this study can be presented. In collisions with the 6 μ m asperity, wear rate comparisons were made between the two local submodel meshes at 1,000 and 1,530 m/s. These results are presented in Figure 3.43 and Figure 3.44 for 1,000 and 1,530 m/s, respectively. In each individual velocity case, the area of damaged elements was similar between the two meshes for the same sliding distance. Consequently, the cumulative average wear rates were also similar. For 1,000 m/s, *SM Mesh 2* and *SM Mesh 4* had average wear rates of 2.28×10^{-2} and 2.18×10^{-2} mm²/mm, respectively. At 1,530 m/s, the average

Table 3.10: Wear Rate per Unit Width, W_{uw} , Various Asperity Radii

Target Velocity (m/s)	R = 6 μm (mm^2/mm)	R = 4 μm (mm^2/mm)	R = 2 μm (mm^2/mm)
10	0.0031	0.0021	0.00035
20	0.0041	-	-
40	0.0045	-	-
100	0.0058	0.0037	0.00073
200	0.0102	-	-
300	0.0147	-	-
500	0.0246	0.0149	0.0042
622	0.0262	-	-
750	0.0236	-	-
1,000	0.0226	0.0141	0.0037
1,250	0.0200	-	-
1,530	0.0166	0.0104	0.0028

wear rates were 1.67×10^{-2} and 1.65×10^{-2} mm^2/mm , respectively. Similarities in these wear rates for the two mesh configurations was another confirmation that *SM Mesh 2* could be used as the optimum local submodel mesh.

3.5.2 Wear Rate for Three-Dimensional, Hemispherical 6 μm Asperity.

In order to convert the wear rate per unit width, W_{uw} , to a wear rate, based on volume of elements damaged, an effective width, w_{eff} , needed to be established. To determine this effective width, additional local submodel slipper/asperity collisions were evaluated with both the 4 and 2 μm asperity radii at five target velocities, namely 10, 100, 500, 1,000, and 1,530 m/s. These five velocities were selected because they spanned the range of sled velocities from the January 2008 test mission.

The same technique used for the 6 μm asperity to determine W_{uw} was incorporated. The 4 and 2 μm asperity wear rate per unit width are listed in Table 3.10 at the five target velocities. The wear rate per unit width calculations for the selected five target velocities and the 4 and 2 μm cases are also presented in Appendix B.

The 4 and 2 μm asperity analyses represent off-center collisions with the 6 μm asperity as shown in Figure 3.45(a). The plane strain analyses for the 6, 4, and 2 μm

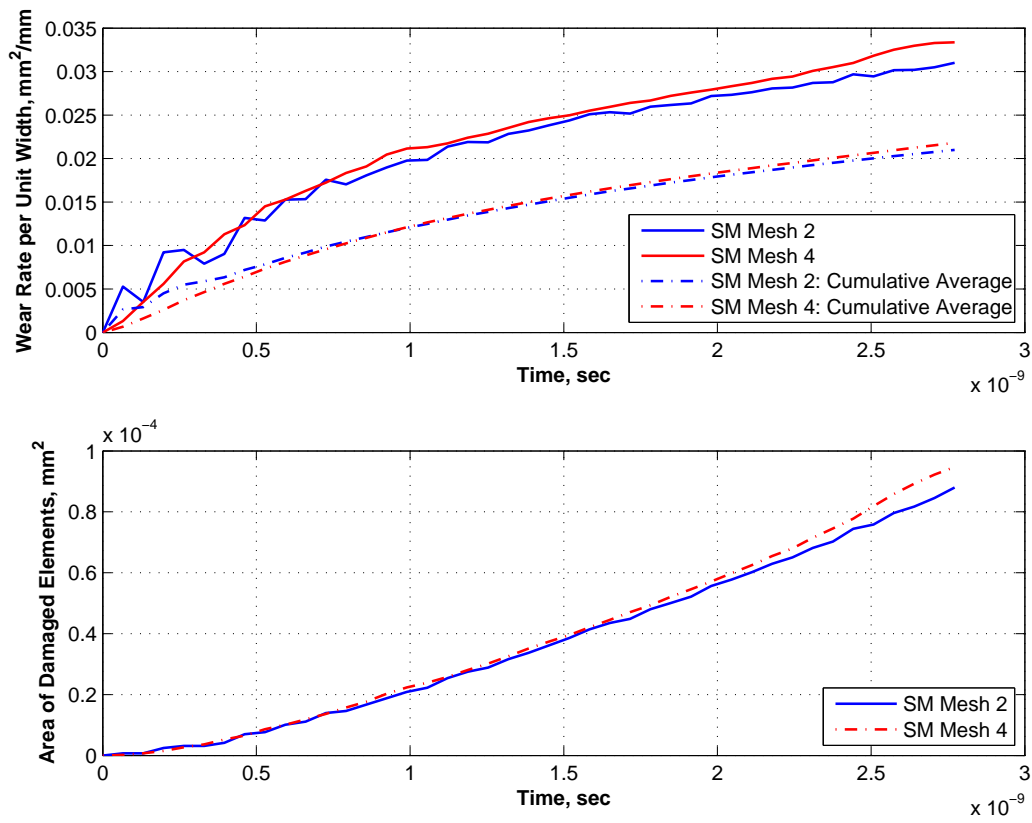


Figure 3.43: Wear Rate Comparison, SM Mesh 2 vs. Mesh 4, $V = 1,000$ m/s

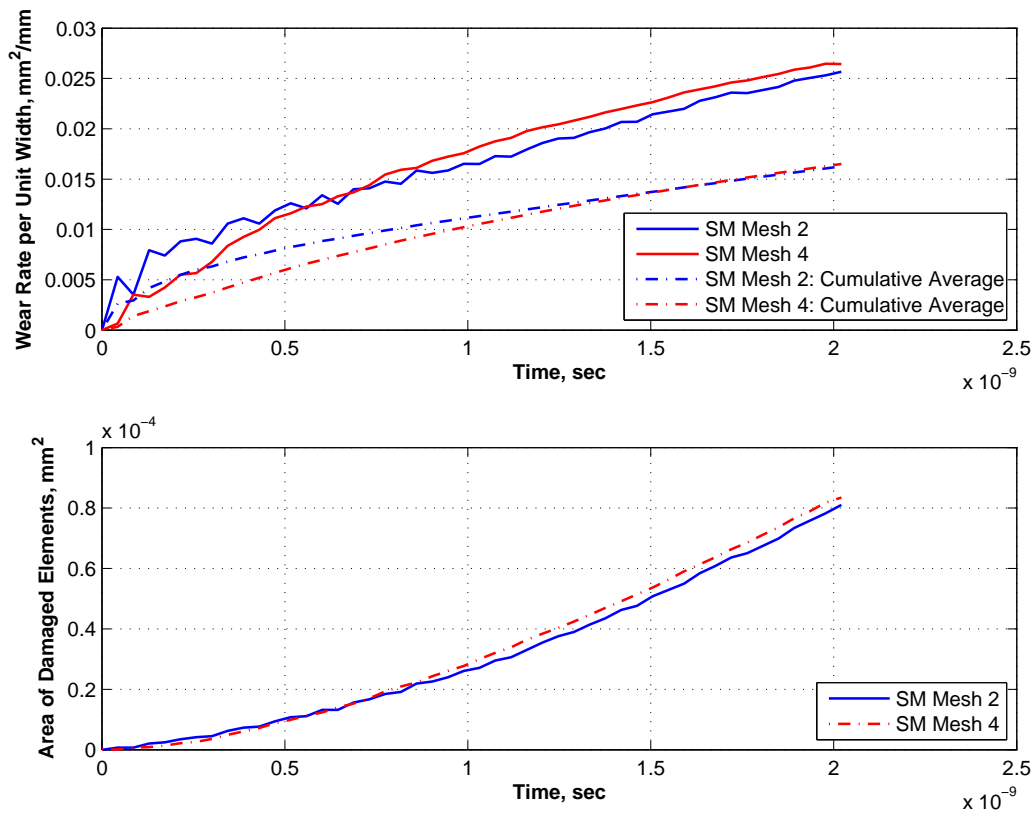
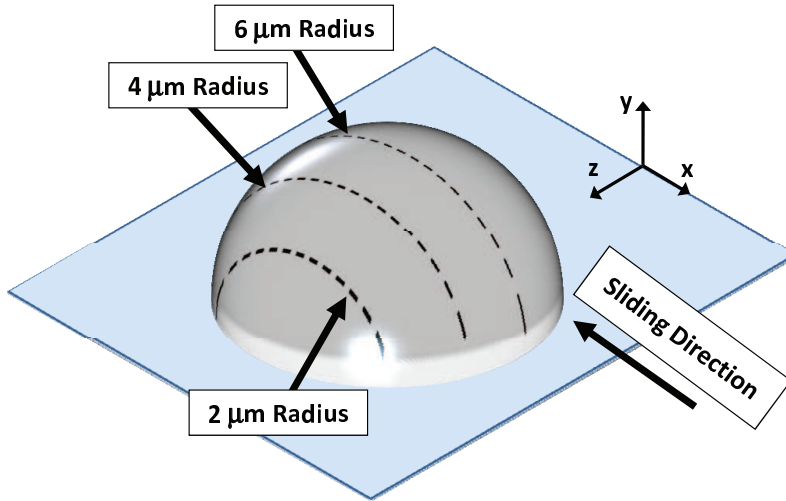
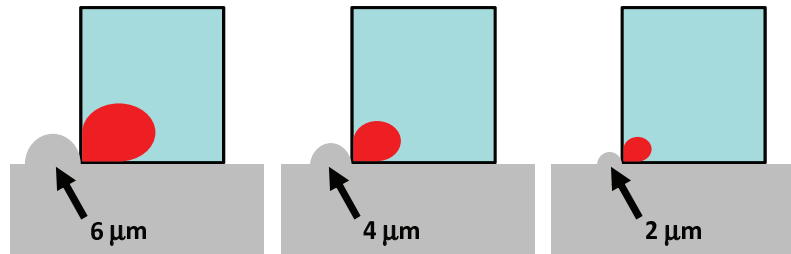


Figure 3.44: Wear Rate Comparison, SM Mesh 2 vs. Mesh 4, $V = 1,530$ m/s



(a) Hemispherical 6 μm Radius Asperity



(b) Plane Strain Analyses at 6, 4, and 2 μm

Figure 3.45: Hemispherical Asperity Model

asperities, shown in Figure 3.45(b), represent the damage area that occurs in each local submodel slipper/asperity collision. At the same target velocity, the damage area will decrease with decreasing asperity radius. The following equation defines the hemispherical coordinates in the yz -plane for a hemisphere of radius, r ,

$$y = \sqrt{r^2 - z^2} \quad (3.21)$$

For the 6 μm asperity, the z -coordinates for the 4 and 2 μm asperity height are 4.47 and 5.66 μm , respectively. For a given velocity, the three W_{uw} values for each asperity size are plotted at the associated z -coordinate, or distance from the center of the 6 μm asperity. The three wear rate per unit width values at 10 m/s are annotated for each asperity radii in Figure 3.46. These annotated W_{uw} values are listed in Table

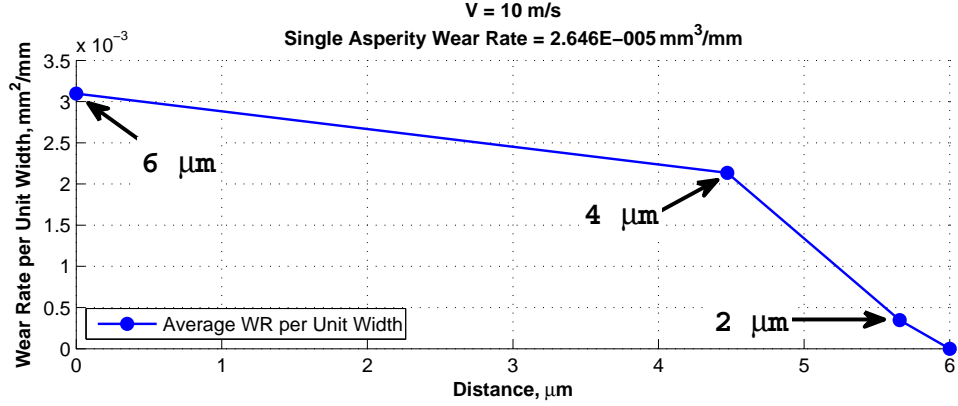


Figure 3.46: Single Asperity Wear Rate, $V = 10$ m/s

3.10 for 10 m/s. It is assumed that at $z = 6$, the wear rate was zero because the no damage occurs unless there is an asperity collision. Consequently, zero damage translates into zero wear rate.

At a given velocity, the single asperity wear rate, W_{sa} , is given by

$$W_{sa} = 2 \int_0^r W_{uw}(z) dz \quad (3.22)$$

where the value of the integral is doubled to account for both sides of the asperity, with radius, r . The single asperity wear rate, W_{sa} , now has units of mm^3/mm , which truly reflect the volume per unit of sliding distance. At 10 m/s, the W_{sa} was $2.646 \times 10^{-5} \text{ mm}^3/\text{mm}$.

The process was repeated for the 100, 500, 1,000, and 1,530 m/s velocities. Figure 3.47 shows W_{sa} at 100 and 500 m/s, and Figure 3.48 shows W_{sa} at 1,000 and 1,530 m/s. For the five velocities, the single asperity wear rates are listed in Table 3.11. The wear rate per unit width calculations for the five target velocities and the 4 and 2 μm asperity cases are also presented in Appendix B.

With the single asperity wear rates established for five velocities, the next step in the process was to use these results to determine the single asperity wear rate for the seven remaining target velocities. For each of the five velocities, the ratio of the

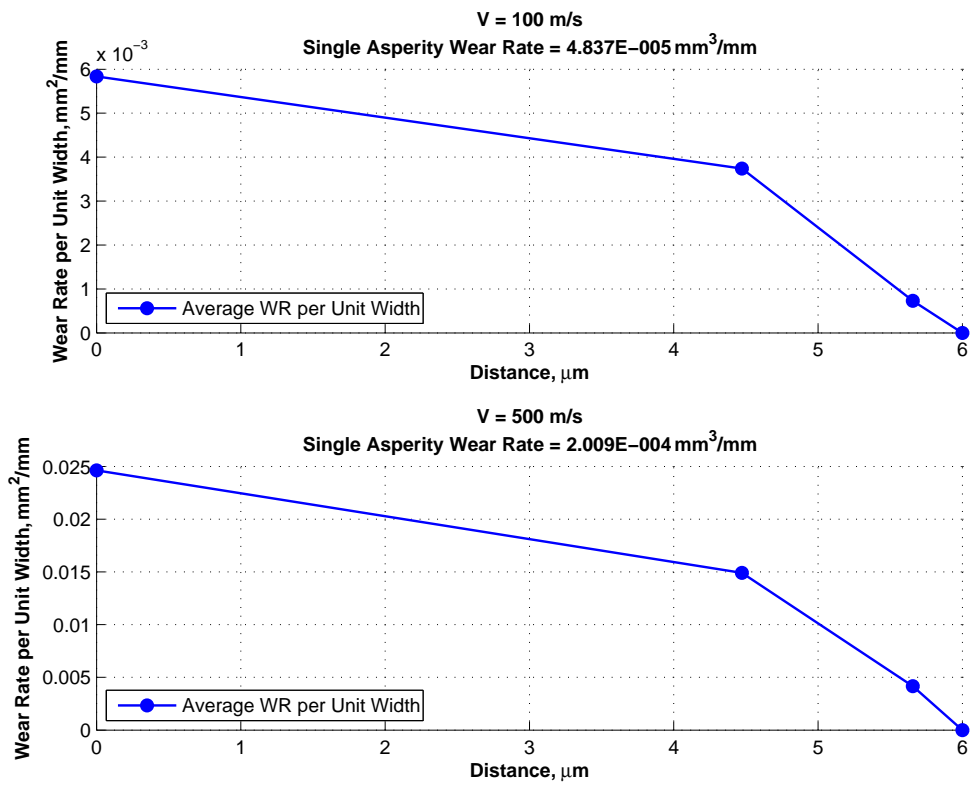


Figure 3.47: Single Asperity Wear Rate, $V = 100$ and 500 m/s

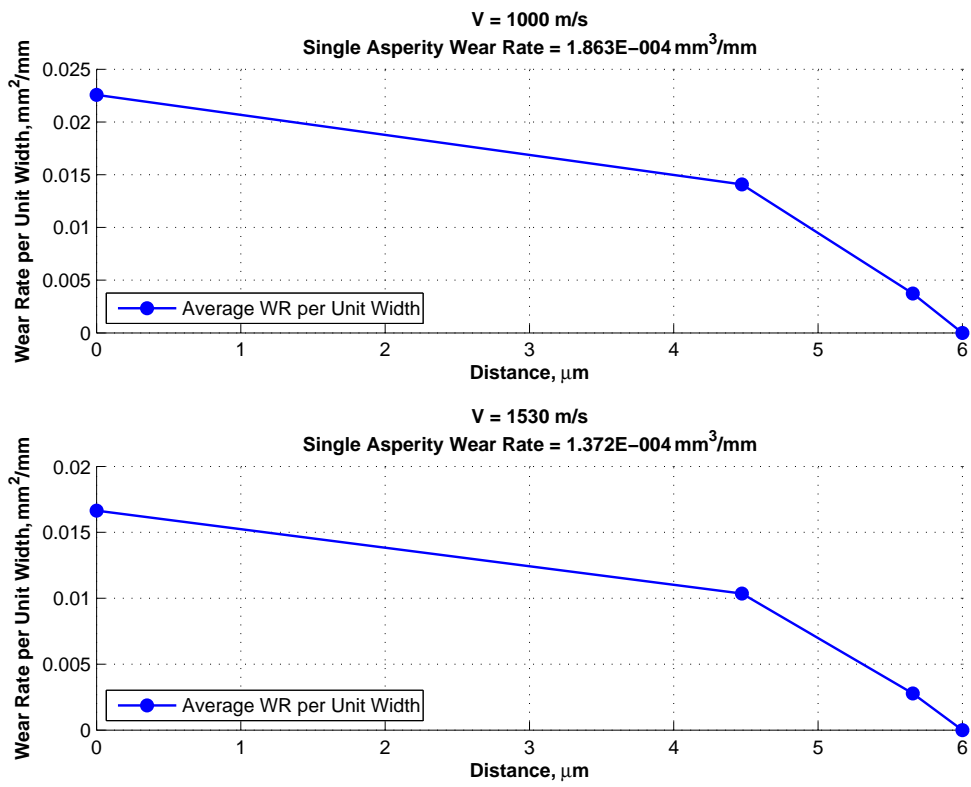


Figure 3.48: Single Asperity Wear Rate, $V = 1,000$ and $1,530$ m/s

Table 3.11: Single Asperity Wear Rates

Velocity (m/s)	W_{sa} (mm ³ /mm)	Ratio: $W_{sa} / 6 \mu\text{m } W_{uw}$ (μm)
10	2.646×10^{-5}	8.54
100	4.837×10^{-5}	8.29
500	2.009×10^{-4}	8.16
1,000	1.863×10^{-4}	8.25
1,530	1.372×10^{-4}	8.24

single asperity wear rate, W_{sa} , to the $6 \mu\text{m } W_{uw}$ was determined. The average of these ratios, listed in Table 3.11, for the five velocities was $8.29 \mu\text{m}$.

Because only $6 \mu\text{m}$ asperity collisions were evaluated at the remaining seven target velocities, the wear rate per unit width for 4 and $2 \mu\text{m}$ asperities was unknown. However, this ratio related the known $6 \mu\text{m}$ wear rate per unit width to the single asperity wear rate. This ratio turns out to be the effective width. The single asperity wear rates for the remaining seven target velocities can be determined by multiplying their respective W_{ua} by the effective width, w_{eff} , value of $8.29 \mu\text{m}$.

3.6 Preliminary Studies and Results

3.6.1 Global to Local Submodel Stress Mapping. A study in this research investigated mapping of the global element state of stress, for any given time that corresponded to one of the target velocities, as the initial condition for the local submodel analysis. Stress mapping refers to taking the stress results from the global model analysis and mapping them onto the submodel domain as stress initial conditions. Nodal coordinate and numbers for both the global and local submodel, along with the σ_{xx} , σ_{yy} , σ_{zz} , and σ_{xy} values at each node were exported from ABAQUS. A Matlab script was written that read in this exported data and interpolated the stress values from the global nodes to the local submodel nodes. Based on the submodel nodal connectivity, and the corresponding stress values for each submodel node, the same σ_{xx} , σ_{yy} , σ_{zz} , and σ_{xy} values were calculated for each local submodel element. The script exported this data in a format that was consistent with ABAQUS input

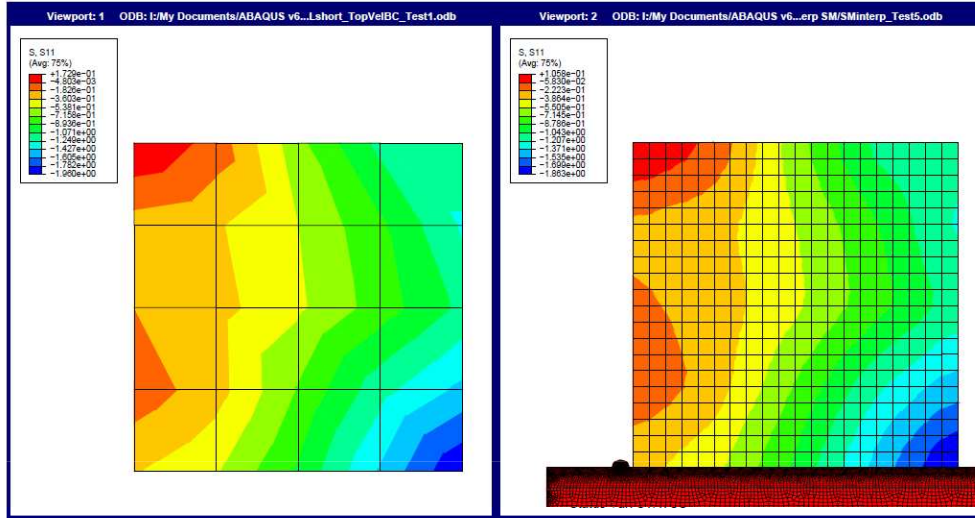


Figure 3.49: Global to Local Submodel Stress Mapping

files. Each “stress mapping” data file was copied into the submodel input file as a predefined field, or initial stress condition. Thus, the global state of stress in the submodel region had been transferred to the local submodel.

The global σ_{xx} , designated by the ABAQUS variable “S.S11”, at an intermediate velocity of 75 m/s is shown on the left side of Figure 3.49. On the right side of the figure, the global σ_{xx} has been mapped to the local submodel. This particular image was generated during the stress mapping study when a uniform, 20x20 element submodel slipper mesh was being used to verify the Matlab script.

During the submodel analysis, the local slipper model collides with a hemispherical, 6 μm radius asperity. The stresses that result during the asperity collision were much larger in magnitude than the initial state of stress. For example, during the 100 m/s targeted velocity analysis, the maximum Mises stress in the submodel was initially approximately 7 MPa, a relatively low magnitude. However, during the collision, Mises stresses in the slipper submodel increased to over 3,000 MPa. As a result of this study, it was determined that the global stress did not need to be mapped to the submodel as an initial condition in subsequent analyses because the stress due to the asperity collision dominated the event.

Despite not needing to map the global stress to the local submodel, the three global models ended up generating the normal pressure profile along the length of entire slipper. This pressure profile is used to determine N , the three-dimensional proportion factor to be discussed subsequently, which helped to relate the effects of a plane strain, single asperity collision to the three-dimensional grouping of all asperities actually encountered by the slipper during the sliding event on the rail.

3.6.2 Acceleration, Deceleration and Constant Velocity Comparison. Recall from the Stage 3 velocity profile, shown in Figure 2.3, that the sled accelerates to a velocity of 1,530 m/s and then begins to decelerate. The Stage 3 sled then departs the end of the track at a velocity of 622 m/s. The “acceleration phase” corresponds to increasing velocity, from 0 m/s to 1,530 m/s. The “deceleration phase” corresponds to decreasing velocity, from 1,530 m/s to 622 m/s. Thus, in the range of 622–1,529 m/s, a given velocity will have two corresponding sled run times on the velocity profile. One time will be in the acceleration phase and the other time will occur during the deceleration phase. From the DADS data, this single velocity at two different times also corresponds to two different upper limit pressures, P_{ul} .

A study was conducted to determine the effect of acceleration and deceleration on W_{uw} at 1,000 m/s. Sled acceleration was extracted from the DADS horizontal acceleration data at each of the two 1,000 m/s velocities. During the acceleration phase, the sled reached 1,000 m/s at 4.15 seconds and the horizontal acceleration was 685.4 m/s², or +69.9 G’s. In the deceleration phase, the sled slowed to 1,000 m/s at 6.12 seconds and the horizontal acceleration was -167.3 m/s², or -17.1 G’s, where the negative sign indicates deceleration. Instead of using a constant 1,000 m/s velocity boundary condition for the submodel, the initial velocity, v_1 , and final velocity, v_2 , were determined such that the average velocity, v_{avg} , was 1,000 m/s as shown in Equation 3.23.

$$v_{avg} = \frac{v_1 + v_2}{2} \quad (3.23)$$

Table 3.12: Acceleration/Deceleration Study Conditions

Condition	Acceleration, m/s ²	v_1 , m/s	v_2 , m/s
Constant Velocity	0	1,000	1,000
Acceleration	685.4	999.99999246	1,000.00000754
Deceleration	-167.3	1,000.00000184	999.99999816

and the average acceleration, a_{avg} , was given by

$$a_{avg} = \frac{dv}{dt} = \frac{v_2 - v_1}{\Delta t} \quad (3.24)$$

Because the time interval for the asperity collision, Δt , was extremely small, v_1 and v_2 were very close in magnitude as shown in Table 3.12, which summarizes the 1,000 m/s acceleration, deceleration, and constant velocity conditions.

During this particular study, several “stress mapping” cases were also evaluated. In the global total contact model, the maximum σ_{yy} along the bottom of the slipper occurred at a location that was 8% of the slipper length, L , from the front edge, or $0.08L$. Stresses were extracted from the global model at the front location, and at the $0.08L$ location.

Nine combinations of the velocity and stress mapping conditions were studied. Stress mapping location is specified by either front or $0.08L$. The three velocity conditions are constant velocity, acceleration, and deceleration which correspond to the conditions outlined in Table 3.12. The resulting wear rate per unit width, W_{uw} , for the combination of accelerations, decelerations, and stress mapping is presented in Table 3.13. All nine of the test conditions yielded almost exactly the same results. The progression of the cumulative average wear rate for the nine study cases is shown in Figure 3.50.

Ultimately, this study showed that the acceleration or deceleration had negligible effect on the overall wear rate at 1,000 m/s. Despite the large differences in the slipper acceleration and deceleration, these effects are negated because the time duration for the local submodel collision is extremely short. Mapping the stress from the global

Table 3.13: 1,000 m/s Acceleration/Deceleration Study Results

Study Case	Velocity Phase	Stress Mapping	Velocity Condition	W_{uw} (mm^2/mm)
1	Accel	None	Constant V	0.0156
2	Accel	Front	Constant V	0.0158
3	Accel	None	Accel	0.0158
4	Accel	Front	Accel	0.0157
5	Accel	0.08L	Constant V	0.0158
6	Decel	Front	Constant V	0.0157
7	Decel	None	Decel	0.0157
8	Decel	0.08L	Constant V	0.0160
9	Decel	Front	Decel	0.0159

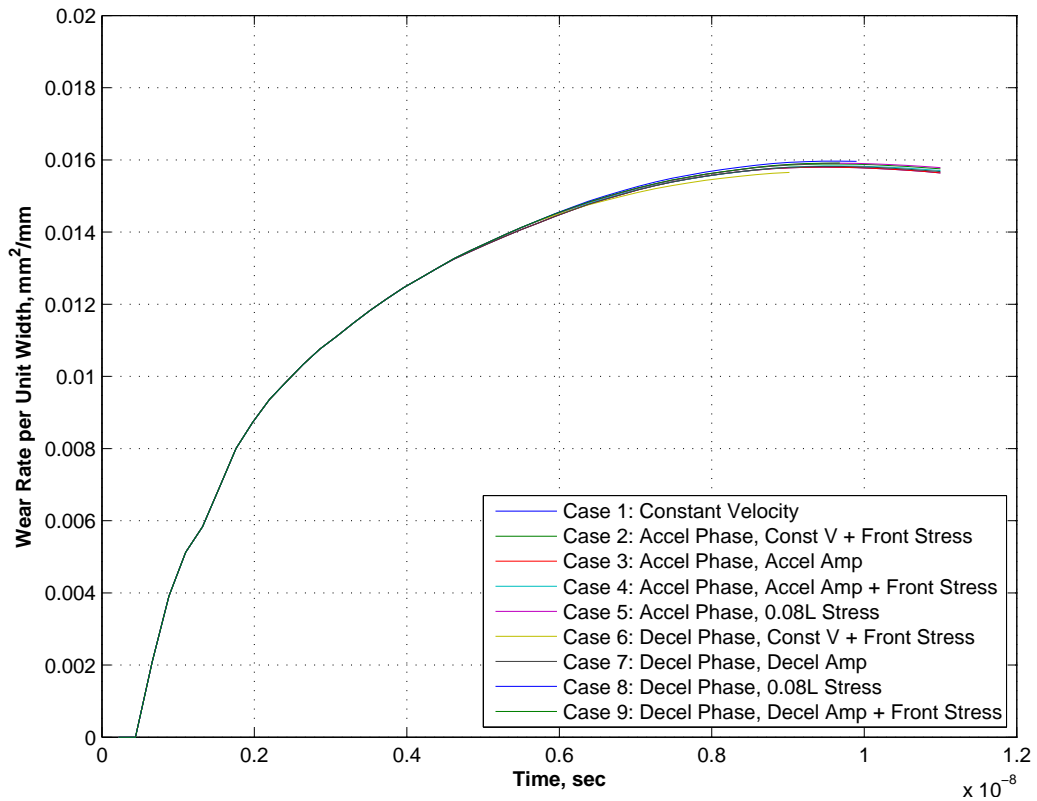


Figure 3.50: Accel/Decel Study Results, $V = 1,000$ m/s

total contact model also had negligible effect. Although the slipper velocity changed during the analysis, it was essentially constant at 1,000 m/s. This study also showed that the build-up of stresses within the slipper did not ultimately affect the wear rate. The history of these dynamic effects was unimportant.

If the local submodel slipper/asperity collisions were evaluated for a much longer time duration, on the order of tenths or hundredths of a second, for example, then the change in acceleration may need to be considered. However, because of the extremely short duration of the slipper/asperity collision, and the negligible effect of acceleration, deceleration, or initial state of stress in the slipper on the overall wear rate per unit width, a constant velocity was used during the local submodel slipper/asperity collision at each target velocity for the remainder of this analysis.

3.7 Global Model Pressure Distributions

This section presents the pressure distribution along the bottom of the slipper for the three global model cases. This pressure distribution was necessary to determine the flash temperature as part of the melt wear rate analysis. For the global total contact model, the pressure distribution was extracted at the instant when the slipper was sliding at the specific target velocity. Unfortunately, because of the $u_y = 0$ vertical displacement boundary constraint at the slipper bottom surface, the pressure distribution resembled the pressure distribution associated with a static (zero velocity) analysis. The pressure distribution was symmetric about the center of the slipper as shown in Figure 3.51. In this figure, the abscissa has been normalized by the global slipper length. For each target velocity and global model, the maximum contact pressure and the DADS pressure that was applied at the top of the slipper surface, are listed in Table 3.14.

For the global quasi-steady model, the pressure distribution was extracted at the end of the analysis for each target velocity. The pressure profiles for this global model case are shown in Figure 3.52. The maximum pressure occurred at the front of the slipper (at $x/L = 0$ where the slipper is moving from left to right in each global

model analysis). For approximately 80% of the slipper length, the pressure is nearly constant. At the aft edge of the slipper ($x/L = 1$), the pressure returned to zero. The maximum contact pressure of 9.58 MPa occurred at the 1,250 m/s target velocity and corresponded to the greatest applied DADS pressure of 4.727 MPa at for the given target velocities.

Finally, the pressure distribution for the global bounce model was extracted at the instant in the analysis when the slipper made contact with the rigid rail. Recall that the slipper initially was displaced by the slipper gap distance of 3.175 mm at the start of this global analysis. As with the global quasi-steady model analysis, the pressure was nearly constant for approximately 80% of the slipper length and returned to zero at the aft edge of the slipper. Also, the maximum pressure occurred at the leading edge of the slipper. However, the magnitudes of each maximum pressure for this global model case were significantly larger than corresponding pressures in the previous global model analyses.

Based on the pressure distributions for the three global models, the global bounce model pressure distribution was eventually selected for use during the subsequent flash temperature analysis. The global total contact pressure distribution was rejected because of the symmetrical aspect that didn't reflect what should have resulted for a moving slipper. However, the global total contact model was used for evaluation of whether a mapped stress or acceleration was necessary. The global quasi-steady state pressure distribution will be used in Section 4.3.3 to determine the three-dimensional proportion factor, N .

3.8 Melt Wear Rate Calculations

To this point in the discussion, the emphasis has been on the determination of mechanical wear rates that are caused by plastic deformation of the slipper and rail material. Melt wear is another contributing factor to the overall wear. As described in Chapter I, melt wear in the slipper occurs because slipper material is removed

Table 3.14: Maximum Contact Pressures for Global Models

Velocity (m/s)	DADS Pressure (MPa)	Total Contact (MPa)	Quasi-steady (MPa)	Bounce Model (MPa)
10	0.180	0.20	0.68	396.0
20	0.226	0.24	0.86	646.1
40	0.309	0.33	1.16	505.8
100	0.500	0.53	1.87	997.1
200	0.778	0.83	2.84	1,004.6
300	1.113	1.19	3.92	1,315.3
500	1.836	1.96	5.81	1,192.3
622	1.373	1.46	4.39	840.2
750	2.141	2.29	6.13	1,608.2
1,000	2.403	2.56	6.18	1,084.5
1,250	4.727	4.24	9.58	1,123.8
1,530	4.037	4.31	8.10	1,385.4

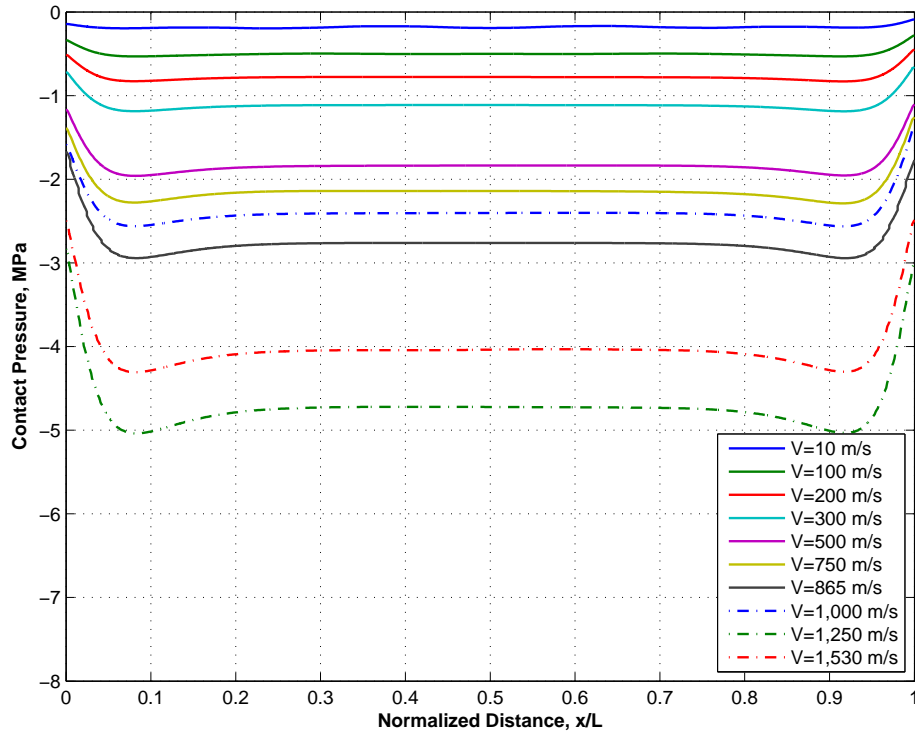


Figure 3.51: Pressure Distribution: Global Total Contact Model

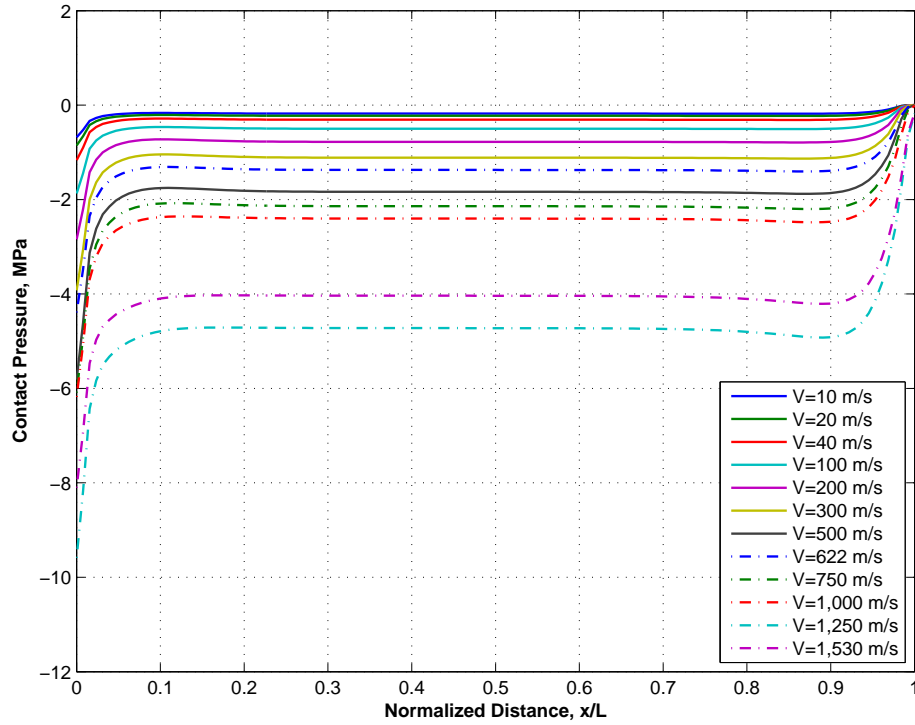


Figure 3.52: Pressure Distribution: Global Quasi-Steady Model

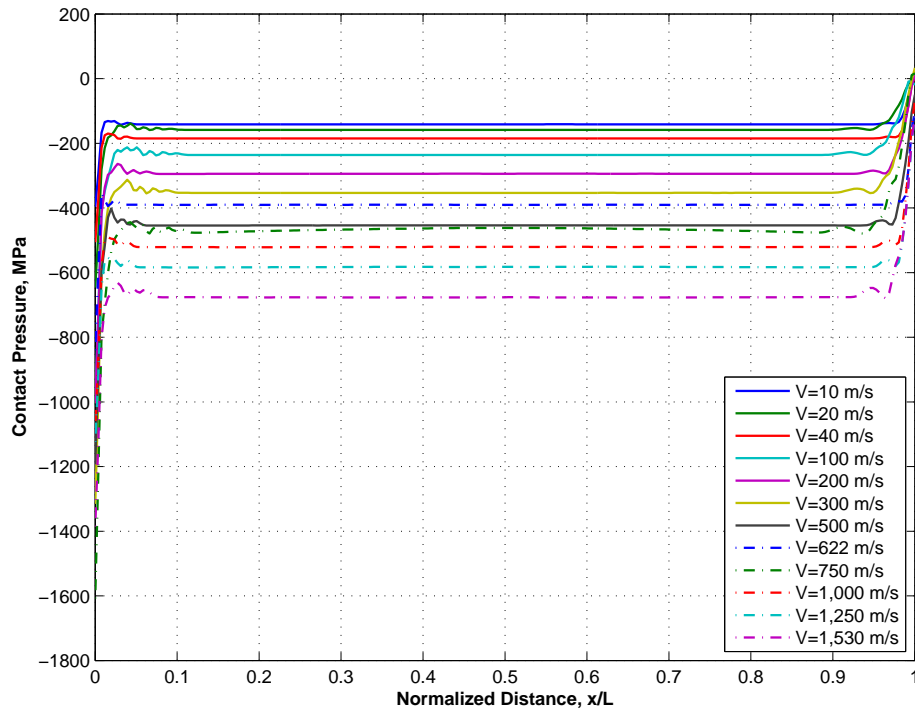


Figure 3.53: Pressure Distribution: Global Bounce Model

due to induced temperatures that surpass the material’s melting temperature. For VascoMax 300, the melt temperature is 1685 K [77].

To determine the melt wear rate in the numerical model, the effects of frictional heating and flash temperature rise were considered. First, the slipper temperature at the slipper surface was determined. Using the pressure profiles from the global slipper analysis, the flash temperature during a 6 μm asperity collision is determined. Finally, the same effective width, w_{eff} , that was calculated in the mechanical wear rate analysis was used to ultimately determine the melt wear rate.

3.8.1 Frictional Heating and Temperature Profile. When two bodies rub together, frictional heating at the contact interface causes the temperature to rise. This temperature rise has been associated with the presence of mechanical energy, which is required to overcome the frictional resistance to sliding at the contact surface [32]. The mechanical energy is dissipated through thermal energy in the form of a temperature rise.

A heat transfer analysis was conducted to determine the temperature profile through the thickness of the slipper. This approach is similar to those of Laird [48] and Cameron [24] in their previous HHSTT research hypervelocity gouging and wear studies, respectively. Laird’s summary of the investigation of frictional heating by Krupovage and Rasmussen [47] is presented here. In their studies at the HHSTT in the early 1980s, Krupovage and Rasmussen related frictional heating to the frictional energy that developed between the slipper and rail. They found that the power developed by friction was directly proportional to the coefficient of friction, the bearing pressure, and sliding velocity. The rate of energy produced by friction, q_f , can be expressed as a function of time, as the product of the frictional force, F_f , and the horizontal sled velocity, v ,

$$\begin{aligned} q_f(t) &= F_f(t)v(t) \\ &= \mu(t)F(t)v(t) \end{aligned} \tag{3.25}$$

where the frictional force, F_f , is the product of the coefficient of friction, μ , and the normal load, F . It should be noted that each term on the right hand side of Equation 3.25 has already been calculated from the DADS data. The normal load, F , is the product of the DADS upper limit pressure, P_{ul} , and the slipper area, A_n , while $\mu(t)$ was determined based on this pressure and sliding velocity as a function of time from Montgomery's data.

Given this relationship and the DADS data, a one-dimensional heat transfer analysis was performed with the following assumptions. First, pressure as a function of time is derived from the DADS statistical analysis. By using this pressure, the statistical DADS pressure no longer can account for the bouncing of the slipper. It is assumed that the slipper remains in contact with the rail for the duration of the sliding event. Second, because the slipper maintains contact with the rail, the heat transfer is treated as a heat conduction event. In reality, during a slipper bouncing event at high velocity, the heat transfer analysis should consider convection effects as high pressure air flows through the slipper gap. In 1968, Korkegi and Briggs [44] formulated a model for this hypervelocity flow field between the slipper and rail. Third, because the thermal conductivities of the VascoMax 300 slipper and AISI 1080 steel rail material are very similar, we assume that 50% of the thermal energy generated by friction is transferred to the rail while the remaining 50% is transferred to the slipper.

With these assumptions in mind, the heat transfer to the slipper in terms of flux is given by

$$q''(t) = \frac{0.5 q_f(t)}{A_n} \quad (3.26)$$

where the 0.5 represents the partitioning of heat into the slipper. The flux will be used as a boundary condition for each time step in the heat transfer solution.

Table 3.15: VascoMax 300 Material Properties

Material Property	Value	Units
Density, ρ	8,000	kg/m ³
Thermal Conductivity, k	31	J/(m s K)
Specific Heat, c_p	420	J/(kg K)
Thermal Diffusivity, α	9.226×10^{-6}	m ² /s
Hardness, H	2.0×10^9	Pa

The variation in temperature, T , in the slipper is governed by Fourier's Law, or the heat conduction equation given by

$$\frac{\partial T}{\partial t} = \alpha \nabla^2 T \quad (3.27)$$

where the thermal diffusivity of the material, α , is related to the density, ρ , thermal conductivity, k , and specific heat, c_p , by

$$\alpha = \frac{k}{\rho c_p} \quad (3.28)$$

Although these material properties are temperature dependent, constant values at 700 K, as listed in Table 3.15 will be used to simplify the analysis. Laird used similar VascoMax 300 material properties in his dissertation research [48]. Detailed derivations of the heat conduction equation can be found in References [16; 39; 40]. Cameron's one-dimensional heat transfer analysis [24] is also implemented in the present study.

By assuming a one-dimensional unsteady heat analysis, Equation 3.27 reduces to

$$\frac{\partial T}{\partial t} = \alpha \left(\frac{\partial^2 T}{\partial y^2} \right) \quad (3.29)$$

where y is the positive direction into the slipper. The solution of Equation 3.29 yields the temperature through the thickness of the slipper as a function of time.

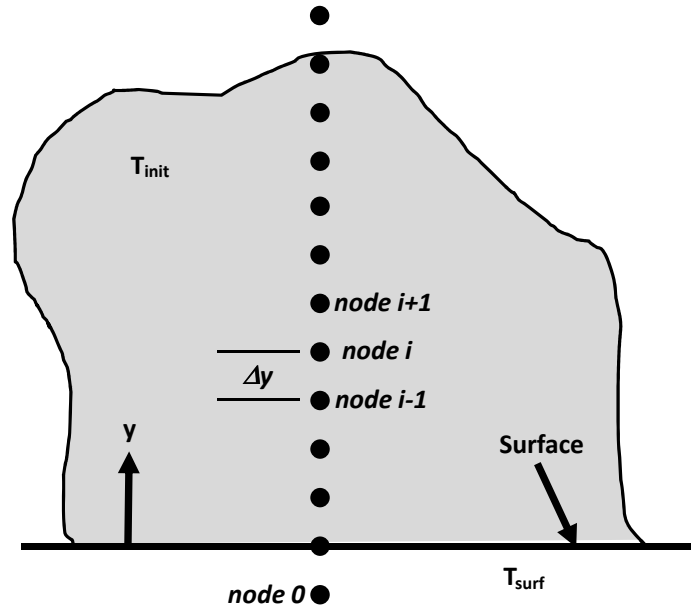


Figure 3.54: One-Dimensional Heat Transfer Analysis Schematic

A finite differencing method was used to solve this one-dimensional heat equation explicitly using a forward difference on time, and central difference in space by

$$T_i^{n+1} = T_i^n + \alpha \frac{\Delta t}{\Delta y^2} (T_{i+1}^n - 2T_i^n + T_{i-1}^n) \quad (3.30)$$

In this equation, the i subscript represents the spatial coordinate, or incremental depth into the slipper. The temporal coordinate, n superscript, refers to the previous time increment, while $n + 1$ refers to the current time step. This equation is solved explicitly for T_i^{n+1} , which is the temperature at the i^{th} location at the current time increment ($n + 1$), because all of the variables in the right hand side of Equation 3.30 are known at the previous time increment, n .

A schematic for the one-dimensional heat transfer analysis is shown in Figure 3.54. Each node through the slipper depth is separated by a constant spatial increment, Δy . The surface is defined as $y = 0$.

If a second-order approximation is used for the boundary condition, the flux condition at the surface, $y = 0$,

$$q''(t) = -k \frac{\partial T}{\partial y} \Big|_{y=0} \quad (3.31)$$

can be represented for each time increment as

$$T_0 = T_2 + \frac{2 \Delta y q''(t)}{k} \quad (3.32)$$

where T_0 is an imaginary point outside of the slipper boundary, as shown in Figure 3.54. This node is used in Equation 3.30 as the T_{i-1}^n variable to calculate the temperature at the surface boundary.

An undesirable feature of the explicit method is that it is conditionally stable. In a transient problem, nodal temperature solutions should continuously approach final, steady-state values as time increases. However, with the explicit method, numerically induced oscillations, which are physically impossible [39] may characterize the solution. The oscillations may cause the solution to become unstable and thus diverge from the final, steady-state solution. To prevent these erroneous results, the time increment, Δt , must be maintained below a certain limit, that depends on the spatial increment, Δy , and the material properties. This dependence is referred to as the stability criterion.

The coefficient on the second term of the right hand side of Equation 3.30 is known as the Fourier number, Fo , where

$$Fo = \alpha \frac{\Delta t}{\Delta y^2} \quad (3.33)$$

To maintain a stable solution, the size of the time increment, Δt , must be limited by the stability criterion. In regards to this stability criterion, Incropera and DeWitt state the criterion is

“determined by requiring that the coefficient associated with the node of interest at the previous time is greater than or equal to zero” [39].

For the one-dimensional case shown in Equation 3.30, the term for the “node of interest at the previous time” is T_i^n . Thus, the stability criterion for an internal, one-dimensional node is $(1 - 2Fo) \geq 0$, or $Fo \leq 0.5$. Upper limits on the time increment can then be determined by selecting the spatial increment and thermal diffusivity, α .

To solve the unsteady, one-dimensional heat equation, one additional boundary condition and one initial condition are required for a solution. The second boundary condition is that in the far-field, the slipper temperature was constant at the ambient temperature of 293 K. The initial condition was that the slipper temperature was also the constant ambient temperature through the slipper thickness.

As the slipper slides down the rail, frictional heating enters the slipper via the flux condition, which in turn, raises the temperature. The maximum surface temperature is limited by 1685 K, which is the melting temperature of VascoMax 300.

Using the initial and boundary condition, and the DADS pressure, slipper velocity, and coefficient of friction, the thermal profile of the slipper was solved for numerically in Matlab. The DADS time increment of 2×10^{-4} seconds was used in the analysis. This increment was selected because pressure, velocity, and coefficient of friction data were already available at this time increment. To maintain stability for this Δt and the thermal diffusivity listed in Table 3.15, the spatial interval was 65 μm .

Results of the one-dimensional, unsteady conduction heat transfer analysis are shown in Figure 3.55. These results are shown for the 8.14 second duration of the January 2008 test mission. Frictional heating, with units of Watts, is depicted in the top subplot. The heat flux, with units of watts per square meter is shown in the middle subplot. Because the heat flux, given by Equation 3.26, scales the frictional

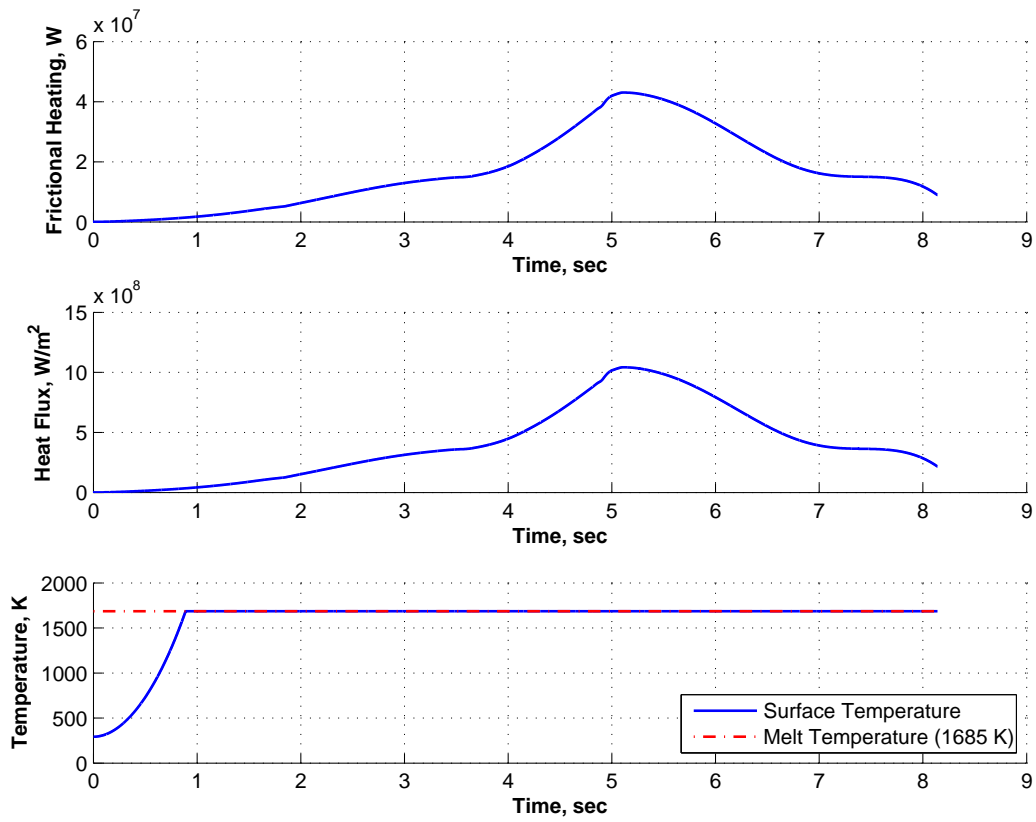


Figure 3.55: One-Dimensional Heat Transfer Results

heating curve by the 0.5 partitioning factor and the constant slipper area, this curve has a similar profile to the one shown above.

The surface temperature of the slipper is shown in the bottom subplot. The surface temperature, limited by the melt temperature of 1685 K, gradually increases from the 293 K ambient temperature. The surface of the slipper first reaches T_{melt} at 0.89 seconds after the start of the run. At this time, the velocity was 175 m/s and the slipper had traveled 80 meters. This 175 m/s “melt transition velocity” is key to the next phase of the heat transfer analysis. At velocities slower than 175 m/s, the surface temperature will be less than T_{melt} . Above this velocity, the surface temperature will be 1685 K.

For the 14.7 mm slipper thickness, the temperature profiles for the low target velocities (10, 20, 40, 100, and 200 m/s) are shown in Figure 3.56. In this plot, the frictional heating surface temperature, T_{frict} , is the value of the temperature profile where it intersects the abscissa. At these low target velocities, the frictional surface temperatures are 298, 311, 362, 733, and 1685 K, respectively. The melt transition velocity of 175 m/s is shown as the red dashed line. Temperature profiles for all twelve target velocities are shown in Figure 3.57. At velocities faster than 175 m/s, the temperature profiles show that the surface temperature is 1685 K. The surface temperature due to frictional heating will be added to the flash temperature to determine the melt wear rate.

3.8.2 Flash Temperature Rise. With the frictional heating temperature at the slipper interface known, the next step in the process of determining melt wear rate was to calculate the flash temperature. The slipper surface temperature, during an asperity collision, is determined by summing up the frictional heating and flash temperatures at a given velocity. Another unsteady, convection heat transfer analysis was accomplished to determine the melt depth during the asperity collision, and ultimately the melt wear rate.

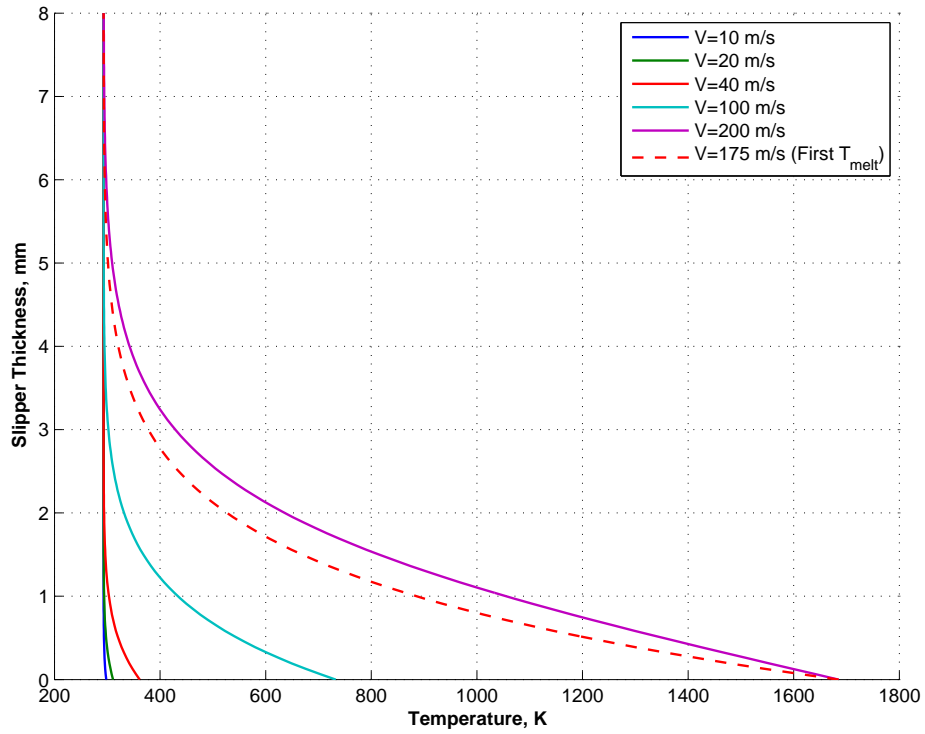


Figure 3.56: Slipper Frictional Heating Temperature Profile, Low Velocities

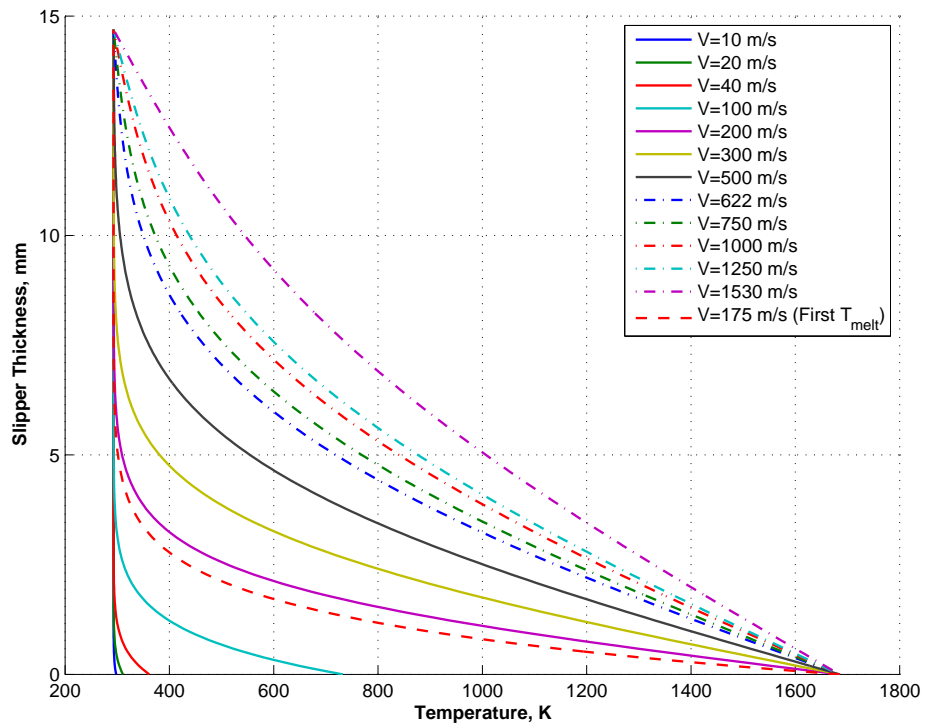


Figure 3.57: Slipper Frictional Heating Temperature Profile

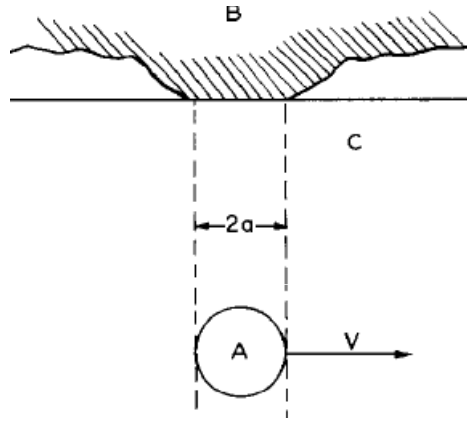


Figure 3.58: Single Contact Area Model [5]

In the late 1950s, Archard [5; 15] studied the temperature of rubbing surfaces. Nearly all of the energy dissipated by friction appears as heat and the temperature between the rubbing bodies is raised appreciably. The high temperatures of short duration, sometimes called flash temperatures, seem to be related to the “hot spots” observed by Bowden and Thomas [20]. Because direct measurement of the flash temperature is difficult, Archard developed a simple theory for determining the flash temperature that focused on the relevant physical considerations. Temperatures were calculated on the assumption that heat was generated at the area of true contact and that this heat was conducted away into the bulk of the rubbing members.

Archard’s model is shown in Figure 3.58 where an asperity on the surface of Body B forms a circular area of contact ($A = \pi a^2$) when sliding at velocity V over a flat, stationary Surface C. In their respective reference frames, Body B receives heat from a stationary heat source while Body C receives heat from a moving heat source. The maximum flash temperature occurs when the maximum possible load is applied at the smallest possible area.

Archard developed flash temperature models based on the type of deformation (elastic or plastic) and the sliding velocity (low or high). The Péclet number, Pe , a dimensionless heat transfer grouping, is also used to describe the range of sliding speeds. This number, which relates the thermal energy transported by the movement of the medium, to the thermal energy conducted away from the region where frictional

energy is being dissipated [32]. The Péclet number is given by

$$Pe = \frac{\rho c_p V L_c}{k} = \frac{V L_c}{\alpha} \quad (3.34)$$

where L_c is a characteristic length, and α is the thermal diffusivity. Based on the metallographic investigation in Chapter II, plastic deformation was noted on the sliding surface of the slipper. While Archard provided models for elastic deformation at high and low Pe numbers, only the flash temperature model for plastic deformation will be used to determine the melt wear rate.

The flash temperature increase, ΔT_{flash} , for plastic deformation at low speed ($Pe < 0.2$) is

$$\Delta T_{flash} = \mu \frac{\sqrt{\pi H}}{8k} W^{0.5} V \quad (3.35)$$

and for plastic deformation at high speeds ($Pe > 200$) is

$$\Delta T_{flash} = \frac{\mu(\pi H)^{0.75} W^{0.25}}{3.25} \sqrt{\frac{V}{k\rho c}} \quad (3.36)$$

where μ is the coefficient of friction, H is the material hardness, W is the normal load, and V is the sliding velocity. Values of k , ρ , c_p , and H are previously listed in Table 3.15.

With flash temperature models for plastic deformation at high and low Pe numbers, it is necessary to determine which model should be used for the slipper/rail interaction at the test track. Using the 6 μm asperity radius for the characteristic length, L_c , and the thermal diffusivity of $9.226 \times 10^{-6} \text{ m}^2/\text{s}$, at the maximum velocity of 1,530 m/s, the Péclet number is 995. In the January 2008 test mission, the velocity at which $Pe > 200$ was 307 m/s which corresponded to a sliding distance of 230 meters, or 4% of the overall sliding distance. Thus, with respect to Pe , the slipper was at high velocity for 96% of the total sliding distance.

Table 3.16: Melt Wear Rate Heat Transfer Analysis Summary

Velocity (m/s)	Collision Time (s)	$T_{y=400\mu m}$ (K)	T_{frict} (K)	ΔT_{flash} (K)	T_{surf} (K)	Melt Depth h_{melt} (μm)
10	3.30×10^{-7}	294.1	298.1	362.1	660.2	0
20	1.65×10^{-7}	299.6	311.0	449.7	760.7	0
40	8.50×10^{-8}	327.1	361.6	566.2	927.8	0
100	3.30×10^{-8}	580.0	732.8	653.6	1,386.4	0
200	1.65×10^{-8}	1,424.0	1,685.0	500.5	2,185.5	0.523
300	1.10×10^{-8}	1,521.4	1,685.0	202.0	1,887.0	0.342
500	6.50×10^{-9}	1,570.8	1,685.0	182.3	1,867.3	0.301
622	5.50×10^{-9}	1,628.5	1,685.0	186.3	1,871.3	0.380
750	4.40×10^{-9}	1,596.4	1,685.0	240.7	1,925.7	0.315
1,000	3.30×10^{-9}	1,602.7	1,685.0	251.8	1,936.8	0.286
1,250	2.65×10^{-9}	1,615.1	1,685.0	284.1	1,969.1	0.285
1,530	2.15×10^{-9}	1,611.1	1,685.0	331.2	2,016.2	0.266

Because the majority of the test mission occurred at higher velocities, which consequently gave $Pe > 200$, only the plastic deformation model was used to calculate the flash temperature increase, ΔT_{flash} , at the twelve target velocities. In Equation 3.36, the product of the maximum contact pressure from the global bounce model and the asperity area ($A_{asp} = \pi(6\mu m)^2$) was used in place of the load term, W . During an asperity collision, the surface temperature increases above the frictional heating temperature such that

$$T_{surf} = T_{frict} + \Delta T_{flash} \quad (3.37)$$

The resulting frictional heating, flash temperature increase and surface temperatures for a given velocity are listed in Table 3.16.

Previously, the mechanical wear rate per unit width, W_{uw} , was determined by dividing the damage area during an asperity collision by the corresponding sliding distance. In the same fashion, a melt wear rate per unit width, $W_{uw,melt}$, was calculated by determining the ratio of the melt area, A_{melt} , to the sliding distance by

$$W_{uw,melt} = \frac{A_{melt}}{d} = \frac{h_{melt}d}{d} = h_{melt} \quad (3.38)$$

The melt area was assumed to resemble a rectangle where one side has the length of the sliding distance, and the other side has length equal to the melt depth, h_{melt} . With this definition, the distance terms, d , in Equation 3.38 cancel so that the melt wear rate per unit width, $W_{uw,melt}$, is the same as the melt depth. The units will be in millimeters, and can be easily converted to units of mm^2/mm , so that they are similar to the units of the mechanical wear rate per unit width.

The next step in the process of determining melt wear rate was calculating this melt depth into the slipper. An unsteady, conduction heat transfer analysis for a semi-infinite solid was used for this analysis. A semi-infinite solid is characterized by a single identifiable surface. If conditions at this surface are suddenly changed, then transient, one-dimensional conduction will occur within the solid [39; 40].

The heat equation for transient conduction in a semi-infinite solid is also governed by the Equation 3.29. An analytical solution is available for this type of heat transfer analysis based on a constant surface temperature. The one-dimensional heat transfer analysis schematic shown in Figure 3.54 is also applicable to the scenario. For any time, $t > 0$, the temperature within the semi-infinite body at any location, y , is given by

$$T(y, t) = T_{surf} + (T_{init} - T_{surf}) \operatorname{erf} \left(\frac{y}{2\sqrt{\alpha t}} \right) \quad (3.39)$$

where the Gaussian error function is defined as

$$\operatorname{erf}(w) \equiv \frac{2}{\sqrt{\pi}} \int_0^w e^{-v^2} dv \quad (3.40)$$

The initial condition for Equation 3.39 is prescribed by $T(y, 0) = T_{init}$. Several possible initial temperatures, T_{init} , were evaluated during this analysis. First, an initial temperature of 293 K was assumed for the slipper. However, this temperature was discarded as it didn't take into account the temperature profile in the slipper that developed during frictional heating. Instead, the temperature of the slipper at a depth

of 400 μm was extracted from these frictional heating temperature profiles. Temperatures at this depth were selected because they are tied to the depth of the heat-affected zone noted in the metallographic analysis of the slipper. The temperature at a depth of 400 μm , $T_{y=400\mu\text{m}}$, also listed in Table 3.16 for a given target velocity, was used as the initial temperature within the slipper semi-infinite solid body. At the surface, where $y = 0$, the boundary condition was given by $T(0, t) = T_{surf}$, which was given by Equation 3.37.

Several assumptions were made to justify the use of a constant surface temperature and semi-infinite solid transient conduction analysis. First, from the Knoop hardness testing, it was determined that the heat-affected zone depth was approximately 400 μm from the slipper wear surface. This depth is much smaller than the initial slipper thickness of 14.7 mm. Second, the asperity collision times are extremely short duration. The times listed in Table 3.16 are the same times used in the local submodel analysis for the 6 μm asperity collision.

For each target velocity, and the associated initial and surface temperatures, the closed-form solution given by Equation 3.39 was evaluated for the asperity collision time, t . Resulting temperature profiles for the first five velocities (10, 20, 40, 100, and 200 m/s) are shown in Figure 3.59. It is easier to point out the key features of this figure by presenting a limited number of temperature profiles. In this figure, the abscissa represents the depth into the slipper, and the ordinate shows the temperature. The temperature for each of these five cases decreased from the surface temperature with increasing depth into the slipper. The VascoMax 300 melt temperature of 1685 K is depicted by the dashed red line. The surface temperature at each velocity is also listed in the figure legend.

Melt depth, h_{melt} , was defined as the depth into the slipper where the temperature within the slipper reached the melt temperature of 1685 K. For 10, 20, 40 and 100 m/s, the initial surface temperature was less than 1685 K, and due to the decreasing nature of the temperature profile, the melt temperature was not reached

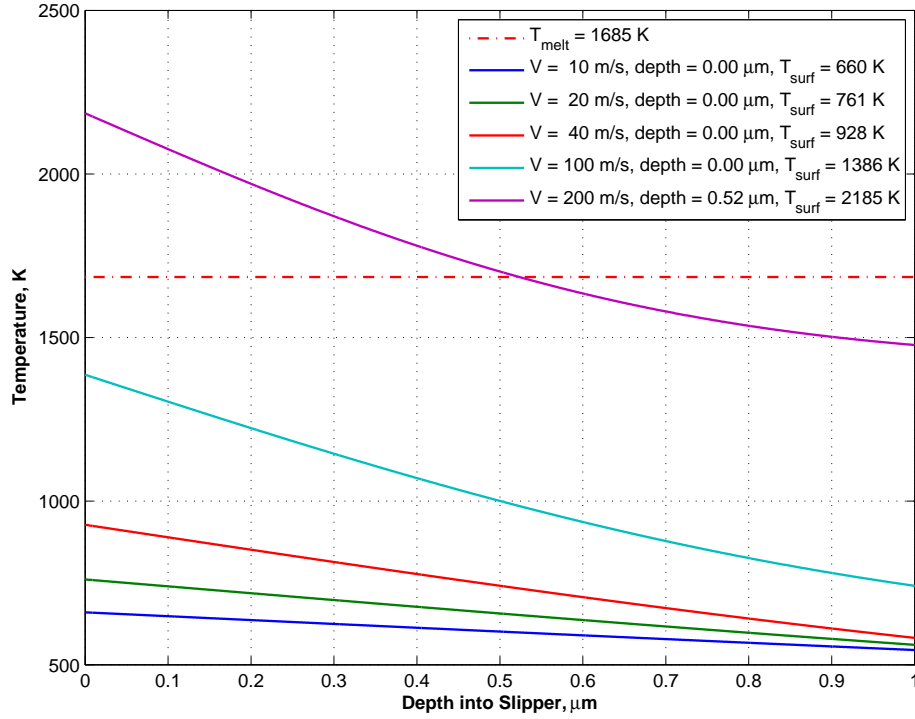


Figure 3.59: Melt Depth Temperature Profile, Low Velocities

for these velocities. Thus, their melt depth is zero, which indicates that no melt wear occurred at these low velocities. At 200 m/s, the slipper temperature reached 1685 K at a melt depth of 0.524 μm . The temperature profiles for the remaining higher target velocities are presented in Figure 3.60.

As was shown previously, the melt depth was also equal to the melt wear rate per unit width, $W_{uw,melt}$. Melt depth distances for each of the target velocities is also presented in Table 3.16. During the mechanical wear rate analysis, the single asperity wear rate, W_{sa} , was calculated as the product of the mechanical wear rate per unit width, W_{uw} and the effective width, w_{eff} . In the same manner, the single asperity melt wear rate, $W_{sa,melt}$ is the product of the melt wear rate per unit width, $W_{uw,melt}$, and this same effective width, w_{eff} . The effective width of 8.29 μm was used for both the mechanical and melt wear rate calculations because both analyses were based on the common 6 μm asperity and slipper collision, for the same time durations.

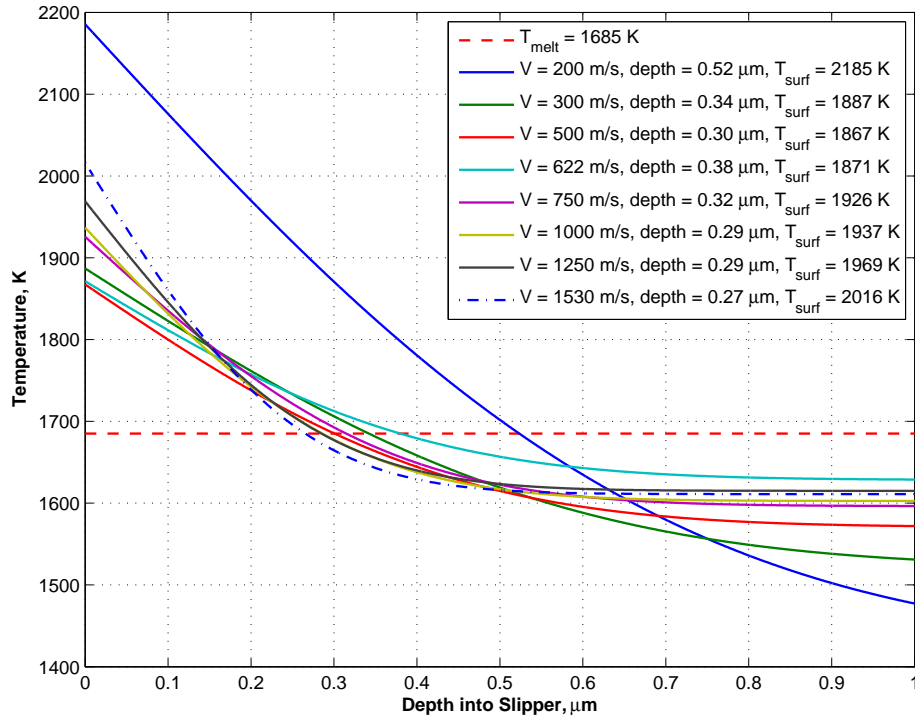


Figure 3.60: Melt Depth Temperature Profile, High Velocities

3.9 Numerical Modeling Summary

Each component of the numerical model for determining mechanical and melt wear rates has been discussed in this chapter. The metallographic analysis of the January 2008 test slipper helped to guide the formulation of the numerical model. Due to the extremely dynamic nature of a slipper sliding down the test track, DADS data, as provided by HHSTT, formed a basis for determining the contact forces, pressures, and velocities for the particular test mission. To account for the frictional relationship between the VascoMax 300 slipper and AISI 1080 rail, Montgomery’s data was incorporated to determine the coefficient of friction based on the pressure velocity.

Using the commercially available, finite element analysis software ABAQUS, global and local submodels were created. A global analysis, which modeled the entire slipper top sliding on a rigid rail surface, was performed to determine the state of stress in the slipper at a given point in time and corresponding distance and velocity

during the test mission. Also, the global model was analyzed to see if dynamics of the global slipper could be captured in the global model. Noting from the metallographic analysis that plastic deformation occurred on the slipper surface at the micron level, a local submodel analysis was created that incorporated a deformable slipper segment and a deformable rail, that included a hemispherical asperity on the rail surface. At various target velocities, the damage area was determined as the area where the maximum Mises stress was exceeded. A strain rate analysis was performed to determine the appropriate Mises stress threshold value. To incorporate viscoplasticity into the model, the Johnson-Cook constitutive model was implemented in the local submodel analyses. Mechanical wear rates per unit width, and the effective width of the $6\ \mu\text{m}$ asperity were determined. The product of these two values lead to the single asperity mechanical wear rate.

In a similar manner, the single asperity melt wear rate was determined based on the calculation of the temperature profile due to frictional heating as the slipper slides on the rail, and the flash temperature rise brought about by the asperity collision. The applied pressure on the slipper from the DADS statistical data was used along with the coefficient of friction to determine the temperature profile of the slipper. For the duration of the slipper/asperity collision, the contact pressure from the global quasi-steady analysis, along with the surface temperature, which was the sum of the frictional heating temperature at the slipper surface and the flash temperature increase, was used to determine the melt wear depth. Ultimately, the melt wear rate for the single asperity was determined by using the same effective width as was used in the mechanical wear rate analysis. Results of the mechanical and melt wear rate analysis are presented next in Chapter IV.

Several key features were noted during the global and local slipper analysis. First, mapping the state of stress in the global slipper to the local submodel had a negligible effect on the mechanical wear rate calculation. The stress that results during the asperity collision is much larger than the initial stress condition transferred from the global model, and therefore, dominates the analysis. Thus, historical state of

stress in the slipper did not effect the wear rate. Secondly, a study that compared acceleration, deceleration and constant velocity conditions in the local submodel showed that a constant velocity could be used for subsequent analyses. Although the actual slipper undergoes accelerations and decelerations during the course of the sled run, there was a negligible effect of a change in velocity over the short time duration of the slipper/asperity collision on the mechanical wear rates.

IV. Results and Discussion

The wear rate results of the numerical model are presented in this chapter. Necessary features of the numerical model were first identified during the metallographic analysis of a VascoMax 300 slipper in Chapter II. Based on this investigation, several global finite element models were created that represented the full size slipper sliding on the rail. The desire was to obtain the state of stress within the global slipper and the pressure distribution along the bottom of the slipper. A local submodel was also developed that modeled the impact of the slipper sliding into a hemispherical asperity on the rail. The feature of the numerics for the finite element model have been developed in Chapter III and are incorporated in this chapter.

From analysis of these finite element models, single asperity wear rates were developed. This chapter presents the mechanical and melt wear rates. A discussion is also included regarding the wave that develops during the slipper and rail asperity impact. Pressure is traced both spatially along a path radiating into the slipper from the location of the rail/asperity impact, and temporally at various nodes along this path.

A relationship for the Archard wear coefficient, k_A , is developed and the cumulative wear volume due to both mechanical and melt wear is calculated for comparison with the total wear volume of the experimental slipper.

4.1 Single Asperity Wear Rate Results

The technique for determining both the mechanical wear rate per unit width, W_{uw} , and the melt wear per unit width, $W_{uw,melt}$, was outlined in Chapter III. Both wear rates are based on the local submodel analysis of the slipper and 6 μm asperity collision. To extend the plane strain wear rate model results into three dimensions, a global discontinuity and an effective width, w_{eff} , were determined by evaluating additional collisions between the slipper and 4 and 2 μm radii asperities.

At each target velocity, the mechanical single asperity wear, W_{sa} , is the product of the mechanical wear rate per unit width, W_{uw} , and the effective width, w_{eff} . The

Table 4.1: Single Asperity Mechanical and Melt Wear Rates

Target Velocity (m/s)	Target Time (sec)	Target Distance (m)	Mechanical, W_{sa} (mm ³ /mm)	Melt, $W_{sa,melt}$ (mm ³ /mm)
10	0.055	1.94	2.63×10^{-5}	0
20	0.100	2.63	3.44×10^{-5}	0
40	0.195	5.49	3.79×10^{-5}	0
100	0.501	26.98	4.88×10^{-5}	0
200	1.017	104.30	8.42×10^{-5}	4.32×10^{-6}
300	1.521	230.08	1.20×10^{-4}	2.80×10^{-6}
500	2.451	593.38	2.00×10^{-4}	2.45×10^{-6}
622	8.140	5,815.50	2.13×10^{-4}	3.09×10^{-6}
750	3.661	1,359.34	1.93×10^{-4}	2.58×10^{-6}
1,000	4.150	1,779.43	1.87×10^{-4}	2.37×10^{-6}
1,250	5.515	3,575.81	1.67×10^{-4}	2.19×10^{-6}
1,530	4.998	2,850.29	1.37×10^{-4}	2.37×10^{-6}

effective width was determined to be $8.29 \mu\text{m}$. Because the melt wear rate analysis also considered a $6 \mu\text{m}$ asperity collision, and utilized the same asperity collision time interval, this same effective width was also used to determine the single asperity melt wear rate, $W_{sa,melt}$. In a manner similar to the mechanical wear rate, the single asperity melt wear rate is the product of the melt wear per unit width, $W_{uw,melt}$ and the effective width, w_{eff} .

A summary of the single asperity mechanical and melt wear rates is given in Table 4.1 for each target velocity. As with Table 3.2, the elapsed time and sliding distance at each target velocity are also listed in this wear rate table. For the duration of this dissertation, the single asperity wear rate will simply be referred to as the “wear rate” and it should now be understood that the units are in terms of wear volume per unit sliding distance.

The mechanical wear rates are also presented in Figure 4.1. The top subplot shows this wear rate as a function of time, while the middle subplot shows the mechanical wear rate as a function of distance. The two subplots at the bottom show the wear rates as a function of velocity. The acceleration phase, where the Stage 3 test sled accelerated from rest to 1,530 m/s, is represented in the left velocity sub-

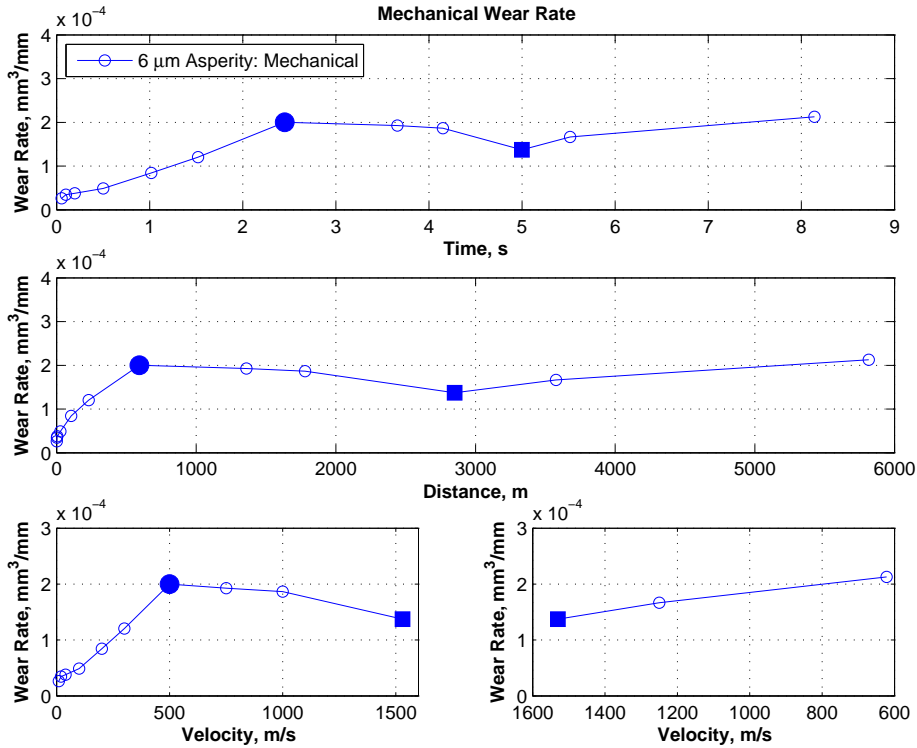


Figure 4.1: Mechanical Wear Rates

plot. Similarly, the deceleration phase, during which the sled slowed from 1,530 m/s to 622 m/s is depicted in the right velocity subplot. Note that the abscissa on the right velocity subplot has been reversed to reflect the range of velocities during the deceleration phase.

Wear rates for two specific target velocities are also indicated by the large circle and square data point markers. The mechanical wear rate for 500 m/s is represented by the large circle. The intent of highlighting the 500 m/s wear rate is to show the relationship on the time, distance, and velocity axes. From Table 4.1, when the Stage 3 pusher sled reached 500 m/s, the elapsed time was 2.451 sec and the sliding distance was 593.38 m. Thus, the 500 m/s mechanical wear rate of 2.00×10^{-4} mm³/mm is plotted versus these target time, velocity, and distances in the three subplots.

The large square marker represents the mechanical wear rate at 1,530 m/s. At this velocity, the sled had traveled 2,850.29 meters in approximately 5 seconds. At

the bottom, the 1,530 m/s data marker is plotted in both velocity subplots as the last point in the acceleration phase and the first point in the deceleration phase.

Several characteristics of the mechanical wear rate can be noted from Figure 4.1. First, from 10–500 m/s, the wear rate increased in a nearly linear fashion from 2.63×10^{-5} to 2.00×10^{-4} mm³/mm. For the duration of the test run, the mechanical wear rate remained almost constant at 2.00×10^{-4} mm³/mm. Despite this variation in applied pressure, the mechanical wear rate from 500 m/s until the end of the test run remained constant. It should be pointed out that the mechanical wear rate was found to be independent of the contribution of the global model. The 500 m/s sliding distance of 593.38 m, is 10.2% of the overall sliding distance of 5,816 m. Thus, the constant mechanical wear rate of 2.00×10^{-4} mm³/mm may be considered applicable for approximately 90% of the total sliding distance.

The melt wear rates are also presented as a function of time, distance, and velocity in Figure 4.2. In a similar manner, melt wear rates for the 500 and 1,530 m/s velocity cases are indicated with the large circle and square data markers, respectively. From Table 3.2, which summarized the DADS statistical data, the applied pressure ranged from 1.113 MPa at 300 m/s to a maximum of 4.727 MPa at 1,250 m/s. As with the mechanical wear rates, the melt wear rates remained fairly constant at an average value of 2.5×10^{-6} mm³/mm for velocities greater than 300 m/s. For velocities below 200 m/s, the melt wear rates were zero because the corresponding melt depths were zero.

At a given target velocity, the melt wear rates are much smaller in magnitude as compared to the corresponding mechanical wear rate. The comparison is shown in Figure 4.3 which plots both the mechanical and melt wear rates as functions of time, distance, and velocity. The mechanical and melt wear rates will be used subsequently to determine the total wear given by the model for comparison with the experimental test slipper that was evaluated in Chapter II.

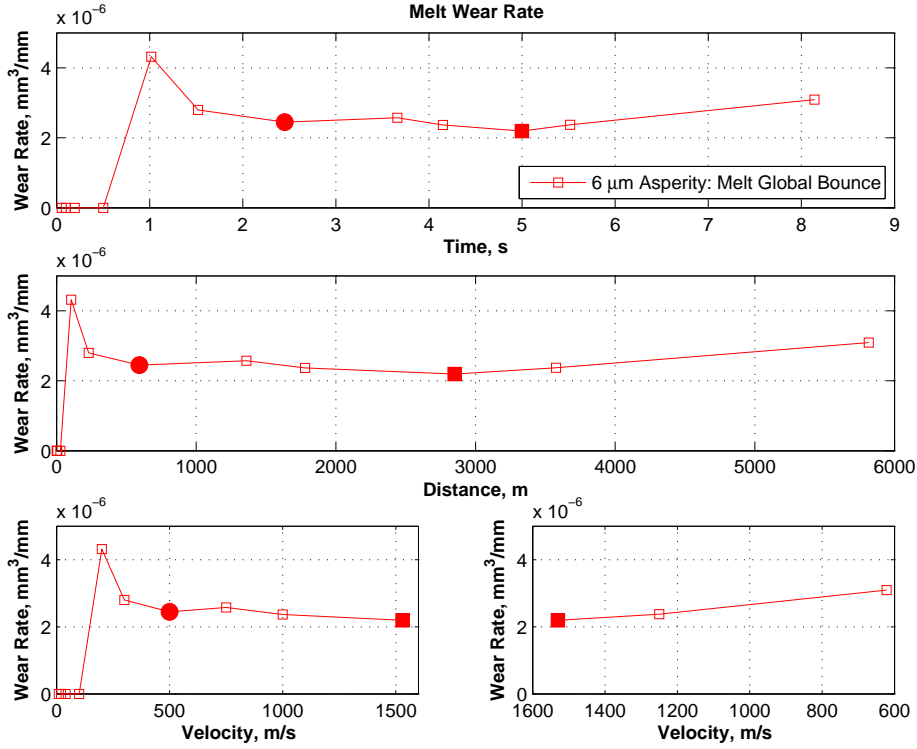


Figure 4.2: Melt Wear Rates

4.2 Slipper/Asperity Impact Wave Analysis

In the local submodel analysis, a pressure impact wave was created when the slipper collided with the asperity. During the short time duration of the submodel analysis, this wave propagated through both the VascoMax 300 slipper and AISI 1080 steel rail materials. The propagation of this wave is shown in Figure 4.4 which depicts the pressure at five different times during the 1,530 m/s collision with a 6 μm asperity. Each image is taken at the time interval of 4.30×10^{-10} seconds, or 20% of the submodel collision time, starting with Figure 4.4(a). Figure 4.4(e) represents the final time of the analysis. The pressure along the specified path is presented in Figure 4.4(f) and will be discussed subsequently in Section 4.2.3.

The pressure wave is analyzed at velocities of 20, 500, and 1,530 m/s as it propagates through the VascoMax 300 slipper material. These velocities were selected

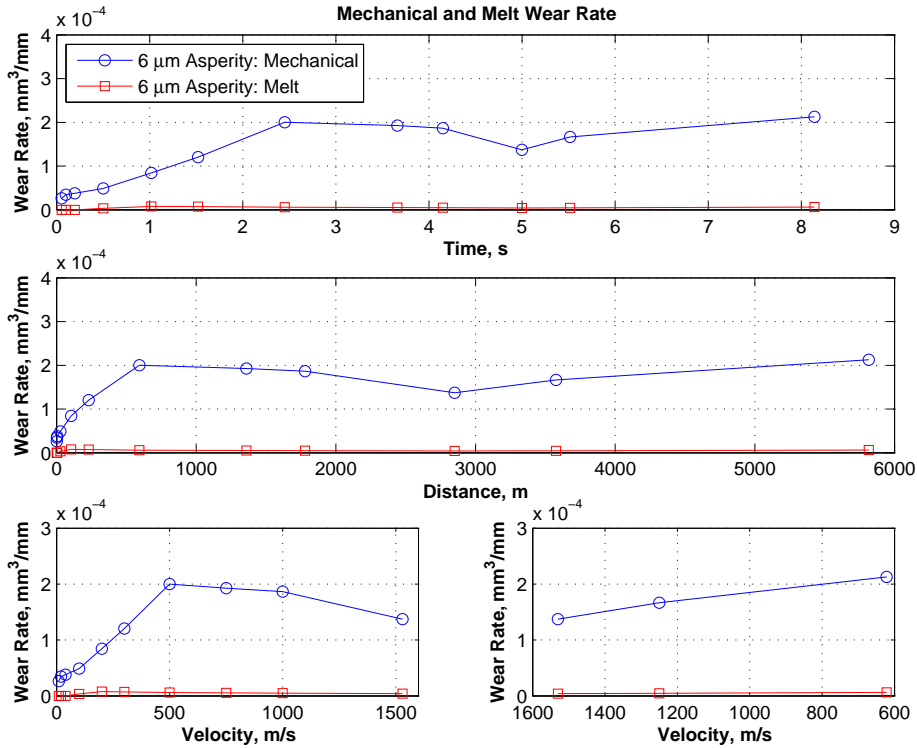


Figure 4.3: Comparison of Mechanical and Melt Wear Rates

because they are representative of low, medium, and high sliding velocities experienced by the slipper during the test mission.

As with the mesh convergence study in Chapter III, a path was created from one of the nodes along the surface of the 2 μm radius fillet at the front edge of the slipper submodel to another node within the interior of the slipper. The nodes that defined the endpoints along with four other nodes, that were in close proximity to this path, were also selected for this analysis. The nodes are labeled in Figure 4.5 as “Node A” through “Node F”.

In the subsequent plots of pressure along the path, the abscissa is normalized over the length of the path, which was 33.6 μm. Table 4.2 shows the actual and normalized distance along the path for these nodes. For each of the three velocity cases, the pressure at each node will be plotted as a function of time as the impact wave propagates through the slipper material.

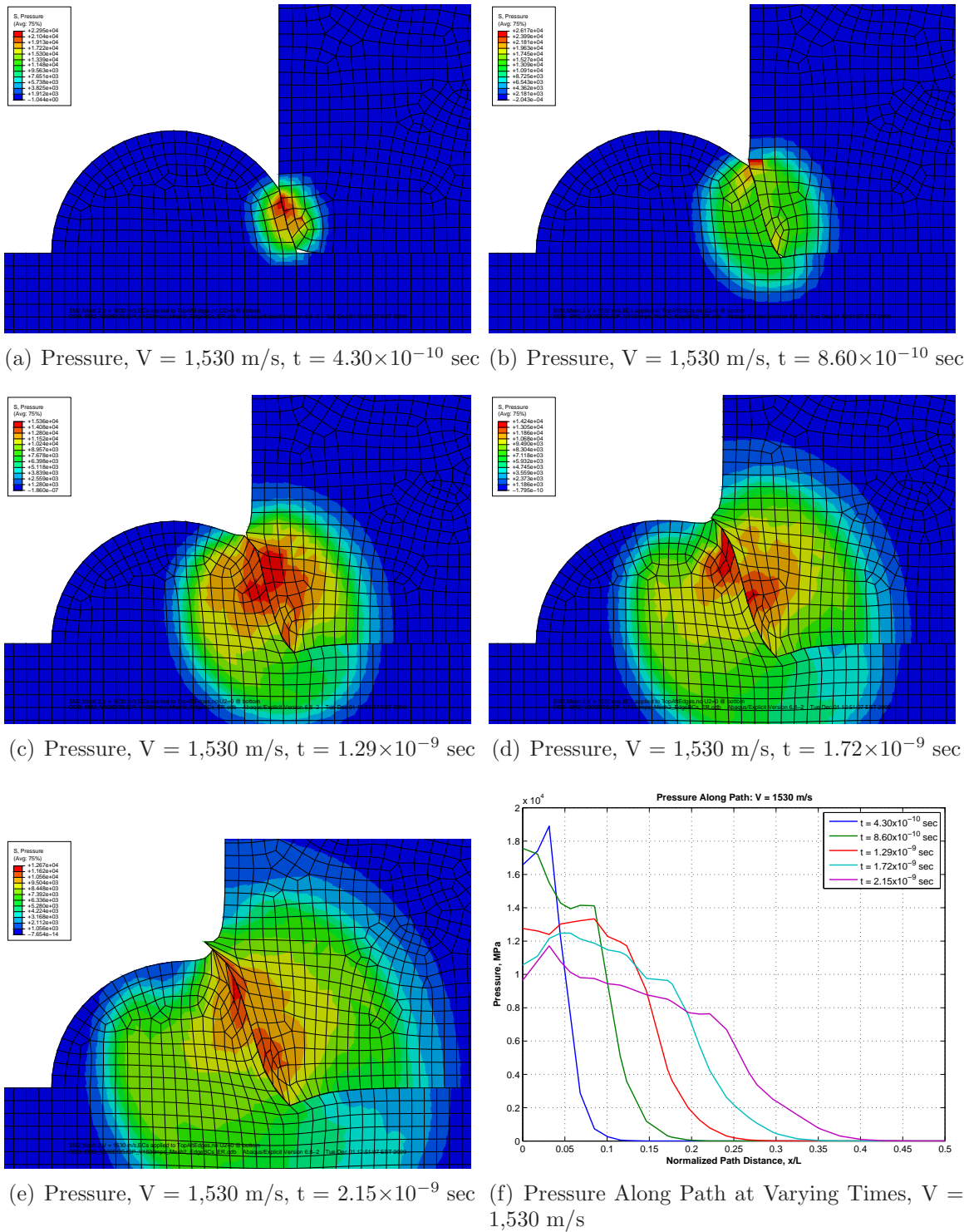


Figure 4.4: Slipper/Asperity Impact Wave Propagation, $V = 1,530 \text{ m/s}$

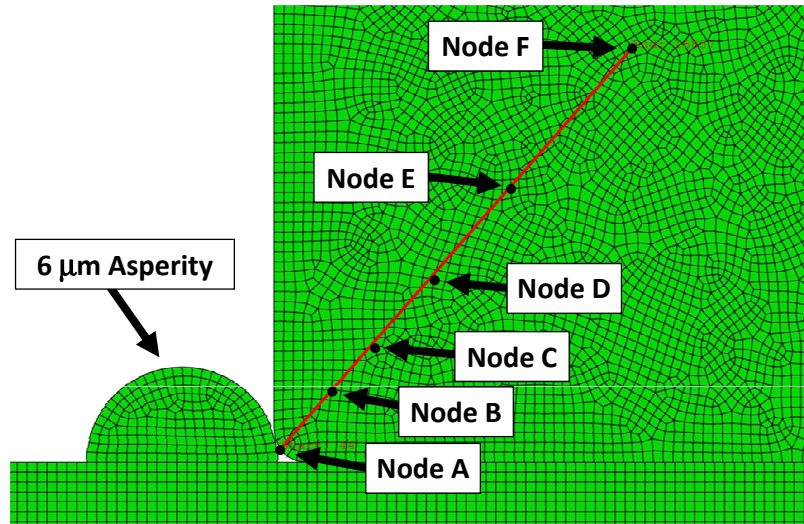


Figure 4.5: Impact Wave Analysis Path and Nodes

Table 4.2: Wave Propagation Nodes Along Path Length

Node Label	Distance Along Path (μm)	Normalized Distance Along Path (%)
Node A	0.00	0.00
Node B	4.40	13.1
Node C	8.80	26.0
Node D	14.4	42.9
Node E	21.9	65.2
Node F	33.6	1.00

The path was selected such that it moved along with the slipper in a Lagrangian reference frame fashion. By keeping the path fixed to the slipper, pressure variations could be compared for the same locations in the slipper during the asperity collision event. Also, the orientation of this path was chosen in the direction of the radially increasing wave propagation direction.

4.2.1 Velocity Case: 20 m/s. The pressure along the path at five different times is shown in Figure 4.6. These times are separated at 3.30×10^{-8} second time intervals over the 1.65×10^{-7} seconds slipper/asperity collision event. In each case, the initially high pressure quickly dissipates when moving along increasing normalized path distance. By definition of how the path was established, higher pressures were expected to be observed near the front of the path, at low normalized path distance. At distances further away from the location of the asperity collision, the pressure was lower because the impact wave had not yet reached the far end of the path at the given time increment. Between the first and second interval, the maximum pressure increased by 51% from 1,970 MPa to 2,980 MPa. At the three subsequent times, the maximum pressure decreases to approximately 2,700 MPa. A shock wave did not develop at 20 m/s. As generally observed in References [79] and [70], the shock wave maintains the initial pressure pulse for the duration of the impact event analysis.

The pressure at Nodes A–F as a function of time during the 20 m/s slipper/asperity collision is depicted in Figure 4.7. Because Node A was at the slipper surface, the pressure was expected to be significantly higher at Nodes B–F. The maximum pressure for Node A was 3,156 MPa and occurred at 6.93×10^{-8} seconds into the analysis, at which time the pressure at this node began to dissipate. By comparison, the highest pressure at Node B was 1,500 MPa and occurred at the final time of 1.65×10^{-7} seconds. For Nodes B–F, the pressure gradually increased during this analysis and never decreased in magnitude.

4.2.2 Velocity Case: 500 m/s. The pressure along the path for the 500 m/s case is shown in Figure 4.8. These times are separated by a 1.30×10^{-9} second

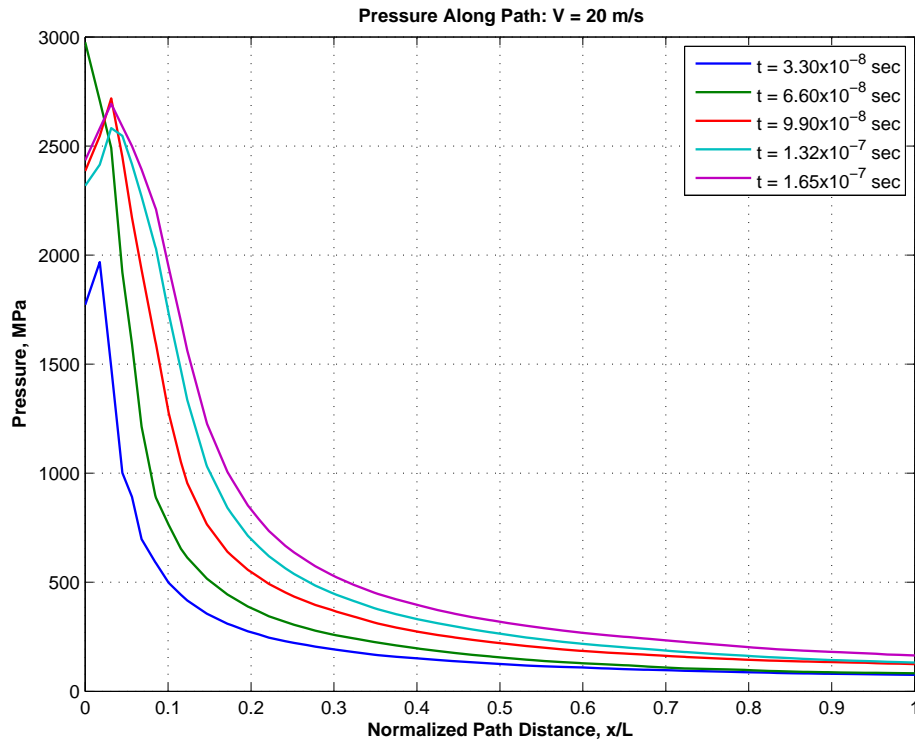


Figure 4.6: Pressure Along Path with Varying Time, V = 20 m/s

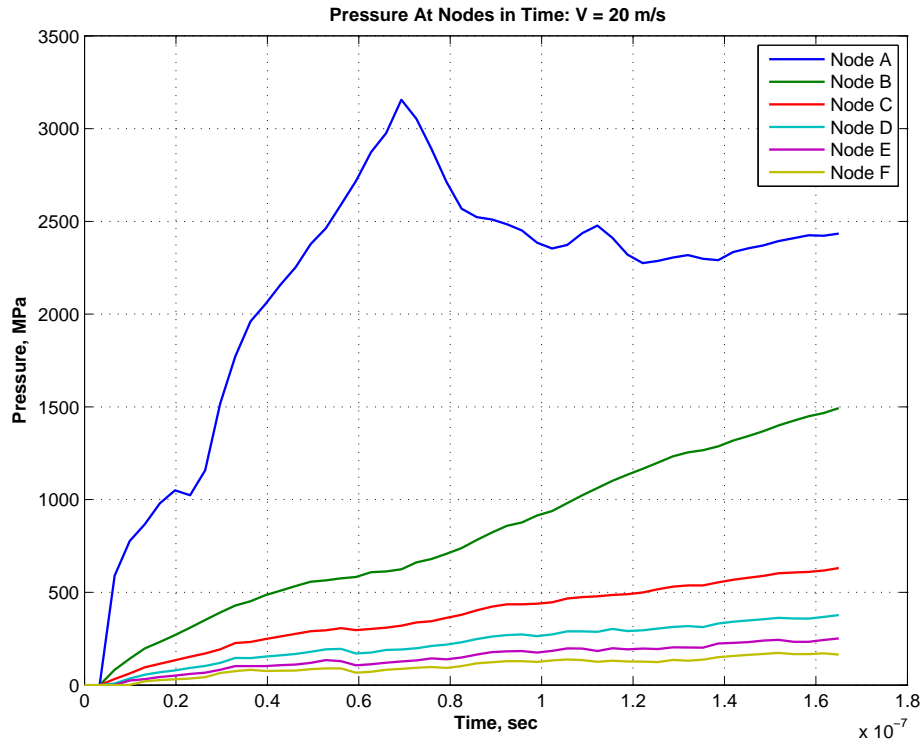


Figure 4.7: Pressure at Nodes in Time, V = 20 m/s

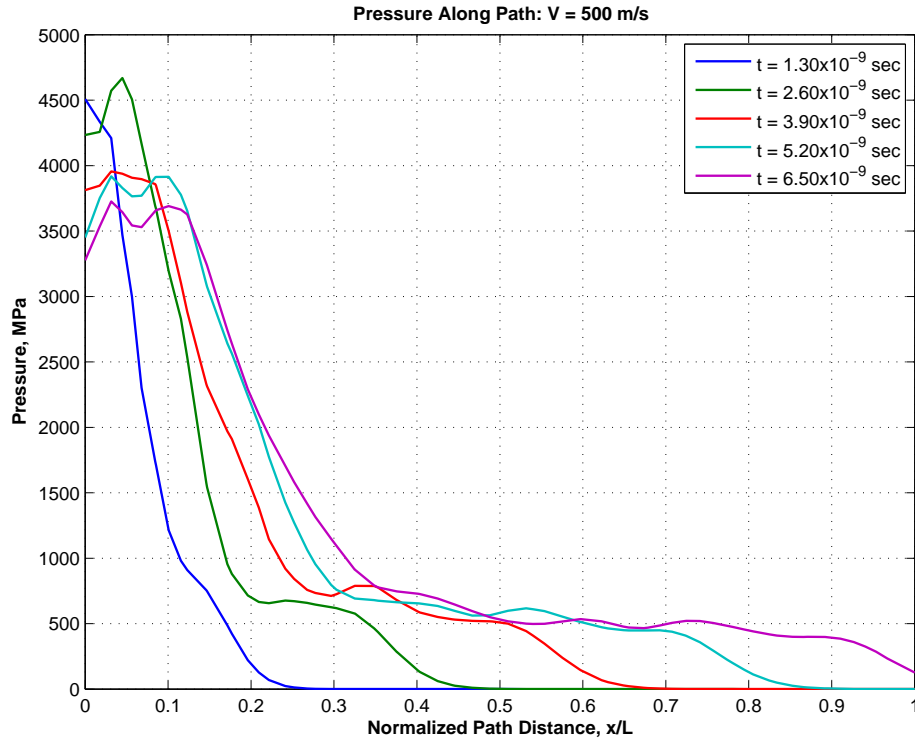


Figure 4.8: Pressure Along Path with Varying Time, $V = 500 \text{ m/s}$

time interval over the 6.50×10^{-9} second collision event. As with the 20 m/s case, the maximum pressure increased from the first to the second interval. With increasing time, the pressure continued to decrease. At 5.20 and 6.5×10^{-9} seconds, the pressure at the beginning of the path which corresponds to Node A is approximately 12% lower than the maximum pressure for each of these intervals. As with the 20 m/s case, a shock wave did not develop at 500 m/s either.

The pressure at Nodes A–F as a function of time during the 500 m/s collision event are shown in Figure 4.9. As was expected, Node A experienced the highest pressure of the six nodes being analyzed. For Node A, the maximum pressure was 5,706 MPa. Nodes B–F also showed the gradual increase in pressure with increasing time. For Node F, the pressure was almost zero for the first 90% of the total time interval.

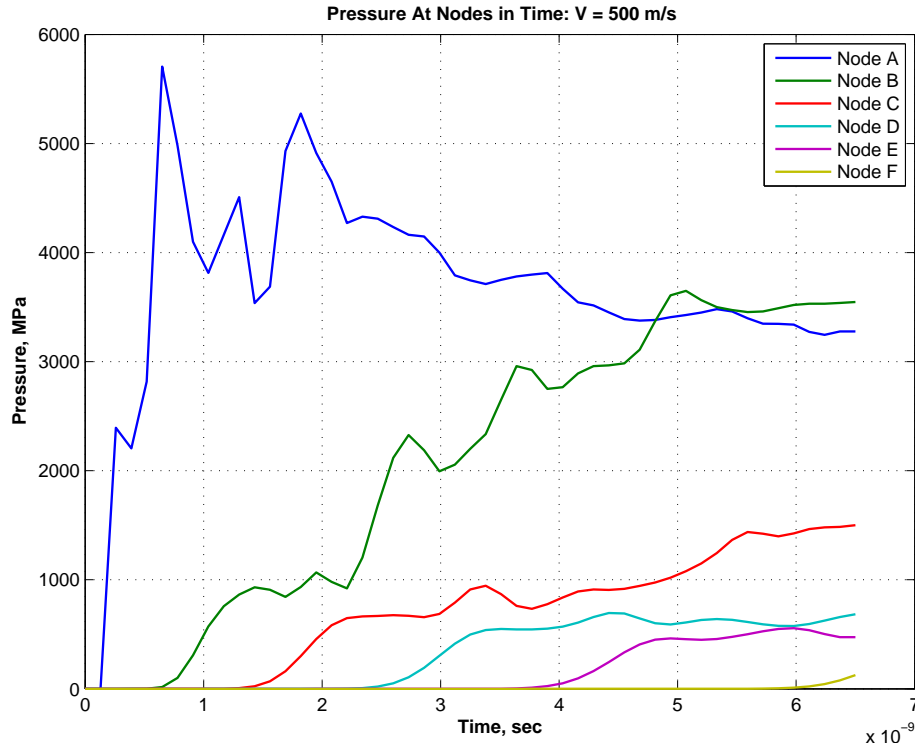


Figure 4.9: Pressure at Nodes in Time, $V = 500$ m/s

4.2.3 *Velocity Case: 1,530 m/s.* The propagation of the pressure wave at 1,530 m/s was shown previously in Figures 4.4(a)–4.4(e) which depict the resulting wave at five different time intervals. The pressure along the path for the high velocity 1,530 m/s case, which was also the highest kinetic energy case for the Stage 3 slipper, is shown in Figure 4.10. For a given constant slipper mass, the maximum kinetic energy occurs at the maximum velocity. It was anticipated that a shock wave in the slipper would develop at this maximum velocity. However, no shock wave developed during the asperity collision event. The times in this analysis are at 4.30×10^{-10} second intervals over the 2.15×10^{-9} second collision event. The range of normalized path distance in the abscissa on this plot has been limited to 0–0.5 because the pressure was zero at all times further along the path. As the analysis time shortened due to higher sliding velocity, the wave that resulted due to the slipper/asperity collision didn't propagate as far as it did at lower velocities.

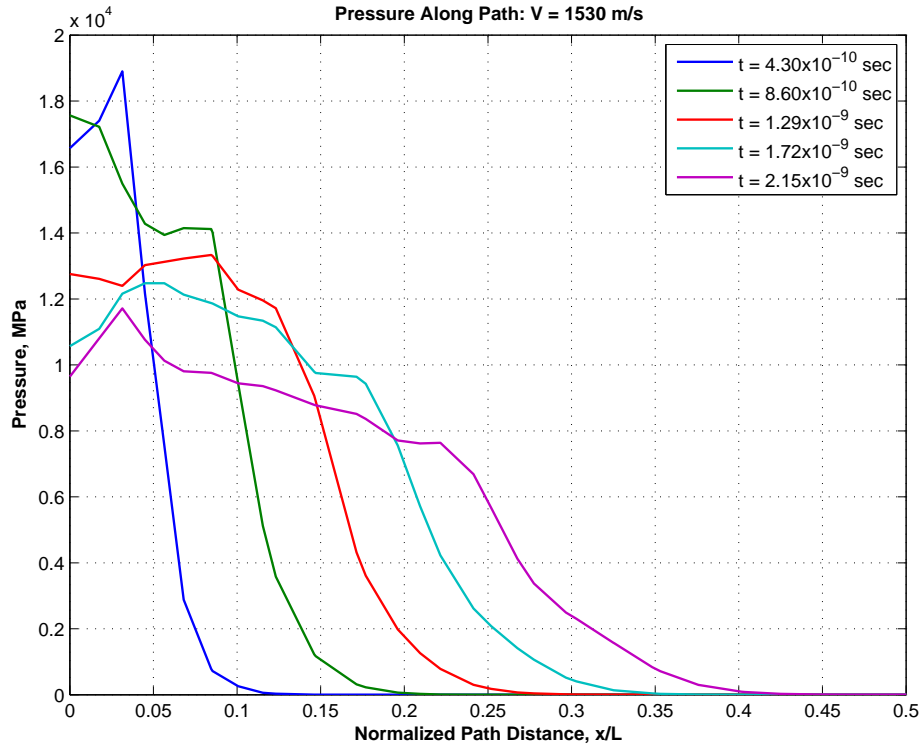


Figure 4.10: Pressure Along Path with Varying Time, $V = 1,530$ m/s

With increasing time, the pressure along the path continued to dissipate. At the first time interval, the maximum pressure was 1.89×10^4 MPa and occurred at a normalized path distance of 0.031. At the final time of 2.2×10^{-9} sec, the maximum pressure also occurred at the same normalized path distance, but had dissipated to 1.17×10^4 MPa.

The pressure at Nodes A–F as a function of time during the 1,530 m/s collision event are shown in Figure 4.11. The maximum pressure for Node A and Node B were 2.111×10^4 and 1.132×10^4 MPa, respectively. It appeared that Nodes D–F did not see any increase in pressure during the 2.15×10^{-9} sec collision event. Closer inspection of the data revealed that the maximum pressure for Node D occurred at the final time and was only 20.13 MPa. For Node E, the maximum pressure was even smaller at 4.626×10^{-7} MPa which was essentially zero. During this analysis interval, the pressure at Node F was zero. This further demonstrated that over the short time interval, the effects of the impact wave were not felt by the nodes that were far from

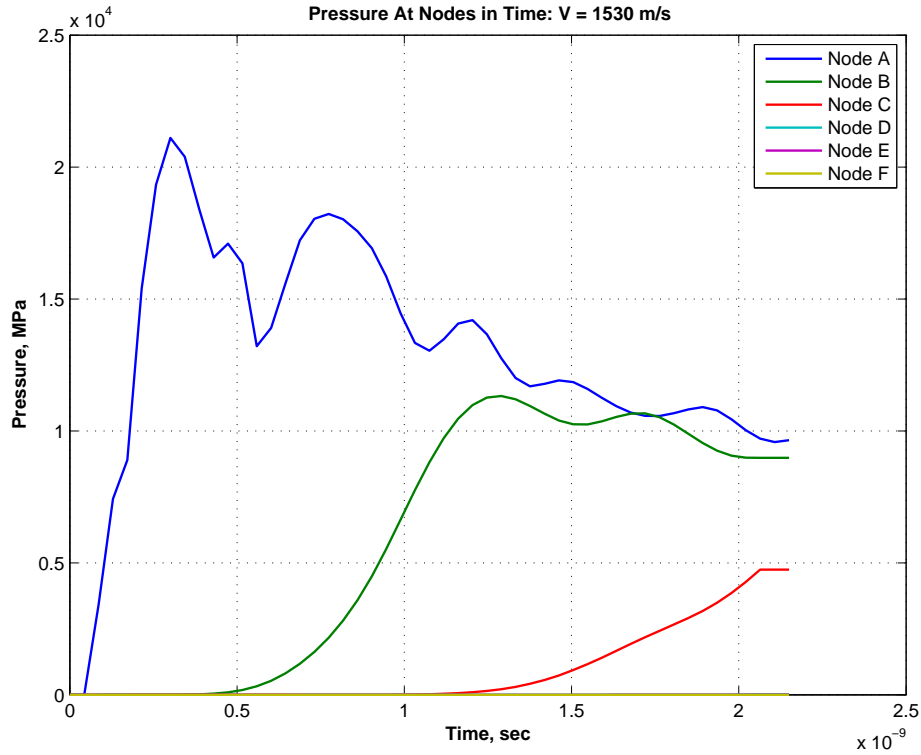


Figure 4.11: Pressure at Nodes in Time, $V = 1,530$ m/s

the impact location. In summary, the impact of the slipper with the asperity produced a wave that propagated through the slipper and rail structures, but never reached the proportions of a shock wave.

4.3 Comparison of Slipper and Model Total Wear Volume

As was mentioned previously, one way to validate the current wear rate model is to compare the total wear with that observed during the metallographic analysis of the January 2008 test slipper. This is a secondary objective of this research.

The total wear volume, based on the current melt and mechanical wear rates, is computed by integrating the wear rate functions over the 5,816 m sliding distance of the January 2008 test mission. Before the total wear can be computed, several relevant features in this calculation must be discussed. The first is in regards to Archard's wear coefficient. The second feature is a three-dimensional proportion factor, N , which

helped to relate the effects of a plane strain, single asperity collision to the three-dimensional grouping of all asperities actually encountered by the slipper during the sliding event on the rail.

4.3.1 Theory of Archard Wear Coefficient. Archard’s wear equation, published in 1953 based on his studies of the contact and rubbing of flat surfaces [4], relates the wear rate, normal load, and hardness of the sliding material by

$$W_A = \frac{k_A F}{H} \quad (4.1)$$

where H is the indentation hardness, F is the normal load, and k_A is the proportionality constant or Archard wear coefficient. This dimensional wear rate has units of volume per unit sliding distance, or $[L^3]/[L]$.

If the load, wear coefficient and hardness remain constant, then the volume of material lost, V , is directly proportional to the sliding distance, s . If the sliding velocity is also, constant, then V is proportional to time. Archard said that k_A corresponds to the probability that an asperity interaction results in the formation of a wear particle. It is also introduced as a means to provide agreement between theory and experiment.

4.3.2 Lim and Ashby Wear Coefficient Study. In the development of their wear-mechanism maps, Lim and Ashby surveyed the published results from many steel-on-steel sliding experiments, typically performed at low velocity with a pin-on-disk test apparatus. During sliding between materials of similar hardness, “flakes or particles of metallic wear debris form and, ultimately, escape from between the surfaces [53]” forming a wear particle. In order for these particles to form, subsurface cracks nucleate and propagate toward the rubbing surface. One of the models that describes this phenomenon is Suh’s delamination theory of wear [71]. The model is based on the following reasoning

1. “The traction at the sliding contact deforms the subsurface layer, generating dislocations and vacancies. Continued plastic deformation leads to the formation of voids in the subsurface layer. When hard second phase particles, such as inclusions and large precipitate particles are present, the formation of voids is enhanced.
2. As the deformation continues the voids coalesce, either by growth or by the shearing action of the surrounding material around hard particles. This eventually results in a crack which is parallel to the wear surface.
3. When the crack reaches a critical length the material between the crack and the surface shears, yielding a sheet-like wear particle. The critical length of the crack is dependent upon the material [72]”

When calibrating their plasticity-dominated wear model, Lim and Ashby state that k_A is typically less than 5×10^{-5} for mild wear, and less than 5×10^{-3} for severe wear. Bhushan states that the values of k_A for mild wear are typically in the range of 1×10^{-8} to 1×10^{-4} , and from 1×10^{-4} to 1×10^{-2} for severe wear for most material combinations [14].

The Archard wear coefficient is not a material property, but varies based on the operating conditions of the test. For example, in the calibration of their wear model, Lim and Ashby’s included some of the steel-on-steel sliding test data as reported by Saka et al. [67]. In this test, a 0.64 cm thick specimen of AISI 304 stainless steel was tested while sliding against a 0.1 m AISI 4150 steel disc at various surface speeds, normal forces, and sliding distances. A portion of the data set reported by Saka et al. is included in Table 4.3. For a given hardness of 2.920 GPa of the stainless steel, k_A values were computed based on Equation 4.1 for the six test conditions. It should also be noted that Lim and Ashby indicated in their wear-mechanism map that these test points were all considered mild wear [53]. Although k_A varies due to the material properties, loading and sliding velocity, it will be treated as a constant value for computing the total wear rate of the experimental slipper.

Based on Suh’s delamination theory of wear model, Lim and Ashby observed the size, shape, and number of inclusions that developed during a sliding wear experiment. During continuous sliding, shearing and compression action caused the shape of voids

Table 4.3: Sample Variation in Wear Coefficient, k_A [67]

Test #	Surface Speed (m/s)	Normal Force (N)	Distance (km)	μ	Wear Rate ($\times 10^{-12}$ m ³ /m)	k_A
1	2.43	11.76	17.70	0.96	4.32	1.07×10^{-6}
2	5.35	11.11	18.97	0.86	4.85	1.27×10^{-6}
3	8.74	13.33	16.72	0.73	3.00	6.57×10^{-7}
4	2.57	35.53	9.51	0.81	12.96	1.07×10^{-6}
5	5.13	31.78	3.23	0.84	12.18	1.12×10^{-6}
6	8.65	29.36	7.83	0.86	9.37	9.32×10^{-7}

around the inclusions to change. By gradually removing horizontal layers of material, the volume fraction of the inclusion, f_v , and the area fraction of the voids, f_A , could be measured. The accumulated plastic shear strain, γ_0 , could also be measured. At a critical area fraction, f_A^* , fracture causes a wear flake to break off from the specimen.

Lim and Ashby developed a relationship between f_v , γ_0 , and f_A^* which was equivalent to the Archard wear coefficient by

$$k_A = \frac{2\gamma_0 f_v}{f_A^*} \quad (4.2)$$

They also give an example calculation for k_A where the critical area fraction of inclusions, $f_A^* = 0.5$, the accumulated plastic shear strain, $\gamma_0 = 1\%$, and the volume fraction of inclusions, $f_v = \times 10^{-3}$. The resulting Archard wear coefficient, based on these experimentally measured parameters, was 4×10^{-5} which was in the mild range. The normalized pressure, \tilde{F} , is the load, F , divided by the product of the contact area, A_n and the material hardness, H . For the Lim and Ashby experimental test conditions, \tilde{F} was 3×10^{-4} .

An Archard wear coefficient for VascoMax 300 was computed by first noting that at 10 m/s, the normalized pressure, \tilde{F} , as calculated from the DADS data was 3.85×10^{-4} . The low velocity condition was selected because it was similar to that used by Lim and Ashby, and Suh et al. With our low velocity normalized pressures very similar to that of the Lim and Ashby experiment, their same critical area fraction

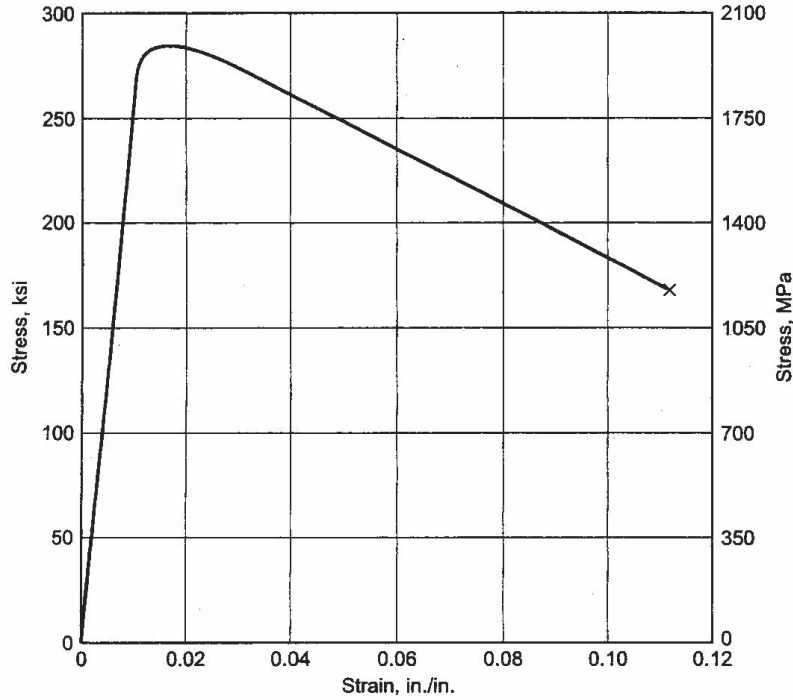


Figure 4.12: VascoMax 300 Stress Strain Curve [1; 77]

of inclusions, $f_A^* = 0.5$, and the volume fraction of inclusions, $f_v = 1 \times 10^{-3}$ was used. These researchers were able to physically measure the voids and inclusions, and through this observation determine the accumulated plastic shear strain. In this research, these measurements were not made, so by similarity to their loading condition, the same values are used in the determination of k_A .

The strain at failure from the VascoMax 300 stress strain curve shown in Figure 4.12 was used to determine the accumulated plastic shear strain, $\gamma_0 = 1.1\%$. When combined with $f_A^* = 0.5$ and $f_v = 1 \times 10^{-3}$, the wear coefficient, based on Equation 4.2, became 4.4×10^{-5} . This mild wear coefficient was used in the subsequent calculation of the total wear volume for the test slipper.

4.3.3 Three-Dimensional Proportion Factor, N. Mechanical and melt wear rates have been computed for a single, hemispherical $6 \mu\text{m}$ radius asperity on the perfectly flat surface of the rail. The slipper wear surface has been idealized by

perfectly flat surface. In reality, both surfaces of the rail and slipper have many, many asperities of various shapes, spacing and sizes. In order to extend our single asperity wear rate model to the fully three-dimensional wear environment, the three-dimensional proportion factor, N , has been developed.

The mechanical single asperity wear rate as computed by the numerical model, W_{sa} , is related to the same mechanical wear rate as computed by Archard's wear model, W_A . This comparison is made at the lowest target velocity of 10 m/s. The relationship between these two mechanical wear rates is given by

$$W_A = NW_{sa} \quad (4.3)$$

where N is the proportionality constant. By substitution of W_A from Equation 4.1, N is then given by

$$N = \frac{k_A F}{W_{sa} H} \quad (4.4)$$

The load, F , in this equation can be replaced by the product of the pressure, P , and slipper area, A_n . At 10 m/s, the mechanical single asperity wear rate from the numerical model was 2.63×10^{-5} mm³/mm. At this same velocity, the maximum pressure for the global quasi-steady model was 0.681 MPa. With k_A equal to 4.4×10^{-5} , the three-dimensional proportion factor N was determined to be 11.77. The mechanical and melt wear rates computed by the numerical model will be multiplied by 11.77 to account for the three-dimensional wear effect.

4.3.4 Total Wear Volume Calculations. The secondary objective of this research was to calculate the total wear volume and then compare it with that observed during the metallographic analysis of the experimental test slipper. Because of the dynamic response of the test sled, the slipper was not in contact with the rail for the full 8.14 second test mission. As was mentioned in Section 3.1.3, the percent of

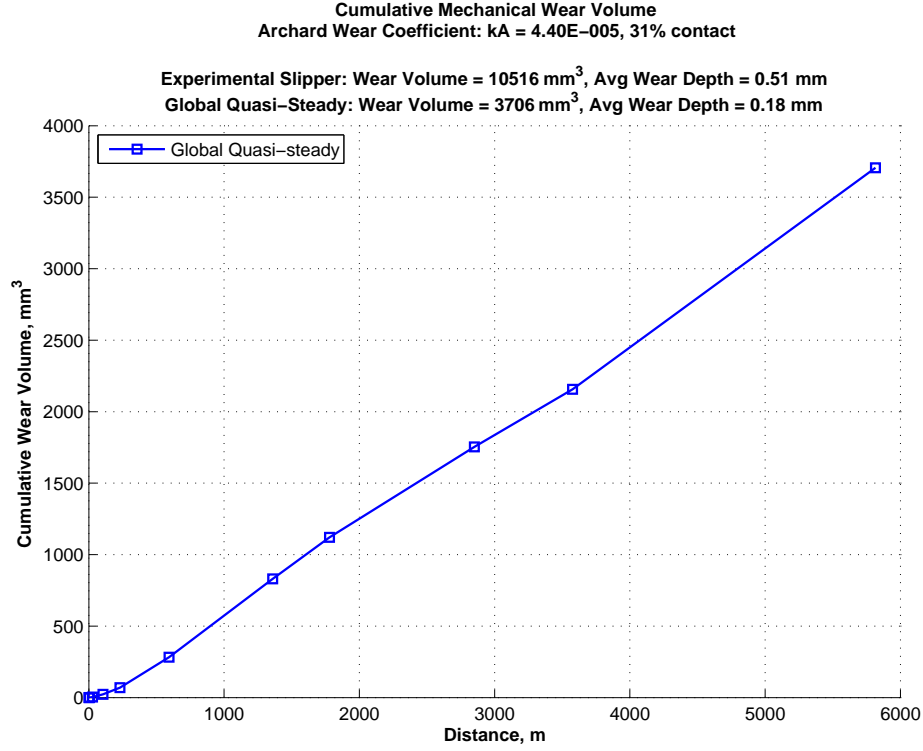


Figure 4.13: Total Mechanical Wear Volume

distance in contact from the 80X-A1 test mission will be used here. From Table 3.1, this distance in contact percentage, d_{pc} , was 30.63%.

The mechanical total wear volume, W_{tot} , was computed by the numerical integration of

$$W_{tot} = Nd_{pc} \int_0^{d_{max}} W_{sa}(s) ds \quad (4.5)$$

where the d_{max} is the total sliding distance of 5,816 meters, and $W_{sa}(s)$ were the single asperity mechanical wear rates at each given target distance. The numerical integration over sliding distance is shown in Figure 4.13 for the cumulative mechanical wear volume, where the global quasi-steady model was used to compute N .

Based on the given wear coefficient, the three-dimensional proportion factor, and the distance in contact percentage, the model predicted a total wear volume of 3,706 mm³. When divided by the slipper area, the average mechanical wear depth

was 0.18 mm. By comparison, the experimental average wear depth, based on the experimental wear volume of 10,516 mm³, was 0.51 mm.

In a similar manner, the cumulative melt wear volume was computed by

$$W_{tot,melt} = Nd_{pc} \int_0^{d_{max}} W_{sa,melt}(s)ds \quad (4.6)$$

where $W_{sa,melt}(s)$ were the single asperity melt wear rates at each given target distance. The model predicted a total melt wear volume of 54 mm³ and an average melt wear depth of 2.61 μ m. Thus, by combining these mechanical and melt wear volumes, the total wear volume was 3,760 mm³, or 35.7% of the experimentally measured total wear volume. It would have been more desirable to have predicted a total wear volume closer to the experimental wear volume. However, the model's prediction is not too far off when considering all of the variables and assumptions that were implemented in the development of the wear rate. The approximations included in the model yielded results that were close to the experimental wear volume.

With this method, the total wear is very susceptible to several factors. Both the proportionality factor, which is a byproduct of the Archard wear coefficient, and the contact percentage were treated as constants in both the total mechanical and melt wear volume equations. Thus, these wear volumes are directly proportional to these parameters. Increasing the contact percentage by 10% will in turn increase the wear volume by the same 10%.

Results of the analysis indicate that mild wear occurred in the test slipper. The total wear volume from the slipper top was 10.52 cm³, which was only 3.49% of the initial slipper top volume. This experimental total wear volume was determined by extending the measured, two-dimensional wear area, taken along the centerline of the slipper top, across the 101.3 cm width of the slipper. In order to make this simplified approach, the assumption was made that the centerline wear area was uniform across the entire width of the slipper. In reality, wear is a three-dimensional event, and the actual volume of worn material may have been slightly more or less than 10.52 cm³.

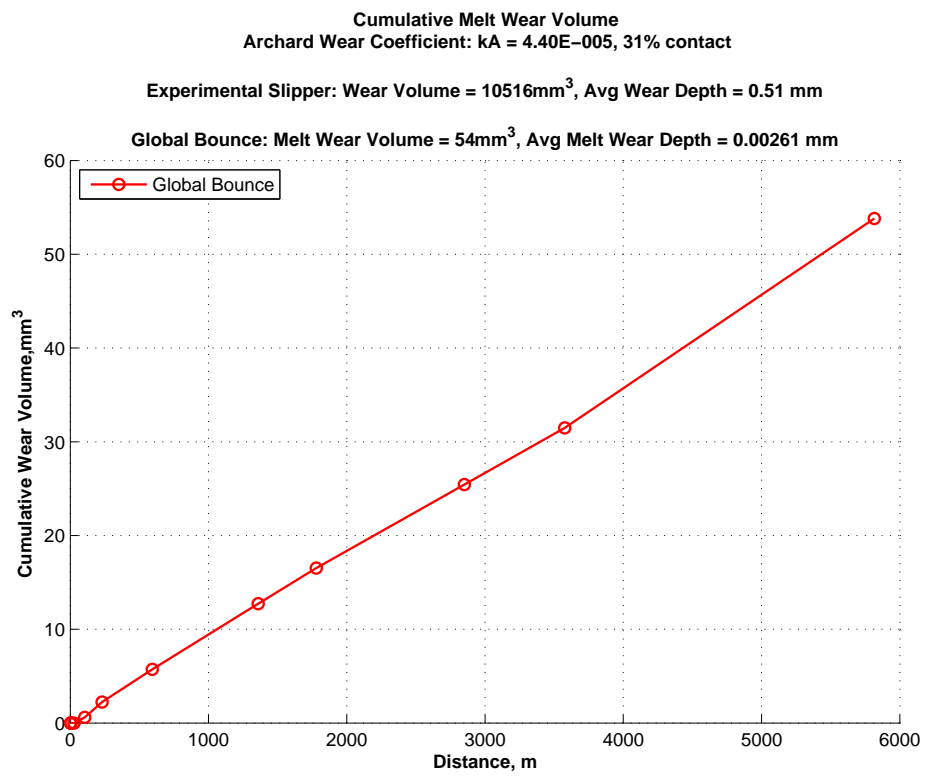


Figure 4.14: Total Melt Wear Volume

V. Conclusions

This study presents an engineering methodology for understanding and quantifying wear rates during high velocity metal-to-metal sliding contact. The research tools have incorporated the frictional coefficient, pressure distribution, sliding velocities, and an approximation of the three-dimensional asperity collision. This led to a model that could characterize wear rate between two materials in contact with a relative sliding velocity of up to 1,530 m/s. Overall, the wear environment is truly three-dimensional. The attempt to characterize three-dimensional wear was not economically feasible because it must be analyzed at the micro-mechanical level to get results. Thus, an engineering approximation was carried out. This approximation was based on a metallographic study identifying the need to include viscoplasticity constitutive material models, coefficient of friction, relationships between the normal load and velocity, and the need to understand wave propagation. A simplified failure criterion was selected even though a true environment must consider wear debris. Results of the finite element model of total wear were within reason when compared to the experimental findings. Specific conclusions drawn from this work are presented here.

The metallographic analysis of the aft right test slipper from the January 2008 test mission provided a greater knowledge of the dry sliding event. This slipper traveled a distance of 5,816 meters in 8.14 seconds and reached a maximum velocity of 1,530 m/s. The wear event was characterized as unlubricated, unidirectional steel-on-steel sliding. The total volume of worn slipper material was 10.52 cm³, which was 3.49% of the initial slipper top volume of 300.9 cm³. For the VascoMax 300 slipper and AISI 1080 steel rail, this was a mild wear event because of the low percentage of worn material.

Several conclusions from the metallographic investigation can be used in developing a numerical model of the wear event. Scanning electron microscopy inspection of the slipper sliding surfaces revealed plastic deformation which occurred as a result of many impacts and collisions between the slipper and rail asperities of varying

size. Certain factors must also be included in any numerical wear rate model. First, the model must account for this plastic deformation by including a viscoplasticity constitutive model for VascoMax 300 slipper and AISI 1080 steel rail. Secondly, the plastic deformations were on the order of $10\ \mu\text{m}$. Thus, the model must account for slipper and micron-sized asperity collisions, and a method of incorporating the coefficient of friction into the slipper/rail interaction must be represented. The sliding event between this slipper and the entire 5,816 m rail is impractical to model in three dimensions. The model must be simplified.

The microindentation hardness testing revealed softening of the VascoMax 300 to a depth of $400\ \mu\text{m}$ below the surface. When compared to the overall initial 14.7 mm thickness of the slipper, we note that the effects of the frictional sliding event were very localized and thus leading to a heat-affected zone near the slipper/rail interface. Thermal energy generated during frictional heating doesn't have time to diffuse through the bulk of the slipper during the 8.14 second sliding event. The melt wear model should also be on the micro scale and reflect this short diffusion distance into the slipper.

The slipper appears to be moving with little rolling action. On the other hand, evidence shows that pitching becomes a major source of wear both from a mechanical and a thermal point of view. The dynamic action of slipper movement creates a contact surface with a greater material hardness. This is attributed to continuous impact. The evidence of sliding interaction is observed through a EDS study whereby the rail and coatings interact with the slipper material.

The dynamic slipper data developed by HHSTT in the form of the DADS data played a significant role in the research. This data provided an understanding of the dynamic forces and motion of the slipper during the test run. Modeling the exact motion and timing of each intermittent slipper contact with the rail would be extremely difficult to model in the finite element model. The DADS statistical analysis provided smooth pressure functions in time that could be implemented into the sim-

plified global finite element model. The coefficient of friction, using Montgomery's concept of pressure-velocity data, was also implemented in the model. This data were particularly useful because they represented a wide range of pressures and sliding velocities.

Several different global models of the slipper and rail interaction were evaluated during this research. These included the total contact model, where due to low normal pressures, the slipper was constrained along the bottom edge to remain in contact with the rail. In this particular model, the entire 8.14 sec sled test was modeled. However, the imposed boundary condition constraints led to a pressure distribution along the slipper/rail interface that resembled a static pressure distribution, instead of a dynamic pressure distribution with increased magnitude near the front of the slipper. The global quasi-steady model analyzed the slipper/rail interaction at a specific velocity. The resulting contact pressure distribution at the slipper/rail interface also was solved for much faster than the previous model. The contact pressure distribution for the global quasi-steady model was used to determine the three-dimensional proportion factor, N , for ultimately determining final total wear volume. In the future, this global model should be used to quickly determine the pressure distribution at a multitude of sliding velocities and applied pressures.

The third global model studied was the global bounce model which attempted to include a quick analysis of the pressures that develop in the slipper as it passes through the slipper gap. The resulting pressure distribution was used for determining the flash temperature as part of the melt wear rate calculations. ,

The results of several initial finite element modeling studies also proved useful for subsequent modeling. First, mapping of the global state of stress to the local submodel didn't affect the overall wear rate at 1,000 m/s. In addition to the pressure mapping, the acceleration or deceleration of the local submodel, over the extremely short duration of the slipper/asperity collision, had a negligible effect on the resulting mechanical wear rate. A constant sliding velocity could be used for the duration of

the local submodel asperity collision event. The local submodel boundary conditions that yielded the best results was a prescribed horizontal velocity applied to the top and aft surfaces of the slipper, and constraints placed on the top surface of the slipper submodel such that vertical displacement and rotation were zero.

The mechanical wear rate per unit width, W_{uw} , could be determined by analyzing several smaller asperity radii collision events. The analysis led to the determination of an effective width, equal to $8.29 \mu\text{m}$ for a hemispherical asperity of radius $6 \mu\text{m}$. The product of the wear rate per unit width and this effective width led to the single asperity mechanical wear rate. This effective width was also used for converting the melt wear rate per unit width into a melt wear rate for the single asperity.

This finite element model can be used for determining the high velocity wear rates between any two sliding surfaces in contact. To do so requires a good viscoplasticity constitutive model as well as an equation of state for the two materials. After changing the materials in the finite element code, the same technique can be followed to develop mechanical and melt wear rates. It is possible to use the Mises failure criteria with relatively good results. Other failure criteria may be substituted for the Mises failure criteria and should yield comparable results.

Through the use of the global and local submodel finite element technique, wear rates associated with a high velocity impact event have been developed. By tracing wave propagation, one can determine if a shock wave has developed. This sliding event occurred over a wide range of velocities up to $1,530 \text{ m/s}$ and normal contact pressures up to approximately 5 MPa . Locally, during the asperity collision at $1,530 \text{ m/s}$, the maximum contact pressure was much larger at $1.89 \times 10^4 \text{ MPa}$. This indicated that the local slipper and asperity collision event dominated generation of an impact wave.

The total wear volume by this modeling technique is highly susceptible to the selection of Archard wear coefficient, k_A , and percentage of contact during the high velocity sliding event. While k_A is not constant for a specific material, choosing a constant Archard wear coefficient in conjunction with the mechanical and melt

wear rates, yields a total wear volume on the order of that observed during the metallographic investigation. For the case of continuous contact between mating pairs, where no separation due to the dynamics occurs, the contact percentage may be treated as 100%.

Development of the mechanical and melt wear rates via this numerical model have provided a basis for ongoing AFIT wear rate research to higher velocities. Currently, as part of his AFIT thesis research, Mr. Steve Meador is using the CTH hydrocode to model wear rates for the Stage 4 sled from the January 2008 test mission. While the Stage 4 slipper was not recoverable, and thus, he is unable to make a comparison of the final total experimental wear volume, we do know that this forebody sled and slippers also experienced the same Stage 3 velocity profile in the present study. Wear rates at velocities greater than 750 m/s from the CTH model are currently yielding results similar to those developed in this research. The CTH model will be extended to develop wear rates for the Stage 4 forebody sled up to the maximum velocity of 2,175 m/s.

Appendix A. DADS Statistical Analysis

This appendix outlines the DADS statistical analysis process used to convert the raw DADS data to a smooth pressure and normal force as a function of time. In the finite element model, the pressure was applied to the top of the slipper. Section 3.1.4 discusses the types of raw DADS data parameters that were provided by the HHSTT.

Initially, an incremental approach was used to determine the normal pressure during a given time interval. The original DADS data that was used by Cameron [23; 24] was for the HHSTT designated 80X-A1 mission. The velocity profile was essentially a constant acceleration from zero to 3,000 m/s in 2.5 seconds. Instead of using the moving window approach, these DADS statistics were calculated for a 0.5 second time interval. For example, the DADS data for the 0–0.5 second interval was evaluated to determine a constant pressure value for the interval. This approach resulted in a step function for the upper limit and mean forces during each interval as depicted in Figure A.1. Originally, the statistical analysis used the DADS data from each of the five time intervals (0.5 seconds in length). While step function data can easily be handled in ABAQUS, the discontinuity introduces undesirable pressure and stress oscillations when transitioning from one pressure to the next.

Instead of dividing the total sled run time into a few time intervals, a moving window analysis was used to determine the DADS statistics. This technique provided for smoother pressure profiles as a function of time. The time window was set at 0.4 seconds with a 0.2 second shift. Thus, the first interval is from $t=0$ to 0.4 sec, the second time interval is from $t=0.2$ to 0.6 sec, etc. The DADS data corresponding to the time interval window were sent to a statistical analysis function for further processing. As raw DADS data was provided for each slipper, this statistical analysis can be run for each of the four slippers.

The following outlines the steps that were accomplished during each moving window's time interval. Figure A.2 depicts the results of this statistical analysis for a sample 0.4 second time interval.

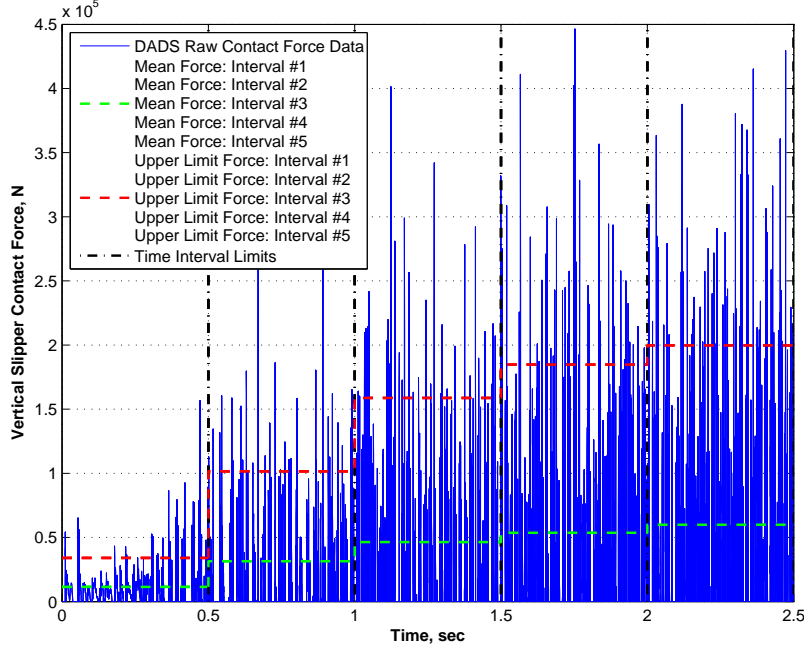


Figure A.1: Incremental Approach with Original DADS Data

- All zero contact forces are removed. Positive contact force values indicate when the slipper and rail are in contact. Zero contact forces indicate when the slipper is not in contact with the rail.
- The gamma distribution coefficients are fit to these non-zero contact forces. The gamma (PDF) probability density function given by Equation A.1 is plotted for the range of forces from zero to the maximum non-zero force in the interval. In this equation, a and b are coefficients, x is the array of non-zero forces, and $\Gamma(a)$ is the gamma function given in Equation A.2.

$$GammaPDF = \frac{1}{b^a \Gamma(a)} x^{a-1} e^{-x/b} \quad (A.1)$$

$$\Gamma(a) = \int_0^{\infty} e^{-t} t^{a-1} dt \quad (A.2)$$

- A histogram of the non-zero contact force data is plotted on the same plot as the gamma PDF. The vertical axis is scaled by the product of the bin width

and number of non-zero force data points. For this analysis, 100 histogram bins were used.

- The mean of the gamma distribution function denotes the Mean Force, F_m , over the range of non-zero contact forces in the time interval. The Lower Limit Force, F_{ll} , is the minimum value of the non-zero contact forces. In Figure A.2 these values are denoted as 9.676×10^3 and 1.111×10^1 N, respectively.
- By definition, the area under the PDF is equal to one. The area under the PDF curve is integrated until the value is 0.95, and the corresponding force becomes the Upper Limit Force, F_{ul} . Thus, the magnitude of 95% of the non-zero contact forces in the time interval are less than this Upper Limit Force. For this sample data, F_{ul} is 3.368×10^4 N.
- The Upper Limit and Mean Forces are converted to pressures by dividing by the entire slipper area ($20,645.12 \text{ mm}^2$), which assumes 100% contact area between the rail and slipper. For this sample data, the Upper Limit Pressure, P_{ul} , and Mean Pressures, P_m , are 1.631×10^{-1} and 4.687×10^{-1} MPa, respectively.
- The initial, mean and final velocity for the time interval are also calculated. The Mean and Upper Limit pressures then correspond to the mean velocity for the given time interval. For the time interval in Figure A.2, the mean velocity is 439.13 m/s.

This process was repeated for each of the windowed time intervals until the final time was reached. When the sled is at rest at zero velocity, the force on each slipper (1852 N) is given by one fourth of the total weight of the sled (7,408 N). This assumes an even distribution of the total sled mass over the four slippers. Zero velocity pressure (0.09 MPa) is calculated by dividing this force by the slipper area.

Upon completion of the incremental statistical analysis, the Mean and Upper Limit results are then plotted as shown in Figure A.3. The top subplot shows the original raw DADS contact force data (sum of Position 3 and 4) as well as the mean

Non-zero Contact Force: Gamma Probability Distribution
Aft Right Slipper, Top of the Rail
 Time Interval: t = 2.00 – 2.40 seconds
 Number of histogram bins = 100, # of Non-zero Contact Force data points = 206

Stats: Max = 8.391E+004 N, Mean = 9.676E+003 N, Std Dev = 1.327E+004, Variance = 1.760E+008
 Gamma Distribution: Mean = 9.676E+003, Variance = 1.255E+008, a = 0.75, b = 12970.58
 Lower Limit Pressure = 5.381E-004 MPa, Mean Pressure = 4.687E-001 MPa, Upper Limit Pressure = 1.631E+000 MPa
 In Contact Percentage = 10.29%, Interval Distance = 175.74 meters

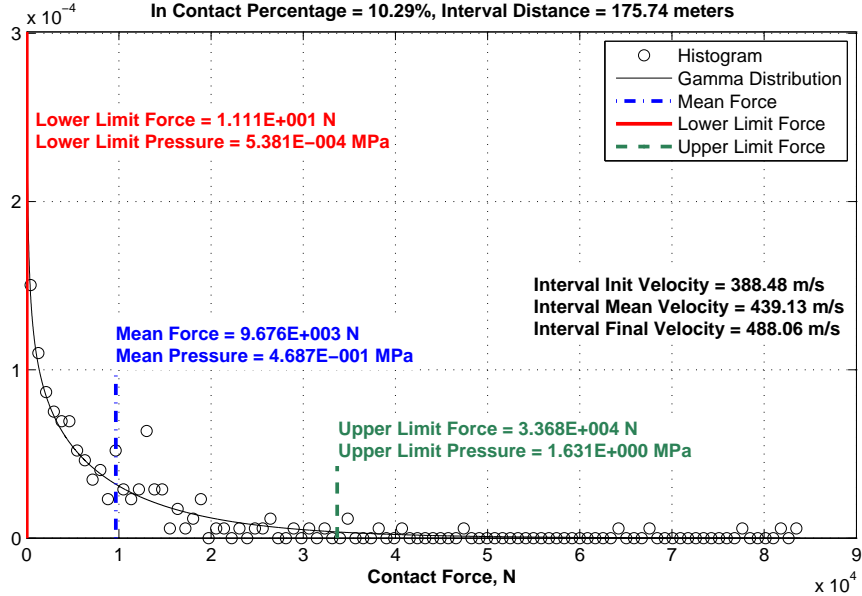


Figure A.2: Sample DADS Statistical Data

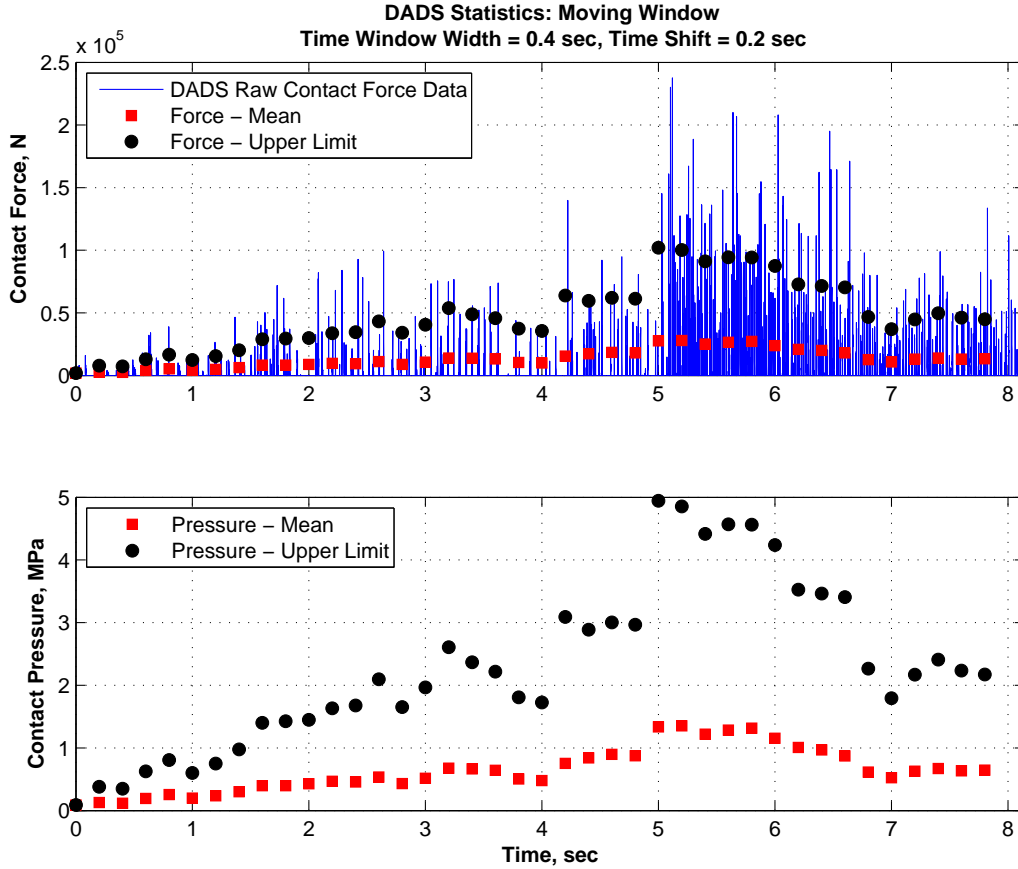


Figure A.3: DADS Statistical Analysis Force and Pressure

and upper limit forces in Newtons from each of the moving time intervals. The bottom subplot shows the corresponding mean and upper limit pressures with units of MPa.

Equation A.3 gives a fifth order Fourier curve fit to the statistical analysis values for pressure as a function of time, $P(t)$. The coefficients for the $P_{ul}(t)$ and $P_m(t)$ are listed in Table A.1.

$$P(t) = a_0 + \sum_{n=1}^5 a_n \cos(nwt) + b_n \sin(nwt) \quad (\text{A.3})$$

Figure A.4 show the mean and upper limit pressures, respectively, as a function of time. In ABAQUS, the upper limit pressure function is used as an amplitude input to the pressure applied at the top of the slipper surface as a function of total time

Table A.1: DADS Upper Limit and Mean Pressure Coefficients

Coefficient	Upper Limit, $P_{ul}(t)$	Mean, $P_m(t)$
a_0	-0.785	0.398
a_1	-3.216	-0.590
a_2	2.946	0.172
a_3	1.786	0.053
a_4	-0.257	0.130
a_5	-0.358	-0.071
b_1	5.005	0.281
b_2	2.197	0.198
b_3	-0.846	0.069
b_4	-1.431	-0.126
b_5	0.261	-0.020
w	0.504	0.549

during the ABAQUS analysis. While computed during this statistical analysis, the mean pressure function was not used during the finite element analysis. The DADS upper limit pressure was used exclusively during this research.

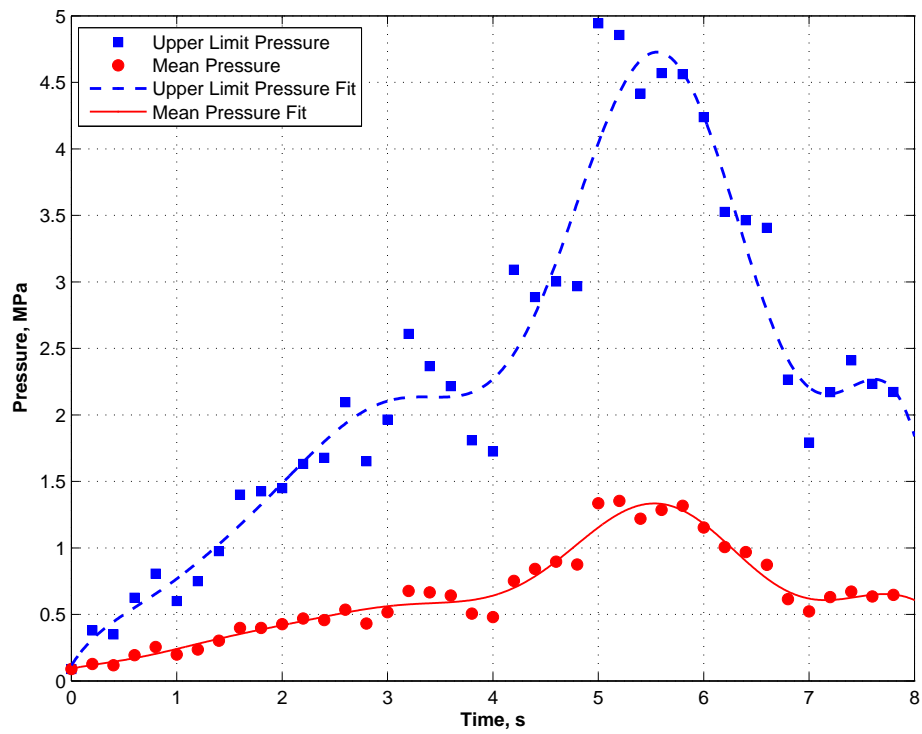


Figure A.4: Mean and Upper Limit Pressure Functions

Appendix B. Wear Rate per Unit Width Results

B.1 Wear Rate per Unit Width: 6 μm Asperity

The wear rate per unit width, W_{uw} , calculations for the 6 μm asperity collision at the twelve target velocities are presented in this section. The methodology of determining W_{uw} is described in Chapter III.

B.2 $R = 6 \mu\text{m}$, $V = 10 \text{ m/s}$

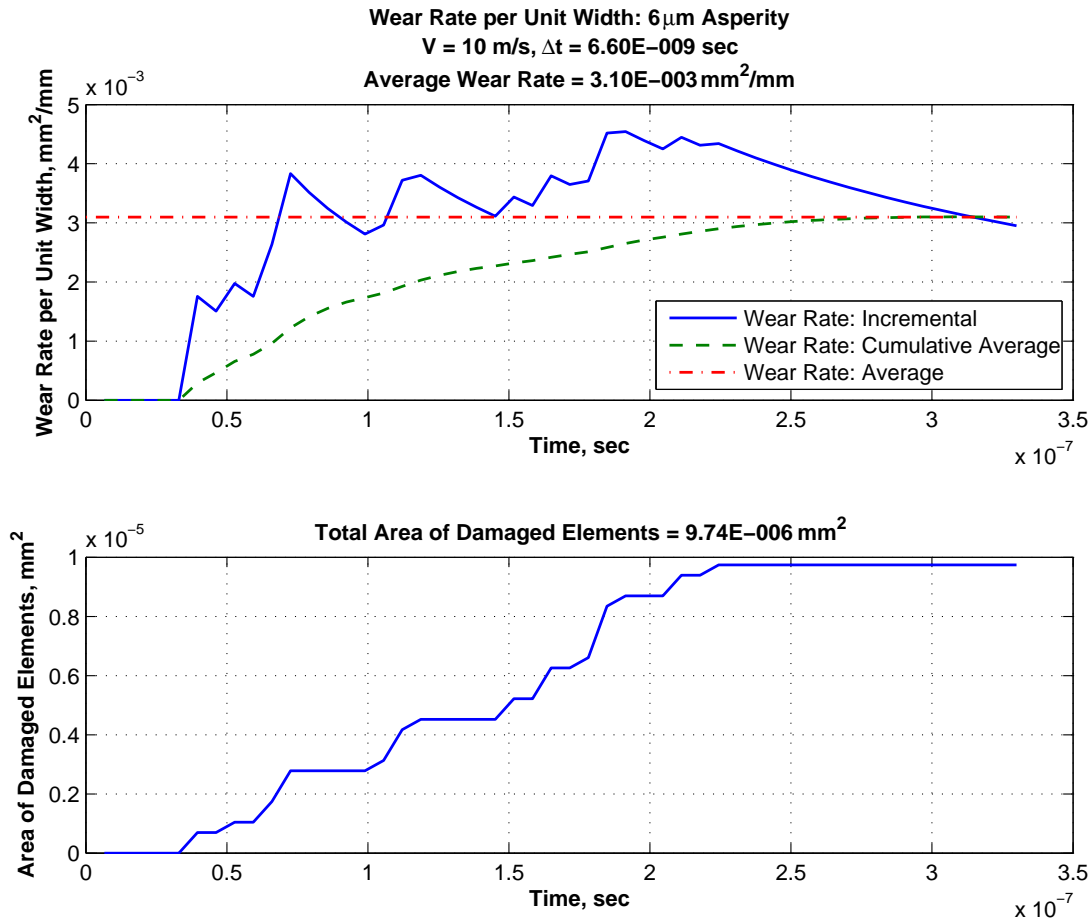


Figure B.1: Wear Rate per Unit Width, 6 μm , $V = 10 \text{ m/s}$

B.3 $R = 6 \mu\text{m}$, $V = 20 \text{ m/s}$

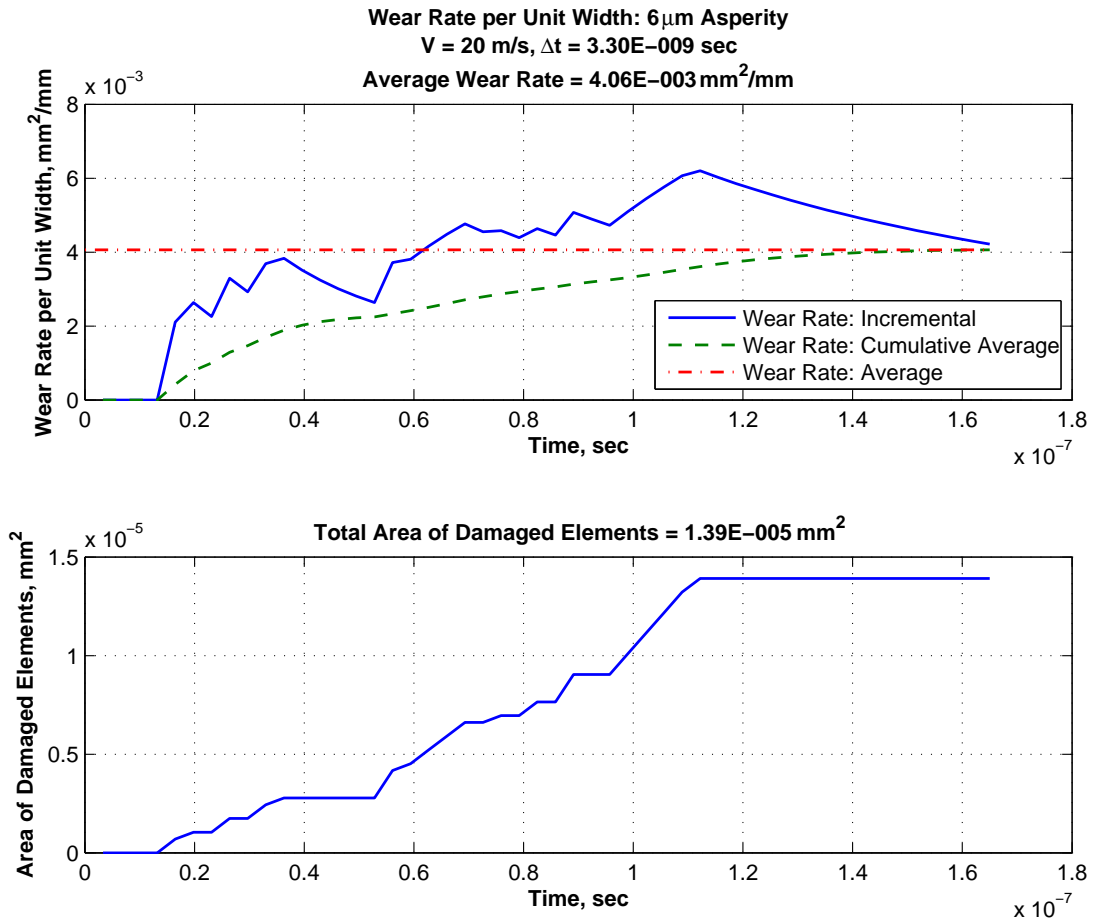


Figure B.2: Wear Rate per Unit Width, $6 \mu\text{m}$, $V = 20 \text{ m/s}$

B.4 $R = 6 \mu\text{m}$, $V = 40 \text{ m/s}$

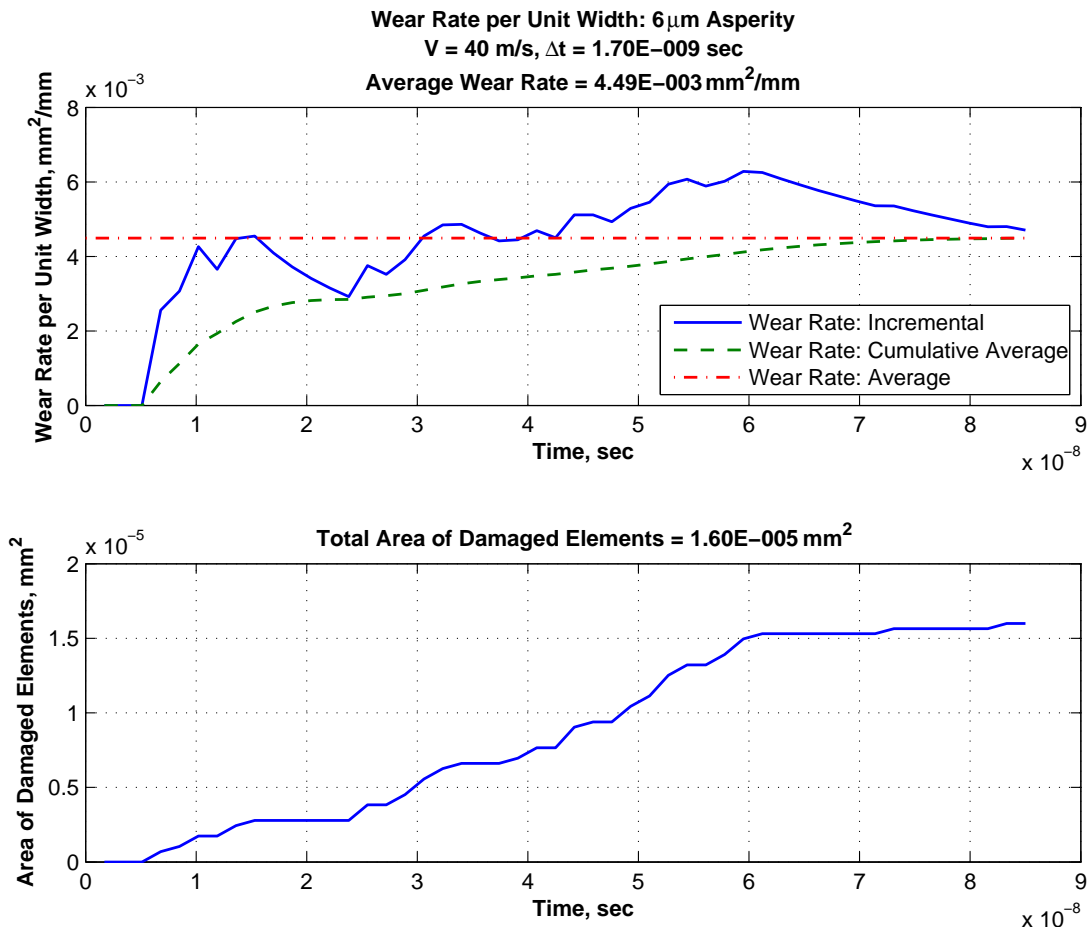


Figure B.3: Wear Rate per Unit Width, $6 \mu\text{m}$, $V = 40 \text{ m/s}$

B.5 $R = 6 \mu\text{m}$, $V = 100 \text{ m/s}$

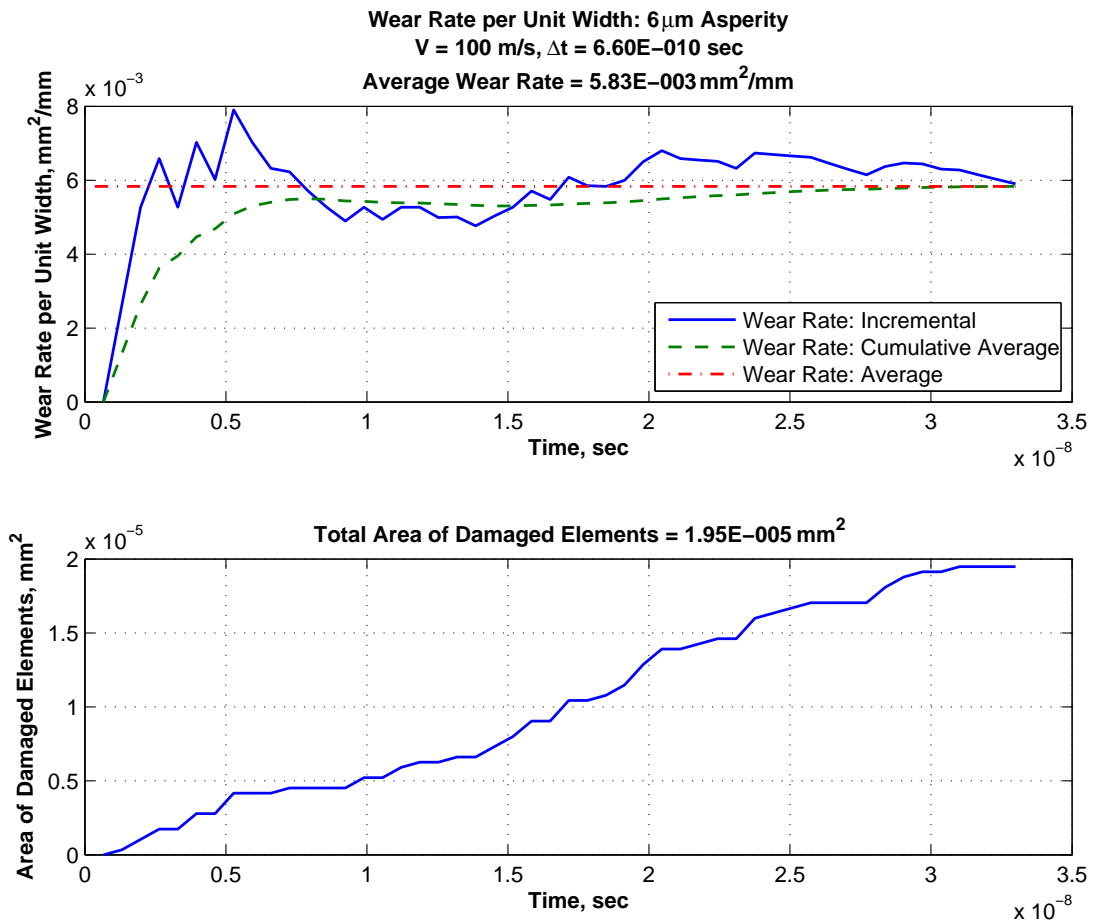


Figure B.4: Wear Rate per Unit Width, $6 \mu\text{m}$, $V = 100 \text{ m/s}$

B.6 $R = 6 \mu\text{m}$, $V = 200 \text{ m/s}$

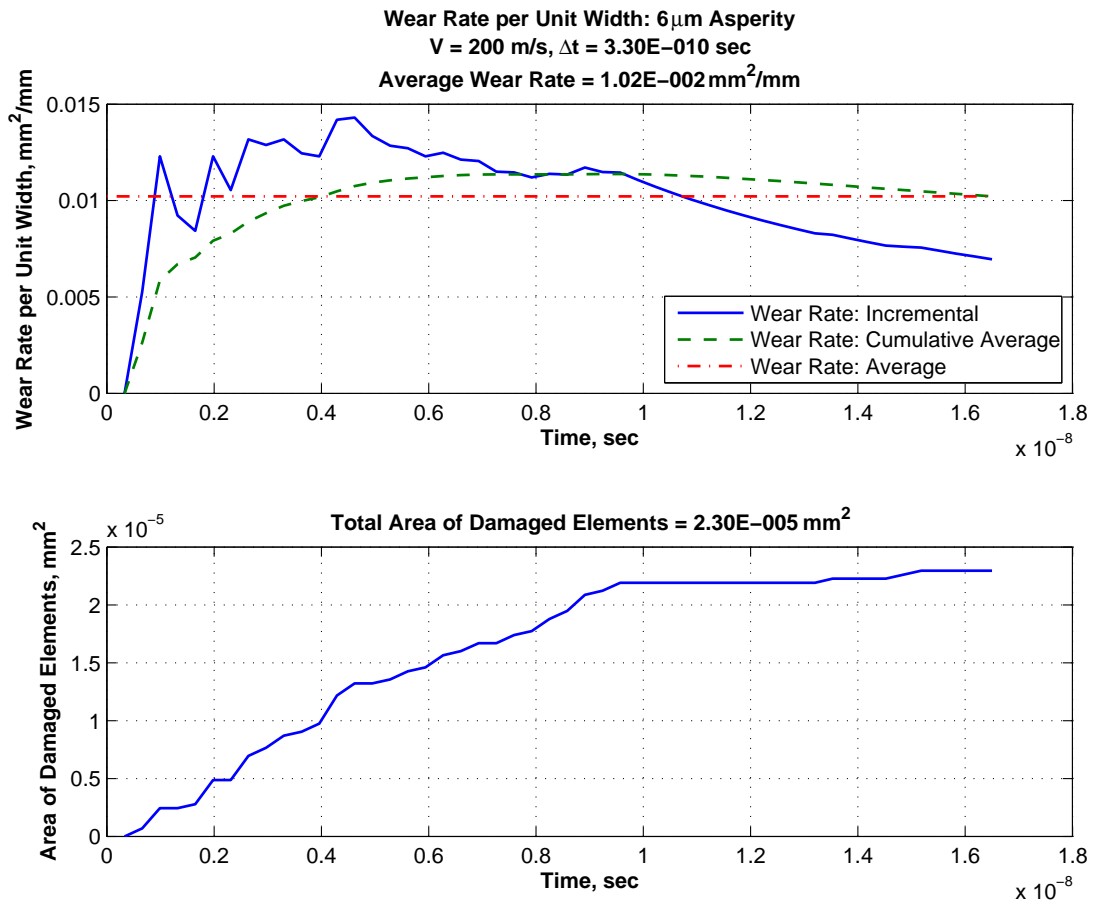


Figure B.5: Wear Rate per Unit Width, $6 \mu\text{m}$, $V = 200 \text{ m/s}$

B.7 $R = 6 \mu\text{m}$, $V = 300 \text{ m/s}$

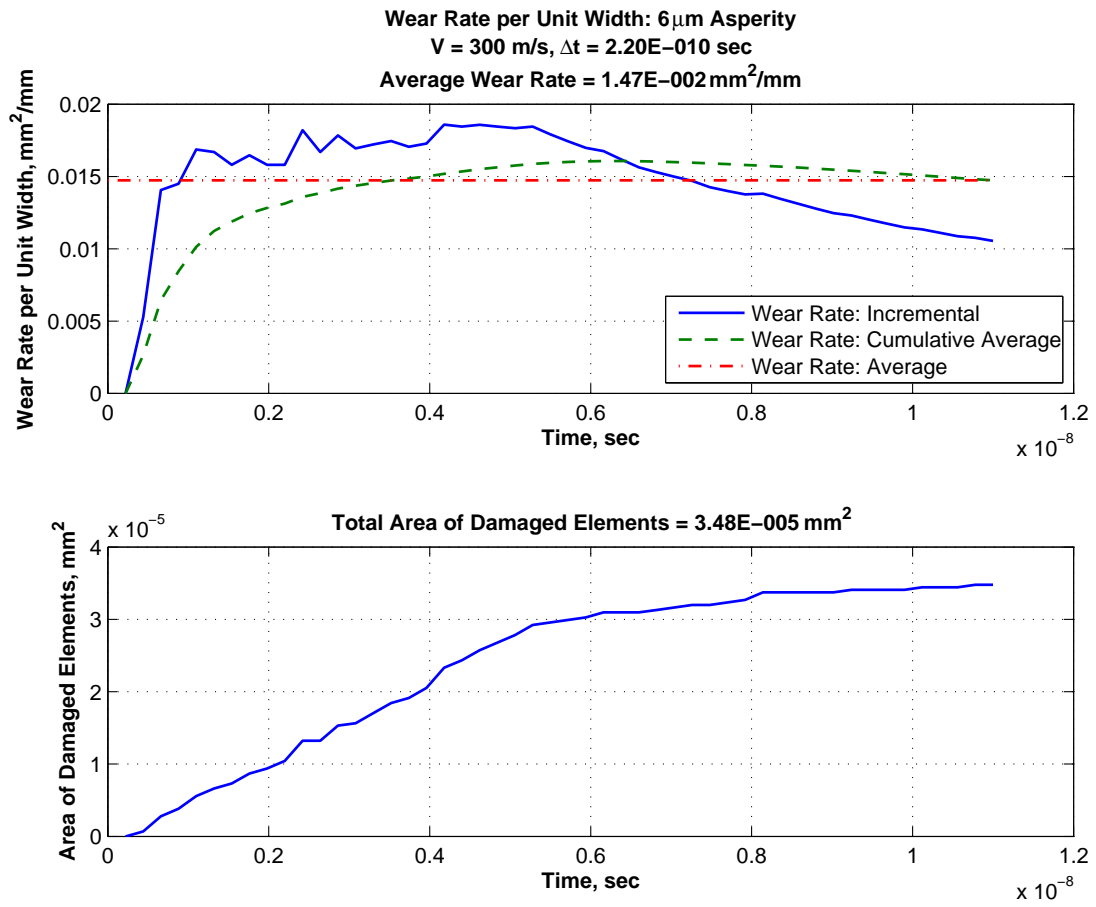


Figure B.6: Wear Rate per Unit Width, $6 \mu\text{m}$, $V = 300 \text{ m/s}$

B.8 $R = 6 \mu\text{m}$, $V = 500 \text{ m/s}$

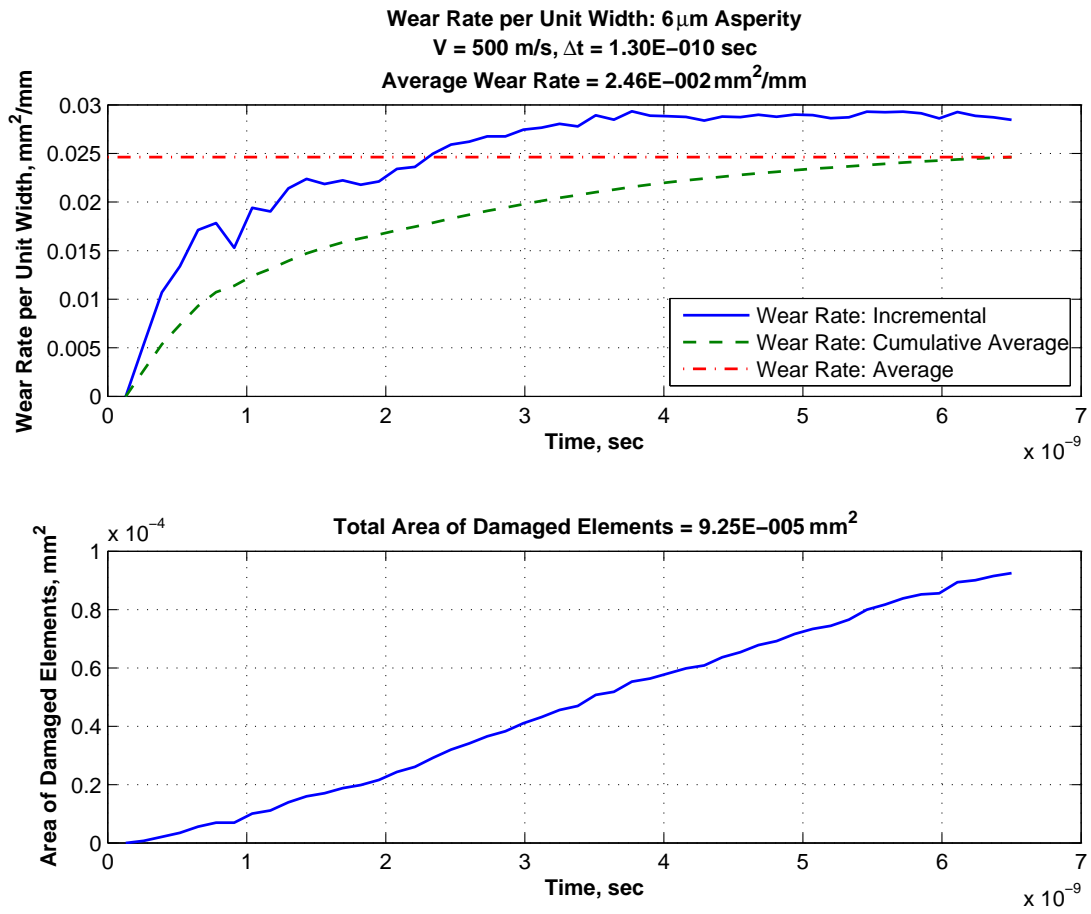


Figure B.7: Wear Rate per Unit Width, $6 \mu\text{m}$, $V = 500 \text{ m/s}$

B.9 $R = 6 \mu\text{m}$, $V = 622 \text{ m/s}$

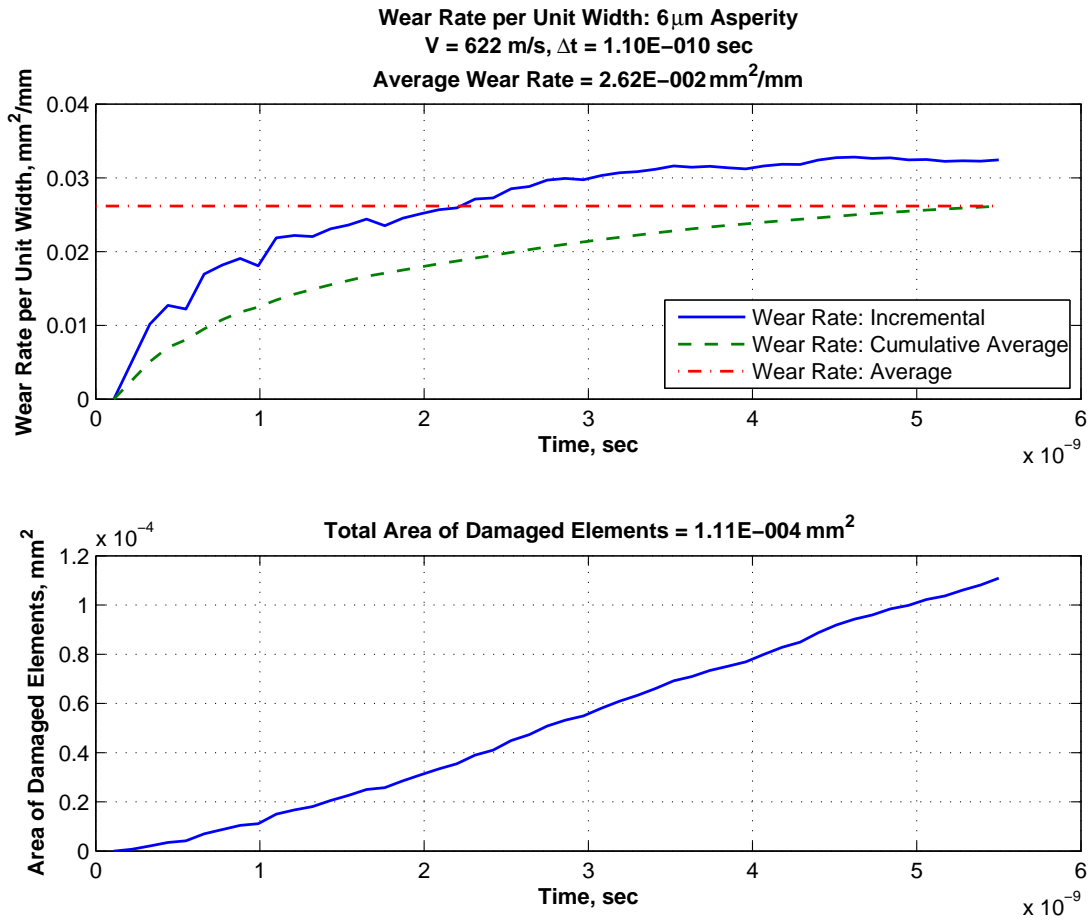


Figure B.8: Wear Rate per Unit Width, $6 \mu\text{m}$, $V = 622 \text{ m/s}$

B.10 $R = 6 \mu\text{m}$, $V = 750 \text{ m/s}$

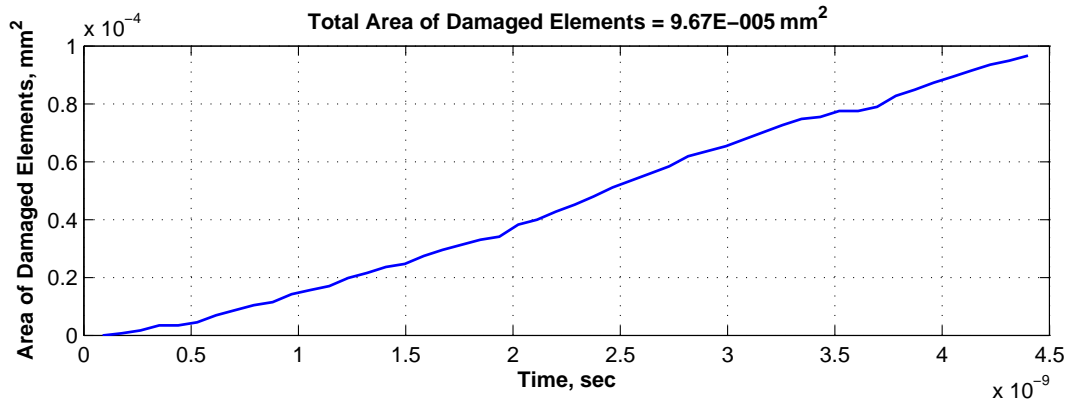
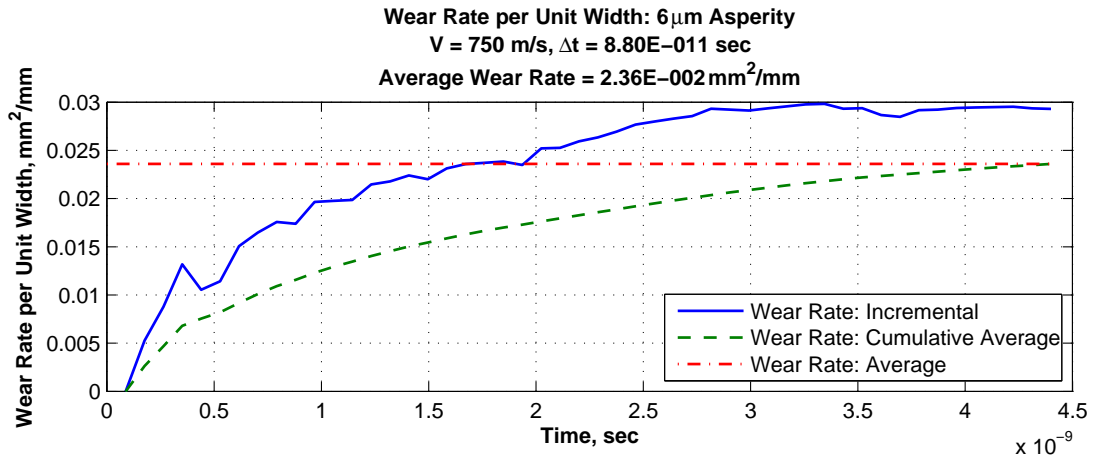


Figure B.9: Wear Rate per Unit Width, $6 \mu\text{m}$, $V = 750 \text{ m/s}$

B.11 $R = 6 \mu\text{m}$, $V = 1,000 \text{ m/s}$

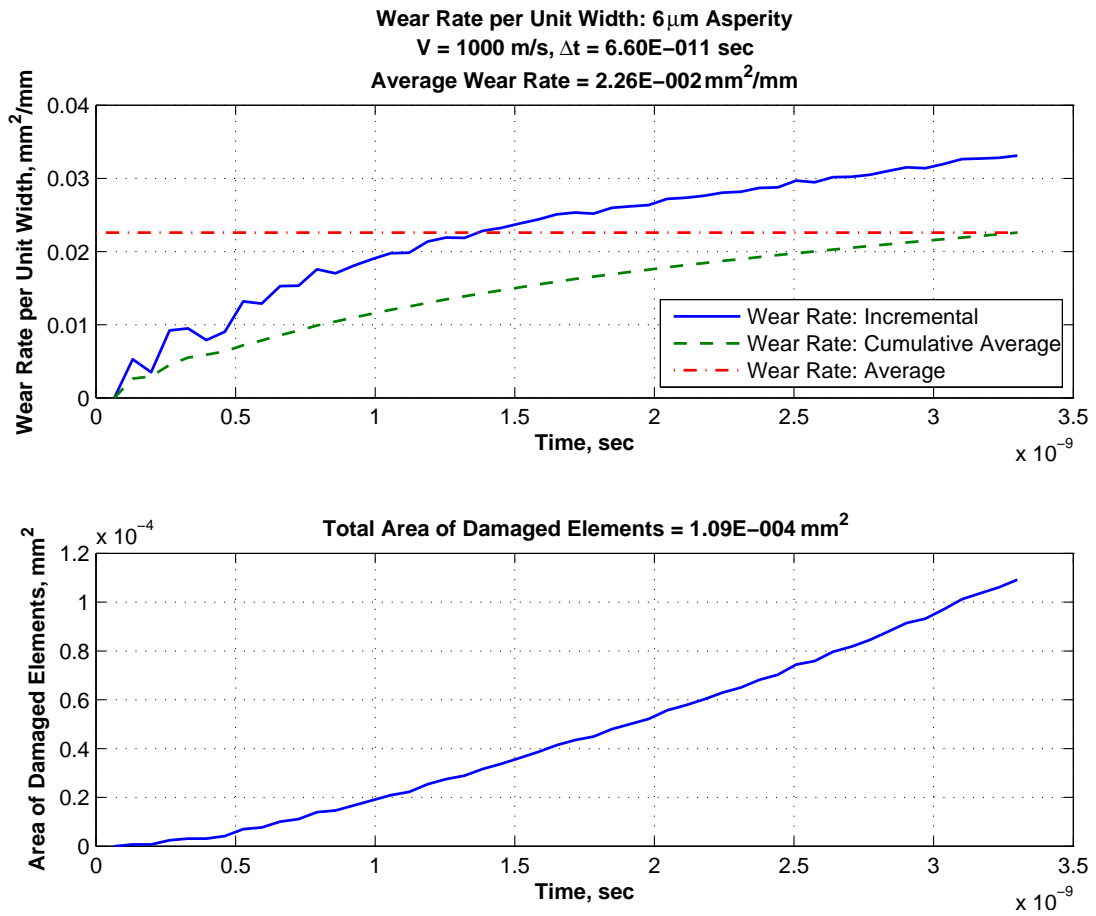


Figure B.10: Wear Rate per Unit Width, $6 \mu\text{m}$, $V = 1,000 \text{ m/s}$

B.12 $R = 6 \mu\text{m}$, $V = 1,250 \text{ m/s}$

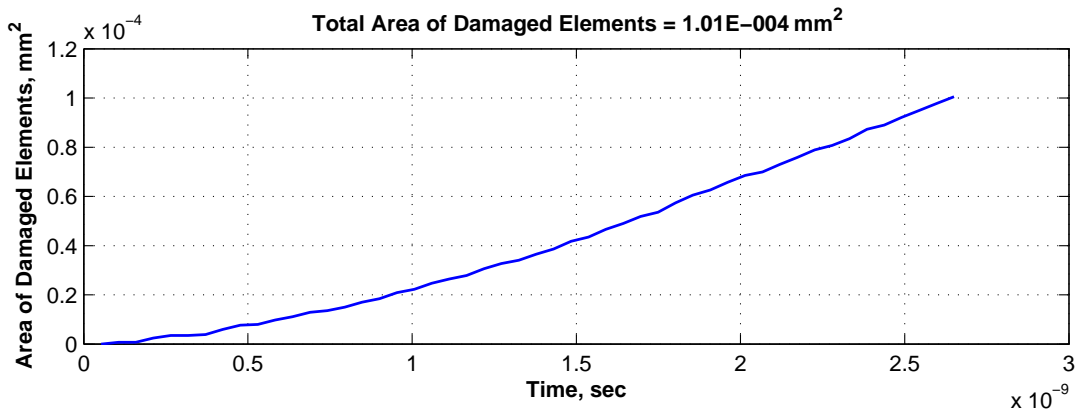
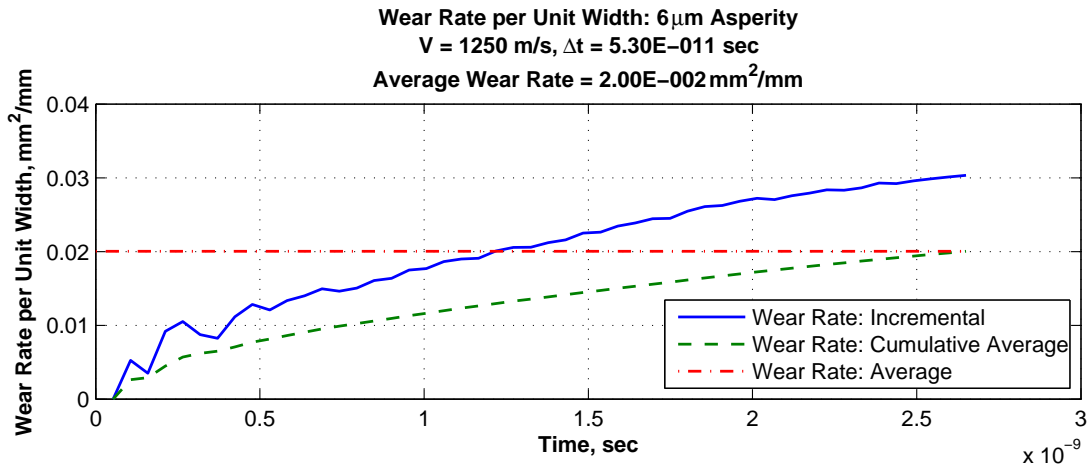


Figure B.11: Wear Rate per Unit Width, $6 \mu\text{m}$, $V = 1,250 \text{ m/s}$

B.13 $R = 6 \mu\text{m}$, $V = 1,530 \text{ m/s}$

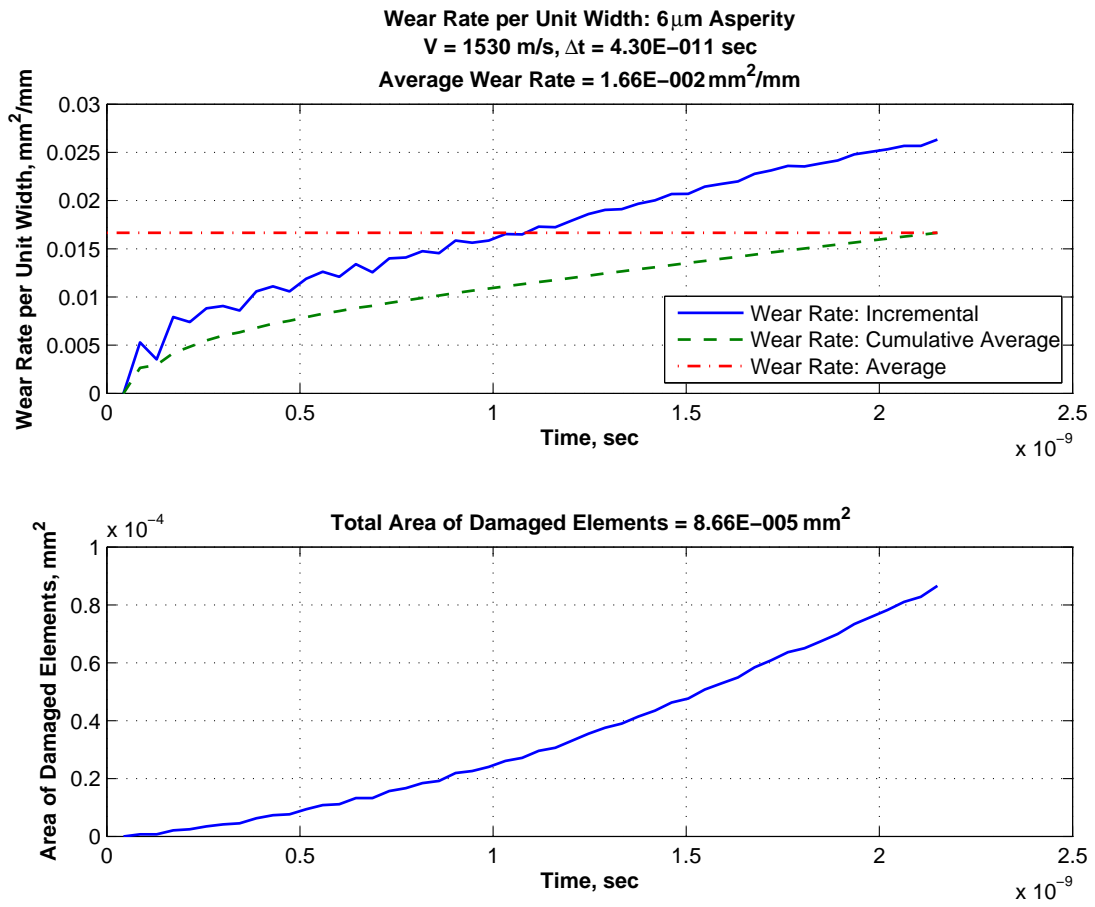


Figure B.12: Wear Rate per Unit Width, $6 \mu\text{m}$, $V = 1,530 \text{ m/s}$

B.14 Wear Rate per Unit Width: 4 μm Asperity

Wear rate per unit width calculations for the 4 μm asperity collision at the five target velocities is presented in this section.

B.15 $R = 4 \mu\text{m}$, $V = 10 \text{ m/s}$

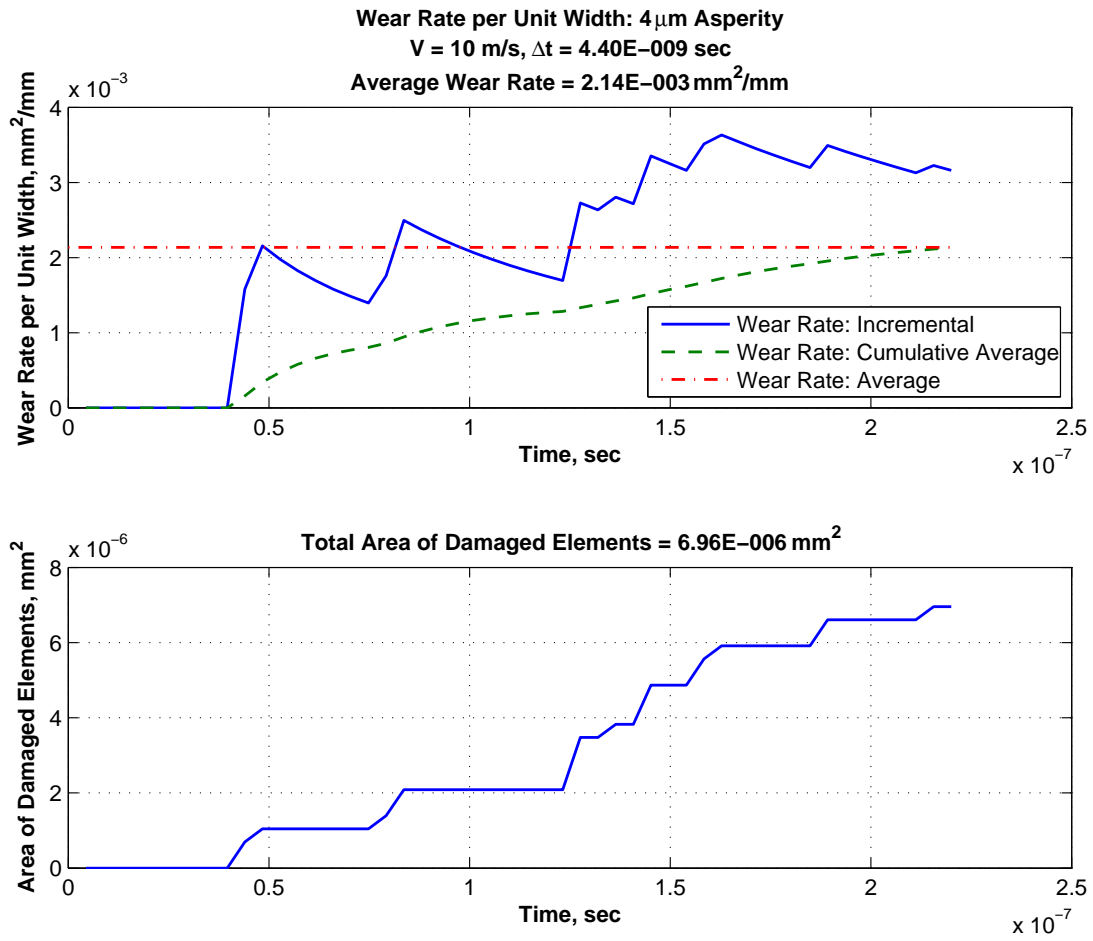


Figure B.13: Wear Rate per Unit Width, 4 μm , $V = 10 \text{ m/s}$

B.16 $R = 4 \mu\text{m}$, $V = 100 \text{ m/s}$

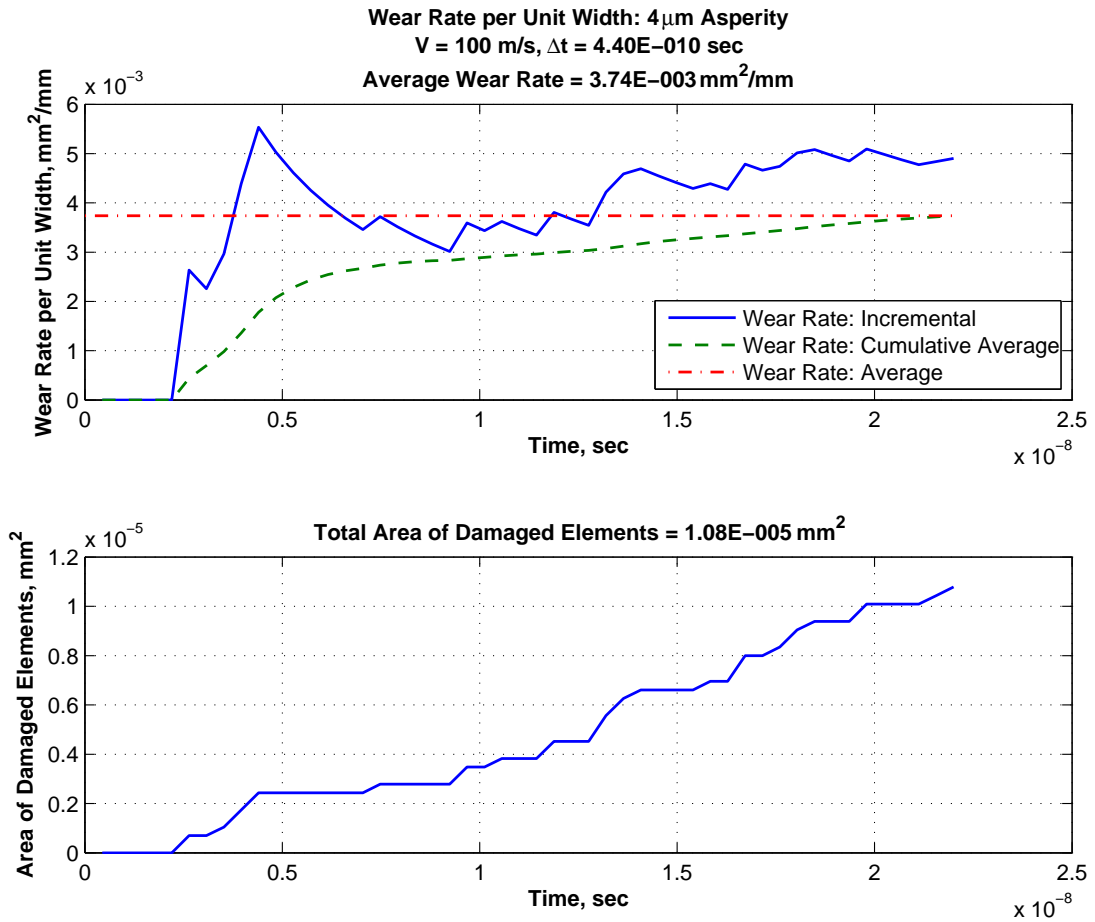


Figure B.14: Wear Rate per Unit Width, $4 \mu\text{m}$, $V = 100 \text{ m/s}$

B.17 $R = 4 \mu\text{m}$, $V = 500 \text{ m/s}$

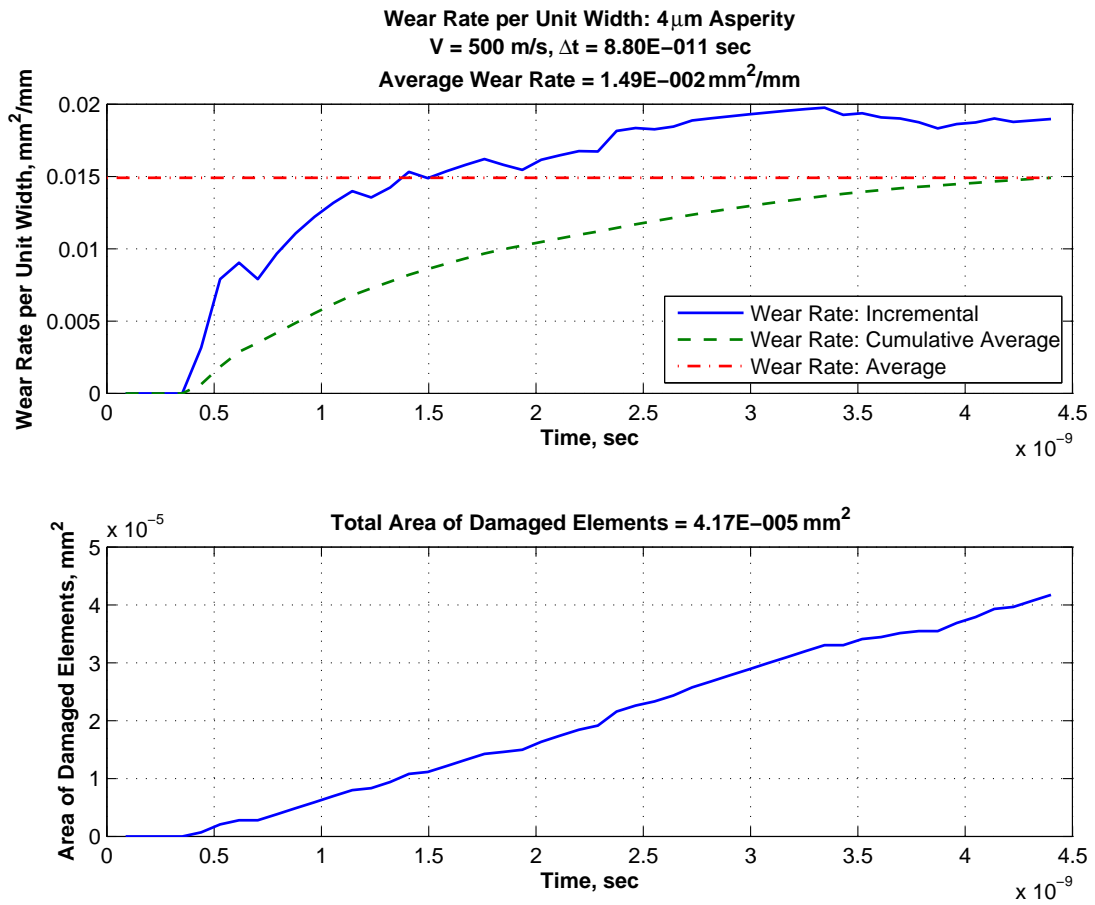


Figure B.15: Wear Rate per Unit Width, $4 \mu\text{m}$, $V = 500 \text{ m/s}$

B.18 $R = 4 \mu\text{m}$, $V = 1,000 \text{ m/s}$

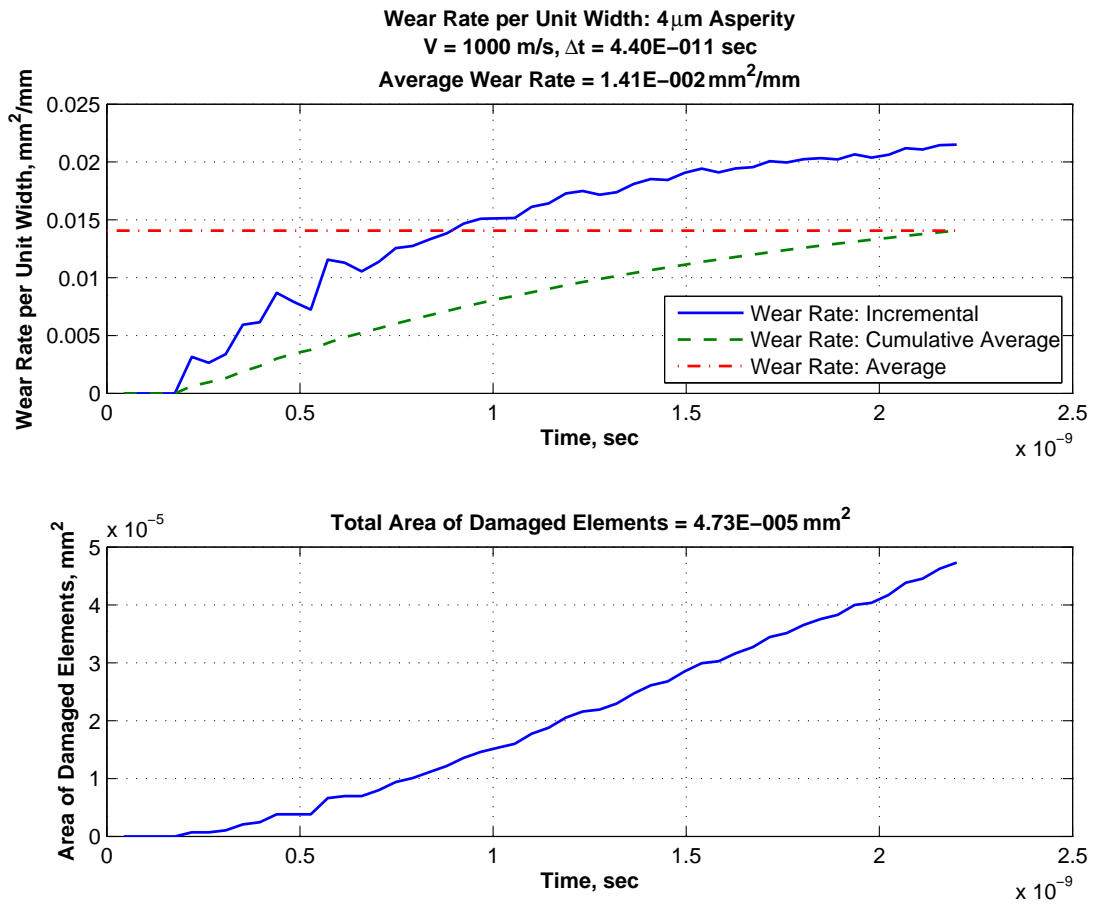


Figure B.16: Wear Rate per Unit Width, $4 \mu\text{m}$, $V = 1,000 \text{ m/s}$

B.19 $R = 4 \mu\text{m}$, $V = 1,530 \text{ m/s}$

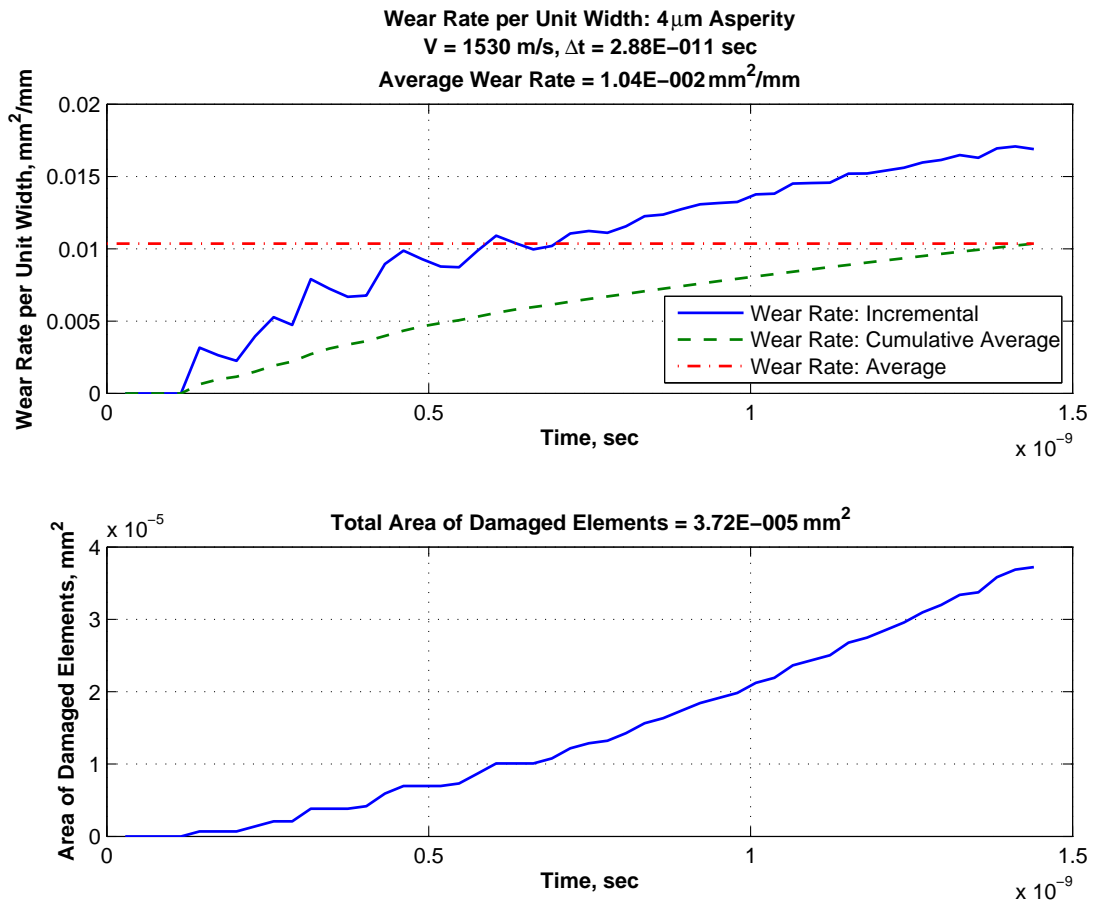


Figure B.17: Wear Rate per Unit Width, $4 \mu\text{m}$, $V = 1,530 \text{ m/s}$

B.20 Wear Rate per Unit Width: 2 μm Asperity

Wear rate per unit width calculations for the 2 μm asperity collision at the five target velocities is presented in this section.

B.21 $R = 2 \mu\text{m}$, $V = 10 \text{ m/s}$

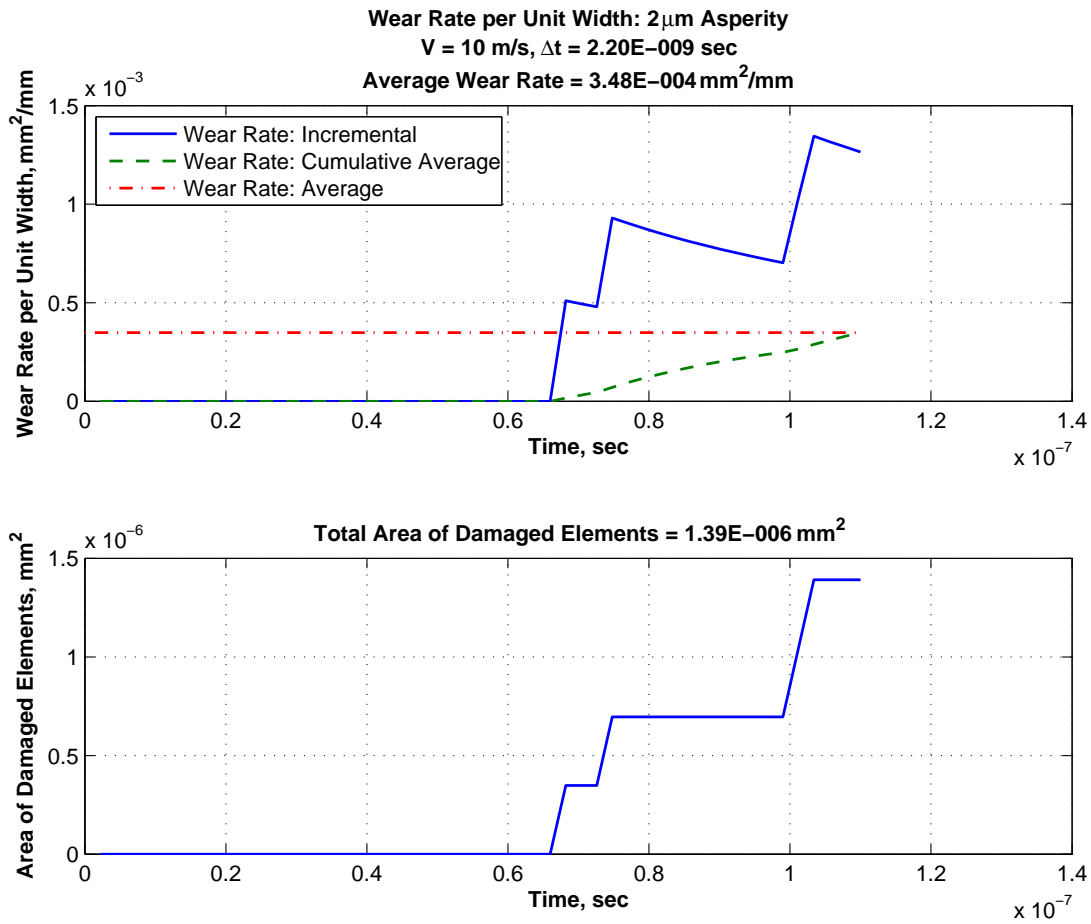


Figure B.18: Wear Rate per Unit Width, 2 μm , $V = 10 \text{ m/s}$

B.22 $R = 2 \mu\text{m}$, $V = 100 \text{ m/s}$

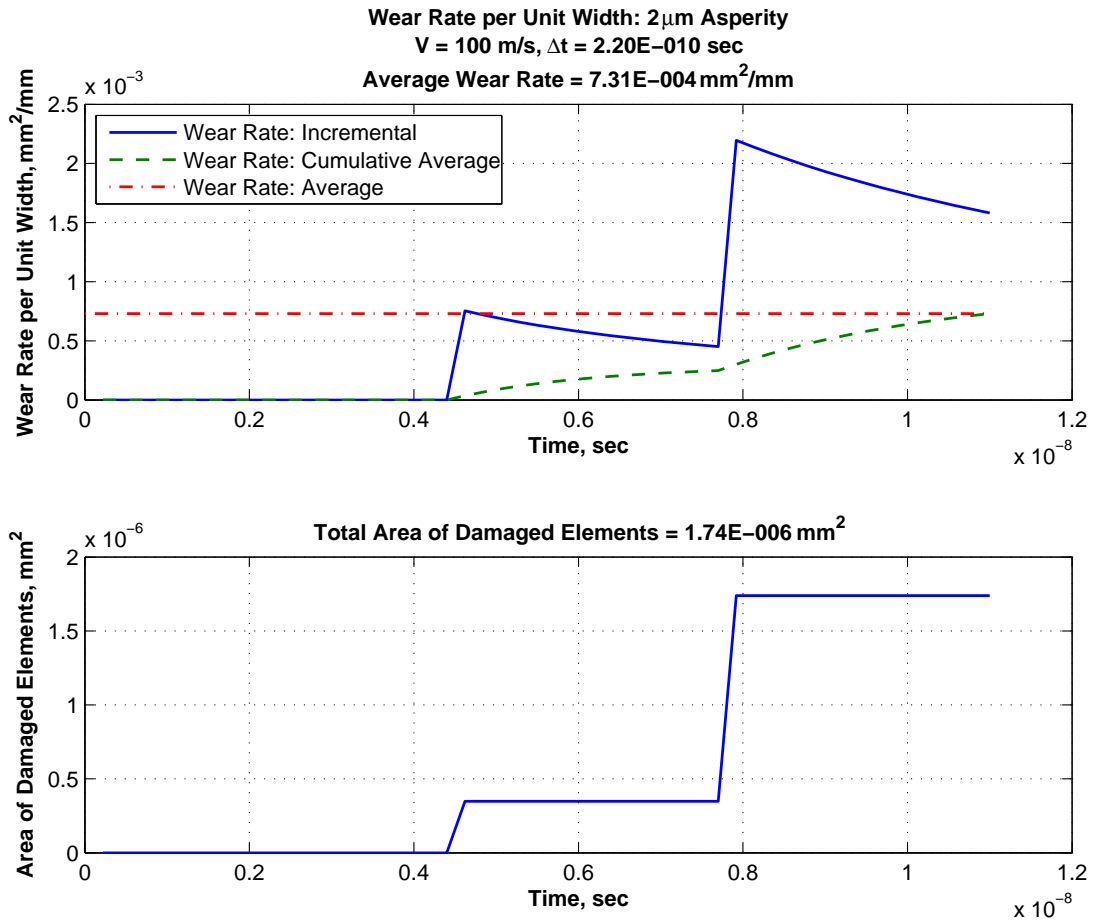


Figure B.19: Wear Rate per Unit Width, $2 \mu\text{m}$, $V = 100 \text{ m/s}$

B.23 $R = 2 \mu\text{m}$, $V = 500 \text{ m/s}$

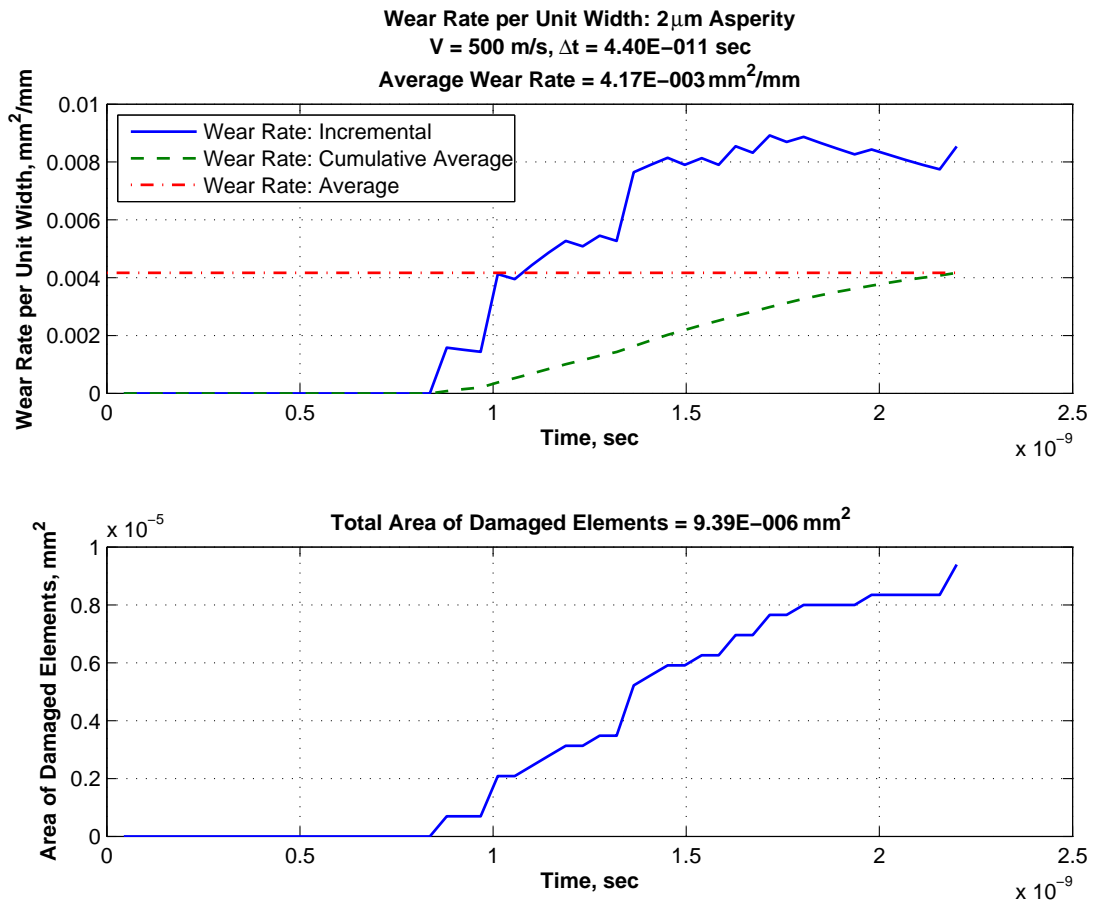


Figure B.20: Wear Rate per Unit Width, $2 \mu\text{m}$, $V = 500 \text{ m/s}$

B.24 $R = 2 \mu\text{m}$, $V = 1,000 \text{ m/s}$

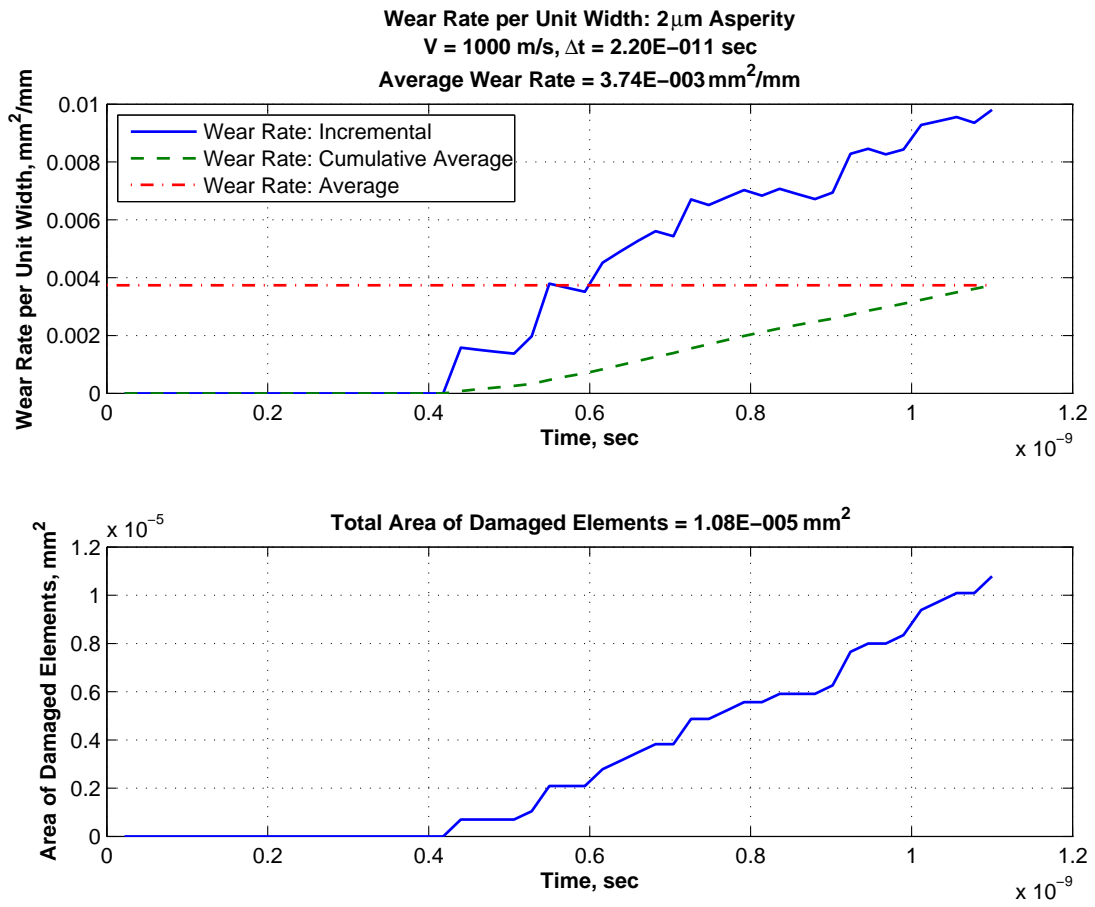


Figure B.21: Wear Rate per Unit Width, $2 \mu\text{m}$, $V = 1,000 \text{ m/s}$

B.25 $R = 2 \mu\text{m}$, $V = 1,530 \text{ m/s}$

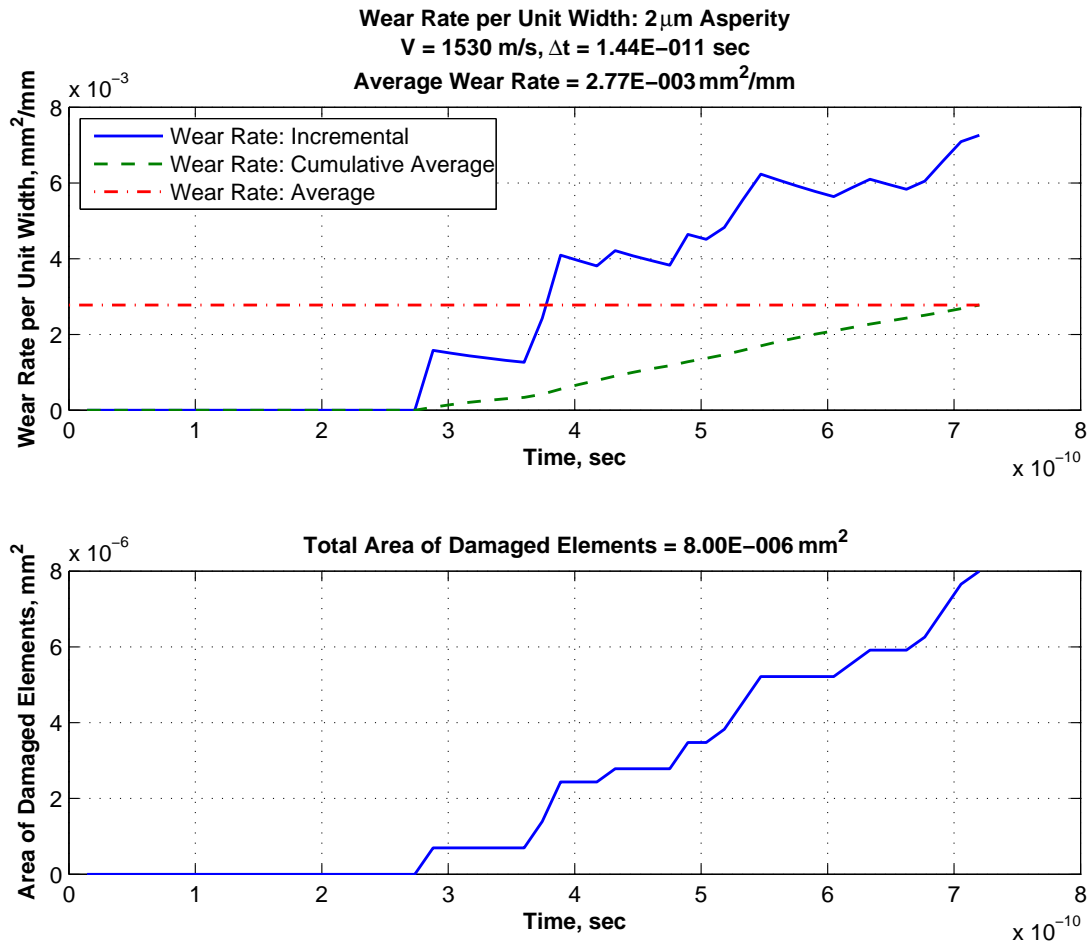


Figure B.22: Wear Rate per Unit Width, $2 \mu\text{m}$, $V = 1,530 \text{ m/s}$

Bibliography

1. *Atlas of Stress-Strain Curves*. ASM International, Materials Park, 2002.
2. *Hypersonic Upgrade Program (HUP) Super Roadrunner Over/Under Data Report, Mission 80X-G1*. Technical Report, 846th Test Squadron, 46th Test Group, Holloman AFB, New Mexico, 2004.
3. *Holloman High Speed Test Track Design Manual*. Technical Report, 846th Test Squadron, 46th Test Group, Holloman AFB, New Mexico, 2008.
4. Archard, J. F. "Contact and Rubbing of Flat Surfaces," *Journal of Applied Physics*, 24(8):981–988, August 1953.
5. Archard, J. F. "The Temperature of Rubbing Surfaces," *Wear*, 2(6):438–455, October 1959.
6. Archard, J. F. and W. Hirst. "The Wear of Metals Under Unlubricated Conditions," *Proceedings of the Royal Society of London. Series A, Mathematical and Physical Sciences*, 236(1206):397–410, 1956.
7. Ashby, M. F. and S. C. Lim. "Wear-Mechanism Maps," *Scripta Metallurgica et Materialia*, 24(5):805–810, May 1990.
8. ASTM. *Standard Terminology Relating to Wear and Erosion, G-40-01*. ASTM International, West Conshohocken, Pennsylvania, 2001.
9. ATI Allvac, Inc., 2020 Ashcroft Ave, PO Box 5030, Monroe, North Carolina, 28110. *VascoMax Technical Data Sheet*, June 2008. [Www.allvac.com](http://www.allvac.com).
10. Bayer, R. G. *Wear Analysis for Engineers*. HNB Publishing, New York, 2002.
11. Bayer, R. G. *Engineering Design for Wear*. Marcel Dekker, Inc., New York, 2004.
12. Bayer, R. G. *Mechanical Wear Fundamentals and Testing*. Marcel Dekker, Inc., New York, 2004.

13. Benabdallah, H. and D. Olender. "Finite Element Simulation of the Wear of Polyoxymethylene in Pin-on-disc Configuration," *Wear*, 261(11-12):1213–1224, December 2006.
14. Bhushan, B. *Introduction to Tribology*. John Wiley & Sons, New York, 2002.
15. Bogdanovich, P. N. and D. V. Tkachuk. "Thermal and Thermomechanical Phenomena in Sliding Contact," *Journal of Friction and Wear*, 30(3):153–163, 2009.
16. Boley, B. A. and J. H. Weiner. *Theory of Thermal Stresses*. Dover Publications, Inc., New York, 1997.
17. Bowden, F. P. and E. H. Freitag. "The Friction of Solids at Very High Speeds. I. Metal on Metal. II. Metal on Diamond," *Proceedings of the Royal Society of London. Series A, Mathematical and Physical Sciences*, 248:350–367, November 1958.
18. Bowden, F. P. and P. A. Persson. "Deformation, Heating and Melting of Solids in High-speed Friction," *Proceedings of the Royal Society of London. Series A, Mathematical and Physical Sciences*, 260:433–458, March 1961.
19. Bowden, F. P. and K. E. W. Ridler. "Physical Properties of Surfaces. III. The Surface Temperature of Sliding Metals. The Temperature of Lubricated Surfaces," *Proceedings of the Royal Society of London. Series A, Mathematical and Physical Sciences*, 154(883):640–656, May 1936.
20. Bowden, F. P. and P. H. Thomas. "The Surface Temperature of Sliding Solids," *Proceedings of the Royal Society of London. Series A, Mathematical and Physical Sciences*, 223(1152):29–40, April 1954.
21. Burton, C. A. *A Finite Element Study Of Sliding Friction Between Rough Surfaces*. Master's Thesis, University of Dayton, Dayton, Ohio, 2009.
22. Burton, C. A. and R. A. Brockman. "Frictional Interactions in High-speed Sliding Contact." *Proceedings of the 50th AIAA/ASME/ASCE/AHS/ASC Structures*,

Structural Dynamics and Materials Conference. AIAA, Palm Springs, California, 4-7 May 2009.

23. Cameron, G. and A. Palazotto. "An Evaluation of High Velocity Wear," *Wear*, 265(7-8):1066–1075, September 2008.
24. Cameron, G. J. *An Evaluation of High Velocity Wear*, AFIT/GAE/ENY/07-M06. Master's Thesis, Air Force Institute of Technology, Wright-Patterson AFB, OH, 2007.
25. Chmiel, A. J. *Finite Element Simulation Methods for Dry Sliding Wear*, AFIT/GAE/ENY/08-M03. Master's Thesis, Air Force Institute of Technology, Wright-Patterson AFB, OH, 2008.
26. Cinnamon, J. D. *Analysis and Simulation of Hypervelocity Gouging Impacts* AFIT/DS/ENY/06-01. Ph.D. Dissertation, Air Force Institute of Technology, Wright-Patterson AFB, OH, 2006.
27. Cinnamon, J. D. and A. N. Palazotto. "Metallographic Examination and Validation of Thermal Effects in Hypervelocity Gouging," *Journal of Pressure Vessel Technology*, 129(1):133–141, February 2007.
28. Cinnamon, J. D., A. N. Palazotto, and N. S. Brar. "Further Refinement of Material Models for Hypervelocity Gouging Impacts." *Proceedings of the 47th AIAA/ASME/ASCE/AHS/ASC Structures, Structural Dynamics and Materials Conference*. AIAA, Newport, Rhode Island, 1-4 May 2006.
29. Cinnamon, J. D., A. N. Palazotto, and Z. Keenan. "Material Characterization and Development of a Constitutive Relationship for Hypervelocity Impact of 1080 Steel and VascoMax 300," *International Journal of Impact Engineering*, 33(1-12):180–189, December 2006.
30. Cinnamon, J. D., A. N. Palazotto, and A. G. Szmerekovsky. "Further Refinement and Validation of Material Models for Hypervelocity Gouging Impacts," *AIAA Journal*, 46(2):317–327, 2008.

31. Cinnamon, J. D., A. N. Palazotto, A. G. Szmerekovsky, and R. J. Pendleton. "Further Investigation of a Scaled Hypervelocity Gouging Model and Validation of Material Constitutive Models." *Proceedings of the 47th AIAA/ASME/ASCE/AHS/ASC Structures, Structural Dynamics and Materials Conference*. AIAA, Newport, Rhode Island, 1-4 May 2006.
32. Cowan, R. S. and W. O. Winer. "Frictional Heating Calculations." *Friction, Lubrication, and Wear Technology: ASM Handbook, Volume 18*, 39–44. ASM International, 1992.
33. Dassault Systèmes. *ABAQUS v6.8 Analysis User's Manual*. Dassault Systèmes, Providence, Rhode Island, 2008.
34. Farrell, R. M. and T. S. Eyre. "The Relationship Between Load and Sliding Distance in the Initiation of Mild Wear in Steels," *Wear*, 15(5):359–372, May 1970.
35. Hall, A. M. and C. J. Slunder. *The Metallurgy, Behavior, and Application of the 18-Percent Nickel Maraging Steels*. Technical Report NASA SP-5051, National Aeronautics and Space Administration, Washington, D.C., 1968.
36. Hooser, M. D. "Simulation of a 10,000 Foot per Second Ground Vehicle." *Proceedings of the 21st AIAA Advanced Measurement Technology and Ground Testing Conference*. AIAA, Denver, Colorado, 19-22 June 2000.
37. Hooser, M. D. and A. Schwing. "Validation of Dynamic Simulation Techniques at the Holloman High Speed Test Track." *Proceedings of the 38th AIAA Aerospace Sciences Meeting and Exhibit*. AIAA, Reno, Nevada, 10-13 January 2000.
38. Hutchings, I. M. "The Challenge of Wear." *Wear - Materials, Mechanisms and Practice*, Tribology in Practice Series, 1–7. Chichester, England: John Wiley & Sons, 2005.
39. Incropera, F. P. and D. P. DeWitt. *Fundamentals of Heat and Mass Transfer*. John Wiley & Sons, New York, 1990.

40. Janna, W. S. *Engineering Heat Transfer*. CRC Press, Boca Raton, 2009.
41. Johnson, G. R. and W. H. Cook. “A Constitutive Model and Data for Metals Subjected to Large Strains, High Strain Rates and High Temperatures.” *Proceedings of the 7th International Symposium on Ballistics*. April 1983.
42. Johnson, R. L., M. A. Swikert, and E. E. Bisson. *Friction at High Sliding Velocities*. Technical Report NACA-TN-1442, Flight Propulsion Research Laboratory, National Advisory Committee for Aeronautics, Cleveland, Ohio, October 1947.
43. Kato, K. “Classification of Wear Mechanisms/Models.” *Wear - Materials, Mechanisms and Practice*, Tribology in Practice Series, 9–20. Chichester, England: John Wiley & Sons, 2005.
44. Korkegi, R. H. and R. A. Briggs. “The Hypersonic Slipper Bearing - A Test Track Problem,” *Journal of Spacecraft & Rockets*, 6(2):210–212, 1969.
45. Krupovage, D. J. *Rail Friction & Slipper Wear on the Holloman High Speed Test Track*. Technical Report, Test Track Division, 6585th Test Group, Holloman AFB, New Mexico, October 1987.
46. Krupovage, D. J., L. C. Mixon, and J. D. Bush. *Design Manual for Dual Rail, Narrow Gage, and Monorail Rocket Sleds*. Technical Report, Test Track Division, 6585th Test Group, Holloman AFB, New Mexico, 1991.
47. Krupovage, D. J. and H. J. Rassmussen. *Hypersonic Rocket Sled Development*. Technical Report AD-TR-82-41, Test Track Division, 6585th Test Group, Holloman AFB, New Mexico, September 1981.
48. Laird, D. J. *The Investigation of Hypervelocity Gouging, AFIT/DS/ENY/02-01*. Ph.D. Dissertation, Air Force Institute of Technology, Wright-Patterson AFB, OH, 2002.
49. Laird, D. J. and A. N. Palazotto. “Effect of Temperature on the Process of Hypervelocity Gouging,” *AIAA Journal*, 41(11):2251–2260, 2003.

50. Laird, D. J. and A. N. Palazotto. "Gouge Development During Hypervelocity Sliding Impact," *International Journal of Impact Engineering*, 30(2):205–223, February 2004.
51. Lesquois, O., J. J. Serra, P. Kapsa, S. Serror, and C. Boher. "Degradations in a High-Speed Sliding Contact in Transient Regime," *Wear*, 201(1-2):163–170, December 1996.
52. Lim, S. C. "Recent Developments in Wear-Mechanism Maps," *Tribology International*, 31(1-3):87–97, January 1998.
53. Lim, S. C. and M. F. Ashby. "Wear-Mechanism Maps," *Acta Metallurgica*, 35(1):1–24, January 1987.
54. Lim, S. C., M. F. Ashby, and J. H. Brunton. "The Effects of Sliding Conditions on the Dry Friction of Metals," *Acta Metallurgica*, 37(3):767–772, March 1989.
55. Meyers, M. A. *Dynamic Behavior of Materials*. John Wiley & Sons, New York, 1994.
56. Minto, D. W. "Recent Increases in Hypersonic Test Capabilities at the Holloman High Speed Test Track." *Proceedings of the 38th AIAA Aerospace Sciences Meeting and Exhibit*. AIAA, Reno, Nevada, 10-13 January 2000.
57. Minto, D. W. "The Holloman High Speed Test Track Hypersonic Upgrade Program Status." *Proceedings of the 22nd AIAA Aerodynamic Measurement Technology and Ground Testing Conference*. AIAA, Saint Louis, Missouri, 24-26 June 2002.
58. Molinari, A., Y. Estrin, and S. Mercier. "Dependence of the Coefficient of Friction on the Sliding Conditions in the High Velocity Range," *Journal of Tribology*, 121(1):35–41, January 1999.
59. Molinari, J. F., M. Ortiz, R. Radovitzky, and E. A. Repetto. "Finite-Element Modeling of Dry Sliding Wear in Metals," *Engineering Computations*, 18(3/4):592–610, 2001.

60. Montgomery, R. S. "Muzzle Wear of Cannon," *Wear*, 33(2):359–368, July 1975.
61. Montgomery, R. S. "Friction and Wear at High Sliding Speeds," *Wear*, 36(3):275–298, March 1976.
62. Montgomery, R. S. "Surface Melting of Rotating Bands," *Wear*, 38(2):235–243, July 1976.
63. Põdra, P. and S. Andersson. "Simulating Sliding Wear with Finite Element Method," *Tribology International*, 32(2):71–81, February 1999.
64. Philippon, S., G. Sutter, and A. Molinari. "An Experimental Study of Friction at High Sliding Velocities," *Wear*, 257(7-8):777–784, October 2004.
65. Rajagopalan, S., M. A. Irfan, and V. Prakash. "Novel Experimental Techniques for Investigating Time Resolved High Speed Friction," *Wear*, 225-229(Part 2):1222–1237, April 1999.
66. Rohrbach, K. and M. Schmidt. "Maraging Steels." *Properties and Selection: Irons, Steels, and High-Performance Alloys: Metals Handbook, Volume 1*, 793–800. ASM International, 1990.
67. Saka, N., A. M. Eleiche, and N. P. Suh. "Wear of Metals at High Sliding Speeds," *Wear*, 44(1):109–125, August 1977.
68. Schmidt, M. and K. Rohrbach. "Heat Treating of Maraging Steels." *Heat Treating: ASM Handbook, Volume 4*, 219–228. ASM International, 1991.
69. The Sherwin-Williams Company, 101 Prospect Avenue N.W., Cleveland, OH 44115. *Macropoxy[®] 646-100 Fast Cure Epoxy, Mill White, Material Safety Data Sheet*, August 2009. Protective.sherwin-williams.com.
70. Smith, W. F. *Principles of Materials Science and Engineering*. McGraw-Hill, Inc., New York, second edition, 1990.
71. Suh, N. P. "The Delamination Theory of Wear," *Wear*, 25(1):111–124, July 1973.

72. Suh, N. P., S. Jahanmir, E.P. Abrahamson II, and A.P.L. Turner. “Further Investigation of the Delamination Theory of Wear,” *Journal of Lubrication Technology*, 96, October 1974.
73. Szmerekovsky, A. G. *The Physical Understanding of the Use of Coatings to Mitigate Hypervelocity Gouging Considering Real-Test Sled Dimensions AFIT/DS/ENY/04-06*. Ph.D. Dissertation, Air Force Institute of Technology, Wright-Patterson AFB, OH, 2004.
74. Szmerekovsky, A. G. and A. N. Palazotto. “Structural Dynamic Considerations for a Hydrocode Analysis of Hypervelocity Test Sled Impacts,” *AIAA Journal*, 44(6):1350–1359, 2006.
75. Szmerekovsky, A. G., A. N. Palazotto, and J. D. Cinnamon. “An Improved Study of Temperature Changes During Hypervelocity Sliding High Energy Impact.” *Proceedings of the 47th AIAA/ASME/ASCE/AHS/ASC Structures, Structural Dynamics and Materials Conference*. AIAA, Newport, Rhode Island, 1-4 May 2006.
76. Voyiadjis, G. Z., A. Lodygowski, and B. Deliktas. *Non-Local Coupling of Friction and Damage in High Velocity Wear*. Technical Report, Louisiana State University, Baton Rouge, Louisiana, 2009.
77. Wei, R. P. “Ultra High Strength Steel, Code 1225: Fe-18Ni-9Co-5Mo-Ti-Al.” *Aerospace Structural Metals Handbook*, 1–39. CINDAS LLC, 1969.
78. Wolfson, M. R. *Wear, Solid Lubrication, and Bearing Material Investigation for High-Speed Track Applications*. Technical Report AFMDC-TR-60-7, Test Track Division, Air Force Missile Development Center, Holloman AFB, New Mexico, March 1960.
79. Zukas, J. A. *Introduction to Hydrocodes*. Elsevier, Amsterdam, 2004.

Vita

Lieutenant Colonel Chad S. Hale graduated from Apple Valley High School in Apple Valley, Minnesota. He entered undergraduate studies at Brigham Young University in Provo, Utah. In April 1994, he graduated with a Bachelor of Science degree in Mechanical Engineering and was commissioned in the United States Air Force. During his first assignment, Chad was a graduate student at the Air Force Institute of Technology (AFIT), Wright-Patterson AFB, Ohio. In December 1995, he earned a Master of Science degree in Aeronautical Engineering. Following graduation from AFIT, Chad was assigned to the B-2 System Program Office where he became the B-2 aircraft performance engineer.

In March 1998, Chad was assigned to the 354th Operations Support Squadron, Eielson AFB, Alaska. During this “career broadening” assignment, he was the Chief, Airspace and Range Scheduling. While stationed in Alaska, he was selected to attend the USAF Test Pilot School (TPS) at Edwards AFB, California. In June 2001, Captain Hale graduated from the Experimental Flight Test Engineer course in TPS Class 00B, and was assigned to the 416th Flight Test Squadron at Edwards AFB. Chad spent three years as an operational flight test engineer for many USAF and foreign F-16 flight test programs.

In June 2004, Chad was assigned to the Operational Flight Program Combined Test Force at Eglin AFB, Florida. He was the Technical Director for all F-15 developmental and operational flight test programs at Eglin AFB, Florida and Nellis AFB, Nevada. While stationed at Eglin AFB, Major Hale was selected to attend AFIT for a Doctor of Philosophy program. In August 2006, he entered the Graduate School of Engineering and Management. Upon graduation, Lieutenant Colonel Hale will be assigned to the Air Force Research Laboratory, Propulsion Directorate at Wright-Patterson AFB, Ohio.

Permanent address: 2950 Hobson Way
Air Force Institute of Technology
Wright-Patterson AFB, OH 45433

REPORT DOCUMENTATION PAGE

Form Approved
OMB No. 0704-0188

The public reporting burden for this collection of information is estimated to average 1 hour per response, including the time for reviewing instructions, searching existing data sources, gathering and maintaining the data needed, and completing and reviewing the collection of information. Send comments regarding this burden estimate or any other aspect of this collection of information, including suggestions for reducing this burden to Department of Defense, Washington Headquarters Services, Directorate for Information Operations and Reports (0704-0188), 1215 Jefferson Davis Highway, Suite 1204, Arlington, VA 22202-4302. Respondents should be aware that notwithstanding any other provision of law, no person shall be subject to any penalty for failing to comply with a collection of information if it does not display a currently valid OMB control number. **PLEASE DO NOT RETURN YOUR FORM TO THE ABOVE ADDRESS.**

1. REPORT DATE (DD-MM-YYYY) 25-03-2010		2. REPORT TYPE Doctoral Dissertation		3. DATES COVERED (From — To) Sept 2006 — Dec 2009	
4. TITLE AND SUBTITLE Consideration of Wear Rates at High Velocity			5a. CONTRACT NUMBER		
			5b. GRANT NUMBER		
			5c. PROGRAM ELEMENT NUMBER		
6. AUTHOR(S) Hale, Chad S., Lieutenant Colonel, USAF			5d. PROJECT NUMBER		
			5e. TASK NUMBER		
			5f. WORK UNIT NUMBER		
7. PERFORMING ORGANIZATION NAME(S) AND ADDRESS(ES) Air Force Institute of Technology Graduate School of Engineering and Management (AFIT/EN) 2950 Hobson Way Wright-Patterson AFB OH 45433-7765				8. PERFORMING ORGANIZATION REPORT NUMBER AFIT/DS/ENY/10-08	
9. SPONSORING / MONITORING AGENCY NAME(S) AND ADDRESS(ES) Air Force Office of Scientific Research Attn: Maj Michelle Ewy 4015 Wilson Blvd, Rm 713 Arlington, VA 22203-1954 (703) 696-7297 michelle.ewy@afosr.af.mil				10. SPONSOR/MONITOR'S ACRONYM(S) AFOSR/NA	
				11. SPONSOR/MONITOR'S REPORT NUMBER(S)	
12. DISTRIBUTION / AVAILABILITY STATEMENT Approval for public release; distribution is unlimited.					
13. SUPPLEMENTARY NOTES					
14. ABSTRACT The development of the research presented here is one in which high velocity relative sliding motion between two bodies in contact has been considered. The experimental results of a VascoMax 300 maraging steel slipper sliding on an AISI 1080 steel rail during a January 2008 sled test mission were considered for the determination of high velocity wear rates. The numerical model, based on a metallographic study of a test slipper, contained all of the physical features present in order to adequately characterize high velocity wear rates. Two-dimensional, plane strain models have been implemented in the explicit finite element code, ABAQUS. Local submodel collisions between the slipper and a 6 μm radius hemispherical asperity were analyzed to determine mechanical and melt wear rates. A simplified damage criterion of maximum Mises stress was used to determine the damaged volume during the slipper and asperity collision. Overall, the model predicts a total wear volume that is approximately 36% of the total wear measured during the metallographic analysis.					
15. SUBJECT TERMS high velocity wear rate, VascoMax 300, Holloman High Speed Test Track (HHSTT), friction, finite element analysis					
16. SECURITY CLASSIFICATION OF:			17. LIMITATION OF ABSTRACT	18. NUMBER OF PAGES	19a. NAME OF RESPONSIBLE PERSON
a. REPORT	b. ABSTRACT	c. THIS PAGE			Dr. Anthony N. Palazotto
U	U	U	UU	241	19b. TELEPHONE NUMBER (include area code) (937) 255-3636, ext 4599